Università degli Studi di Torino
Scuola di Dottorato in Scienza ed Alta Tecnologia
Indirizzo di Fisica ed Astrofisica

3D silicon pixel detectors for the CT-PPS tracking system

Supervisor
Prof. Ada Solano

Co-supervisor
Dr. Margherita Obertino

Candidate
Fabio Ravera

XXIX ciclo
Anni accademici 2014-2015-2016
Settore Scientifico Disciplinare: FIS/01

“With one thousand volts you can take out a signal also from a brick.”

Gino Bolla

Sommario - Abstract

La misura dei processi di produzione centrale esclusiva permetterà di estendere il programma di fisica di LHC sia nel settore elettrodebole sia in QCD, con una particolare sensibilità per la fisica oltre il Modello Standard. A questo scopo è stato recentemente installato il CMS-TOTEM Precision Proton Spectrometer, disegnato per operare nelle normali condizioni di funzionamento di LHC ad alta luminosità. Lo spettrometro è costituito da rivelatori di posizione e di tempo, installati a circa 210 m dal punto d'interazione da entrambe le parti di CMS, all'interno di strutture mobili chiamate 'Roman pot' che permettono di avvicinarsi al fascio. I protoni diffusi che emergono intatti dall'interazione, avendo perso solo una piccola parte del loro impulso, vengono deviati dai magneti di LHC all'esterno dell'inviluppo del fascio e misurati con piani di rivelatori a pixel di silicio. I rivelatori di tempo sono invece necessari per determinare il vertice primario, facendo uso delle informazioni sul tempo di arrivo dei due protoni nei due lati, e in base a questo ridurre fortemente il fondo dovuto ai molti eventi di pile-up. A causa dell'alta fluenza di radiazioni a cui saranno soggetti i rivelatori, stimata in $\sim 3 \times 10^{15}$ $\mathrm{n_{eq}/cm^2}$, per il tracciatore di CT-PPS sono stati scelti sensori a pixel di silicio detti 3D. Sensori provenienti dai tre principali produttori (CNM, FBK e SINTEF) sono stati misurati in laboratorio e su fascio, prima e dopo averli irraggiati, per valutarne le caratteristiche e le prestazioni. Nel rivelatore finale vengono utilizzati i sensori CNM, unitamente al chip di lettura sviluppato per l'upgrade di Fase 1 del tracciatore a pixel di CMS. Due stazioni di sei piani ciascuna sono state assemblate, testate e installate alla fine dello shutdown invernale 2016/2017 di LHC. Il commissioning del rivelatore è in corso di svolgimento, attraverso l'uso del software di acquisizione sviluppato a partire da quello del tracciatore a pixel centrale. Il rivelatore è stato calibrato ed è in grado di prendere dati all'interno della catena di acquisizione di CMS. I dati del primo run di allineamento sono stati raccolti con successo e la loro analisi è in corso.

The measurement of central exclusive production will allow extending the LHC physics program in both the electroweak sector and in QCD, with unique sensitivity to physics beyond the Standard Model. To this purpose, the CMS-TOTEM Precision Proton Spectrometer (CT-PPS), with capability to operate in regular LHC high-luminosity conditions, has been recently installed. It consists of tracking and timing detectors located at $\simeq 210$ m from the CMS interaction point on both sides, within movable structures called Roman pots that can go very close to the beam. Scattered protons emerging intact from the interaction with only a small fraction of their momentum lost are bent by the LHC magnets out of the beam envelope and measured by means of planes of silicon pixel detectors. The primary vertex determination, obtained using the timing information of the two protons on both arms, allows to strongly reduce the expected background due to the large number of pile-up events. Because of the high irradiation fluence ($\sim 3 \times 10^{15}$ n_{eq}/cm^2) that the detectors will have to stand, 3D pixel sensors have been chosen for the CT-PPS tracker. Devices from the main 3D sensor producers (CNM, FBK e SINTEF) were measured in laboratory and on beam, before and after irradiation, in order to evaluate their characteristics and performances. CNM sensors, bump-bonded to the readout chips developed for the Phase I upgrade of the CMS pixel tracker, are used in the final detector. Two stations of six planes each have been assembled, tested and installed at the end of the 2016/2017 LHC winter shutdown. The commissioning of the detector is presently ongoing, making use of the DAQ software developed from that of the CMS central pixel tracker. The detector has been calibrated and is able to run within the CMS DAQ chain. Data of the first alignment run have been successfully collected and their analysis is in progress.

Contents

Introduction

The search for central exclusive production (CEP) in high energy proton-proton collisions at the Large Hadron Collider (LHC) could open new lines of analysis in the field of the physics beyond the Standard Model. CEP events $pp \to pXp$ are characterized by colliding protons that remain intact after the interaction, losing only a small fraction of their momentum, and by a centrally produced system X well separated in rapidity from the scattered protons. Thanks to the absence of proton remnants, CEP provides a unique method to search for rare events in a particularly clean environment. If the kinematics of the leading protons can be measured and the central system X is identified, the event is fully reconstructed so that the background for these processes is low and the sensitivity high.

The CMS-TOTEM Precision Proton Spectrometer (CT-PPS) has been added to the Compact Muon Solenoid (CMS) experiment in order to reconstruct the leading protons. The LHC magnets between the interaction point and the detector stations are used for deflecting the scattered protons out of the beam envelope. Detectors are housed into Roman pots, a movable mechanical structure that allows going very close to the beam $(10-20\sigma)$. Knowing the magnet properties, the so-called optics, it is possible to determine energy and momentum of the protons by reconstructing their trajectory. In order to precisely measure the proton kinematics, the required resolution of the tracking detectors is a few tens of micrometers. For this reason, silicon pixel detectors have been chosen for this application.

With the aim of studying low cross-section electroweak and quantum chromodynamics physics in CEP, the CT-PPS apparatus has been designed for taking data in nominal, high luminosity, running conditions of the LHC. For reducing the background due to the expected large number of pile-up interactions per bunch crossing, it is crucial to match the two leading protons with the event measured in the central detector. Timing detectors have been installed on both sides of the interaction point to measure the difference in arrival time of the two protons in order to determine the vertex position. A time resolution of a few tens of picoseconds is required to have a vertex resolution of a few millimeters.

CT-PPS operated for the first time in 2016 with detectors in a preliminary configuration. Silicon strip and diamond detectors, for tracking and timing respectively, allowed to collect ~ 15 fb^{-1} of data, which are currently being analyzed.

The high irradiation fluence the CT-PPS detectors have to stand makes the choice of radiation tolerant technologies a requirement for this application. 3D silicon pixel sensors demonstrated a superior radiation hardness and were hence chosen as baseline for the tracker design. Thanks to the columnar electrodes implemented perpendicularly to the sensor surface, the inter-electrode distance can be strongly reduced with respect to the planar technology, improving the charge collection efficiency after irradiation.

The subject of this thesis is the study of 3D sensors and their use in the construction of the CT-PPS pixel tracker.

3D sensors from different producers were considered for the module production and tested in laboratory and with beams in order to evaluate the characteristics of the different layouts. Based on these results and the producer availability, sensors for CT-PPS were fabricated at CNM Barcelona.

Sensors bump-bonded to the readout chips were qualified and assembled in the final detector packages, which were tested in the expected conditions of cooling and secondary vacuum before installing them in the LHC tunnel at the end of the extended technical stop 2016/2017. Since then the commissioning work is going on and protons from the first collision runs have been successfully detected.

The thesis is organized as follows:

- Chapter 1 presents the CT-PPS physics case. Particular attention is dedicated to central exclusive production and specifically to two promising channels for the search of new physics: exclusive dijet production and central WW production for its sensitivity to anomalous quartic gauge couplings.
- Chapter 2 describes the CMS and the CT-PPS detectors.
- Chapter 3 is an introduction to silicon sensor features and the pixel detector concept.
- Chapter 4 introduces the 3D sensors technology and describes the studies done in laboratory and at test beams of different 3D sensor technologies to evaluate their characteristics.
- Chapter 5 is dedicated to the 3D sensor production by CNM for the final CT-PPS tracker detector assembly. Results of the tests done in laboratory and with beams to verify that the module performances fulfill the CT-PPS requirements are discussed.
- Chapter 6 describes the detector assembly, test, installation, and commissioning. The DAQ software developed for calibrations and data taking is also described.
- Chapter 7 presents the summary and conclusions of the work done for this thesis.

Chapter 1

The CT-PPS physics case

The CMS-TOTEM Precision Proton Spectrometer (CT-PPS) is a magnetic spectrometer that uses the LHC magnets between the CMS Interaction Point (IP) and the detector stations at $\simeq 210$ m from the IP on both sides to bend protons that have lost a small fraction of their momentum out of the beam envelope. It consists of a silicon tracking system to measure the position and direction of the protons, and a set of timing counters to measure their arrival time.

Detectors in a preliminary configuration ("Exploratory phase") have been operational since June 2016, whilst the baseline detectors will start taking data in June 2017 and are expected to integrate as much as possible of the Run 2 luminosity (about 100 fb^{-1}). The system will allow extending the LHC physics program in both the electroweak sector (W, Z and photons) and in Quantum Chromodynamics (QCD), with unique sensitivity to physics beyond the Standard Model (SM) [1].

The main physics goal of the CT-PPS apparatus is the study of the central exclusive production (CEP) [2] process, $p + p \to p \oplus X \oplus p$, where $\oplus$ indicates a "rapidity gap" between the outgoing protons and the object X centrally produced, a particle or a more complex but well defined state. The rapidity gaps are regions in which no primary particle is found. CEP provides a unique method to access a variety of physics topics, in particularly clean experimental conditions thanks to the absence of proton remnants.

The X state can be characterized by the central detector, while its four-momentum can be derived from the two scattered protons, irrespective of the decay mode. Moreover, the use of proton timing information for the primary vertex determination allows reducing the expected background due to the copious number of interactions per bunch crossing (mean number of pile-up events $\mu \gtrsim 30$) during nominal, high luminosity running conditions of the LHC. Further rejection is achievable by requiring the kinematics of the system measured in the central detector to match with the kinematics of the two protons and, in some channels, by requiring a small number of tracks associated to the primary vertex.

The mass of the central state X can be easily determined from the fraction of momentum lost by the two reconstructed protons, ξ_1 and ξ_2, with the formula $M_X = \sqrt{\xi_1 \xi_2 s}$, where $\sqrt{s}$ is the energy in the center of mass of the two incoming protons. At the LHC, the M_X values that can be reached are therefore significantly larger than at previous colliders (ISR, SPS and Tevatron). The lower limit on the measurable ξ, and hence on M_X, is fixed by the minimal distance of approach of the CT-PPS detectors to the beam. This value, usually expressed in terms of standard deviations of the beam transverse dimension at the detector z position, in high luminosity conditions can be reasonably assumed to be 15σ. As a consequence, the X mass accessible with CT-PPS is $M_X \gtrsim 300$ GeV. The CEP reactions producing such high masses have a cross section in the order of 1 fb, and therefore require high integrated luminosities.

CEP is a t-channel process and the four-momentum-transfer squared, t, follows in first approximation an exponentially decreasing law. Since the two protons remain intact after the interaction, the carrier in the t-channel must be neutral in flavour, color and charge. In the SM the possible allowed t-channel exchanges are therefore photons, gluons (if their colour is neutralised) and Z-bosons:

- In the case of gluon-gluon interactions, the color exchange results in a multi-hadron final state. However, in multi-jet exclusive production a third gluon of opposite colour is exchanged to screen the colour charge. Such reactions provide accessibility to the proton structure and QCD studies. Further details will be given in Sec. 1.1. Because the outgoing protons remain intact and scatter through small angles, to a very good approximation the di-gluon system obeys a $J_z = 0$, C-even, P-even, selection rule [3], where J_z is the projection of the total angular momentum along the proton beam axis. The rule allows an immediate determination of the quantum numbers (J^{PC}) of any new resonance found in CEP events, in addition to the mass derived from the two scattered protons.

- In the case of γ-gluon interactions, the virtual photon emitted by one proton scatters with the color singlet formed by gluons emitted by the second proton, yielding to the photoproduction of vector mesons (ρ, ϕ, J/ψ, $\psi(2S)$, υ). However, since the masses of the final states are lower than the minimum mass reconstructed by CT-PPS, it is not possible to reconstruct both the scattered protons.

- In the case of $\gamma\gamma$ interactions, LHC can be seen as a photon-photon collider, with a maximum center of mass energy of $\sqrt{s_{\gamma\gamma}} \sim 1$ TeV, much larger than at any other e^+e^- collider, even if with a lower luminosity. The most interesting X states are lepton couples (e^+e^-, $\mu^+\mu^-$ or $\tau^+\tau^-$) and di-boson (W^+W^-, ZZ) and $\gamma\gamma$ pairs. In the former case, the possibility to match the mass measured from the two protons with the mass reconstructed from the two leptons, M_X^{ll}, allows to obtain an almost background free sample. For $M_X^{ll} \gtrsim$ 300 GeV, the production cross section is only $\sim$ 1.5 fb [4, 5] per flavour, however with still enough events for the 100 fb^{-1} foreseen to be collected by CT-PPS. The $\gamma\gamma \to ZZ$ and $\gamma\gamma \to \gamma\gamma$ processes are suitable for searches of new physics. The WW channel will be described in detail in Sec. 1.2.

Whilst CT-PPS is conceived to work at high luminosity and hence, as said above, gives access to low cross section processes, a wide range of higher cross section processes becomes accessible to CMS and TOTEM (with a different configuration of the TOTEM detectors than for CT-PPS) varying the integrated luminosity and the dispersion function β^* at the interaction point [6, 7]. Figure 2.11 shows the TOTEM proton acceptance for different β^* values. Any CEP mass can be studied provided the cross section is of order 1 pb or higher. At intermediate β^* of 90 m, the CMS and TOTEM Collaborations collected data together in special runs in 2012 and 2015, obtaining excellent pseudorapidity coverage for both tracking and calorimetry, ideal condition for studies of exclusive production and semi-hard diffraction in the range of four-momentum-transfer $|t| \gtrsim\sim 10^{-2}$ GeV^2 [8].

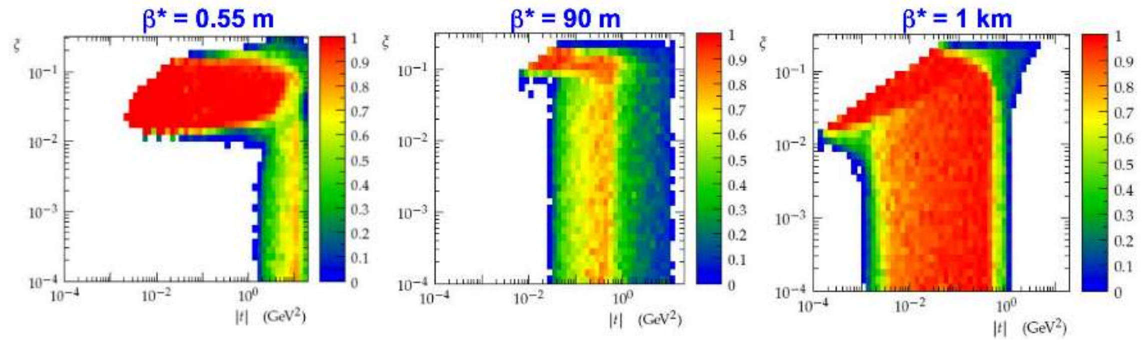

Figure 1.1: Simulated TOTEM proton acceptance as a function of the four-momentum transfer squared t and of the fractional momentum loss ξ [8].

1.1 Jet diffractive production

In gluon-gluon interactions the color exchange results in multi-hadron production. In the case of multi-jet events in central exclusive production, $p + p \to p \oplus X \oplus p$, in order to preserve the color singlet a further gluon is exchanged between the two protons. One or more rapidity gaps are formed if no other parton interactions occurs. The probability that this does not happen, and therefore the rapidity gap survives, is called rapidity gap survival probability and indicated with $\hat{S}^2$.

Hard exclusive QCD processes with $X = jj$ or $X = jjj$, where j represents a jet, are described in QCD as originating from $gg \to gg$, ggg or $q\bar{q}g$, while $q\bar{q}$ dijet are strongly suppressed by the $J_z = 0$ rule, in favour of pure gluon dijets in most cases [9]. Exclusive two- and three-jet events allow interesting studies of both perturbative and non-perturbative QCD. The cross section depends on the unintegrated generalized parton distribution functions, on the Sudakov suppression of gluon radiation (which would cause additional hadron production) and on $\hat{S}^2$. It is sensitive to the gluon density in the Pomeron[1] [10] and allows constraining the diffractive parton distribution functions determined at HERA and testing the Pomeron universality between HERA and LHC.

1.1.1 Exclusive dijet production

The potential to measure exclusive dijet events in CEP was investigated for the CT-PPS TDR [11]. Those studies are based on the 2015 optics with $\beta^* = 0.8$ m and crossing angle at the IP between the two beams of 290 μrad. The signal sample was simulated with ExHuME (v1.3.2) [12], while for the background Single Diffractive (SD) and Double Pomeron Exchange (DPE) exclusive events were generated with POMWIG (v2.0) interfaced with HERWIG (v6.521) [13], and multijet QCD events were simulated using PYTHIA (v8.175) [14]. The generated events were processed through the GEANT4 (v9.4p03) [15] simulation of the CMS central detector and the standard reconstruction chain. Proton transport from the IP to the CT-PPS detectors was performed with HECTOR [16], which is integrated in the CMSSW (CMS SoftWare) [17] detector simulation and reconstruction package.

The acceptance for dijet events when requiring that both protons are reconstructed in CT-PPS is shown in Fig. 1.2(a). Assuming a detector approach to the beam at 15σ, exclusive systems with masses in the $350 - 1700$ GeV range can be reconstructed with an efficiency greater than 5%. The expected mass resolution as a function of the dijet invariant mass is shown in Fig. 1.2(b).

The correlation between the time-of-flight difference Δt of the two leading protons arriving

[1] Pomeron $I\!P$ is historically the name of the colorless exchange

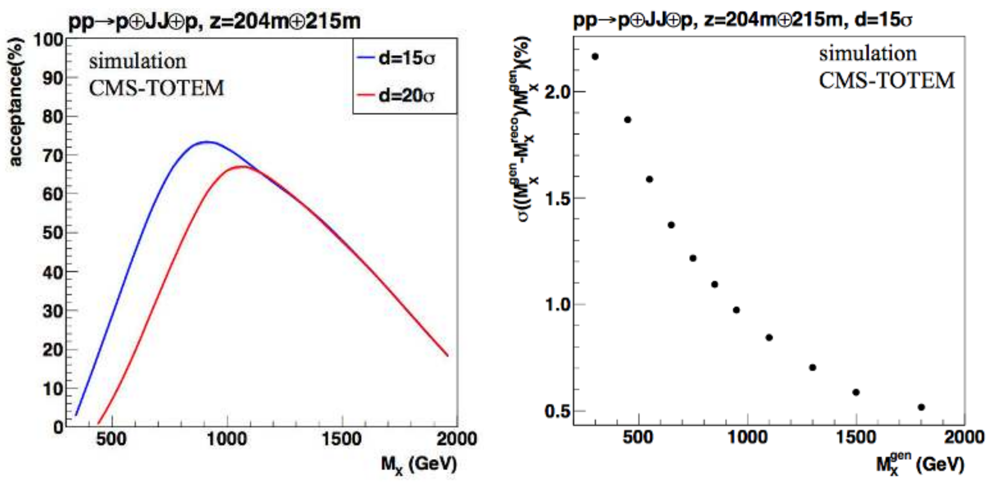

(a) Dijet invariant mass acceptance.

(b) Mass resolution as a function of the dijet invariant mass.

Figure 1.2: Dijet mass acceptance (a) and resolution (b) assuming the tracking detectors approach the beam at 15σ [11].

in opposite arms and the leading-jet z-vertex position is shown in Fig. 1.3. Considering a CT-PPS timing resolution of 10 (30) ps approximately 60% (50%) of signal events are kept while reducing the backgrounds by a factor of 33 (18).

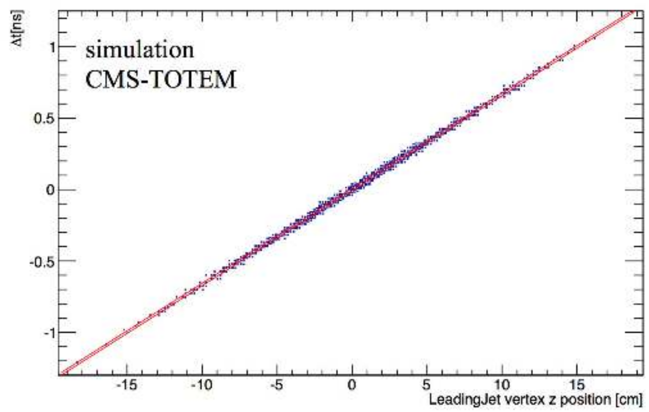

Figure 1.3: Correlation between the leading-jet z-vertex position and the time-of-flight difference between the two leading protons measured by CT-PPS on opposite sides of the IP[11]. The distribution is shown for exclusive dijet events assuming a time resolution of 10 ps. The two straight lines contain $\sim 60\%$ of the events.

A further event selection is achieved by matching the kinematics of the two protons and that of the dijet system. A constrain can be set through the ratio $R_{jj} = M_{jj}/M_X$ between the mass reconstructed from the dijet system, M_{jj}, and that from the protons, M_X: $0.70 < R_{jj} < 1.15$. Another cut is imposed on the difference between the rapidity of the dijet system, y_{jj}, and that from the central system reconstructed from the protons, y_X, requiring $\|(y_{jj} - y_X)\| < 0.1$. Figure 1.9 shows the distributions of these two variables for signal and background events.

The track multiplicity associated to the dijet vertex can also be used to discriminate between exclusive signal events and background. The technique, developed in Ref. [18], accounts for the exclusivity of the process by means of the variables N^{ϕ}_{tracks} and N^{η}_{tracks}, which count the extra tracks both in ϕ and η, respectively. N^{ϕ}_{tracks} counts the number of particles that are per-

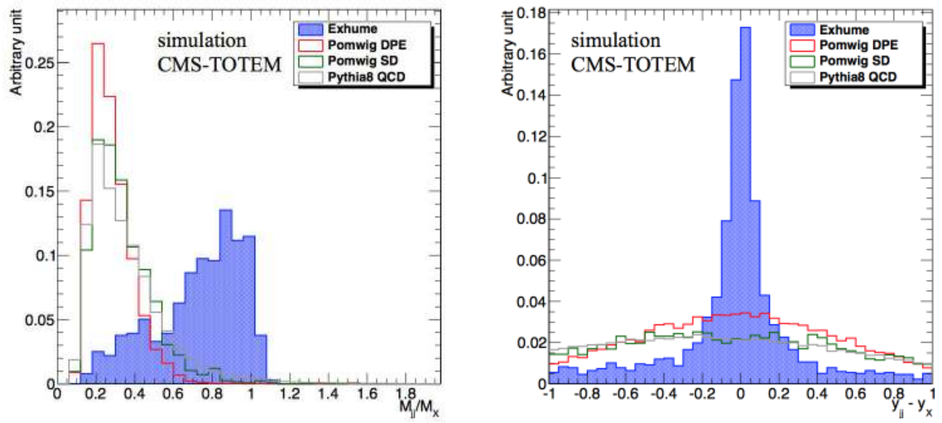

(a) Dijet mass fraction $R_{jj} = M_{jj}/M_X$.
(b) Rapidity difference of dijet system, y_{jj}, and proton system, y_X.

Figure 1.4: Dijet mass fraction (a) and dijet- and proton-system rapidity difference (b) distributions for signal and backgrounds [11].

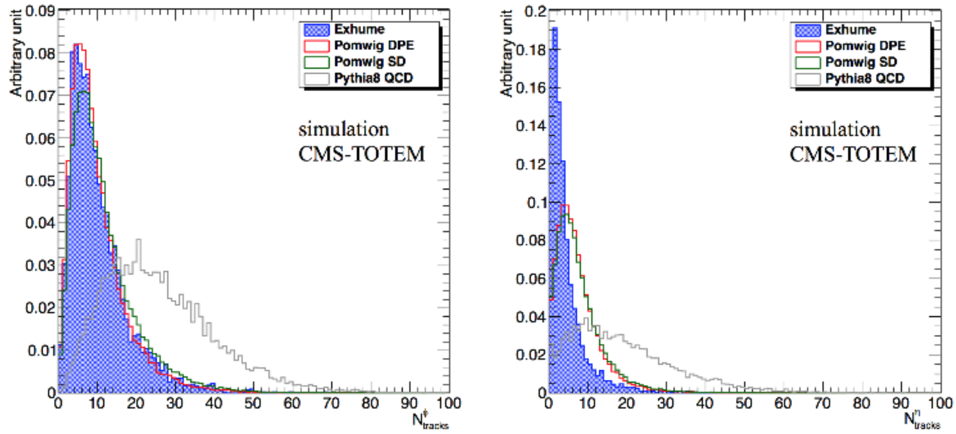

(a) N^{ϕ}_{tracks} distribution.
(b) N^{η}_{tracks} distribution.

Figure 1.5: Number of tracks outside the dijet system in ϕ (a) and η (b) associated to the dijet vertex for exclusive dijet and background processes [11].

pendicular to the plane formed by the two-jet system in the region $0.54 < \phi < 2.60$. Indicating with $j^{\eta max}$ the jet which has the maximum η and with $j^{\eta min}$ the one with the minimum η, N^{η}_{tracks} is the sum of all particles with $\eta > \eta_{j^{\eta max}} + 1$ and with $\eta < \eta_{j^{\eta min}} - 1$ with $|\eta| < 2$. The distributions of these variables, for both signal and background, are shown in Fig. 1.5. Events are kept if $N^{\phi}_{tracks} \leq 9$ and $N^{\eta}_{tracks} \leq 2$.

Figure 1.6 shows the evolution of signal and background as a function of the mentioned cuts. A timing resolution of 10 ps and a scenario with mean pile-up of $\mu = 50$ events are considered. At the end of the selection procedure, the signal-over-background ratio is $S : B \simeq 1 : 8$, which allows interesting studies of QCD as well as the search for new resonances. Similar studies have also been done in a lower pile-up condition, $\mu = 25$, and the signal-over-background ratio increases to $S : B \simeq 1 : 3$.

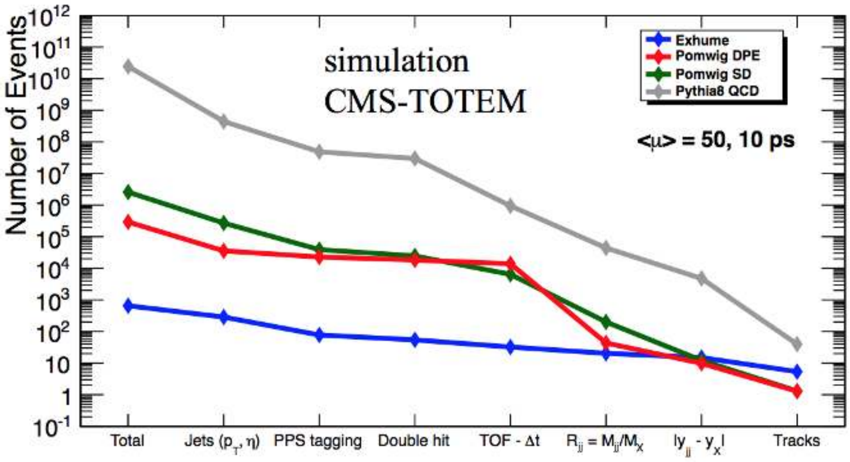

Figure 1.6: Event yields for signal and background processes as a function of the cuts applied [11]. A time resolution of 10 ps and an average pile-up multiplicity of $\mu = 50$ are assumed. Yields are normalized to an integrated luminosity of 1 fb^{-1}.

1.2 Sensitivity to anomalous quartic gauge coupling

The measurement of the photon-photon production of a pair of W-bosons provides sensitivity to Anomalous Quartic Gauge Couplings (AQGCs) of the gauge bosons. Measurements of exclusive two-photon production of W-boson pairs in the process $pp \to pW^+W^-p$ were performed at $\sqrt{s}$ of 7 and 8 TeV with the CMS detector [19, 20], using an integrated luminosity of 19.7 fb^{-1} and considering $\mu^{\pm}e^{\mp}$ final states without proton tagging.

For the CT-PPS TDR [11], the possible improvement in the measurement of this process was investigated, assuming a total collected luminosity for the LHC Run 2 of 100 fb^{-1}. The $\gamma\gamma \to WW$ signal was generated with FPMC (v1.0) [21] using HERWIG 6.5 to simulate the W-boson decay, with the assumption of an AQGC which would enhance the SM signal. The dominant SM backgrounds come from inclusive W$^+$W$^-$ and exclusive Drell-Yan (DY) production of $\tau^+\tau^-$, which were simulated with PYTHIA (v6.426) and FPMC respectively. For the CT-PPS detectors, a closest approach to the beam of 15σ, a time resolution of 10 ps, and a tracking resolution of 10 μm were assumed.

The process is characterized by a primary vertex from the two leptons l^+l^- (where $l = e, \mu$) coming from the W-boson decays and no other tracks. Large transverse momentum of the dilepton system, $p_T(l^{\pm}l^{\mp})$, and large invariant mass, $M(l^{\pm}l^{\mp})$, are also expected. Therefore, a cut on the transverse momentum of the dilepton pair, $p_T(l^{\pm}l^{\mp}) > 30$ GeV, can reject almost all the DY background, with only a 20% reduction of the signal. Only the $e\mu$ final state was considered. The ee and $\mu\mu$ final states could also be included to enhance the sensitivity to AQGCs. However, in this case the gain is mitigated as, in order to reduce the DY background, additional cuts may be necessary. For the event selection, two leptons of opposite sign with $p_T > 20$ GeV and with a common vertex were required. Moreover, scattered protons had both to be reconstructed in the CT-PPS tracking and timing detectors.

As already described for dijet events in Sec. 1.1, the WW vertex can be correlated to the vertex reconstructed from the two protons, thanks to the time-of-flight difference measured by the CT-PPS timing detectors. The correlation is shown in Fig. 1.7(a) for signal and in Fig. 1.7(b) for background events, assuming a timing resolution of 10 ps. In these conditions, the WW background can be reduced by a factor of 10.

The number of extra tracks associated to the dilepton vertex is significantly larger for inclusive WW events. A selection cut $N_{tracks} < 10$ is expected to suppress $\sim$ 90% of the background while keeping $\sim$ 90% of the signal. A signal-to-background ratio of 1 : 1 can be

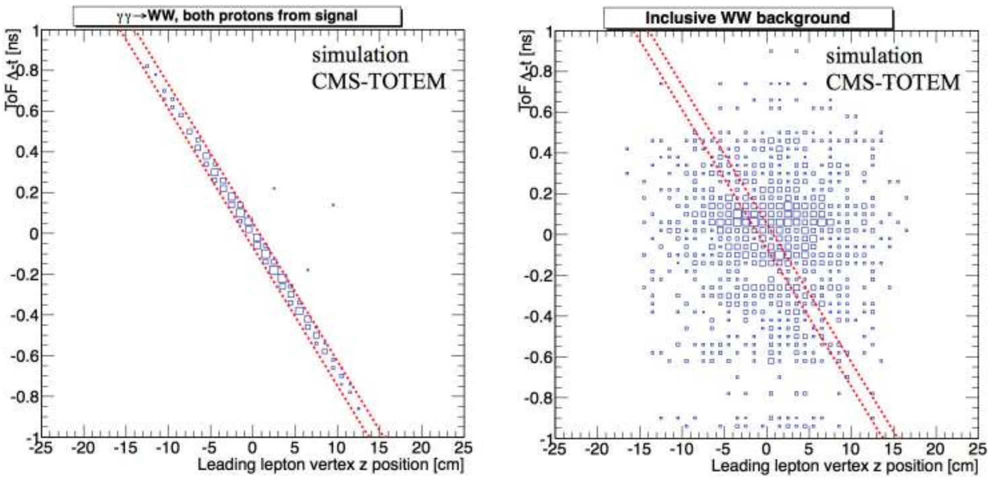

(a) WW exclusive signal. (b) WW inclusive background.

Figure 1.7: Time-of-flight difference between the two leading protons arriving in the CT-PPS detectors on opposite sides of the IP as a function of the z coordinate of the vertex reconstructed from the two leptons [11]. The dotted lines show an ideal window retaining close to 100% of signal events.

achieved applying a cut on the maximum number of tracks in the central detector.

The mass acceptance for WW signal events, requiring both protons reconstructed in the tracking detectors, and the mass resolution obtained from the measurement of the proton kinematics are shown in Fig. 1.8. The cross section times the acceptance for the SM exclusive WW process is already sizable at the small masses which can be reconstructed by CT-PPS ($M_X \simeq 300 \div 400$ GeV). A closer approach to the beam of 10σ could increase the signal yield by a factor of two, still maintaining the misreconstructed signal event yields more or less constant.

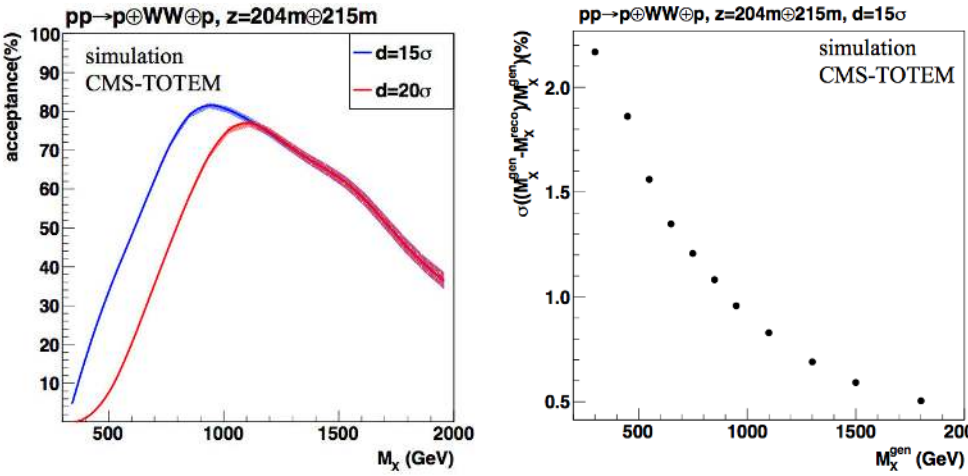

(a) WW invariant mass acceptance. (b) Mass resolution as a function of the WW invariant mass.

Figure 1.8: WW mass acceptance (a) and resolution (b) assuming an approach to the beam of the tracking detectors at 15σ [11].

The selected events have been used to estimate the expected limits on the AQGC parameters a_0^W/Λ^2 and a_C^W/Λ^2. Figure 1.9(a) shows the 95% Confidence Level (CL) limits for these two parameters that would be reached after 100 fb^{-1} of collected luminosity, considering a timing resolution of 10 and 30 ps. A comparison with the 2011 CMS results [19] is shown in Fig. 1.9(b), where an improvement of 2 orders of magnitude is visible.

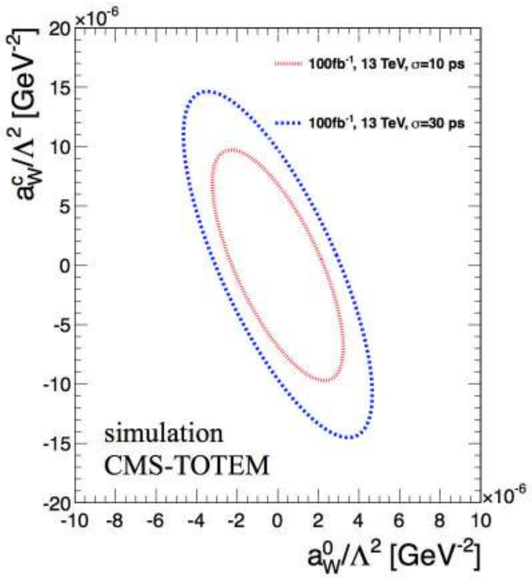

(a) 95% CL limits on AQGC coupling constants for 10 and 30 ps timing resolution.

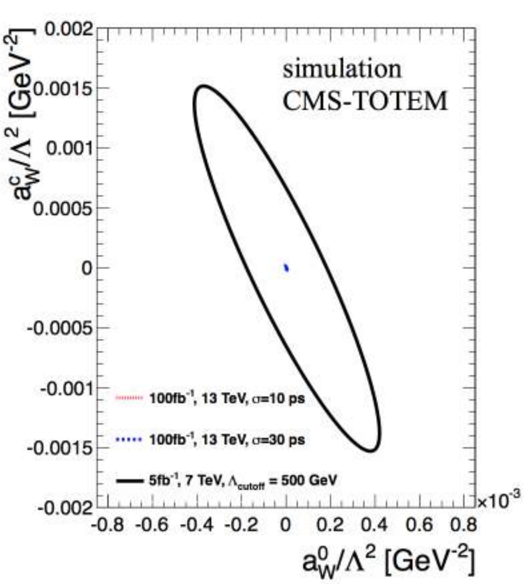

(b) Comparison between limits imposed by 2011 CMS results [19] and CT-PPS expectations.

Figure 1.9: 95% CL limits on AQGC coupling constants with CT-PPS (a) and comparison with 2011 CMS results (b) [11].

1.3 Status of the CT-PPS 2016 data analysis

CT-PPS operated for the first time in 2016 and collected a total of $\sim$ 15 fb^{-1} in regular, high-luminosity runs of LHC. Several analyses are ongoing on this data sample, summarized here. The results are not yet public.

The search for central semi-exclusive production of dimuon pairs [22, 23], $pp \to p\mu^+\mu^-p^{(*)}$ with mass $m(\mu\mu) > 110$ GeV, is one channel currently investigated. The two muons produced in the interaction are measured in the central CMS apparatus and one final state proton in CT-PPS. The second proton may either remain intact or dissociate into a low mass state, indicated by the symbol p^*, and escapes undetected in the forward region opposite to that of the measured proton.

Central dimuon production is dominated by the diagrams shown in Fig. 1.10, in which both protons radiate quasi-real photons that interact and produce the two muons. The left and center diagrams result in at least one intact final state proton and this interaction is considered for the analysis ongoing. However, since the acceptance for detecting both protons starts only above invariant dimuon masses of $\sim$ 400 GeV, the Standard Model cross section of dimuon production with both leading protons detected is very small.

By using events with only a single proton tagged, the final sample will contain a mixture of elastic ($pp \to p\mu^+\mu^-p$) and single proton-dissociation ($pp \to p\mu^+\mu^-p^*$) events, but the acceptance is extended to lower masses where the cross section is non-negligible. The rightmost diagram is considered as a background as well as Drell-Yan events in which a proton from another interaction in the same bunch crossing (pile-up) is associated to the dimuon system.

Central semi-exclusive dimuon production has never been measured directly and is of interest

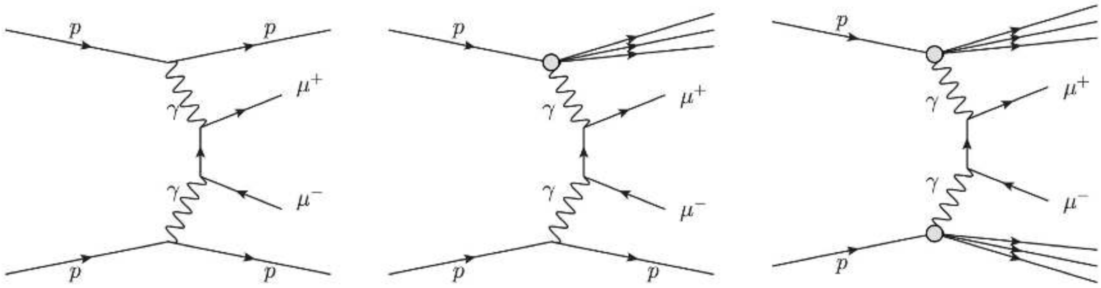

Figure 1.10: Production of muon pairs by $\gamma\gamma$ fusion. The elastic (left), single proton dissociation (center), and double proton dissociation (right) topologies are shown.

because it constitutes a background to the exclusive reaction $pp \to p\mu^+\mu^-p$ when the final-state protons are not measured. In turn, the exclusive process is interesting because deviations from the expected cross section, which is well known, may be an indication of new physics.

In central semi-exclusive events, the momentum of the two muons can be used to determine that of the proton, and hence the proton fractional momentum loss ξ. This indirect measurement of ξ can be compared with the direct one obtained with CT-PPS. The comparison can be used to suppress the background; it also provides proof of the correct functioning of CT-PPS and can be used to estimate its resolution. An analysis on the dimuon channel is ongoing on the first ~ 10 fb^{-1} of the 2016 data taking and it is waiting for the approval hence the results are not yet public[2].

On the same dataset, also the search for dielectron events is ongoing. The interactions considered are the same of the dimuon channel. Also in this case the cross section with both leading protons detected is very small and hence the sample considered is a mixture of CEP events with only one proton detected and single proton-diffractive dielectron events.

Large efforts are also being made to investigate the diphoton channel in central exclusive production. Fig. 1.11 shows the SM leading processes with two photons and two intact protons in the final state. The first diagram (Fig. 1.11(a)) corresponds to exclusive QCD diphoton production via gluon exchange, where the second gluon ensures that the exchange is colorless leading to intact protons in the final state; the second diagram (Fig. 1.11(b)) corresponds to the diphoton production channel. It is worth noticing that quark, lepton and W loops need to be considered in order to get the correct SM cross section for diphoton production as shown in Fig. 1.12. The QCD induced processes from the Khoze-Martin-Ryskin model [24] are dominant at low masses whereas the photon induced ones (QED processes) dominate at higher diphoton masses.

In the assumption of a new physics mass scale Λ heavier than the experimentally accessible energy E, all new physics manifestations can be described using an effective Lagrangian valid for $\Lambda \gg E$. Among these operators, the pure photon dimension-eight operators

$$\mathcal{L}_{4\gamma} = \zeta_1^{\gamma} F_{\mu\nu}F^{\mu\nu}F_{\rho\sigma}F^{\rho\sigma} + \zeta_2^{\gamma} F_{\mu\nu}F^{\nu\rho}F_{\rho\lambda}F^{\lambda\mu} \tag{1.3.1}$$

can induce the $\gamma\gamma\gamma\gamma$ process, highly suppressed in the SM [26].

Loops of heavy charged particles contribute to the 4γ couplings as $\zeta_i^{\gamma} = \alpha_{\text{em}}^2 Q^4 m^{-4} N c_{i,s}$, where $c_{1,s}$ is related to the spin of the heavy particle of mass m running in the loop and Q is its electric charge. The factor N counts all additional multiplicities such as color or flavour. These couplings scale as $\sim Q^4$ and are enhanced in the presence of particles with charges greater than

[2]At the time of closing the writing of the thesis, the first CMS Public Analysis Summary (PAS) based on the 2016 CT-PPS data has been made available: "Evidence for proton-tagged, central semi-exclusive production of high-mass muon pairs at 13 TeV with the CMS-TOTEM Precision Proton Spectrometer", CMS-PAS-PPS-17-001, May 24th, 2017.

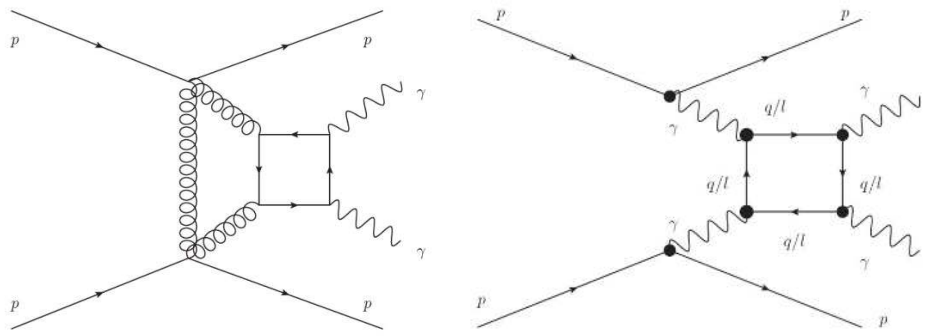

(a) Diphoton QCD exclusive production. (b) Diphoton production via photon exchanges.

Figure 1.11: Diphoton leading order production diagrams allowed by SM with intact protons in the final state [25].

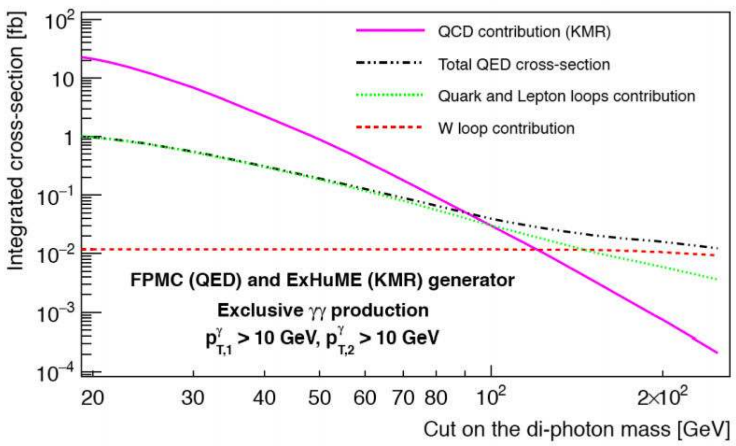

Figure 1.12: Diphoton production cross section as a function of the diphoton mass requesting two intact protons in the final state and the photons to have a transverse momentum larger than 10 GeV. The QCD exclusive processes (Khoze-Martin-Ryskin model) in full line dominate at low masses while QED diphoton production dominates at higher masses (dashed lines). Dashed lines correspond to W-loop and dashed-dotted lines to total QED diphoton cross section [25].

unity. For example, certain light composite fermions, characteristic of composite Higgs models, have typically electric charges of several units. For a 500 GeV vector (fermion) resonance with $Q = 3(4)$, large couplings ζ_i^γ of the order of $10^{-13} - 10^{-14}$ GeV^{-4} can be reached.

Moreover, also some SM extensions foresee non-renormalizable interactions of neutral particles that can contribute to ζ_i^γ. Such theories can contain scalar, pseudo-scalar and spin-2 resonances that couple to the photon and generate the 4γ couplings by tree-level exchange as $\zeta_i^\gamma = (f_{sm})^{-2} d_{i,s}$, where $d_{1,s}$ is related to the spin of the particle. Warped-extra dimensions also feature Kaluza-Klein (KK) gravitons [27], that can induce anomalous couplings [28]

$$\zeta_i^\gamma = \frac{\kappa^2}{8\tilde{k}^4} d_{i,2} \tag{1.3.2}$$

where $\tilde{k}$ is the IR scale that determines the first KK graviton mass and κ is a parameter that can be taken $O(1)$. For $\kappa \sim 1$, and $m_2 \lesssim 6$ TeV, the photon vertex can easily exceed $\zeta_2^\gamma \sim 10^{-14}$ GeV^{-4}.

The search for 4γ processes can be probed via the detection of two intact protons in the forward proton detectors and two energetic photons in the electromagnetic calorimeters. The backgrounds for this channel can be strongly suppressed by requiring the proton missing invariant mass to match the diphoton invariant mass within the expected resolution and the diphoton system rapidity and the rapidity of the two protons to be similar. Diphoton to missing proton mass ratio (left) and rapidity difference (right) are shown in Fig. 1.13 for background and signals with coupling values of 10^{-12} and 10^{-13} GeV^{-4} for a collected luminosity of 300 fb^{-1}.

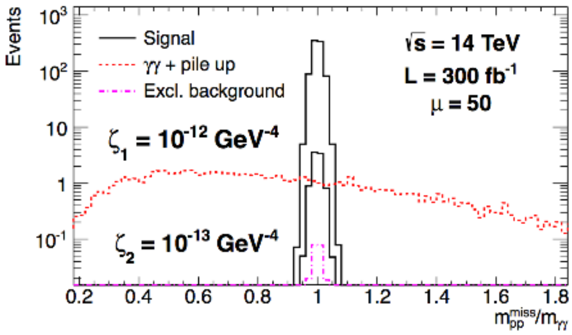

(a) Diphoton to missing proton mass ratio.

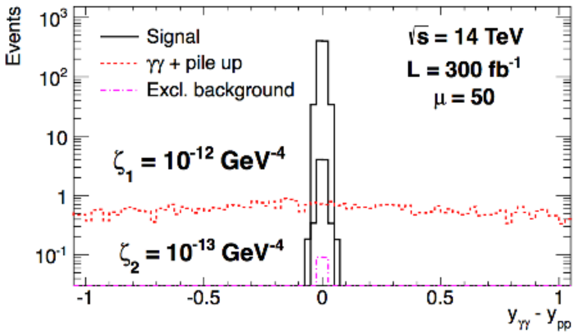

(b) Diphoton to missing proton rapidity difference.

Figure 1.13: Diphoton to missing proton mass ratio (a) and rapidity difference (b) distributions for signal coupling values of 10^{-12} and 10^{-13} GeV^{-4} and for backgrounds after requiring that the two photons are back-to-back and have about the same transverse momenta. At least one converted photon is required. The integrated luminosity is 300 fb^{-1} and the average pile-up is $\mu = 50$ [25].

Exploiting the full event kinematics with the forward proton detectors allows to completely suppress the background with a signal selection efficiency after the acceptance cuts exceeding 70%. Tagging the protons is absolutely needed to suppress the $\gamma\gamma$ + pile-up events. The sensitivities on photon quartic anomalous couplings for an integrate luminosity of 300 fb^{-1} extends up to 9×10^{-15} GeV^{-4}, justifying the search for diphoton events in central exclusive production.

Chapter 2

Detector apparatus

The CT-PPS detector will be installed as a new subsystem of the CMS experiment, which is one of the four multipurpose detectors (CMS [29], ATLAS [30], LHCb [31] and ALICE [32]) ot the Large Hardon Collider (LHC) [33].

The LHC machine is the largest accelerator ever built, with a designed center-of-mass energy up to $\sqrt{s} = 14$ TeV. It is located at CERN (Conseil Européen pour la Recherche Nucléaire, Geneva) and placed in a ring-shaped tunnel 26.7 km long, dug at ~ 100 m underground at the border between France and Switzerland. The LHC has two vacuum pipes where protons or lead nuclei circulate in opposite directions. The beams cross each other in four points (Interaction Points or IPs), in correspondence of the four experiments. Proton beams are guided in the collider thanks to superconductive dipoles kept at a temperature below 2 K, that provide magnetic fields of $\sim$ 8 T. Protons are organized in bunches of $\sim 1.1 \cdot 10^{11}$ protons separated by 25 ns. Each beam may contain up to 2808 bunches that are accelerated by 16 radiofrequency cavities.

In Fig. 2.1 the CERN accelerator complex is shown. The acceleration of protons is done in steps, starting from H_2 molecules entering in a duoplasmatron proton source that ionizes the hydrogen. Protons then enter in the Linac2 where they are accelerated to 50 MeV. The next step is the Proton Synchrotron Booster (PSB), which is composed of four rings where the particle energy is increased to 1.4 GeV. Protons are then injected in the Proton Synchrotron (PS) where their energy rises to 26 GeV. The successive acceleration is provided by the Super Proton Synchrotron (SPS), which injects the bunches in the LHC with an energy of 450 GeV. The final boost is provided by the LHC that increments the beam energy up to 7 TeV.

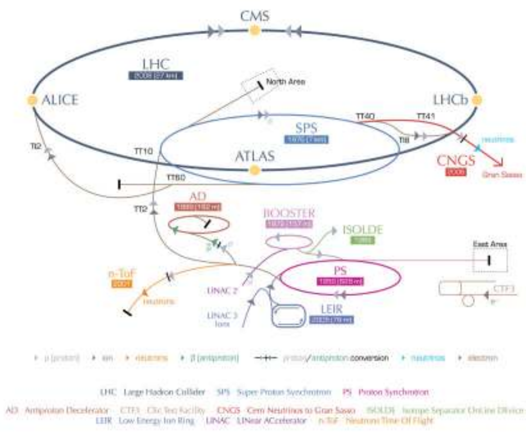

Figure 2.1: The complex of accelerators at CERN [34].

In 2016, the LHC reached an instantaneous luminosity peak of $1.2 \cdot 10^{34}$ cm^{-2}s^{-1}. The instantaneous luminosity can be expressed as

$$\mathcal{L} = \frac{N_b N_p^2 f}{S_{\text{eff}}} \tag{2.0.1}$$

where N_b denotes the number of colliding bunches, N_p the number of protons per bunch, and f is the revolution frequency around the ring. S_{eff} is the effective cross section of the beam and depends on the beam focus as well as on the beam crossing angle and the size of the bunches.

The rate dN/dt of events of a given physics process can be calculated multiplying the instantaneous luminosity by the cross section σ of the process under investigation:

$$\frac{dN}{dt} = \sigma \cdot \mathcal{L} \tag{2.0.2}$$

The integrated luminosity L is obtained integrating the value of $\mathcal{L}$ as a function of time, and determines the total expected number of events for a certain physics channel.

In this Chapter the CMS and TOTEM detectors will be described (Sec. 2.1 and 2.2), with particular attention to the CT-PPS tracking and timing detectors (Sec. 2.4). Section 2.5 is dedicated to the Roman Pots, movable devices which will host the CT-PPS detectors and approach them very close to the LHC beam.

2.1 Compact Muon Solenoid (CMS)

The Compact Muon Solenoid (CMS) [29] is a general purpose detector which allows the accurate measurements of trajectory, momentum and energy of the particles produced in the high-energy *pp* collisions of the LHC. It is made of different subdetectors such that the sum of their measurements allows to fully characterize the *pp* events. These components can be gathered together in four main subsystems:

- the superconducting solenoid of 6 m internal diameter, providing a magnetic field of 3.8 T that bends charged particles as a function of their mass and momentum;
- the tracking detector, composed of pixel and strip detectors that precisely determine the particle trajectories. The measured curvature gives the information of the particle momentum;
- the calorimetry system, made of electromagnetic and hadronic calorimeters that measure the energy of particles;
- the muon system, constituted of resistive plate chambers, drift tubes and cathode strip chambers that measure muon trajectories.

Each detector is designed to deal with multiple collisions (pile-up or PU) occurring during each bunch crossing (or BX). Bunch crossings have a frequency of 40 MHz, hence all detectors need a fast readout together with a fine granularity, which is needed to deal with the huge amount of particles produced in each collision. Another consequence of the high luminosity of the LHC is that the detectors have been built to face with a high radiation damage.

The CMS detector is located at the so-called Point 5 (P5) of the LHC ring, in a underground cavern near Cessy, France. It is cylindrically symmetric around the beam pipe and also symmetric along the direction of the beam with respect to the interaction point. The overall size reaches 28.7 m of length and 15.0 m of diameter, and with its 14000 tons CMS is the heaviest detector ever build. A sketch of the CMS detector is shown in Fig. 2.2. Within the solenoid volume are a silicon pixel and strip tracker, a lead tungstate crystal electromagnetic calorimeter, and a brass and scintillator hadron calorimeter, each composed of a barrel and two endcap sections. Forward calorimeters extend the pseudorapidity coverage provided by the barrel and endcap detectors. Muon detectors are embedded in the steel flux-return yoke outside the solenoid, being muons the only particles exiting the detector inner layers.

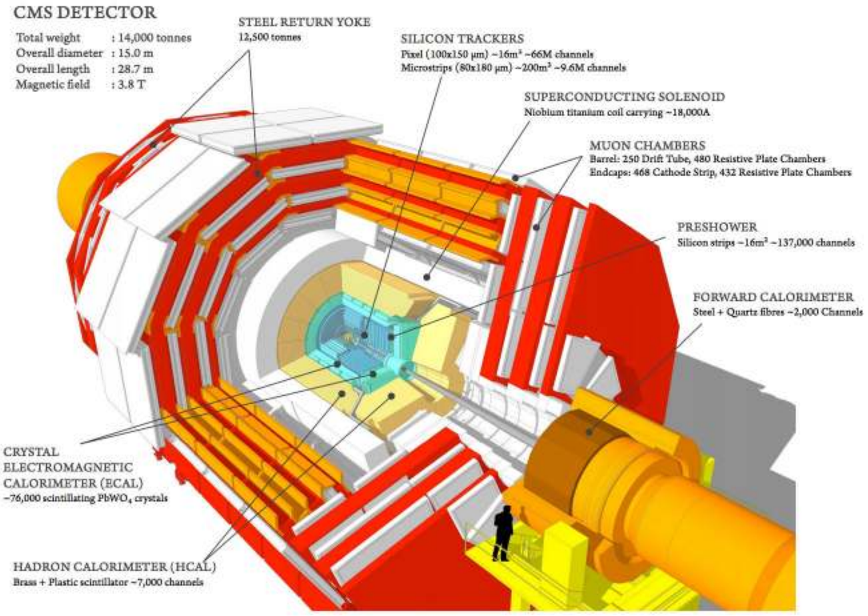

Figure 2.2: A cutaway view of the CMS detector [34].

A conventional coordinate system is used for the CMS detector. The origin is located at the nominal collision point position, the x-axis points to the center of the accelerator ring, the y-axis points vertically upwards and the z-axis points along the beam axis to make the coordinate system right-handed. Since the detector has a cylindrical symmetry around the beam pipe, it is often used a cylindrical or spherical coordinate system. The azimuthal angle ϕ is measured in the range $(0,2\pi)$ starting from the x-axis in the x-y plane and the polar angle θ in the range $(0,\pi)$ from the positive the z-axis. The radial coordinate r is measured from the axis origin.

Instead of the polar angle, two other variables are often used: the pseudorapidity

$$\eta = -\ln\left(\tan\frac{\theta}{2}\right) = \frac{1}{2}\ln\frac{|\vec{p}| + p_L}{|\vec{p}| + p_L} \tag{2.1.1}$$

where $\vec{p}$ is the particle momentum and p_L is its longitudinal component, or the rapidity

$$y = \frac{1}{2}\ln\frac{E + p_L}{E + p_L} \tag{2.1.2}$$

where E is the particle energy.

It is also common to use transverse components of energy and momentum, E_T and p_T, respectively. These variables are defined in the x-y plane and are useful since the their initial value is zero and it is expected to be the same in the final state, allowing the search for non-detected particles.

In the following subsections the CMS components will be briefly described starting from the innermost and proceeding towards the outer ones. The last subsection will be dedicated to the trigger event selection.

2.1.1 Pixel tracking detector

The pixel detector is located at the closest distance from the interaction point [35]. Until 2016 it was composed by three coaxial barrel layers (BPix), 53 cm long, at a radius of 4.4, 7.3

and 10.2 cm, and two forward disks (FPix) on both positive and negative z sides at ± 34.5 and ± 46.5 cm. Fig. 2.3 shows a sketch of the this pixel detector.

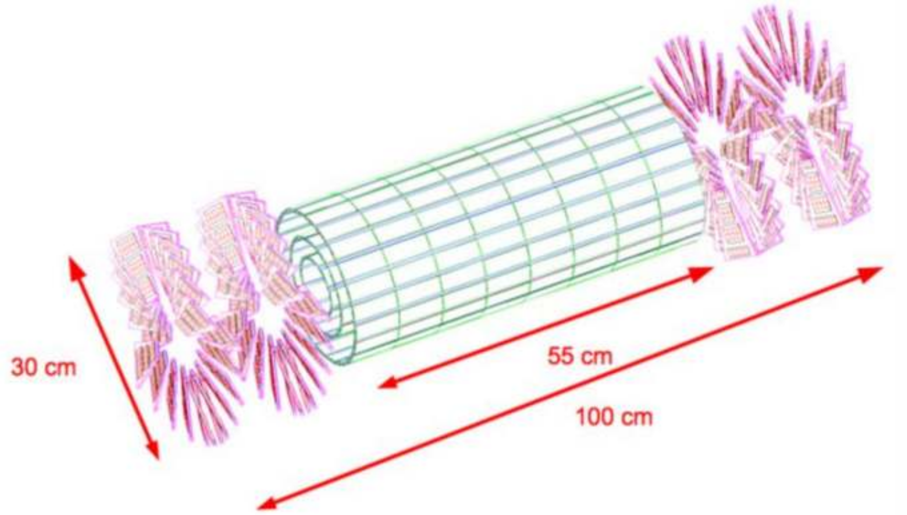

Figure 2.3: Schematic view of the CMS pixel derector [36].

The detector consisted of 1440 silicon sensors modules segmented with a pixel pitch of 100×150 μm^2 for a total of ~ 66 million channels operating in a zero-suppression mode. Only hit pixels send the information to the front-end electronics, with an analog signal containing the address of the pixel, coded in multi-threshold levels [37], and the charge deposited in the pixel. This last value can be used to measure the charge sharing in case the particle crosses multiple pixels.

The geometry was carefully chosen to yield optimal spatial resolution: barrel modules are oriented parallel to the magnetic field, while endcap sensors are tilted by 20°. By this, the charge carriers produced by a charged particle traversing the detector are distributed over several pixels, either by the Lorentz drift or by the geometrical arrangement, and the resolution can improve up to 10 μm in $r\phi$ direction and $20 - 45$ μm along the z-axis, depending on the incidence angle of the particle track [38].

The pixel detector covers a pseudorapidity region up to $|\eta| < 2.2$ with 3 hits and $2.2 < |\eta| < 2.5$ with 2 hits, with a single hit detection efficiency greater than 99%.

The detector was designed and optimized for a luminosity of 10^{34} cm^{-2}s^{-1} and a maximum level-1 trigger rate of 100 kHz. However, the LHC already exceeded its design luminosity limit and in case it would reach twice this value, the inefficiency coming from the pixel detector would be unacceptable for the operations. For this reason, a new pixel detector has been just installed in the extended year-end technical stop 2016/2017 of the LHC.

The new pixel detector is shown in Fig. 2.4 compared to the old one. The new configuration has four barrel layer, improving the track quality, and 3 disks for each side, allowing 4 measurements per track up to $|\eta| < 2.5$.

The pixel sensor has remained the same, but a new ReadOut Chip (ROC) has been developed, which is able to cope with a higher pixel occupancy and has a digital output with higher readout speed. The same ROC is used for the CT-PPS tracking detector, therefore its characteristics will be presented in detail in Sec. 4.2.

2.1.2 Strip tracking detector

Around the pixel detector, the silicon strip tracker is located [40]. In contrast with the pixel sensors, strips are segmented only on one direction, strongly reducing the manufacturing costs

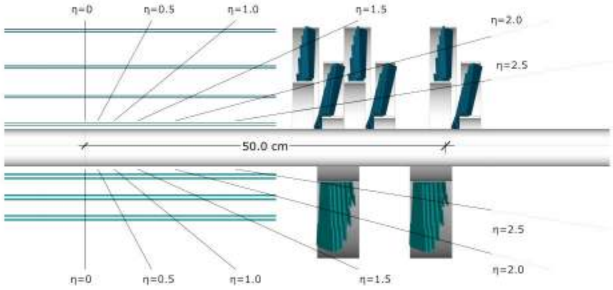

Figure 2.4: A comparison of the layers and disks in the old (bottom) and new pixel detectors (top). For the upgraded design, there are three endcap disks per side, each separated into an inner and outer ring. The inner ring is tilted by 12° towards the interaction point. The disks are positioned to maximize the four-hit coverage [39].

of both sensors and electronics and allowing the coverage of large areas.

The layout of the CMS tracker is shown in Fig. 2.5. The Tracker Inner Barrel (TIB) and Tracker Inner Disks (TIDs) are located around the pixel detector, while the Tracker Outer Barrel (TOB) and the Tracker EndCaps (TECs) are the outer most part of the tracker. The whole tracker (pixels and strips) is thermal shielded from the rest of the detector for operating it at low temperature (since the first long shutdown, or LS1, the detectors are operated at -10°C and -15°C for pixels and strips, respectively) to mitigate the effects from radiation damage and reduce the leakage current through the sensors. An air-tight sealing shields the tracker volume from the surrounding detector and allows flushing it with dry air.

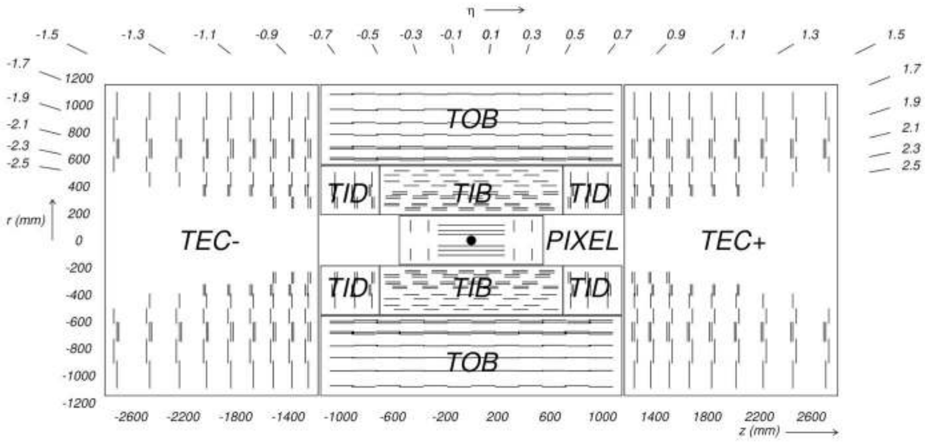

Figure 2.5: Section of the CMS tracking system on a radial plane, with the positions of the subdetectors and their modules [29]. Double lines indicate back-to-back mounted modules for stereo angle interpolation.

Some of the modules consist of two strip sensors mounted back-to-back and rotated by a small stereo angle with respect to each other to provide a measurement of the missing coordinate. This can be done in the offline analysis by matching the information of the two detectors, but it works only for low occupancy events due to ambiguities.

2.1.3 Electromagnetic calorimeter

The CMS Electromagnetic CALorimenter (ECAL) [41] measures the energy of particles primarily interacting via the electromagnetic force. ECAL is a hermetic detector up to a pseudorapidity of $|\eta| < 3$. It is divided in a Barrel (EB) and an Endcap (EE) calorimeter and the last one is completed by the additional presence of a preshower (ES). A quarter of the detector is shown in Fig. 2.6.

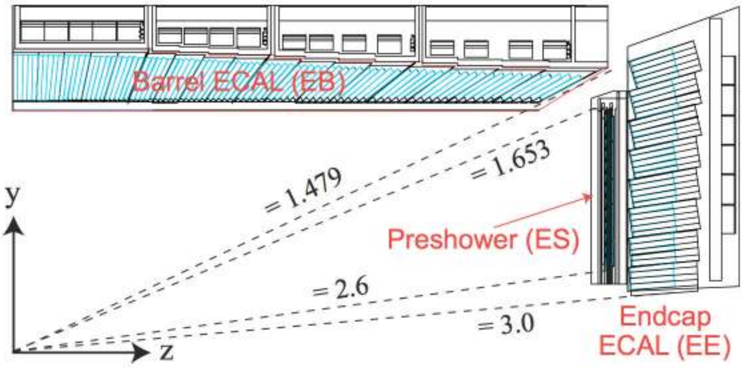

Figure 2.6: Tranverse section geometry of the CMS Electromagnetic Calorimeter [42]. Positions of the EB, the EE and the ES detectors are shown.

The detector consists of lead tungstate ($PbWO_4$) scintillator crystals, a material that provides very fast response time [43] and high radiation tolerance, both crucial aspects for ECAL. The high density of 8.3 g/cm^3 allows the construction of a relatively compact calorimeter that still contains most of the shower. With a crystal length of 23 cm in the barrel and 22 cm in the endcaps, ECAL provides 25.8 X_0[1] (22 X_0) of showering material in the barrel (endcap). Additional 3 X_0 are provided in the pseudorapidity range $1.65 < |\eta| < 2.6$ by the ES, a lead absorber with silicon strip sensors.

Crystal faces of size 22×22 mm^2 in the barrel detector and 28.6×28.6 mm^2 in the endcaps provide a fine granularity, which allows a precise matching with the tracking information. The light output of the crystals is strongly dependent on the temperature and makes necessary temperature stabilization of the ECAL.

The scintillation light of each crystal is detected by avalanche photo-diodes and vacuum photo-triodes in the EB and EE partition, respectively. Both devices were extensively tested in magnetic field and after high irradiation, ensuring stable operation for more than 10 years.

2.1.4 Hadronic calorimeter

The hadronic calorimeter (HCAL) measures the energy of hadrons through the shower produced in the detector. It is a sampling calorimeter composed by absorbing brass layers alternated to plastic scintillator tiles. Analogously to other subsystems, it is divided into a barrel part comprising the barrel (HB) and tail-catching outer calorimeter (HO) with a pseudorapidity coverage of $|\eta| < 1.3$, and two endcap disks. The endcaps have an endcap calorimeter (HE) in the range of $1.3 < |\eta| < 3$ and an additional forward calorimeter (HF) that extends the coverage up to $|\eta| = 5.2$. Fig. 2.7 shows the HCAL location.

The division of the barrel detector into HB and HO arises from the limited space available. The HB, located inside the superconductive coil of the magnet, is supplemented by the HO located outside the solenoid, right before the muon chambers. The HO works as tail-catcher to improve the energy measurement of jets and E_T^{miss} [44, 45], using the solenoid itself as absorber material. Combining HB and HO, the hadronic barrel calorimeter provides 11.8 interaction lengths λ_{int}.

[1]The radiation length in $PbWO_4$ is $X_0 = 0.86$ cm. It corresponds to the distance an electron should traverse in a specific material to reduce its energy by a factor of $1/e$ and to 7/9 of the mean free path for a pair production by a photon.

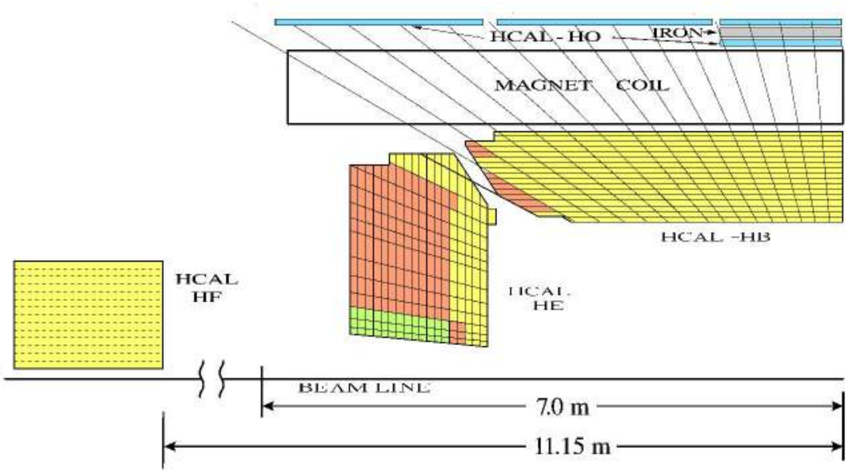

Figure 2.7: Quarter view of the CMS hadron calorimeter.

The scintillation light collected by the plastic tiles is converted by wavelength shifting fibers and measured by hybrid photodetectors (HPD). To improve the detection of early showers, the first scintillator tiles are placed between ECAL and the first absorber layers.

The HF detector is located at 11.2 m from the IP on both sides of CMS. Average energies of about 760 GeV are deposited in HF, compared to an average of 100 GeV in the rest of HCAL. For this reason, a steal absorber is used with embedded quartz fibers, which detect the Cherenkov light produced by charged particles in the showers and are thus mainly sensitive to the electromagnetic fraction of the shower.

2.1.5 Solenoid magnet

The design of the CMS detector is centered on its superconductive solenoid magnet. With its 3.8 T magnetic field, it allows a precise measurement of the particle momenta thanks to the large bending power. The magnet is made of a 12.5 m long coil with an inner radius of 6 m, able to host the tracking and calorimeter detectors. This allows to improve the energy resolution since particles are measured before loosing energy in the coil.

The magnet is made of reinforced and Al-stabilized NbTi conductor and works at a temperature of $\sim$ 5 K. The operating current is $\sim$ 18 kA, giving a stored energy of 2.3 GJ. The magnet coil is surrounded by a 12-sided iron structure interleaved with the muon detectors. This return yoke is made of 3 layers reaching a diameter of $\sim$ 15 m and it guides the return flux for a precise measurement of muon momenta.

2.1.6 Muon detectors

Muons at moderate energies go across both tracker and calorimetry systems with minimum loss of energy, and therefore can me measured outside the magnet coil, providing further tracking information. Thanks to the fact that no other charged particle can pass the inner detectors without interacting, the muon identification has a superior signal-to-noise ratio and is heavily used in both trigger and physics analyses.

Th CMS muon detector is the outermost detector system of CMS and it is integrated in the return yoke of the magnetic field. Due to the large area coverage, gaseous detectors have been chosen since they provide cost-efficient coverage of almost the full solid angle.

Depending on their position in the experiment, three different detector technologies have been employed: Drift Tubes (DT), Resistive Plate Chambers (RPC) or Cathode Strip Chambers (CSC). A layout of the CMS muon detector is shown in Fig. 2.8. DT planes are mounted in the barrel region, where the magnetic field is homogeneous and both the muon rate and the neutron-induced backgrounds are relatively low. The four layers of DT modules cover a pseudorapidity up to $|\eta| < 1.2$. Each DT station hosts 12 individual gas-filled tubes with a diameter of 4 cm and a center electrode. Most of the tubes run along the z axis providing measurements in rϕ, whereas the first three layers also feature tubes for z measurement.

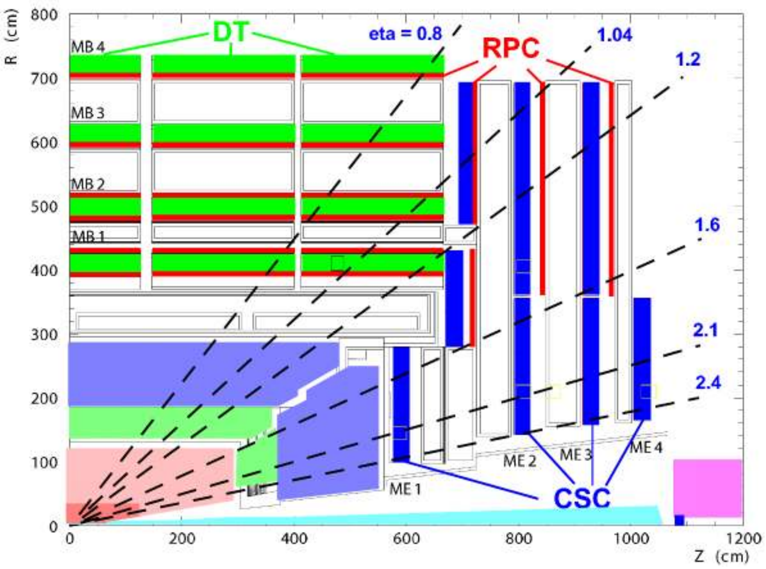

Figure 2.8: A longitudinal view of the muon system with the location of the three detector types contributing to the muon spectrometer [29].

The endcap regions of the muon detector ($0.9 < |\eta| < 2.4$) suffer for a stronger and less homogeneous magnetic field together with a higher muon flux. Therefore CSCs are used in this region which feature faster response time, higher granularity, and better radiation hardness. These detectors are trapezoidal multi-wire proportional chambers with cathode strips running radially from the beam pipe, hence providing a two-dimensional measurement.

Both barrel and endcaps are instrumented with RPC planes which cover a pseudorapidity up to $|\eta| < 1.6$. This detector consists of two high-resistivity plastic planes with readout strips interleaved by a gas chamber and they are operated in avalanche mode. At the cost of a coarse position resolution, RPCs provide a precise timing information of the order of 1 ns mainly used for bunch crossing assignment and by the trigger system.

2.1.7 Trigger

The LHC provides high rates in both proton-proton or heavy-ions collisions. For *pp* interactions, the beam crossing interval is 25 ns, corresponding to a frequency of 40 MHz. Depending on the luminosity, several collisions occur for each bunch crossing, leading to an average data size of $\sim$ 1 MB per BX. Since it would be technically impossible to store data at a rate of $\sim$ 40 TBs^{-1}, a drastic reduction of the rate is needed.

The reduction of the event-recorded rate is provided by the trigger system. The task of the trigger is to select only events potentially interesting for further analysis while reducing the rate to a manageable value of a few hundred Hz.

CMS implements the rate reduction in two subsequent steps called Level-1 (L1) Trigger [46] and High-Level Trigger (HLT) [47], respectively. The L1 trigger is fully hardware-implemented in Field Programmable Gate Arrays (FPGAs) and Application Specific Integrated Circuits (ASICs), and it takes the trigger decision with a latency of 3.2 μs, lowering the event rate to a maximum of 100 kHz.

During the L1 latency, data are buffered in pipelines in the detector electronics. Muon and calorimeter systems contribute to L1 triggers. Their data are processed separately for each subsystem with simplified local reconstruction algorithms and the resulting primitives are then merged to obtain the final L1 global decision. If the trigger is accepted, all the subdetectors send their data belonging to that event to back-end electronics.

Data are then collected and synchronized by the event builder and sent to the HLT. This is a software-based algorithm running on several thousand of CPUs which performs the full reconstruction of all events passing the L1 stage. Since the HLT latency of limited to 50 ms, time consuming algorithm, like tracking of the full silicon tracker, are only applied to the region of interest indicated by the L1. If at least one of the trigger paths configurable by the "trigger menu" is satisfied, the event is stored for offline analysis.

In case of high rate channels, trigger paths can also be prescaled to store on disk only a fraction on the triggered events. This is the case of minimum bias data, which are subjected to only few constraints and are used to model underlying events. Summing up all the trigger path contributions, the final event rate at which data are transferred to the CERN Tier-0 computing center and stored on tape is about 100–300 Hz.

2.2 TOTEM detector

The TOTEM (TOTal Cross Section, Elastic Scattering and Diffraction Dissociation Measurements at the LHC) experiment [48] is dedicated to the precise measurement of the total *pp* cross section, to the study of the elastic *pp* scattering and of diffractive processes. The experiment is composed by three detectors located symmetrically on both sides of the interaction point, the same as CMS (IP5): T1, T2 and the Roman Pot (RP) stations. Fig. 2.9 shows a schematic representation of the detector locations.

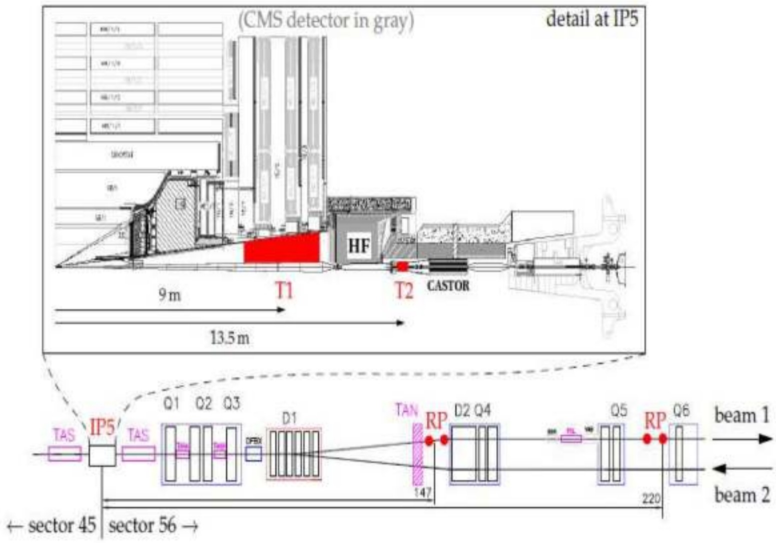

Figure 2.9: Location of TOTEM detectors for one of the two CMS sides [49]. Top: the TOTEM forward trackers T1 and T2 embedded into the forward region of the CMS detector. Bottom: the TOTEM Roman Pot locations along the LHC beam line at a distance of about 147 m (RP147) and 220 m (RP220) from the interaction point IP5.

The T1 telescope [50] is installed in the CMS endcap region, covering a pseudorapidity range of $3.1 < |\eta| < 4.7$. It is composed of five planes of cathode strip chambers equally spaced in z at a distance of 7.5 to 10.5 m from the IP. Each plane consists of 6 trapezoidal shaped detectors. These detectors are multiwire proportional chambers with anodic wires used for radial measurement and strip cathodes on the two planes having an angle of ±60° with respect to the wire orientation. This arrangement of the cathodic strips and anodic wires provides the hit measurement in three coordinates, allowing a good ghost discrimination and a spatial resolution of ~ 1 mm.

The T2 telescope, placed at about 14 m from the IP, detects charged particles produced in the pseudorapidity range $5.3 < |\eta| < 6.5$. Each arm T2 have a set of 20 triple-GEM (Gas Electron Multipliers) detectors that are combined into 10 semicircular chambers mounted on each side of the vacuum pipe [51]. The electrons produced by the charged particles that ionize the gas are multiplied by three layers of GEM foils placed in cascade and the electron cloud is read out by a board with a double pattern electrodes: concentric circular strips for the radial measurement and a pad matrix for the track azimuthal reconstruction. These last pads also contribute to the TOTEM level-1 trigger.

The detection of the leading protons from diffractive and elastic interactions is performed by movable beam devices called "Roman Pots" (RP). The Roman Pot technique was introduced at the ISR[52] and successfully used in later colliders like the $Sp\bar{p}S$, Tevatron, HERA, and RHIC. Silicon strip detectors are placed inside a secondary vacuum vessel and moved into the primary vacuum of the machine through vacuum bellows. In this way, detectors are physically separated from the primary vacuum, which is preserved against an uncontrolled out-gassing of the detector materials. Moreover, once a stable beam condition is reached, they can be moved very close to the beam axis, which allows to detect protons scattered at very small angles. A more detailed description of the Roman pots used by TOTEM and later adapted to the CT-PPS requirements is provided in Sec. 2.5.2.

The RP system of the TOTEM experiment consists of four pairs of stations, 2 on each side of CMS. Each station is composed by one horizontal pot and two vertical ones, such that sensors can approach the beam laterally, from the top and from the bottom. Each Roman pot is equipped with 10 planes of silicon strip detectors (see Sec. 2.4.1) that measure the protons deflected by the LHC magnets. The two stations of a pair are separated by a distance of ~ 4 m to determine the trajectory of the impinging protons.

In the original configuration, the first pair of stations was located at ~ 140 m and the other at ~ 220 m from IP5. The closest one to the IP was moved to ~ 210 m during the Long Shutdown 1 (February 2013 to March 2015) to satisfy the CT-PPS requirements. More details will be given in Sec. 2.4.

Protons that emerge intact but losing energy in the pp interaction are displaced with respect to the beam after passing through the bending magnets. Therefore the measurement of their kinematics strongly depends on the beam optics. The so-called "optical functions" determine the explicit path of the proton through the magnet elements as a function of the particle parameters at the IP (Fig. 2.10). The optical functions depend both on the magnet configuration and on the beam characteristics.

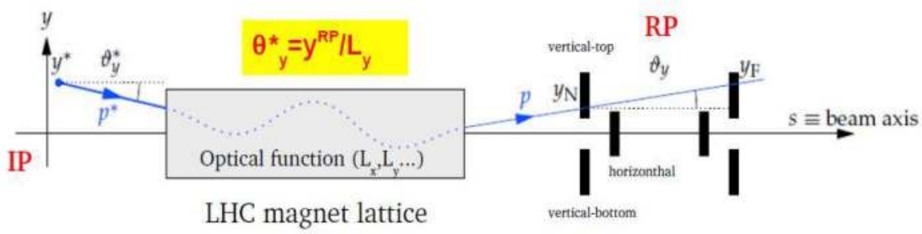

Figure 2.10: Scheme of the proton transport from the IP to the RP stations [49].

The kinematic quantities of the proton ($\vec{d}$) at a given point of the LHC can be derived as a function of its properties in the IP ($\vec{d^*}$) through the equation

$$\vec{d} = T \cdot \vec{d^*} \tag{2.2.1}$$

where the vector $\vec{d} = (x, \theta_x, y, \theta_y, \xi)^T$ describes the proton transverse positions (x, y), the projections of the polar angle in the xy and yz planes (θ_x, θ_y), and the fractional momentum lost by the proton (ξ). The transport matrix T is defined as

$$T = \begin{pmatrix} v_x & L_x & m_{13} & m_{14} & D_x \\ \frac{dv_x}{ds} & \frac{dL_x}{ds} & m_{23} & m_{24} & \frac{dD_x}{ds} \\ m_{31} & m_{32} & v_y & L_y & D_y \\ m_{41} & m_{42} & \frac{dv_y}{ds} & \frac{dL_y}{ds} & \frac{dD_x}{ds} \\ 0 & 0 & 0 & 0 & 1 \end{pmatrix} \tag{2.2.2}$$

where the magnification $v_{x,y} = \sqrt{\beta_{x,y}/\beta^*} \cos \Delta\phi_{x,y}$ and the effective length $L_{x,y} = \sqrt{\beta_{x,y}\beta^*} \sin \Delta\phi_{x,y}$ are function of the betatron amplitude $\beta_{x,y}$ and of the relative phase advance up to the RP location $\Delta\phi_{x,y} = \int_{IP}^{RP} ds/\beta(s)_{x,y}$. Together with the dispersion $D_{x,y}$, they are of particular importance for the reconstruction of the proton kinematics.

The amplitude function at the interaction point, β^*, can be expressed as a function of the beam cross section σ and the transverse emittance ϵ:

$$\beta^* = \frac{\pi\sigma^2}{\epsilon} \tag{2.2.3}$$

Considering Eq. 2.0.1 and that in first approximation $S_{\text{eff}} = 4\pi\sigma^2$, the instantaneous luminosity can be expressed as a function of β^*:

$$\mathcal{L} = \frac{N_b N_p^2 f}{4\epsilon\beta^*} \tag{2.2.4}$$

As a consequence, lower is the β^* higher is the luminosity. In 2016, LHC standard operation was at $\beta^* = 0.4$ m.

Another important parameter which depends on β^* is the beam divergence at the IP $\sigma_\theta = \sqrt{\epsilon_n/\beta^*}$, with ϵ_n the normalized emittance. In order to maximize the sensitivity of the position measurement to the scattering angle, while minimizing its dependence on the vertex position, special optics can be designed with minimum σ_θ and therefore large β^*.

Special LHC runs with high β^* values ($\geqslant$ 1 km), in which the protons are deflected at very low $|t|$, are dedicated to TOTEM for the measurement of the total cross-section, elastic scattering, soft diffraction and forward multiplicity [53].

2.3 Merging TOTEM and CMS

CMS and TOTEM have interest in a common physics program that needs the ability of TOTEM in detecting very forward protons to complement the event measurement with CMS in the central pseudorapidity region. A wide range of processes becomes accessible varying the integrated luminosity, which is related to the β^* at the interaction point. Figure 2.11 shows the TOTEM proton acceptance for different β^* runs.

At intermediate beta ($\beta^* = 90$ m), the two Collaborations collected data together in special runs in 2012 and 2015, obtaining excellent pseudorapidity coverage for both tracking and calorimetry, an ideal condition for studies of exclusive production and semi-hard diffraction in the range of $|t| > 10^{-2}$ GeV^2 [8]. These runs at relative low luminosity provide high sensitivity only to processes with sufficiently high cross section. The joint data taking allowed to measure

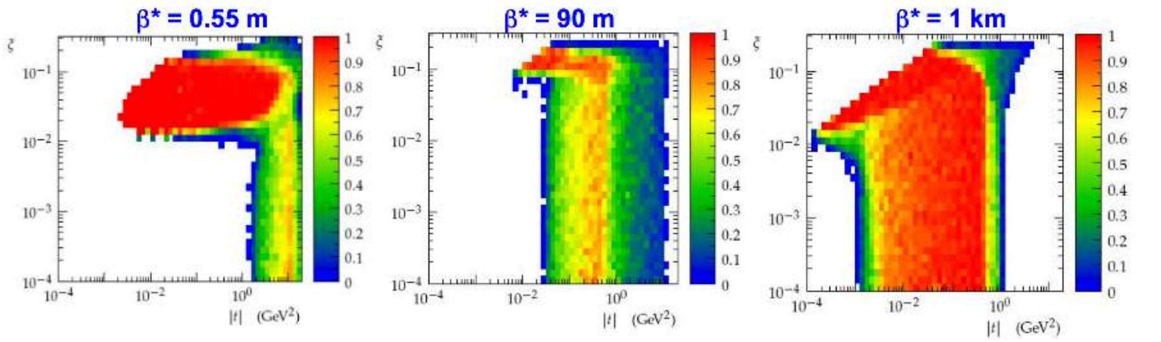

Figure 2.11: Simulated TOTEM proton acceptance as a function of the four-momentum transfer squared t and fractional momentum loss ξ [8].

for example single-diffractive jet events, detecting the diffractive proton and at the same time the jet system produced in the central pseudorapidity region.

With the aim of studying, during standard low beta running at high luminosity, low cross section Electroweak (EW) and QCD physics in central exclusive production (CEP), CMS has integrated in its detector apparatus a proton spectrometer able to measure the scattered protons.

TOTEM, with its own apparatus and relative upgrades, will continue pursuing the high cross section forward physics program up to 14 TeV in high beta special runs, which will be supported by CMS as joint runs in terms of trigger and detector readout. But at the same time, TOTEM is also interested in studying low cross section EW and QCD physics in CEP with CMS.

Indeed, central exclusive production provides a unique method to access a variety of physics topics, such as new physics via anomalous production of W and Z boson pairs, high-p_T jet production, and possibly the production of new resonances. These studies can be carried out in particularly clean experimental conditions thanks to the absence of proton remnants. The detection of the two final state protons provides a striking signature. The measurement of the leading protons allows to fully determine the kinematics of the central system. Well defined final states in the CMS central detector matching the protons kinematics can then be selected and precisely reconstructed.

In December 2013, CMS and TOTEM signed a Memorandum of Understanding stating that the two Collaborations were willing to combine efforts to jointly undertake the initial phase of the CEP low cross section physics program.

In September 2014, a Technical Design Report (TDR) [11] of the joint project CMS-TOTEM Precision Proton Spectrometer (CT-PPS) was approved by the two Collaborations and submitted to the LHCC, which endorsed the planning of CT-PPS in December 2014.

2.4 CT-PPS detector concept

The CT-PPS project aims at measuring central exclusive production, namely the process $pp \to pXp$, during normal high-luminosity LHC running. For reaching this goal, three main challenges need to be addressed: operate the Roman pots close to the beam line $(10-15\sigma)$ at high luminosity without preventing LHC stable operation; run detectors in a high radiation environment; cope with the high pile-up of normal LHC running.

The CT-PPS detectors consist of a silicon tracking system to measure the position and direction of the protons, and a set of timing counters to measure their arrival time. This in turn allows the reconstruction of the mass and momentum of the centrally produced system as well as the z coordinate of the primary vertex.

In standard LHC high-luminosity optics, the scattered protons can be observed, thanks to their momentum loss, via their horizontal deviation from the beam center produced by the bending power of the LHC magnets. Both the tracking and timing CT-PPS detectors are thus located in horizontal Roman pots.

The baseline design consists of two tracking Roman pots in each arm, followed by two timing pots. For the tracking system, two previous TOTEM stations are used, while for the timing detectors new cylindrical Roman pots were designed. During the Long Shutdown 1 (LS1 - winter 2015/16), two TOTEM stations were moved from 147 m to 203 m and 214 m from the IP to allocate the tracking system, while only one timing station was installed at 216 m. Figure 2.12 shows the layout of the beam line in the 200 m region with the CT-PPS stations indicated in red, together with the TOTEM ones in green. Downstream the detectors a new collimator (TCL6) was also installed by the machine in order to protect subsequent quadrupole Q6 from shower particles originating in the CT-PPS stations.

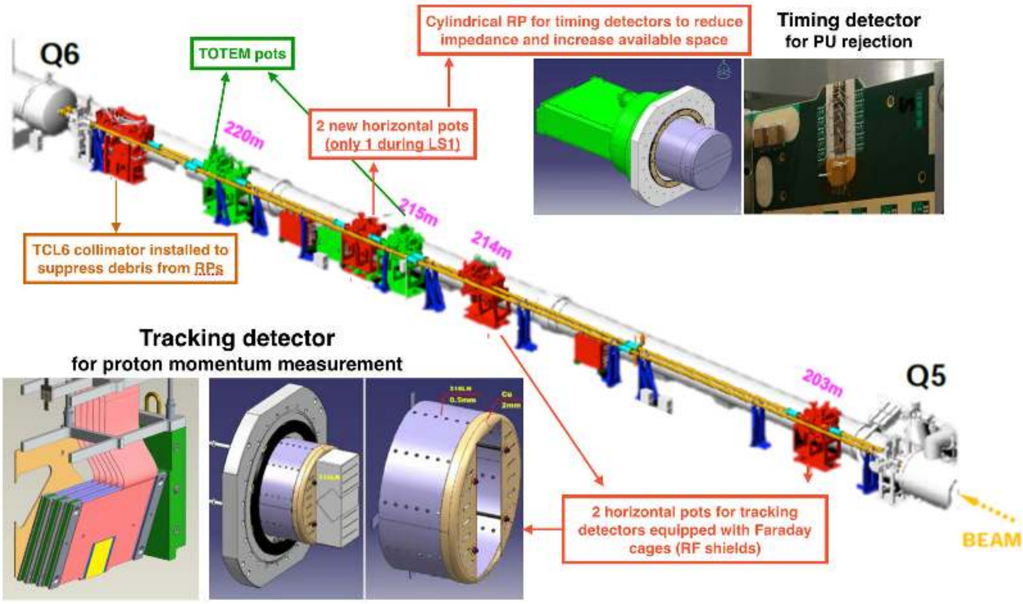

Figure 2.12: Layout of the beam line in the 200 m region after LS1. The new cylindrical Roman pot is equipped with timing detectors for pile-up rejection. The upgraded box-shaped Roman pots are equipped with silicon tracking detectors.

The CT-PPS detectors are designed to be integrated in the CMS trigger and data acquisition system and the electronics is largely based on existing components. The process of merging the TOTEM DAQ with the CMS one has been successfully completed.

The various components of CT-PPS are described in the following subsections.

2.4.1 Tracking detector

The CT-PPS tracking system is designed for a position resolution of $\sim$10 μm and 30 μm in x and y directions, respectively.

Another important requirement is the reduction of the insensitive area at the sensor's edge facing the beam, in order to increase the acceptance for high-momentum protons and therefore extend the acceptance to centrally produced systems with lower masses.

Finally, because of the small distance from the beam, one of the main requirements is the detector radiation hardness. Figure 2.13 shows the simulated proton fluence. For an integrated luminosity of 100 fb^{-1}, a maximum flux of 5×10^{15} protons/cm^2 is expected, which corresponds to a fluence between 1 and 3×10^{15} n_{eq}/cm^2 (see Sec. 3.2). The uncertainty is due to the lack of measurements of proton damage in silicon at the TeV scale.

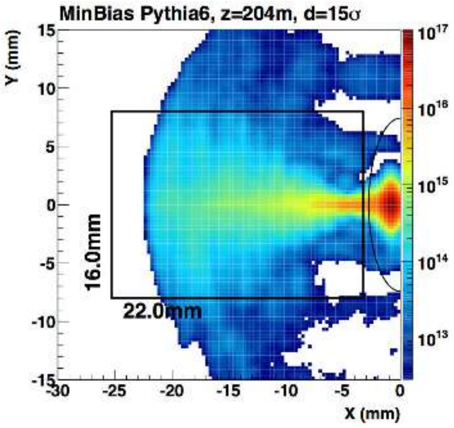

Figure 2.13: Simulated proton fluence in the tracking station at 204 m from the IP for an integrated luminosity of 100 fb^{-1}. The rectangle indicates the detector surface transverse to the beam, assuming a detector tilting angle of 20°. The ellipse shows the 15σ beam contour. At the detector edge a value of the order of 5×10^{15} protons/cm^2 is obtained. This value is compatible with an extrapolation from TOTEM data. [11].

In the following, the pixel tracking system designed for CT-PPS as well as the strip tracking system of TOTEM, used in the 2016 and 2017 data taking, will be described.

TOTEM strip tracking detector

For the data taking in 2016, the existing TOTEM silicon strip detectors have been installed in the two horizontal Roman pots foreseen for the CT-PPS tracking system. The aim of this exploratory phase was: prove the ability to operate detectors close to the beam-line at high luminosity, showing that the beam impedance caused by the RPs and the losses caused by particles interacting in the CT-PPS components do not prevent the stable operation of the LHC beams and do not affect significantly the luminosity performance of the machine and integrate the CT-PPS detectors into the CMS trigger and DAQ system. Both goals were reached, with the CT-PPS RPs inserted regularly at 15σ from the beam during CMS runs.

Each tracking RP was equipped with a stack of 10 silicon strip detectors designed with the specific objective of reducing the insensitive area at the edge facing the beam. Sensors are implemented on a very high resistivity n-type silicon wafer (> 10 kΩcm), 300 μm thick. The 512 strips with 66 μm pitch of each plane are oriented at an angle of $+45°$ for half on the planes and $-45°$ for the other half with respect to the detector edge facing the beam.

The physical edge of the strip sensor is provided with a "Current Terminating Structure", where the potential applied to bias the device is also applied across the cut edges via a guard-ring running along the die cut and surrounding the whole sensor. This external guard-ring, also called "Current Terminating Ring", collects the current generated in the highly damaged region at the cut edge, avoiding its diffusion into the sensitive volume. With this technique, the TOTEM silicon strip detectors allow a fully efficient particle detection already at a few tens of micrometers from the cutting edge of the sensor [54].

As it is for the TOTEM experiment, besides the horizontal pot each station is also composed by two vertical pots instrumented with the same silicon strip detectors. This allows during the alignment run, done with a special fill with only one colliding bunch in the LHC and with the RPs at a few sigmas (usually 5σ) from the beam, to have an overlap between pots as shown in Fig. 2.14. Using all hits from this run, the relative alignment between RPs of each station can be obtained. If instead only elastic events are chosen, the alignment with respect to the beam can be derived.

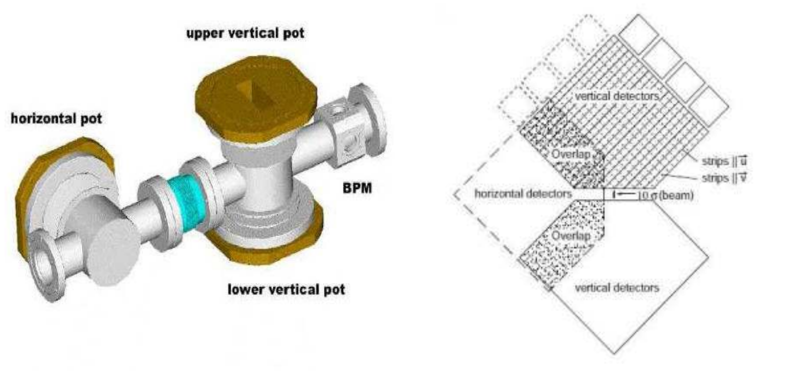

(a) scheme of a Roman pot station. (b) Overlap among the horizontal and vertical silicon detectors.

Figure 2.14: Overlap of the detectors in horizontal and vertical pots used for the alignment [49].

This procedure is fundamental for physics reconstruction and rely on the fact that the optics does not change between alignment and physics runs.

In high β^* runs, the optics deflects vertically a proton having lost a fraction of its momentum, and therefore the horizontal pot is used only for the alignment. Vice versa, in the low β^* optics, protons that interacted in the IP are measured in the horizontal detectors and only this pot is inserted since it is the only one certified for high-luminosity standard runs, as better explained in Sec. 2.5.

TOTEM strip detectors have been qualified up to fluences of 1.5×10^{14} protons/cm^2 [55], however it was decided to use them for the 2016 high-luminosity data taking to explore the diffractive channel in the search of diphoton events at 750 GeV [2]. Indeed during data taking the strips experienced a substantial efficiency loss in the highest irradiated region.

To monitor this issue an evaluation based on the number of hits has been considered, since the strips are read out binary and the collected charge cannot be measured. In Fig. 2.15 the used approach is shown: the number of hits in the selected region is compared with the one in the reference area.

This ratio is plotted in Fig. 2.16 for the four RP stations used in the 2016 high-luminosity data taking. To evaluate the degradation of the sensors it is necessary to refer to the initial value indicated by the horizontal red line. At the beginning of June, a reduction of the ratio due to the efficiency loss in the damaged area is evident. This degradation is then observed in other two periods in June, interleaved with recoveries in correspondence of two stops of the data taking indicated by the two vertical dashed lines, the first due to a technical stop and the second one to four days without beam. This recovery is attributed to a drift of the defects created by the irradiation towards the less irradiated regions.

Because of this effect, it was decided to stop the data taking with the TOTEM strips at the end of June 2016, and after some studies it was restarted at the end of August with the bias voltage increased from 100 to 250 V. All the 4 strip packages had to be replaced with new ones

[2]At the end of 2015 both ATLAS and CMS experiments observed a moderate enhancement at a mass of ~ 750 GeV in the diphoton production channel [56, 57]. Assuming that this effect was caused by a new particle, the constraint on the spin from the diphoton decay (0 or 2) would in principle allow the production of this particle in CEP events [58]. Moreover, the mass of the particle would be close to the CT-PPS acceptance peak. For these reasons, it has been decided to anticipate the CT-PPS detector installation by one year with respect to the schedule in order to collect data during the 2016 runs. The possible enhancement has been reabsorbed in the background with the analysis of the 2016 data [59, 60].

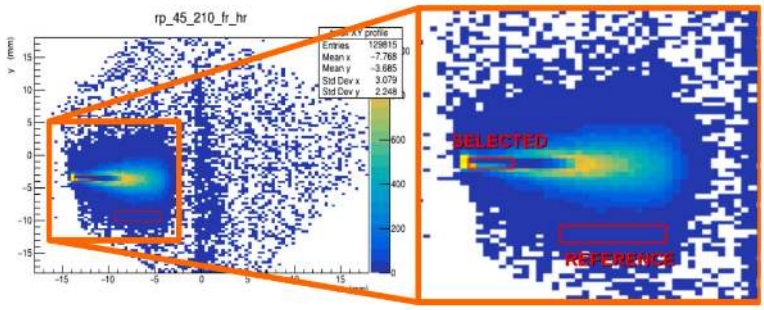

Figure 2.15: Hit map of a Roman pot after damage due to the irradiation. The TOTEM strip damage monitor is based on the ratio between the hits in the selected region (the damaged one) and the one in the reference area [61].

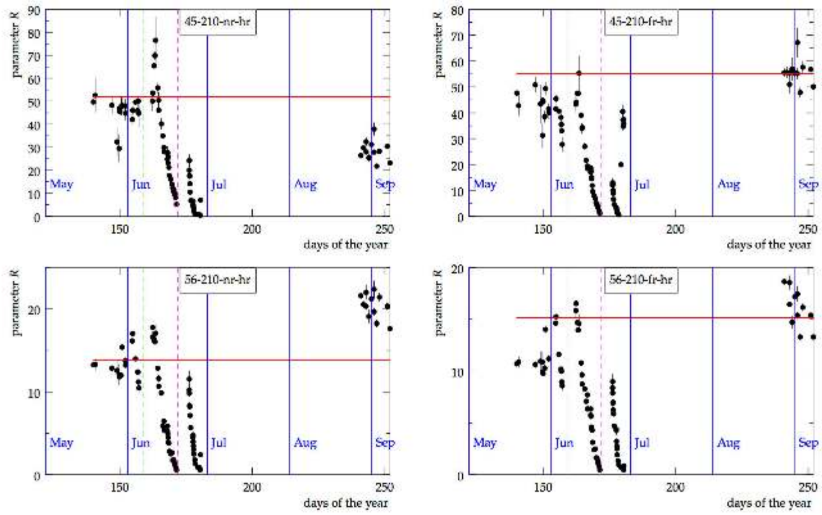

Figure 2.16: Hit ratio between more and less irradiated regions as a function of time [61]. The red horizontal line indicates the inital value before irradiation. The vertical dashed lines are two periods in which no data have been collected.

during the technical stop at the beginning of September 2016 in order to be able to collect data up to the end of the year.

Pixel tracking detector

In multi-track conditions, a tracking detector with strips oriented in two directions, as the TOTEM one, is affected by ambiguities due to the pattern matching of hit strips in different orientations. In general, for n simultaneous tracks, n^2 points are reconstructed.

In the high pile-up conditions expected for low β^* LHC running, $\sim$ 20% of the events recorded in the Roman pot stations have more than one track. The result is that a large amount of statistics would be rejected due to problems in the track reconstruction. To overcome this limitation, a pixel detector has been chosen for CT-PPS to be installed in the Roman pots during the 2016-17 extended winter LHC shutdown.

The baseline CT-PPS tracking system is based on 3D silicon pixel sensors, which have been chosen because of their intrinsic radiation hardness and the possibility to implement slim edges. An extended description of these sensors, which are the main subject of this thesis, is given in Sec. 4.1.

Each RP station consists of one stack of six detector planes, called RPix modules, where each plane contains a 1.6×2.4 cm^2 pixel sensor read out by six PSI46dig ReadOut Chips (ROCs) Each ROC reads 52×80 pixels with dimensions 150×100 μm^2. Given the small area of the detector, covered by a small number of individual sensors, we have chosen a number of planes that provide comfortable redundancy making the system resilient to possible failures.

Each plane is tilted by 18.4° to increase the charge sharing and therefore improve the resolution. This value has been chosen based on the results presented in chapter 4 and compatibly with the space inside the RP.

The design of the front-end electronics and of the DAQ is based on that developed for the Phase 1 upgrade of the CMS silicon pixel detectors. The complete readout chain of one detector package is shown in Fig. 2.17.

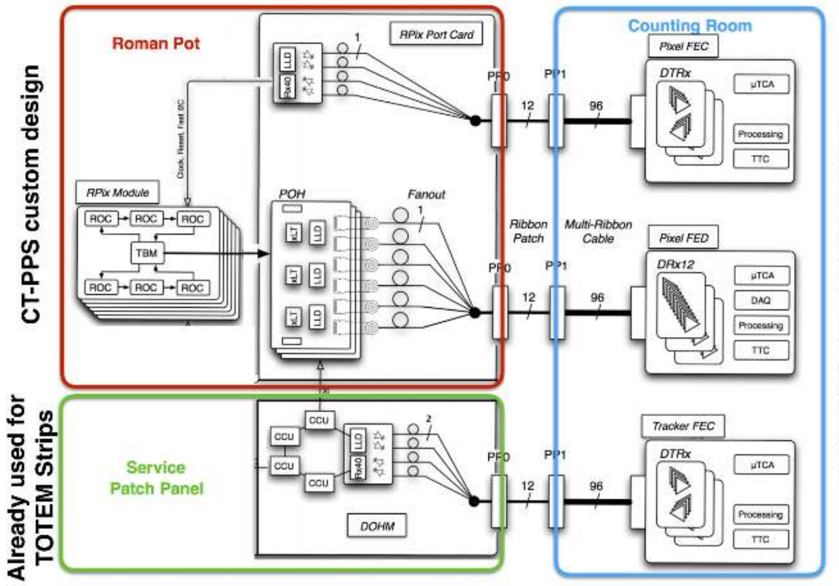

Figure 2.17: Detector readout blocks. The RPix modules and the RPix portcards are located inside the RP, the DOH Mezzanine (DOHM) is installed inside the service patch pannel in the LHC tunnel, and the FEDs and FECs are hosted in the counting room.

Each RPix module consists of a flexible hybrid circuit hosting: the silicon sensor, six PSI46dig ROCs bump-bonded to the silicon sensor, and one Token Bit Manager (TBM) chip. ROCs are responsible for charge collection, charge discrimination and data buffering, while the TBM reads out the six ROCs of the module using a token ring protocol and serializing the data over a single output line. Characteristics of the ROC and the TBM are described in Sec. 4.2 and 6.1.1, respectively.

The flexible circuit with the detector module is glued on top of a Thermal Pyrolytic Graphite (TPG) layer, a low density material consisting of stacked graphite sheets and with an extremely high thermal conductivity. Since it is a very fragile material, an aluminum encapsulation is needed for a proper handling. An exploded view of a module is shown in Fig. 2.18.

The RPix portcard is custom-designed, based on the TOTEM portcard that fits inside the Roman pot, but with most of the components of the Phase I central pixel detector. The board receives the output data from the six RPix modules and transmits them on six optical fibres towards the Pixel Front-End Driver (FED) DAQ module, using a POH7 opto-electrical converter mezzanine card [62].

The portcard also receives fast configuration commands from the Pixel Front-End Controller (FEC) via optical fibers, translates these signals using Detector Optical Receivers (DOH) and dispatches them to the modules. Moreover the RPix portcard integrates other components such as the radiation sensors, part of the TOTEM DCS (Detector Control System) radiation

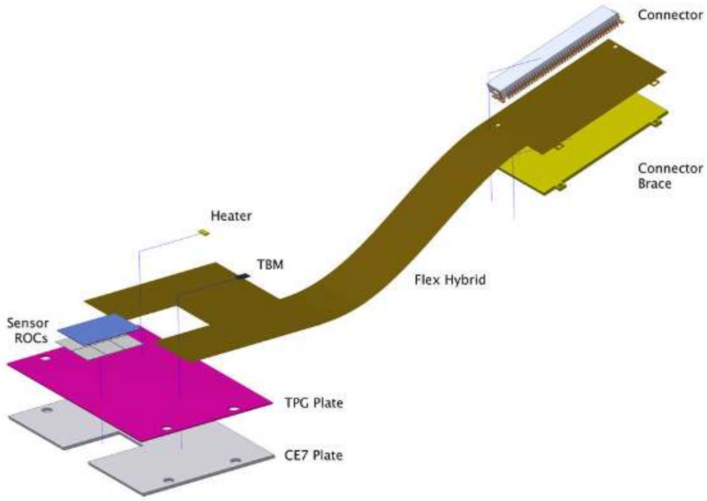

Figure 2.18: Exploded view of a RPix module [11]. The support plate consists of two layers: the first one is made of aluminum while the second one is made of Thermal Pyrolithic Graphite (TPG). A long kapton flexible hybrid circuit is glued on top of the TPG layer. The circuit hosts the silicon sensor with the ROCs and the TBM and provides the connections to the readout board.

monitoring, and the CMS Tracker Optical Control Link components that are capable of receiving and decoding the commands sent from the Tracker FEC.

The prototype, produced by INFN-Genova, is shown in Fig. 2.19 with most of the component mounted on it. One feature not present in the equivalent board for the Phase I pixel detector upgrade is the possibility to switch the low voltages independently for each module. This allows, in case of a module failure, to operate the other detectors. Moreover, also the high voltage channels are independent for each module and hence a shorted sensor would not affect the operation of the others.

For the back-end DAQ and control systems, composed by a FED and two FECs, μTCA crates are used. These boards, developed for the Phase 1 Pixel Upgrade project, replace the VME standard used so far for the CMS and TOTEM DAQ. Crates are located in the service cavern of CMS in order to be also accessible during data taking.

The mechanical structure of the detector (Fig. 2.20) is designed to ensure a positioning accuracy comparable to the resolution of the detector and to provide at the same time a proper thermal conductivity for the detector cooling. Since most of the support is outside of the track acceptance, the material budget of the mechanical structure is not an issue, except for the area below and in front of the sensors. The layout of the detector assembly was realized to be easily integrated with the existing TOTEM cooling system.

The TPG and aluminum layers hosting the modules are screwed to two aluminum support bars, each one machined in a single piece to ensure the best thermal contact. These bars are in tight contact with the cooling pipes to maximize the heat exchange.

The requirement of the existing TOTEM cooling system [50] for the strip detector ($<$ 20 W per package at $-10°$ C) is quite close to the pixel one ($<$ 10 W per package at $-20°$ C) and hence no modification was required. The system is designed to remove a thermal load from sensors, electronics and RF coupling up to $\sim$ 50 W per pot. However, since the pixel RPs are equipped with the Radio-Frequency (RF) shielding, only $\sim$ 10 W are expected when the pot approaches the beam to $\sim$ 1 mm [11].

The main part of the refrigeration system is installed in the underground service cavern of CMS (referred to as USC55) in order to be always accessible. A fluorocarbon evaporative

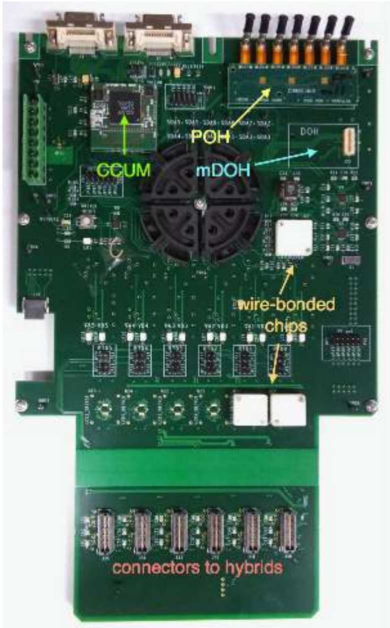

Figure 2.19: RPix portcard prototype with most of the components mounted on it. The six connectors at the bottom provide the connections to the hybrid flexes and are located inside the secondaty vacuum of the pot, while the remaining part of the board sits outside.

cooling [63] strategy has been adopted since it can transport fluid over long distances (from USC55 to the RP stations at 210 m and 220 m) with limited heat losses. The fluid is supplied in liquid phase and at high pressure to the RP circuit inlet, through two thin-walled copper-nickel pipes, one for each side of the detector package. The throttling of the fluid is done in the pot and is based on metal capillary tubes. An isenthalpic expansion process through the capillaries decreases the pressure and tunes the temperature to the design evaporation value of $-30°$ C. The coolant in gas phase is exhausted via larger diameter pipes. The C_3F_8 fluorocarbon dielectric fluid has been selected because it is non-flammable, non-conductive and radiation resistant.

A cooling test was performed in the SPS H8 test beam area, which is equipped with a cooling system identical to the TOTEM one. The results are well in accordance with the requirements and moreover it was demonstrated the possibility of running the detector even if one of the two lines gets clogged.

2.4.2 Timing detector

One of the difficulties of operating forward detectors in high pile-up conditions is the association of the leading protons with the corresponding vertex in the central detector. To cope with this problem, timing detectors can be installed for measuring the difference in the arrival time of the protons in the two arms of the spectrometer. A baseline time resolution of $\sigma(t) = 10$ ps, corresponding to a vertex resolution of $\sigma(z_{pp}) = 2.1$ mm, is set as an ambitious target of the CT-PPS project.

Another important requirement is the fine segmentation because several events with more than one proton are expected and it is important to discriminate between them. As for the tracking detector, radiation hardness and slim edge of the sensor are required.

Two physics processes have been considered for the CT-PPS timing detectors: Cherenkov light and charge ionization. Cherenkov light is produced by every charged particle traveling in a medium to a speed higher than the speed of light in that medium. The main advantage is that it is a prompt reaction and therefore ideal for fast timing, although the amount of light is

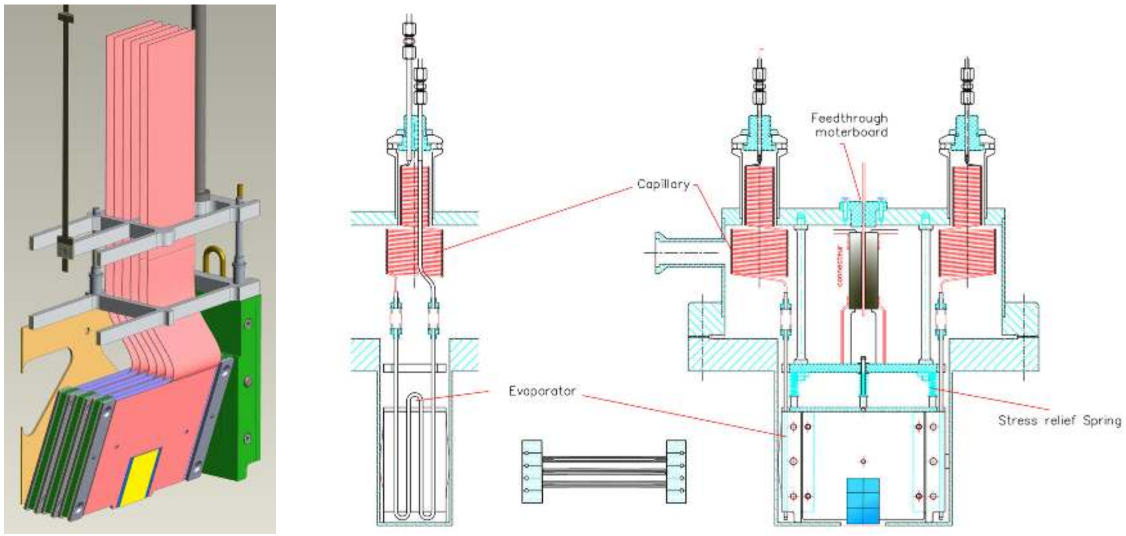

(a) The detector package.

(b) Overview of the RP inner volume.

Figure 2.20: a) Layout of the 6 modules mounted in each RP station. The TPG layer is in contact with the aluminium structures in which the cooling lines are inserted; b) Detector package location inside the RP. The cooling lines are coloured in red [11].

small compared to that in a scintillator. Radiators need to be transparent, preferably into the ultraviolet ($\lambda \sim 200$ nm), where most of the photons are generated, and must be read out by photodetectors, which convert the light into an electric signal. On this line, two technologies have been studied for the application in CT-PPS: QUARtz TIming Cherenkov (Quartic) and GAS Time Of Flight (GasToF) detectors. Despite the intrinsically fast response, the small number of photons generated via the Cherenkov effect requires a large detector thickness, preventing the use of large number of detectors per spectrometer arm because of the material budget. Moreover, the minimum channel dimension is in the order of few mm^2, limiting the double track resolution.

The other approach is based on sensors collecting the charge produced by ionization and two technologies have been considered: diamond detectors and Ultra Fast Silicon Detectors (UFSD). In this case, to improve the time resolution it is necessary to reduce the noise and/or to increase the steepness of the signal [64]. Diamond sensors show a very low noise, thanks to the large energy gap, and very good mobility meaning short collection time. On the other hand, UFSD improve the resolution by increasing the signal slew rate thanks to a small gain. The main advantage of the charge ionizing approach is that the sensor can be finely segmented and is very thin, allowing the stack of multiple sensors. This in turns allows to compensate for the lower timing performances with a resolution gain of $1/\sqrt{N}$ using N detector planes.

The four detectors considered for CT-PPS will be briefly described in the following subsections. Diamond detectors have been used for the 2016 data taking, since most of the technology was already developed by TOTEM [65]. For the 2017 data taking, the two timing pots, each per arm, have been equipped with a detector package consisting of three planes of diamond detectors and one of UFSD.

For what concerns the readout electronics, already available components have been chosen: the amplifier-discriminator NINO and the time-to-digital converter HPTDC, as shown in Fig. 2.21.

NINO is an 8-channel amplifier and discriminator implemented in CMOS 250 nm [66]. Each channel is a fully differential ultra fast (≤ 1 ns peaking time) preamplifier-discriminator. Thanks to the circuit saturation, the NINO output is a voltage pulse. The output pulse width

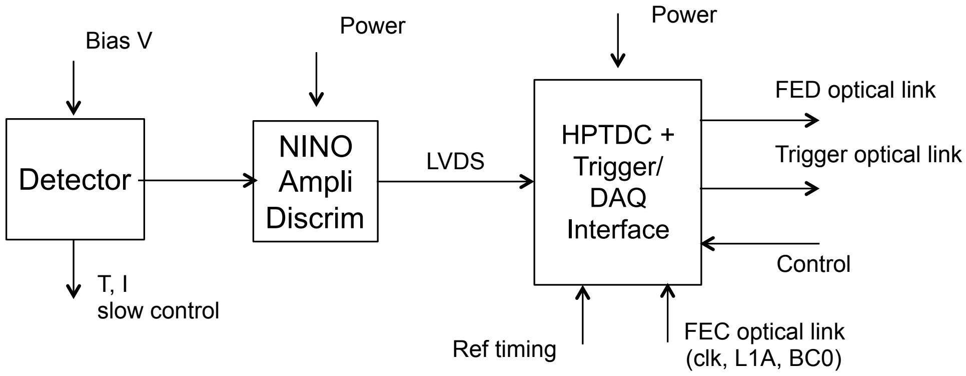

Figure 2.21: Diagram of the timing readout system [11].

is equal to the time-over-threshold, and therefore is a function of the input pulse amplitude. The intrinsic time resolution of the NINO chip was measured to be below 10 ps of RMS.

The LVDS output of the NINO is fed into the High Performance Time to Digital Converter (HPTDC) [67]. The time base for the TDC measurement is a Delay Locked Loop (DLL) with 32 delay elements and a clock synchronous counter, both driven by the same clock reference. The clock reference can be taken directly from the clock input of the TDC chip or can come from an on-chip Phase Locked Loop (PLL). The HPTDC provides the option of dual time measurement, in which both the raising and falling edges of the input pulses are determined, allowing to measure the time-over-threshold and therefore the detector pulse amplitude. The intrinsic time resolution is expected to be $\sim$ 20 ps. The interface between the HPTDC and the timing FEC and FED is done by means of an FPGA in the front-end board installed in the tunnel.

The CT-PPS timing measurements require a complementary timing system able to provide a very low jitter ($\sim$ 1 ps) replica of the master clock to the front-end TDCs. In order to achieve sub-picosecond time synchronization, single electronics modules are placed in each arm, synchronized via an RF feedback system, operating at a frequency of about 480 MHz over a single coaxial cable. This scheme is based on a system in use at SLAC for the synchronization of the Linac Coherent Light Source (LCLS) experiments with the electron accelerator beam [68].

Quartic detector

The Quartic detector is composed of an array of 3×3 mm^2 L-shaped bars of fused silica (quartz) [69]. This shape allows to position one side parallel to the beam such that the proton, crossing the entire bar, maximizes the amount of Cherenkov photon produced, while the other side acts as a light guide towards the SIlicon Photon Multiplier (SiMP). In this way, the photodetectors are located at $\sim$ 8 cm from the beam in the horizontal plane and can be partially shielded to reduce their radiation dose. The schematic of a Quartic L-bar is shown in Fig. 2.22(a).

The Cherenkov angle is the complement of the critical angle for total internal reflection on the bar sides, and as the proton paths are almost exactly parallel to the bars, all the Cherenkov light is internally reflected to the back end of the radiator. Most (about 2/3) of the light is transmitted to the SiPM through total internal reflection.

One module consists of 4×5 independent bar elements (Fig. 2.22(b)). This allows a time measurement of two or more protons from the same bunch crossing if they are in different channels of the detector. The active area is 12.6 mm (vertically, y) $\times$15.8 mm (horizontally, x).

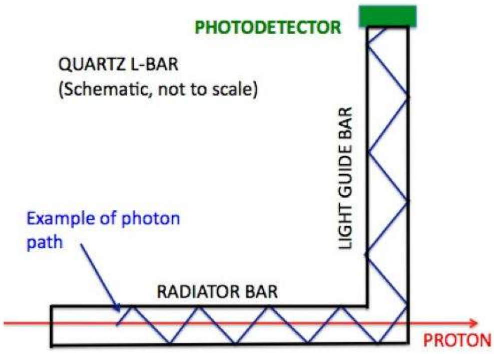

(a) Cherenkov light path in a Quartic L-shaped quartz bar.

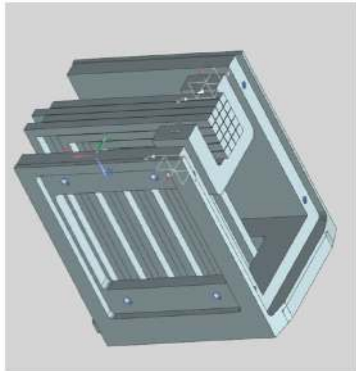

(b) Design of the Quartic bar array.

Figure 2.22: The CT-PPS Quartic detector is composed of L-shaped quartz bar (left plot) arranged in a 4×5 array (right plot) in order to reduce the double hit probability in the same channel [11].

This includes 200 μm spacers to separate the bars, for improving total internal reflection and avoiding light leakage.

The ends of the light guide bars arrive at an array of SiPMs manufactured by Hamamatsu. SiMPs are solid state photon counters comprised of a large number of avalanche photodiodes (APDs) of order 50 μm dimensions, with a high gain (up to 10^6) in Geiger mode, with an applied voltage just above the breakdown voltage. Thanks to the charge amplification, the SiMP output can be directly fed into the NINO amplifier.

Quartic bar prototypes have been tested on beam reaching an intrinsic resolution of $\sigma(t) =$ 31 ps and since it would be possible to install two detectors per arm, the expected global resolution becomes $\sigma(t) = 22$ ps [69]. It would not be possible to install more than two Quartic detectors due to the relatively high fraction of nuclear interactions in the quartz bars, which produces showers that can trigger the beam dump.

One of the main limitations of this approach is that multiple hits in the same crystal cannot be resolved. In presence of high pile-up with an average of 50 iterations per bunch crossing, the crystal bar closer to the beam would have an occupancy of $\sim 70\%$, hence resulting in a large number of events in which the timing information cannot be measured.

GasToF detector

GasToF is a gas Cherenkov detector with direct detection of the light cone. Since a gas is used, with refraction index close to 1, the light cone has a very small angle and it can be detected without use of internal reflections. To avoid installing active elements in a high radiation area, a flat 45° mirror is used to reflect the light onto a photocathode of a Micro Channel Plate photomultiplier (MCP-PMT) located on top of the gas chamber. The advantage of this technique with respect to Quartic is that its optics is trivial and only a small amount of material is introduced near the beam, hence little multiple scattering and nuclear interactions.

The foreseen radiator is relatively dense, the inert C_4F_{10} gas, with refraction index $n \sim$ 1.002. By changing the gas pressure one can vary the light-cone angle and hence the amount of Cherenkov light. An advantage of using a gas radiator is that, together with a relatively large particle velocity threshold, the small light-cone angle makes it immune to stray, soft backgrounds.

Numerous tests with the fastest single-anode MCP-PMTs confirmed that the GasToF performance is eventually driven by the photodetector transit-time spread, and demonstrated an

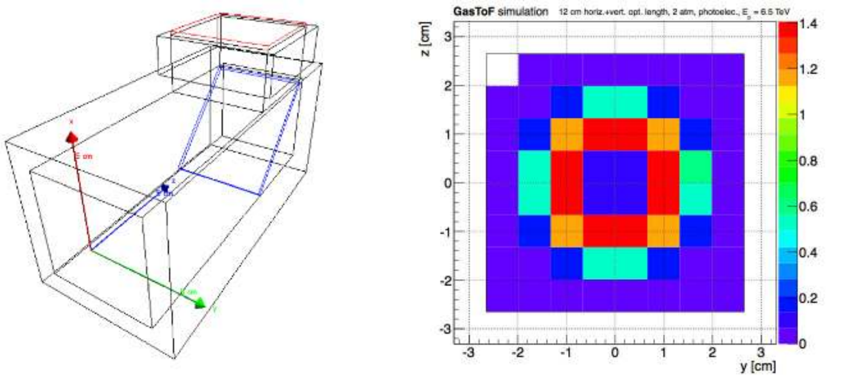

(a) GasToF schematic view.

(b) Average number of photoelectrons per readout channel.

Figure 2.23: a) Schematic representation of the GasToF detector. The 45° mirror is indicated in blue, while the photocathode in red; b) Average channel occupancy for a 6.5 TeV proton crossing the detector in its center [11].

ultimate time resolution of ~ 15 ps for single-photoelectron signals, using a 6 μm pore device. However, such a single-channel detector is not capable of dealing with multiple simultaneous hits.

For the CT-PPS high luminosity running, a new GasToF design has been proposed using the Photonis XP85112 8×8 anode 10 μm pore MCP-PMTs with a 35 ps transit-time spread. Considering its photoelectron efficiency, in a 12 cm C_4F_{10} gas chamber at a pressure of 2 atm, an average of 7 photoelectrons are expected to be collected for one high-energy proton. In Fig 2.23(b), an average distribution of photoelectrons at the photocathode placed 12 cm above the detection plane is shown.

On average, the signal of 7 collected photoelectrons is spread out over about 25 readout channels, resulting in a low ($\sim 30\%$) channel occupancy. Even two protons which are perfectly collinear can be well measured, almost without affecting each other, if they are separated in time by $\gtrsim 50$ ps.

The use of GasToF in CT-PPS is not yet scheduled being the development of this detector slightly behind with respect to the other technologies.

Diamond detector

Solid state detectors with high segmentation are a natural choice to reduce the channel occupancy.

Diamond detectors present advantages for measuring timing in the CT-PPS conditions. First at all, the pixel size does not affect the signal response. Since the pixel pad shape is just given by the metallization pattern, pixels of different size can be easily implemented on the same diamond crystal. Moreover, these detectors are radiation hard, thanks to the diamond structure. On the other hand, the charge released from a diamond sensor is small in absolute numbers ($\sim$ 12000e for a 500 μm thick sensor) and a low noise amplifier is needed to keep the signal/noise (S/N) ratio large enough. Because of the small charge collected, the output signal cannot be fed directly into the NINO and needs to be amplified by discrete components a fine impedance adaptation have been realized on the diamond board.

Diamond detectors were under study in view of the TOTEM upgrade [70], but after the hint of a possible enhancement of the diphoton spectrum at 750 GeV it was decided by the CT-PPS project to revise the diamond geometry and to install them in the cylindrical RPs for the 2016 data taking. Due to a last change in the optics for the 2016 LHC running, the acceptance of the tracking station closer to the IP for $m_X = 750$ GeV was strongly reduced with respect to the expected performances (see Sec: 2.5.2). Since better acceptance was expected for the cylindrical RP, the geometry of the diamond detector was optimized to provide the best tracking resolution achievable while maintaining 12 readout channels per plane, so to preserve the characteristics of the TOTEM upgrade design.

The structure of the diamond detector is based on four planes, each one formed by four 4×4 mm^2 diamond sensors with different patterns of the pads. As shown in Fig. 2.24, each plane has different sensor arrangements, which are rotated and swapped while keeping small-size pads near the beam where a higher occupancy is expected. In this configuration, a space resolution of ~ 150 μm can be reached [71] (~ 125 μm by neglecting 5% of outliers). The time resolution of this detector measured with beam tests is 100 ps per plane.

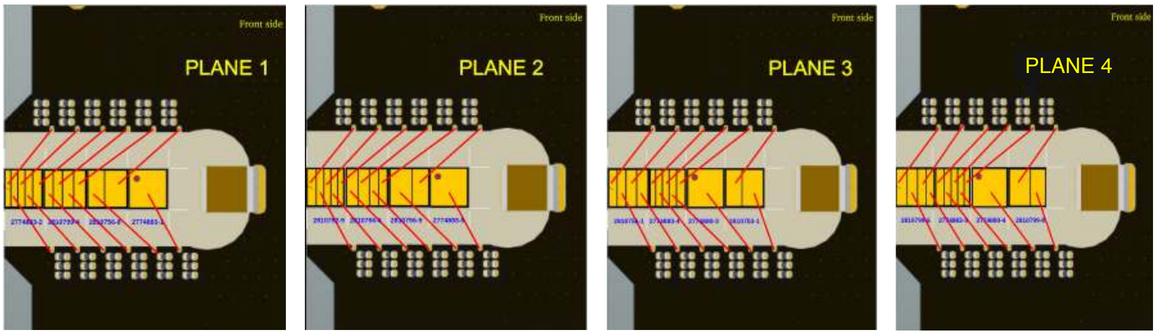

(a) Plane 1. (b) Plane 2. (c) Plane 3. (d) Plane 4.

Figure 2.24: Diamond detector plane layout [71]. Diamond sensors with different pad configurations are swapped or rotated in the four panes in order to maximise the spacial resolution.

The diamond planes were installed in the cylindrical RP during the technical stop in the second week of June 2016 (TS1), but due to an issue that required an access in the LHC tunnel to be solved, the commissioning phase only started after the technical stop in the middle of September (TS2).

For the 2017 data taking, three planes of diamond detectors have been installed in each cylindrical RP, being the fourth substituted by an UFSD.

Ultra Fast Silicon Detector (UFSD)

An alternative to diamond detectors are silicon-based timing detectors. Considering that for improving the timing resolution it is important to have a steep slew rate, a thin sensor would be preferable for a fast collection of the charge. However, at the same time a thin sensor means a small produced charge. A solution proposed a few years ago [72] is to recover a reasonable amount of charge by means of a small internal gain.

The development of Low-Gain Avalanche Diodes (LGAD) [73] allowed to produce silicon detectors with output signals that are about a factor of 10 larger than those of traditional sensors. This increased signal brings many benefits, such as the possibility of developing thin detectors with large enough signal, good performance even for small charge collection efficiency, and it is a key for excellent timing capability. LGADs have therefore made possible the development of silicon sensors optimized to achieve excellent timing performance, the so-called Ultra-Fast Silicon Detectors (UFSD) [64].

Low-Gain Avalanche Diodes are n-in-p silicon sensors with a high ohmic p bulk that have a p^+ implant extending over several microns underneath the n-implant. Fig. 2.25 shows the structure of a LGAD. The extra deep p^+ layer creates a strong electric field that generates charge multiplication with a moderate gain $(5 - 80)$.

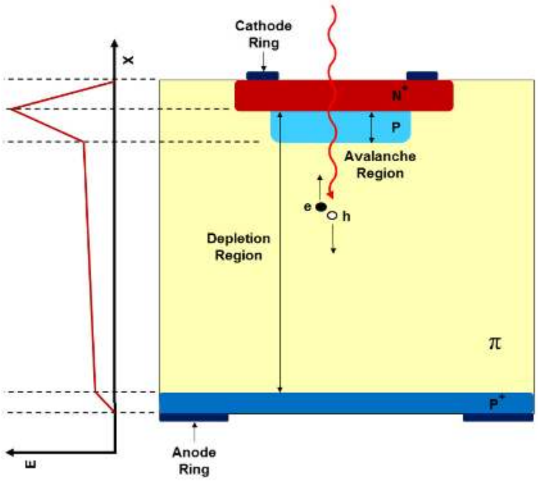

Figure 2.25: Layout of a Low-Gain Avalance Diode with electric field behavior as a function of the sensor depth [74].

Several laboratory and beam tests have been done on UFSDs from different vendors and various thicknesses. In particular, at a test beam with 180 GeV/c pions it was demonstrated that an UFSD with an active thickness of 45 μm and 1.7 mm^2 pad size can reach a timing resolution of 35(26) ps at a bias voltage of 200(240) V [75]. These results are in good agreement with the ones obtained with the Weightfield2 simulation tool developed in Torino [76]. As each UFSD plane is very thin, up to 6 planes of UFSD can be housed in a RP, while a cylindrical RP can house several more. Assuming 9 independent time measurements, an overall resolution of less than 10 ps can be achieved.

Sensors with a layout compatible with the CT-PPS requirements have been produced at CNM (Barcelona, Spain) in 2016. Each sensor, whose geometry is shown in Fig. 2.26, has an active area of 12×6 mm^2 and a thickness of 50 μm. The sensor pads are organized in a matrix of 16 columns and 2 rows. The pixel size varies as a function of the distance from the beam: the 8 pads for each column closer to the RP edge have a dimension ~ 2 mm^2, while the others have an area of ~ 3 mm^2.

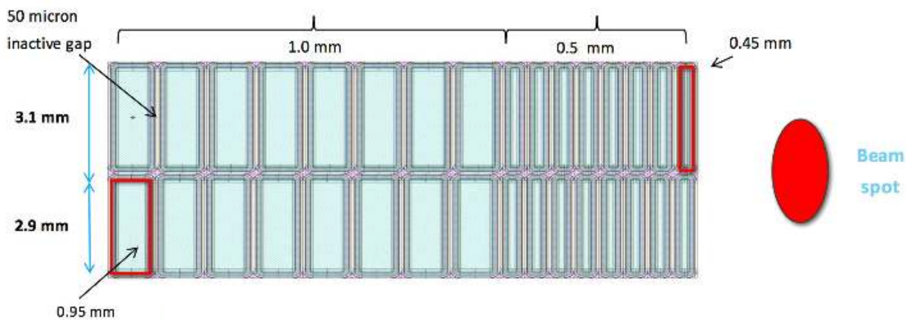

Figure 2.26: Schematic layout of an UFSD produced for the CT-PPS timing detector [74]. Each sensor has 32 channels organized into 2 rows. Pads of different rows are staggered in order to recover for bad performance regions at the pixel edges by placing sensors on neighboring plains back-flipped.

Since regions between two pixels are expected to have bad timing capability, the pixels belonging to the two rows are slightly staggered and the two rows have a different height. This design allows with only one sensor layout to recover low performance regions by arranging detector planes back-flipped one respect to the other.

A possible limitation for using UFSDs as timing detectors in CT-PPS is the radiation hardness. The gain behavior as a function of the bias voltage is strongly dependent on the doping magnitude of the deep p^+ layer. Increasing the radiation dose, the boron of this layer is deactivated and the gain reduces. R&D studies are ongoing to investigate this effect and try to mitigate it using other dopant atoms as for example gallium.

For the readout electronics, it was chosen to use the same of diamonds (NINO + HPTDC) in a first stage. But since in this case an amplification is required, it was decided to produce a custom ASIC (Application Specific Integrated Circuit) which could read the UFSD signal and provide directly the output to the HPTDC.

This ASIC, called TOFFEE, has been designed in Torino in UMC 110 nm CMOS technology [77], and has 8 channels. Each channel consists of an amplifier, a single threshold discriminator, a delay line to stretch the discriminator output, and a LVDS (Low-Voltage Differential Signaling) driver for HPTDC connection. The ASIC simulation indicates a time resolution of $\sim$ 45 ps considering the combination of an UFSD with TOFFEE. The first TOFFEE prototype has been produced and is currently under test. An improved version of the ASIC is expected for winter 2017.

2.5 Roman pots for CT-PPS

Roman pots, inside which tracking and timing detectors are placed, are a key part of the CT-PPS project. They are required to approach the detectors as close as possible to the beam without preventing stable beam operation. At the same time, they have to maintain stable the detector working conditions, as for example the temperature that due to radio frequency coupling increases when moving towards the beam.

In this section the design of the CT-PPS RPs will be described, together with the insertion tests done in 2015 and 2016 to validate them in standard high-luminosity running.

2.5.1 Roman pot design

The Roman pots for the CT-PPS tracking system are a slightly revised version of those from TOTEM, to ensure running in high-luminosity conditions. They are made in 316LN with a box shape of dimensions 50×124 mm^2, and a 2 mm wall thickness. A Ultra-High Vacuum (UHV) flange is welded to the box by electron beam welding. The bottom side of the flange is connected to a bellow, to tight the machine vacuum. The opposite side is connected to the pot itself equipped with the detectors, which tights the secondary vacuum volume.

Since it is crucial to reduce the insensitive material close to the beam, the RPs are equipped with a thin window of thickness 150 μm. With the requirements of a flatness better than 50 μm, UHV leak tightness, and capability to stand the limit pressure of 1.5 bars, a brazing assembling procedure was chosen to realize the thin window: the first step consists in brazing a thin window in 316L on the bottom part. Successively, the milling of the lateral sides is done, obtaining a 0.5 mm window.

In October and November 2012 several test insertions of the RPs, in normal high-luminosity fills at $\sqrt{=}8$ TeV with $\beta^* = 0.6$ m, were performed. The first evidence was that new collimators were needed downstream the pot position to run safely in high-luminosity conditions. These collimators were installed during the LHC Long Shutdown 1 (LS1).

Moreover, while the horizontal pots were stationary at 14σ from the beam center for about 30 minutes, the temperature sensors on the detector hybrid boards in those RPs registered a temperature increase by about 4°C, despite the active cooling of the detector packages. This effect can be explained by the impedance heating of the ferrite collar mounted around the box-shaped housing on the beam vacuum side. A direct temperature measurement near the ferrite was not available, but given the long thermal conduction path from the heat source to the detector package, and the absence of convection inside the pot due to the secondary vacuum, the temperature of the ferrite might have reached values well above 100°C, which is the Curie temperature[3] of the ferrite (material 4S60 from Ferroxcube) above which it is ineffective. Another piece of evidence for substantial heating of the ferrite was given by the vacuum deterioration observed after the very close insertion of the horizontal RPs. Laboratory tests showed that the ferrite material installed around the pots was subject to substantial outgassing at high temperatures.

A first improvement implemented to the RPs for CT-PPS was the exchange of the TOTEM ferrite with a material with much higher Curie temperature and acceptable outgassing. Furthermore, to reduce the impedance of the box-shaped pots, they were equipped with 1 mm thick cylindrical copper RF shields. The shield is retracted by 30 mm from the box window facing the beam, in order not to intercept any signal protons with the shield material.

This new RP layout, shown in Fig. 2.27, has been first implemented in the tracking stations at 203 and 214 m in 2016. For the 2017 running, the same upgrade has been made to the TOTEM horizontal pot at 220 m to allow also its insertion in high-luminosity runs for increasing the detector acceptance at small invariant mass values.

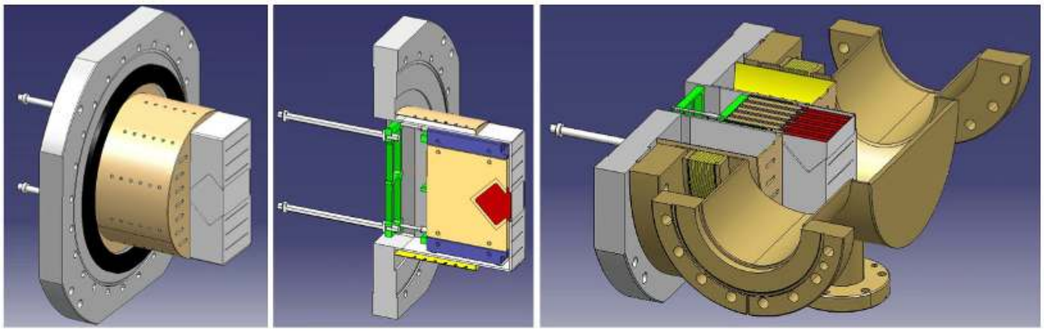

Figure 2.27: Drawings of the box-shaped horizontal RP with the cylindrical RF shield [11].

A cylindrical RP has been newly designed to house timing detectors, optimized with respect to material budget and RF interaction with the LHC beam. The new design was required in case Cherenkov detectors were to be installed, because of the bigger space needed.

The choice of a cylindrical profile provides the necessary space for all potential technologies of timing detectors and at the same time reduces the beam coupling impedance by minimizing resonant cavities. The ferrite in this design is integrated with a ring geometry in the flange rather than mounted on the moving detector housing. Furthermore, all vacuum-side surfaces of the RP station receive a 2 μm thick Non-Evaporative Getter (NEG) coating to reduce the outgassing and hence improve the LHC vacuum stability. As for the box-shaped RP, also the cylindrical one implements a thin window for a closer approach of the detectors to the beam, in this case 300 μm thick. The drawings of the cylindrical vessel are shown in Fig. 2.28.

During the LHC LS1 one cylindrical RP station has been installed at $\sim$ 215 m from the IP on each side of CMS. In the future it is foreseen the installation of a second station right after the ones already installed.

2.5.2 Roman Pot insertion

Given the impedance heating and the resulting vacuum deterioration observed in the high-luminosity insertion tests in late 2012, an insertion campaign for commissioning the RPs started right after LS1. The RP insertion tests were carried out using the end of fill, in order to minimize

[3]the Curie temperature is the value at which certain materials lose their permanent magnetic properties.

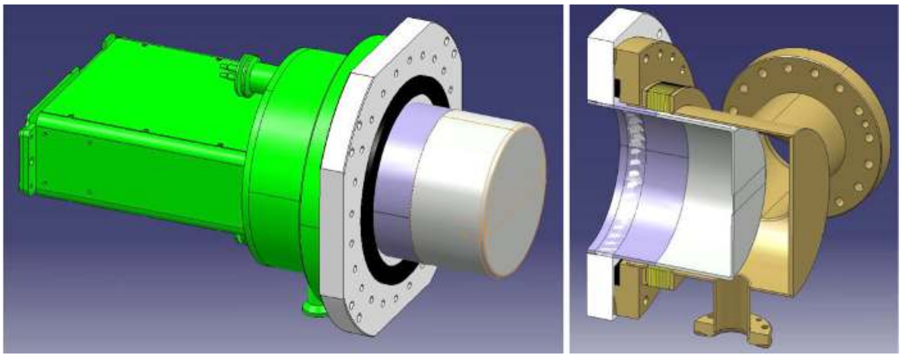

Figure 2.28: Drawings of the cylindrical detector housing for the new RPs designed to accomodate timing detectors [11].

the impact of possible beam dumps. The goal of these insertion tests was to find an optimal set of positions not only of the RPs but also of the TCL4, TCL5 and TCL6 collimators, so to offer sufficient protection for the magnets downstream the RPs without cutting too much the proton acceptance of the detectors.

Several parameters need to be kept under control in order to carefully monitor the two main effects when approaching the RPs to the beam: beam losses and RP impact on impedance.

The beam losses are monitored thanks to an extended Beam Loss Monitor (BLM) system that have been installed during LS1, consisting of one BLM after each RP plus a BLM right after the collimator TCL6, installed for filtering the shower produced by the cylindrical RP. The last one is the most important since it measures the dose rate received by the quadrupole downstream and eventually triggers the beam dump in case a pre-determined threshold is exceeded.

For studying the RP impact on impedance several parameters are recorded. The RF coupling with the RP volume produces the heating on the vessels, which is monitored by several temperature sensors that are installed inside the RPs and on the pot floor towards the beam. Another effect of heating is the degradation of the LHC vacuum, due to pot outgassing. The vacuum monitoring is done by five gauges installed in the RP sector and controlled by the CMS Detector Control System (DCS). Finally, the RP insertion may also affect the beam orbit stability.

During 2015 data tacking, pots have been inserted in all steps of the 50 ns and 25 ns intensity ramp-up, up to an instantaneous luminosity of 3.9×10^{33} cm^{-2}s^{-1}. The distance of closest approach of the horizontal RPs to the beam has been reduced during the year from the very conservative distance of $\sim 30\ \sigma$ down to $20.7\ \sigma$, plus a 0.5 mm of safety margin. Since one of the considered timing detectors would require the installation of quartz bars in the cylindrical RP, which could create an amount of showers large enough to trigger the beam dump, a dummy aluminum bar was installed in September 2015 to mimic the Quartic detector.

Figure 2.29 shows the BLM dose rate measurement for both arms (sectors 4-5 and 5-6) downstream the cylindrical pot (E6), downstream the last collimator before the magnet (TCL6), and in the middle of the first subsequent quadrupole crossed by the beam (MQML). The plot for sector 5-6 (Fig. 2.29(b)) shows the increase of dose due to the dummy aluminum bar, which increases the dose rate at the BLM(E6) by a factor of ~ 2. The linear extrapolation at an instantaneous luminosity of 10^{34} allowed to estimate a dose of only $\sim 7\%$ of the beam-dump threshold.

The LHC vacuum, measured with gauges close to the RPs, is shown in the top plot of Fig. 2.30. As expected, the measured pressure increases during the beam ramp up. In correspondence to the RP insertion, a significant but not problematic rise of the pressure is observed. The temperature, measured by sensors located on the cylindrical pot floor towards the beam,

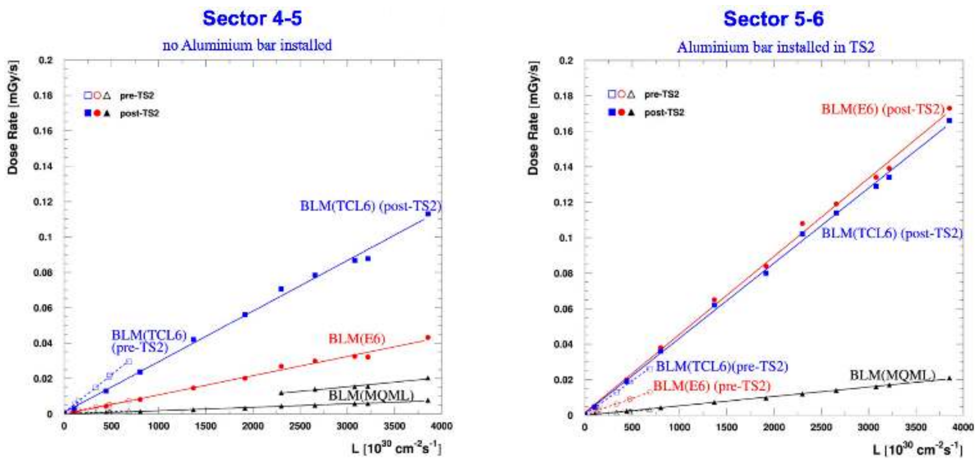

(a) BLM Measurement in sector 4-5.

(b) BLM Measurement in sector 5-6.

Figure 2.29: BLM response before (hollow marker) and after (full marker) September 2015 [78], when a dummy aluminum was installed inside the cylindrical RP of sector 5-6 to simulate the Quartic detector.

slowly increases approaching an equilibrium value, as shown in the bottom plot of Fig. 2.30. The maximum value is 36° C at 3 mm from the beam center without cooling. The significant improvement with respect to the previous RP design is demonstrated when comparing to the 41°C on the RP electronics card (4 cm from beam) in an insertion in 2011.

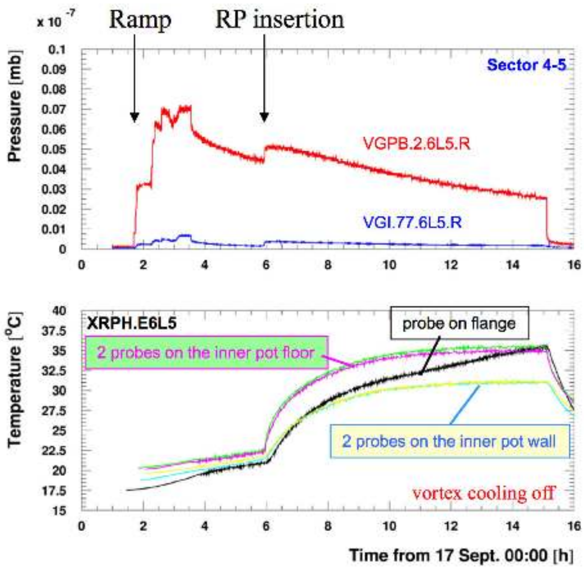

Figure 2.30: LHC beam pipe vacuum pressure (top) and temperature at cylindrical RP floor during an insertion at 25 σ with beam luminosity of $\sim 1.9 \times 10^{33}$ cm^{-2}s^{-1} [78].

Because of the enhancement observed in 2015 by CMS and ATLAS in the diphoton invariant mass, it was decided for the 2016 run to push the LHC luminosity as much as possible in order to discriminate between a new particle signal or a statistical fluctuation. To reach this goal, the squeeze of the beams in the CMS and ATLAS IPs was increased, reducing the β^* from 0.8 m to 0.4 m, and also the crossing angle was changed from 290 μrad to 370 μrad. Figure 2.31 shows the positions of the Roman pots for different configurations of the machine optics as a function of the beam horizontal sigma and dispersion. The position is set requiring to have acceptance for rapidities up to 0.5 for a central mass of 750 GeV. For a better understanding, diagonal lines indicate the distance of approach to the beam in number of standard deviations.

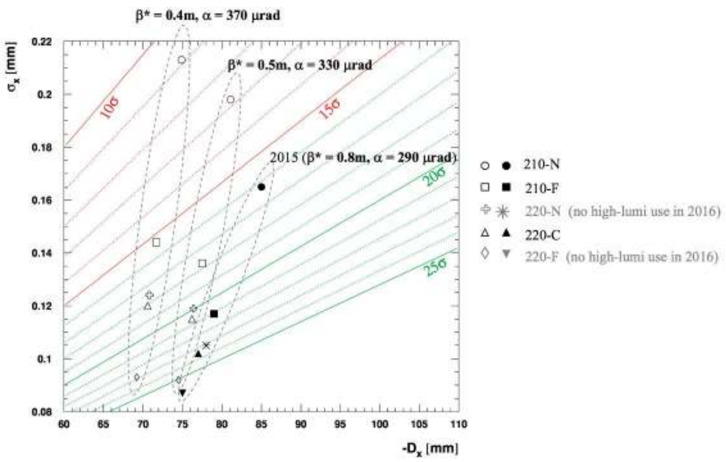

Figure 2.31: Roman pot positions for different optics configurations, requiring to have acceptance for rapidities up to 0.5 for a central mass of 750 GeV, as a function of the beam horizontal sigma and dispersion. Lines indicate the distance of approach to the beam in units of standard deviation [79].

The changes in the optics were disadvantageous for the search in the exclusive diphoton channel. In particular, it is visible in Fig. 2.31 that the acceptance of the tracking station closer to the IP (indicated as 210-N) is strongly reduced with respect to the previous running conditions. Instead, the cylindrical RP (220-C) has good acceptance, where diamond detectors are housed and thanks to their geometry can be also considered to be used for tracking.

One can also notice that the TOTEM-only RPs (220-N and 220-F) have good acceptance, but could not be used in 2016 since they were not upgraded for the high-luminosity running. RF shielding has then be installed on the 220-F RP during the 2016-2017 extended winter shutdown to make it available also for 2017.

A degree of freedom is the beam dispersion that can be increased including orbit bumps, with the aim of increasing the acceptance to low masses. In Fig 2.32, three optic tunings are shown (mild, intermediate and aggressive) compared to the nominal crossing configuration. For the 2016 running, it was eventually chosen to use the mild approach which guaranties a good acceptance at least for the second tracking station and the timing one.

Once fixed the optics configuration for the 2016 data taking, it was possible to evaluate the acceptance as a function of the mass and the rapidity of the central state. As shown in Fig. 2.33 if it is required that all RPs have acceptance for 750 GeV, the total acceptance is quite limited. But if one takes advantage of the diamond tracking capability and therefore only one station for tracking plus one for timing are required to reconstruct the track, the rapidity coverage extends to $-0.58 < y < 0.65$ assuming an RP approach at 15σ. This close distance was reached on May 30th, 2016, when the 0.5 mm safety margin was successfully removed, and then kept for standard insertion from that day on.

The final choice of the 2017 optics is still under discussion at the time of this thesis writing. A few possible choices with their consequences on the measurement of the minimum and maximum mass of the central system are shown in Fig. 2.34. For 2017 data taking, pots 210-F and 220-F will be used for the strip and pixel tracking detectors, respectively, and pot 220-C for the timing detectors. Full and hollow markers are for pots in Beam1 and Beam2, respectively. The optics configuration called "ATS option 3bis" is presently favoured and foresees a closest approach to the beam at 12σ plus a safety margin of 0.3 mm. The safety limit below which pots will not be allowed to go is shown by the horizontal line. The corresponding acceptance as a function

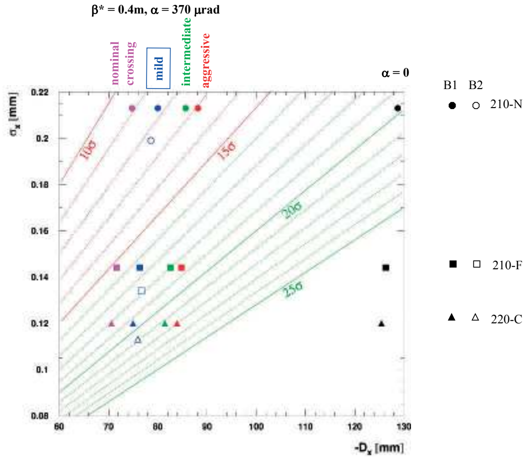

Figure 2.32: Roman pot positions for different dispersion values when requiring to have acceptance up to rapidities of 0.5 for a central mass of 750 GeV [79].

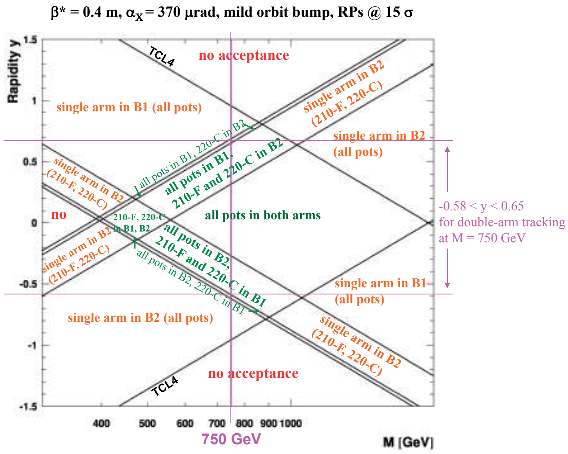

Figure 2.33: Acceptances as a function of invariant mass and rapidity of a centrally produced system for the 2016 LHC optics [79].

of invariant mass and rapidity for this favorite 2017 optics is shown in Fig. 2.35.

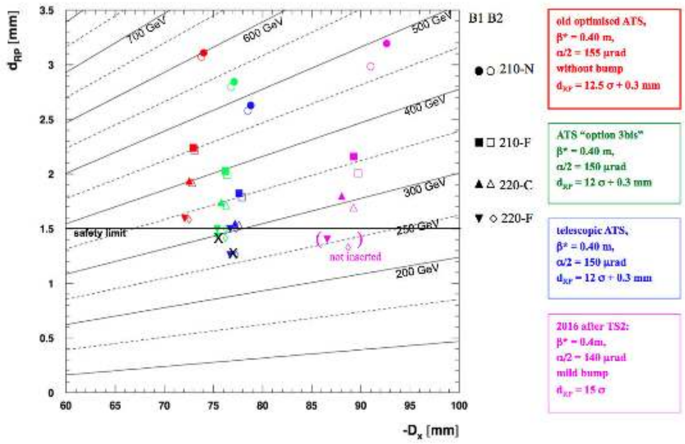

(a)

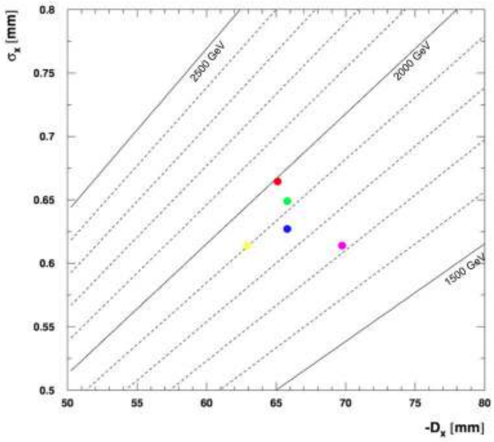

(b)

Figure 2.34: Minimum (a) and maximum (b) measurable mass of a centrally produced system for a few different choices of the 2017 LHC optics [80].

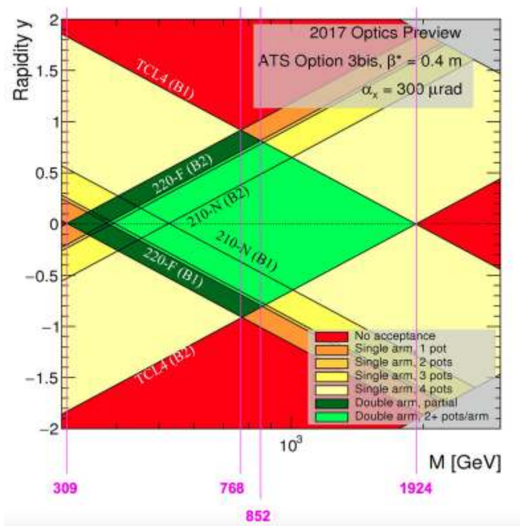

Figure 2.35: Acceptances as a function of invariant mass and rapidity of a centrally produced system for the presently favorite 2017 LHC optics [80].

Chapter 3

Silicon pixel sensors

Tracking detectors are crucial components of all experiments in high energy physics. They provide the possibility to measure the trajectory of the charged particles produced in a collision and, thanks to the magnetic field used to bend the particles, to determine their momentum with high precision. Moreover, in case of high detector occupancy as it is in modern colliders, tracking detectors help in advanced reconstruction techniques by tracing single particles within dense jet structures. The performance of tracking detectors is for example fundamental for heavy flavour physics, which often rely on a superior resolution of secondary decay vertices for b-quark tagging.

The favored technology by most of the current high-energy-physics experiments is silicon semiconductor detectors, because of various advantages over alternative detector concepts. Silicon sensors are solid-state ionization chambers in which incident charged particles create electron-hole pairs. These charge carriers drift to the electrodes under the influence of an electric field. The induced current at the electrodes is then amplified, shaped, and read out by the front-end electronics.

The mean energy required to create an electron-hole pair is much smaller than the one needed in gaseous detectors. On average, about 73 electron-hole pairs are created per μm of silicon [81] by an incident minimum ionizing particle (MIP), so that it is possible to realize really thin sensors ($\sim$ 200 μm) with still a sufficiently large signal response ($\sim$ 15 ke). This allows the installation of multiple layers in a limited space for reconstructing the full trajectory of the passing particle. Furthermore the high charge-carrier mobility leads to a relatively short collection time of O(10 ns), that makes these detectors of special interest at accelerators like the LHC.

Another advantage of silicon with respect to other solid state materials is that it is widely used, and the design and manufacturing of silicon tracking detectors profit from well established fabrication processes available in industry.

The high position resolution of silicon detectors is achieved by finely segmenting the electrodes in strips, obtaining a single dimension information, or in pixels, providing two coordinates for the incidence point. With modern devices, spatial resolutions of 10 μm or lower can be reached.

In this chapter, a brief overview of silicon detector characteristics will be given, with particular attention to the damage induced by radiation in order to provide information for the discussion of results presented later in this thesis. The last part of the chapter is dedicated to hybrid pixel detectors, since this technology has been chosen for the CT-PPS tracking system.

3.1 Silicon sensor features

Silicon has four valence electrons, which form covalent bounds with four nearby atoms. Its structure, projected on a plane, is shown in Fig. 3.1. Owing to the density of energy levels in the lattice structure of a crystalline material, some simplifications to the description can be made. When forming the lattice structure, the atomic orbitals of the constituents start overlapping and the energy state density increases because of shifts caused by the interaction. Eventually, a continuous band structure forms, which can be used to describe the electrical properties of the material.

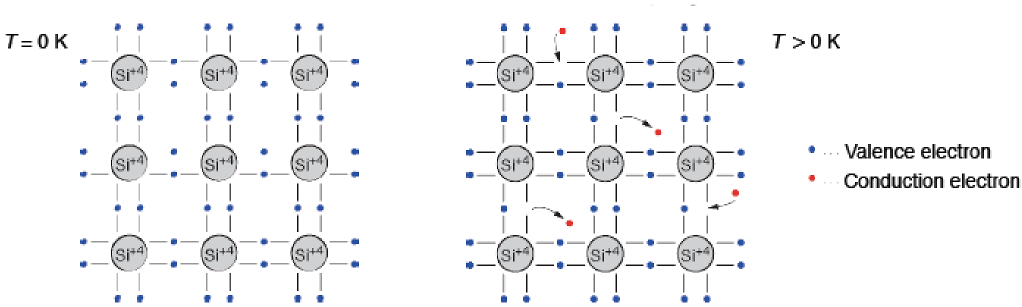

Figure 3.1: Two-dimensional representations of the silicon lattice, showing the different behaviour of the material at different temperatures.

Since electrons must follow the Pauli exclusion principle[1], the energy state occupancy follows the Fermi-Dirac distribution. Therefore, the probability of finding an electron in a state with energy E can be expressed as

$$f(E) = \frac{1}{1 + e^{\frac{E-E_F}{kT}}} \tag{3.1.1}$$

where E_F is the Fermi energy, T the absolute temperature of the system and k the Boltzmann constant. The Fermi energy denotes the energy at which the occupancy probability is 1/2. The Fermi-Dirac distribution at different temperatures is shown in Fig. 3.2.

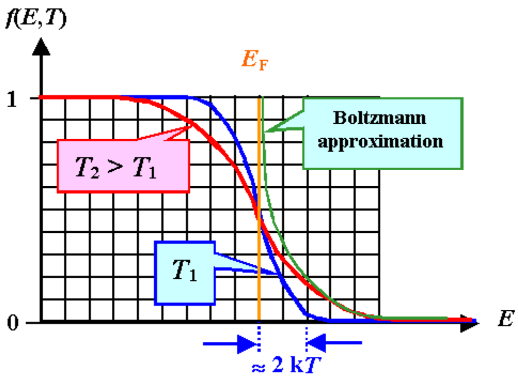

Figure 3.2: The Fermi-Dirac distribution at different temperatures.

At $T = 0$ K all energy states up to E_F are filled, while at higher temperatures some electrons will occupy excited states above the Fermi energy. In the energy band model, the valence band represents the highest band completely filled with electrons at $T = 0$ K. The next higher energy band is called conduction band. At temperatures higher than 0 K it is partially filled with

[1]The Pauli exclusion principle says that the probability of finding two fermions (particles with spin 1/2) in the same state is null.

electrons, which thanks to free available energy states within the band can move within the crystal lattice and thus contribute to the conductivity. At the same time, since a state is freed in the valence band, then another electron can occupy that state. The resulting effect is a movement of empty states which participate to the conduction. This empty state is called hole.

Figure 3.3 shows the configuration of valence and conduction bands for metal, insulator and semiconductor materials with respect to the Fermi energy. Metals have conduction and valence bands that overlap, which means that electrons can easily move participating to the conduction. In insulators, the valence band is well separated from the conduction band by an energy gap with the Fermi energy lying in the gap region. Semiconductors have a similar structure, but the energy gap is much smaller and it allows thermally excited electrons to reach the conduction band.

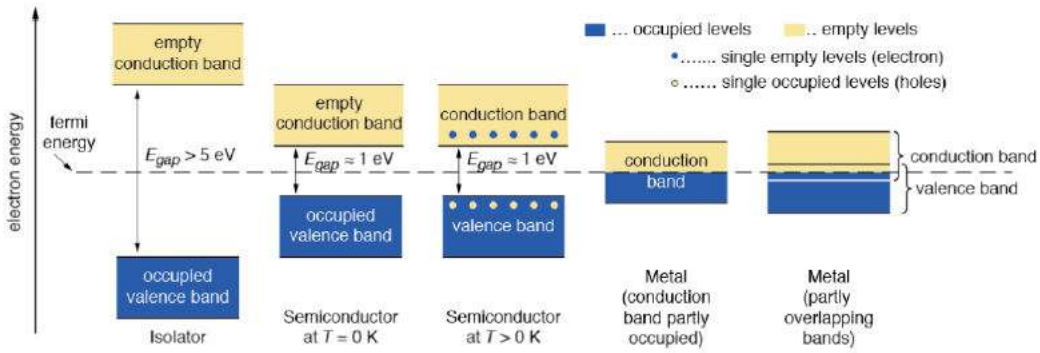

Figure 3.3: Band structure for isolators, semiconductors and metals.

The size of the gap between the conduction and valence bands, E_G, depends on the material and strongly influences its characteristics. Germanium has a relatively small energy gap of about $E_G = 0.74$ eV, which results in a very low mean ionization energy. Thus, it offers excellent properties for gamma ray spectroscopy. However, the small E_G determines a high thermal noise and germanium detectors need to be operated at cryogenic temperature (normally 77 K), which is not feasible for a tracking detector.

Diamond has opposite characteristics: thanks to $E_G = 5.5$ eV, it has an extremely low noise and can be operated without cooling, allowing a substantial material budget reduction. On the other hand, the signal generated by a particle is small and the production costs limit the use of diamond to small devices.

Silicon has an intermediate energy gap ($E_G = 1.12$ eV at room temperature), which is higher enough for operating with limited noise at temperatures achievable in tracking detectors (usually between 0 and $-20°$ C), but that at the same time allows large signals.

Gallium arsenide has characteristics similar to silicon ($E_G = 1.42$ eV), however it has been shown that it is less radiation hard than silicon and that by increasing the particle fluence the charge collection efficiency degrades [82]. This characteristic limits the use of gallium arsenide for tracking detectors in favour of silicon.

In intrinsic silicon, which means that no impurities are present in the crystal, at each free electron corresponds a hole in the valence band. Thus, the carrier density for electrons n_n and for holes n_p is the same ($n_i = n_n = n_p$, which is $\sim 1.45 \cdot 10^{10}/\text{cm}^3$ at room temperature[83]) and it is a function of the temperature:

$$n_i \propto T^{\frac{3}{2}} \cdot \exp\left(-\frac{E_G}{2kT}\right) . \tag{3.1.2}$$

The drift velocity of the carriers is written as

$$\vec{v}_{p,n} = \pm\mu_{p,n}\vec{E} \tag{3.1.3}$$

where $\overrightarrow{E}$ is the electric field and $\mu_{p,n}$ are the mobilities of holes and electrons given by

$$\mu_{p,n} = \frac{e\,\tau_{p,n}}{m_{p,n}} \tag{3.1.4}$$

with e the electron charge, $\tau_{p,n}$ the mean free time between two collisions, and $m_{p,n}$ the effective mass of holes and electrons. In silicon, the mobilities of the two carriers are constant to a good approximation when the electric field is below 1 kV/cm. At the temperature of 300 K the mobilities are:

$$\mu_n \sim 1400 \text{ cm}^2\text{V}^{-1}\text{s}^{-1} \tag{3.1.5}$$

$$\mu_p \sim 450 \text{ cm}^2\text{V}^{-1}\text{s}^{-1} \tag{3.1.6}$$

To define the resistivity both charge carriers must be considered:

$$\rho = \frac{1}{e\,(\mu_n n_n + \mu_p n_p)} \tag{3.1.7}$$

Using the values above, the intrinsic silicon resistivity can be evaluated to be ~ 230 Ωcm at a temperature of 300 K.

For using silicon to detect particles, it is necessary that the charge deposited in the material is well distinguishable from the amount of free carriers due to thermal effects. Considering an intrinsic silicon detector of thickness $d = 300$ μm and area $A = 1$ cm^2 at the temperature of 300 K, the amount of free carriers due to thermal effects, which is the noise, can be expressed as

$$noise = n_i \cdot d \cdot A \sim 4.35 \cdot 10^8\, e^- h^+\, pairs \tag{3.1.8}$$

The mean energy needed for producing an electron-hole pair in silicon is $I_0 = 3.62$ eV. A MIP in silicon has an energy loss for path length unit of $dE/dx = 3.87$ MeV/cm. Thus, the expected signal is:

$$\frac{dE/dx \cdot d}{I_0} \sim 3.2 \cdot 10^4\, e^- h^+\, pairs \tag{3.1.9}$$

which is four orders of magnitude lower than the noise. As a consequence, intrinsic silicon cannot be used for particle detection and a different solution must be found to drastically reduce the noise of the device. To this purpose, silicon must be doped and then depleted from free carriers by means of a p-n junction, as explained in the next section.

To dope a semiconductor, impurities are artificially introduced in the crystal lattice in order to change its electric characteristics. Doping silicon with a group-V element, such as phosphorus, adds an additional valence electron that is only loosely bound. The shallow donor state is located close to the conduction band, as shown in Fig. 3.3 (left), and thus the quasi-free electron can be easily excited, leaving the phosphorus atom as a positive ion. This material is referred to as n-type silicon, with the majority of the charge carriers being electrons.

Shallow acceptor states close to the valence band, as shown in Fig. 3.3 (right), are created by introducing a group-III element, such as boron, into the silicon crystal. With one valence electron less, this effectively introduces a hole which can be occupied by valence band electrons. The majority of the charge carriers are holes and the material is referred to as p-type silicon.

The Fermi level of a semiconductor lies very close to the middle of the gap. By introducing impurities in the silicon crystal, the occupancy of the energy states changes. In particular, with the addition of acceptor or donor atoms, the Fermi level shifts towards the valence or the conduction band, respectively [83]. This effect is the basis of the $p-n$ junction, which is needed to strongly reduce the free charge of the intrinsic silicon.

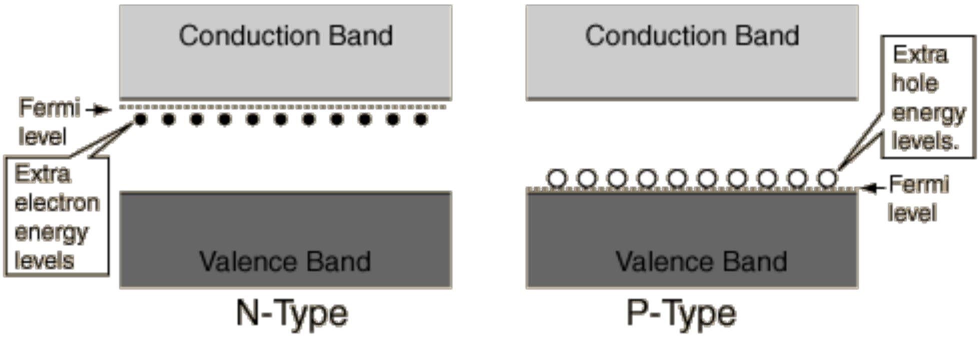

Figure 3.4: Band structure modification due to silicon doping. In n-doped silicon, shallow donor levels are introduced close to the conduction band and the Fermi energy shifts up. In p-doped silicon, additional shallow acceptor levels are located close to the valence band and the Fermi energy shifts down

3.1.1 p-n junction

A p-n junction is formed when two regions of p- and n-type semiconductor materials are joined together.

At equilibrium, the total current flowing in the device must be zero. Since it is possible to demonstrate that the total current is proportional to the gradient of the Fermi level [84], it follows that in a p-n junction the Fermi level at equilibrium must be constant. As a consequence, the valence and conduction bands must bend as shown in Fig 3.5. E_C (E_V) indicates the energy of the lowest (highest) energy state of the conduction (valence) band.

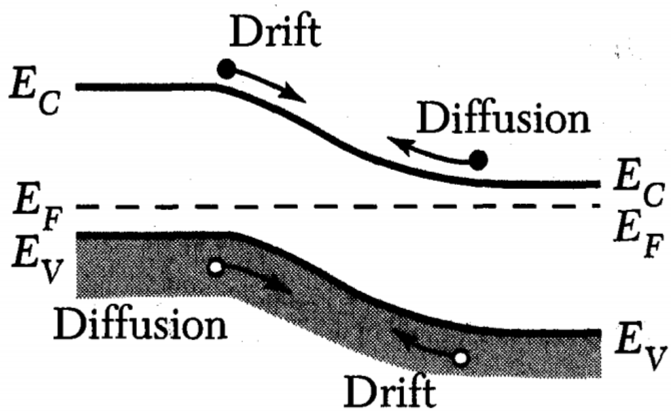

Figure 3.5: p-n junction in thermal equilibrium [84].

A gradient of the E_C and E_V levels different from zero corresponds to a not null electric field, which determines a drift of holes from n-type to p-type silicon and an opposite motion of electrons [84].

At the same time, a variation of the difference between the E_V (E_C) and E_F levels creates a gradient in the hole (electron) density that translates in a diffusion of holes (electrons) towards the n- (p-)type region of the device [84]. In other words, electrons from the n-type region diffuse towards the p-type, which has a much smaller concentration of them, while the holes make the opposite process. Diffusion leaves behind regions with fix charges due to acceptor and donor ions, creating an electric field in the region around the junction.

The current density $J_{p,n}$(diff) due to diffusion and the current density $J_{p,n}$(drift) due to drift can be evaluated as

$$J_{n,p}(\text{diff}) = \pm q\, D_{n,p} \frac{dn_{n,p}}{dx} \tag{3.1.10}$$

$$J_{n,p}(\text{drift}) = q \mu_{n,p} n_{n,p} E \tag{3.1.11}$$

where $D_{n,p}$ are the diffusion constants of electrons and holes, respectively.

The equilibrium is reached when the current produced by the electric field is equal to the one due to diffusion:

$$q\, D_n \frac{dn}{dx} + q \mu_n n_n E = 0 \tag{3.1.12}$$

$$-q\, D_p \frac{dp}{dx} + q \mu_p n_p E = 0 \tag{3.1.13}$$

As a consequence, the so-called built-in potential V_{bi} is induced in the junction and the region nearby the junction, called depletion region (Fig. 3.6(a)), becomes empty of free charges. The *p*-*n* junction allows to use doped silicon as particle detector since the charge deposited by a particle will not be hidden by the noise as it happens in intrinsic silicon.

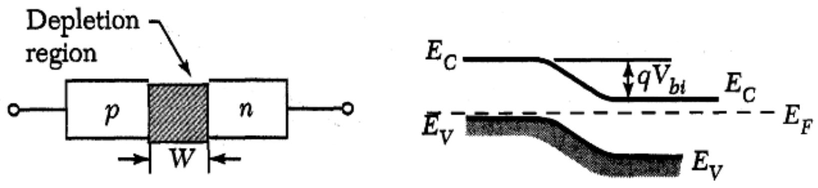

(a) Thermal equilibrium.

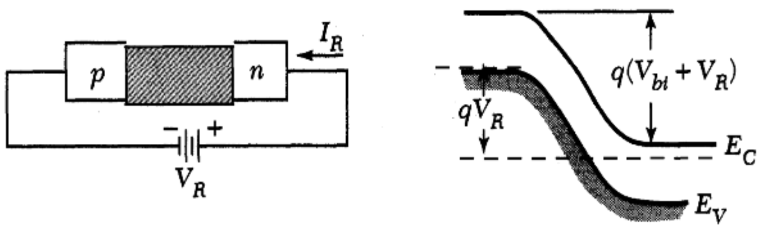

(b) Reverse bias.

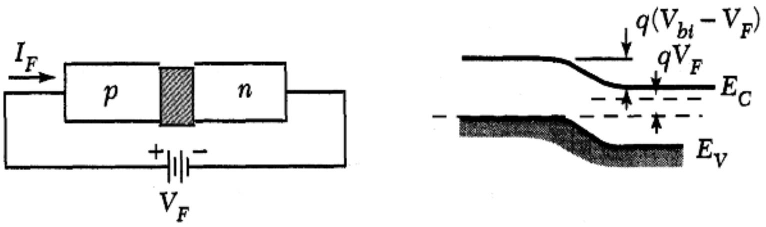

(c) Forward bias.

Figure 3.6: Schematic representations of depletion layer width and energy band diagram for a *p*-*n* junction under various biasing conditions [84].

The extension of the depletion region in the two different substrates (W_{Dp} in the *p*-type and W_{Dn} in the *n*-type) depends on the doping concentration of acceptors (N_A concentration) and donors (N_D concentration) [83]:

$$W_{Dp} = \sqrt{\frac{2\varepsilon_0\varepsilon_{Si}V_{bi}}{q}\frac{N_D}{N_A(N_A+N_D)}} \tag{3.1.14}$$

$$W_{Dn} = \sqrt{\frac{2\varepsilon_0\varepsilon_{Si}V_{bi}}{q}\frac{N_A}{N_D(N_A+N_D)}} \tag{3.1.15}$$

with ε_{Si} the relative dielectric constant of silicon.

By changing the doping concentrations, it is thus possible to unbalance the extension of the depletion region in one direction with respect to the junction contact, and also to modify the total width:

$$W_D = W_{Dp} + W_{Dn} = \sqrt{\frac{2\varepsilon_0\varepsilon_{Si}}{q}\frac{N_A+N_D}{N_AN_D}V_{bi}} \tag{3.1.16}$$

In case of an abrupt junction (p^+-n or n^+-p where the + apex indicates a high concentration doping[2]), the depletion region expandes in the less doped side and its width can be reduced to

$$W_D = \sqrt{\frac{2\varepsilon_0\varepsilon_{Si}V_{bi}}{qN}} \tag{3.1.17}$$

where N is N_D or N_A depending on whether $N_A \gg N_D$ or vice versa.

p-n junctions are the basis for photoelectric cells, because in the depletion region the electron-hole pairs generated by photons do not recombine thanks to the electric field described above, and holes and electrons can drift towards the opposite sides and be collected.

In the case of a particle detector, the built-in potential is not sufficient to provide a good enough collection efficiency of the produced charges, and therefore an external potential must be applied. As shown in Fig. 3.6(b), applying a potential of the same sign of the built-in potential (reverse bias), the bending of conduction and valence bands is further pronounced and it is possible to increase the depletion width and so the region in which a particle can be measured. In particular, for a bias much larger that the built-in one, the width of the region which is empty of free charges is proportional to the root square of the bias potential V_R applied:

$$W_D = \sqrt{\frac{2\varepsilon_0\varepsilon_{Si}}{q}\frac{N_A+N_D}{N_AN_D}(V_{bi}+V_R)} \sim \sqrt{\frac{2\varepsilon_0\varepsilon_{Si}}{q}\frac{N_A+N_D}{N_AN_D}V_R} \tag{3.1.18}$$

The best working condition for a silicon particle detector occurs when the complete volume is depleted from free charges. The reverse voltage at which this condition is verified is the so-called full depletion voltage, which can be written as

$$V_{FD} = \frac{qNd^2}{2\epsilon_s} \tag{3.1.19}$$

From the above equation it is evident that a silicon bulk with higher impurity concentration requires a higher reverse voltage to be depleted.

By applying a potential of the opposite sign of the built-in one (forward bias), the depletion region reduces and a current starts flowing between the two doped sides of the junction. Figure 3.6(c) shows the effect of a forward bias on the depletion region and on the energy bands.

The presence of a region without free charge carriers makes the diode behaving like a capacitance. The value of this capacitance depends on the depletion region extension and therefore on

[2]For very high concentrations p^{++} or n^{++} are also used.

the voltage applied. For a planar junction, the capacitance per unit area can be approximated to

$$C_D = \frac{\epsilon_s}{W_D} = \sqrt{\frac{q\epsilon_s N}{2}} (V_{bi} - V)^{-1/2} \tag{3.1.20}$$

with N the impurity concentration in the substrate. From the above equation one can write

$$\frac{d1/C_D^2}{dV} = -\frac{2}{q\epsilon_s N} \tag{3.1.21}$$

3.1.2 Leakage current

As already observed in the previous section, by applying an external bias voltage to the *p-n* junction, valence and conduction bands bend, with the results that also the Fermi level, which at equilibrium is constant on the entire device, bends. This means that drift and diffusion components of the current are not anymore in equilibrium and a net current is produced.

If a forward bias is applied, minority carriers[3] experience a lower voltage barrier opposing their diffusion through the depletion region. On the opposite, if the diode is reverse biased, the diffusion reduces and the carrier drift creates a net current through the device. It is important to note that the drift component does not increase much with the reverse bias since the drift velocity saturates with increasing the electric field.

The current density J as a function of the applied bias voltage V of an ideal diode is given by the Shockley equation:

$$J = J_0 \left[\exp\left(\frac{qV}{kT}\right) - 1 \right] \tag{3.1.22}$$

where J_0 is the saturation current when a reverse bias is applied. The ideal current-voltage characteristic is shown in Fig. 3.7.

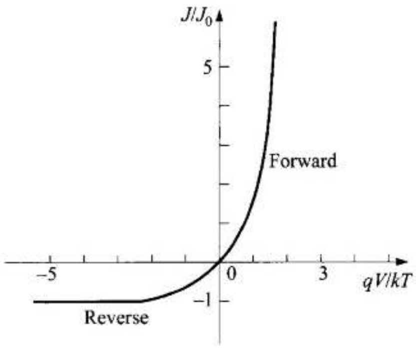

Figure 3.7: Ideal current-voltage characteristic [84].

The Shockley equation adequately predicts the current-voltage characteristics of germanium *p-n* junctions at low current densities. For Si and GaAs *p-n* junctions, the agreement is only qualitative. Departures from the ideal equation are mainly due to: generation in reverse bias and recombination in forward bias condition of carriers in the depletion layer; parasitic IR drop due to series resistance; tunneling of carriers between states in the bandgap; and surface effects.

Surface effects are primarily due to ionic charges on or outside the semiconductor surface that induce image charges in the semiconductor, and thereby cause the formation of the so-called surface channels or surface depletion-layer regions. Once a channel is formed, it modifies the junction depletion region and gives rise to a surface leakage current, and the saturation foreseen by the ideal law does not occur.

[3] The less abundant charge carriers are called minority carriers; in n-type semiconductors they are holes, while in p-type semiconductors they are electrons.

In addition, when a sufficiently high potential is applied, the junction breaks down and conducts a very large current. This effect is mainly due to two reasons: tunneling or an avalanche multiplication. The first case occurs when the electric field approaches 10^6 V/cm and a significant current begins to flow by means of this band-to-band tunneling process. To obtain such a high field, the junction must have relatively high impurity concentrations on both the $p-$ and $n-$side, which is usually not the case for silicon detectors. The second case occurs when the electric field in a semiconductor is above a certain value and the carriers gain enough energy to excite electron-hole pairs by a process called impact ionization, resulting in a avalanche multiplication.

3.2 Radiation damage

In high energy physics experiments, silicon detectors are mainly used in the innermost layer closer to the interaction point since, thanks to their high granularity, they are able to resolve between different tracks. As a consequence, they are subjected to a high fluence of particles and need to tolerate high radiation doses.

Big efforts have been done so far and are ongoing by the experiment collaborations for improving the radiation resistance of sensors and front-end electronics, in order to optimize these detectors for future experiments in which the radiation damage due to high luminosity conditions will be higher than the current technologies could face.

Radiation in silicon produces two main types of damage: bulk and surface defects. This section gives a brief description of these damage mechanisms and of their impact on the detector performance.

3.2.1 Bulk damage

The bulk damage produced in silicon detectors by hadrons (neutrons, protons, pions, etc.) or high energetic leptons is mainly caused by the displacement of a primary knock-on atom (PKA) out of its lattice site, resulting in a silicon interstitial and a vacancy (Frenkel pair). Both can migrate in the lattice and form point defects by combining with impurity atoms in the silicon.

In order to displace a silicon atom from the lattice (considering silicon atoms only is a good approximation since the impurity concentrations are negligible with respect to the silicon one), the energy released by a massive particle must be higher than the displacement threshold of ~ 25 eV [85]. It is also possible that the recoiling atom has a high energy and can itself displace other silicon atoms besides loosing energy by ionization. At the end of the recoil range, non-ionizing interactions prevail and a dense agglomerate of defects (also called cluster) is formed. Point defects together with clusters are responsible for the change of the silicon properties while ionization losses can be neglected since they do not affect the lattice structure.

The maximum energy imparted by a particle impinging a silicon atom can be evaluated, without considering relativistic effects, by the formula:

$$E_{R,\max} = 4E_P \frac{m_P m_{\text{Si}}}{(m_P + m_{\text{Si}})^2} \tag{3.2.1}$$

where m_P and E_P are mass and energy of the particle and m_{Si} is the mass of the silicon atom. Considering an energy threshold of 25 eV for producing a Frenkel pair and 5 keV for a cluster, it can be derived that the energy needed by a neutron for producing a point defect is ~ 185 eV and ~ 35 keV for a cluster. In the case of an electron, due to the much smaller mass, these energies need to be raised to ~ 255 keV and ~ 8 MeV, respectively. Photon irradiation of a silicon bulk is often done with a ^{60}Co source, which emits gammas with energies of 1.17 and 1.33 MeV. These photons can transfer to electrons, via the Compton effect, a maximum kinetic energy of about 1 MeV and only point defects can be generated.

Low energy charged particles interact with silicon atoms mainly via Coulomb interactions and hence most of the energy is lost by ionization, which is fully reversible in silicon. On the other hand, neutrons interact with nucleons only. In order to have an independent measurement unit, radiation damage is scaled to the non-ionizing energy loss (NIEL), which represents the energy deposited by a particle that it does not go in the process of ionization.

This representation is valid under the assumption that any displacement-damage induced change in the material scales linearly with the amount of energy imparted by the displacing collision. To evaluate that, the displacement damage cross section (indicated with $D(E)$) is used, which keeps into account all possible interactions of a particle with energy E with the lattice atoms and also all the damages due to the recoiling atoms. The trend of this quantity as a function of energy for different particles is shown in Fig. 3.8.

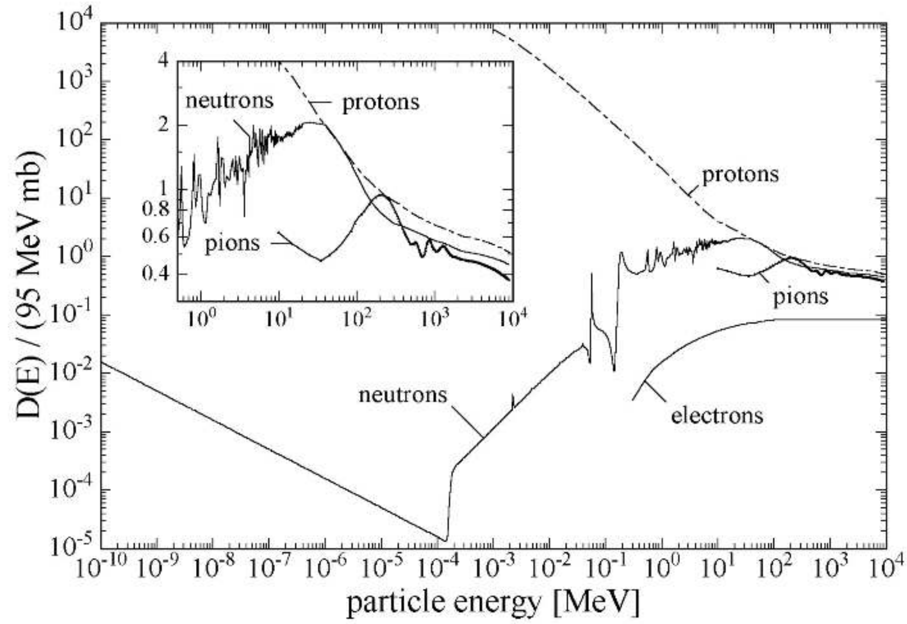

Figure 3.8: Displacement damage cross section as a function of energy for different particles [86]. Due to the normalization to 95 MeV mb the ordinate represent the damage equivalent to 1 MeV neutrons.

Using the displacement damage cross section it is possible to compare the irradiation with different particles and energies, and neutrons of 1 MeV are used as reference particles. The conversion is done by means of the hardness factor κ [87], defined by the equation

$$\kappa = \frac{\int D(E)\phi(E)dE}{D(E_n = 1\text{MeV}) \cdot \int \phi(E)dE} \tag{3.2.2}$$

with $\phi(E)$ the particle flux as a function of energy. Therefore, a generic particle fluence Φ can be converted in 1 MeV neutron equivalent (n_{eq}) fluence Φ_{eq} by simply multiplying it by the hardness factor.

The primary Frenkel pairs can move in the lattice at temperatures above 150 K and if they annihilate no damage remains. On the other hand, vacancies and interstitial silicon atoms can bound to other impurities or substitute dopants in the lattice. At microscopic level, new energy states are created, resulting in the change the silicon properties at macroscopic level. An extensive description of the microscopic effects of radiation damage can be found in [86]. In the following, the main macroscopic changes in the silicon properties due to radiation will be described: increase of the leakage current, effective doping change, and charge trapping.

Leakage current

The irradiation introduces energy levels in the energy gap that, acting as generation-recombination centers, produce an increase of the leakage current in reverse bias condition. The increase of leakage current per unit volume as a function of the irradiation fluence is shown in Fig. 3.9 and it is independent of the different types of silicon material.

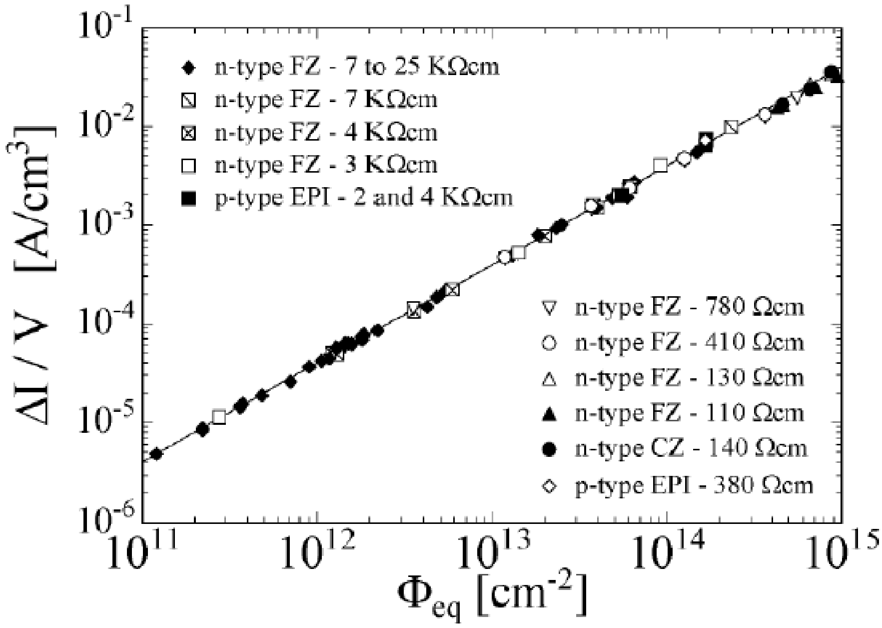

Figure 3.9: Induced leakage current for different types of silicon as function of the fluence. The current has been measured after an annealing step at 60 ℃ for 80 minutes [86]

The increase of current is directly proportional to the fluence and can be expressed as

$$\Delta I = \alpha \Phi_{eq} V \tag{3.2.3}$$

where α is the current-related damage rate. Its value, measured after an annealing of 80 minutes at 60°C, is quoted to be $(3.99 \pm 0.03) \times 10^{-17}$ A/cm [86].

The value of α strongly depends on the annealing time and temperature, as shown in Fig. 3.10. It can be noticed that the current continuously decreases with the annealing time and that a higher temperature speeds up the current reduction. The trend of the curves can be fitted with a sum of exponentials, which well represent the recombination of different defects with different annealing time constants.

For the application of silicon detectors in high energy physics experiments, the increase of leakage current needs to be kept under control. In particular, the amplifier that reads the deposited charge needs to be able to sustain the current flowing through the input stage. Moreover, also the power supply has to be correctly dimensioned. An annealing of the sensors at high temperature would in principle help in reducing the leakage current, but the impact on other irradiation-related damages limits this procedure in experiments.

Effective doping

The change due to irradiation observed in the effective doping concentration (N_{eff}) for a n-type 300 μm-thick planar diode is shown in Fig. 3.11, together with the variation of the depletion voltage. Two concurrent processes contribute: the donor removal, which is negligible

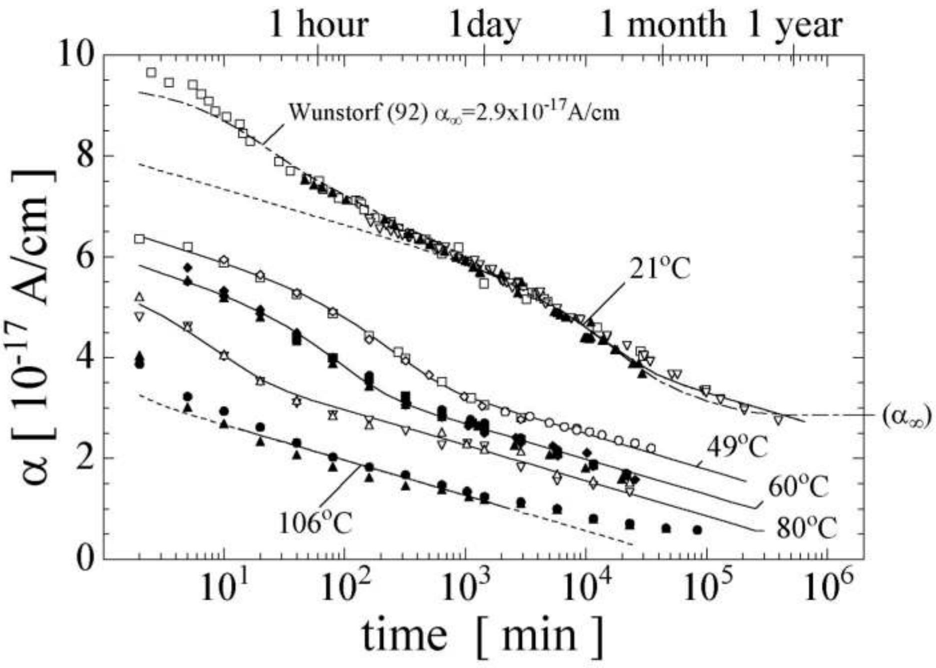

Figure 3.10: Current-related damage rate as a function of the annealing time at different temperatures [86].

for *p*-type silicon, and the generation of acceptor-like states. They finally lead to the type inversion of *n*-type silicon.

Although the change of the effective doping depends on the material, the final result is that, after the type inversion, N_{eff} increases linearly with the fluence. This implies that the bias voltage needed to fully deplete the sensor increases, becoming a demanding request for the power supplies and the bias distribution.

In contrast to what happens for the leakage current, the time dependence of the irradiation effect in N_{eff} is not only subject to a beneficial annealing but also to the so-called reverse annealing. This two components are shown in Fig. 3.12. In the beginning the effective doping reduces, partially recovering the damage, and this is usually interpreted as an acceptor annealing. However, in the long term the space charge becomes more negative and this is attributed to the build up of acceptors. This effect limits the use of sensor annealing to reduce the leakage current.

Trapping

Besides creating generation and recombination centers, which lead to an increase of the leakage current, and changing the effective dopant concentration, which leads to an increase of the needed bias voltage, radiation damage has the effect of introducing energy states in the band gap that act as traps. These traps are mostly empty in the depletion region, due to the lack of free charge carriers, and can hold or trap part of the signal charge for a time longer than the collection time, thus reducing the signal amplitude.

The dependence of this effect on the radiation fluence is expressed in terms of the trapping time τ_t:

$$\frac{1}{\tau_t} = \frac{1}{\tau_{t,\Phi=0}} + \gamma\Phi \tag{3.2.4}$$

where γ is a parameter that is measured to be $0.41 \cdot 10^{-6}$ cm^2/s for electrons and $0.60 \cdot 10^{-6}$ cm^2/s for holes after neutron irradiation [88].

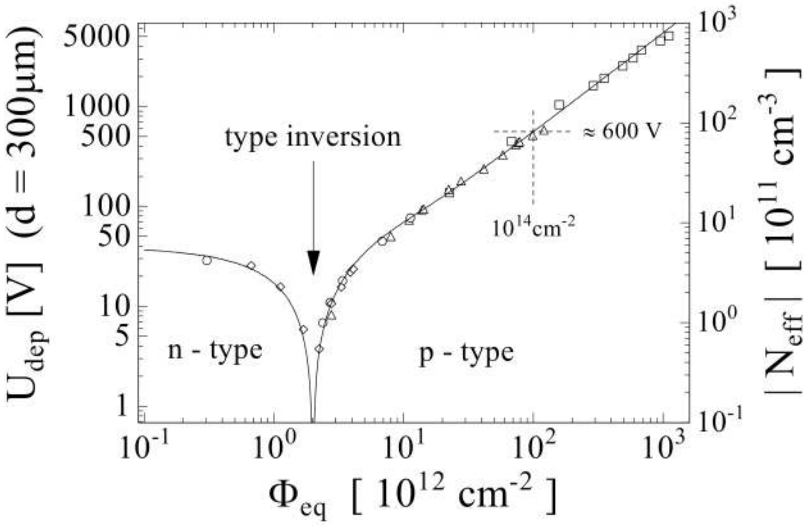

Figure 3.11: Change of full depletion voltage and absolute effective doping as a function of irradiation in a n-type 300 μm-thick silicon sensor [86].

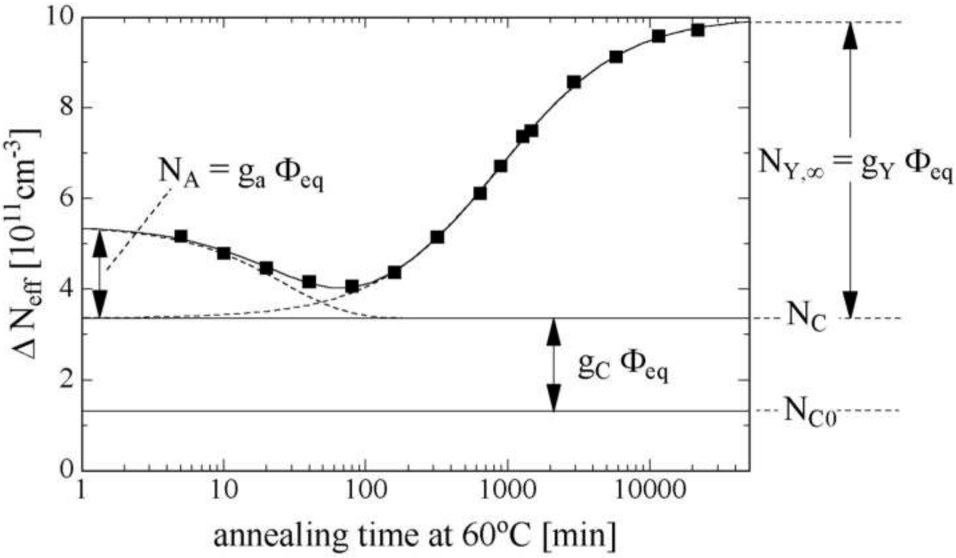

Figure 3.12: Effective doping as a function of the annealing time [86].

For devices which do not need to stand a high fluence this effect is not so relevant. In fact, for a fluence of 10^{14} n_{eq}/cm^2 the signal for a 300 μm-thick planar silicon sensor is still about 90% of the original one. However, for higher levels of irradiation, this effect becomes crucial: for a fluence of 10^{15} n_{eq}/cm^2 the signal decreases to $\sim 50\%$.

Trapping acts as a mean free path: the larger the drift space the bigger the trapping probability. In order to mitigate the charge loss due to trapping, studies are ongoing for developing detectors with a shorter collection distance, like 3D and slim planar sensors.

3.2.2 Surface damage

Despite the quality of the fabrication, silicon dioxide is known to contain defects [89]. These defects can be located inside the oxide or at the interface with silicon. The former defect type can be further divided in categories: oxide fixed charges are positive and placed close to the SiO_2-Si interface, and they will attract negative charges on the opposite side of the interface; oxide trapped charges can be positive or negative and they are typically the result of ionization or avalanche injection and anneal at low temperatures; finally, oxide mobile charges are mainly caused by ionic impurities as Na^+, Li^+ and H^+. Interface trapped charges are instead positive or negative charges caused by structural or oxidation defects or metal impurities. They can also be caused by unterminated Si bounds. The traps located at the SiO_2-Si interface can be charged up or discharged through the capture or emission of electrons and holes; Their main effect on the device properties is the increase of the surface recombination velocity.

Ionization in the silicon dioxide is not a fully reversible process. Electrons in the SiO_2 have a high mobility ($\mu_{n,oxide} \sim 20$ $cm^2V^{-1}s^{-1}$) and are collected by the nearest positive biased electrode. Holes, instead, have a very low mobility ($\mu_{p,oxide} \sim 2 \cdot 10^{-5}$ $cm^2V^{-1}s^{-1}$) because of the large number of shallow hole traps. When a hole in the oxide comes close to the interface with the silicon bulk it may be stopped permanently, resulting in an increase of the oxide total charge. Radiation can also induce bond breaking, leading to an increase of the interface state concentration.

The evolution of surface defects with radiation has been deeply studied [90]. The oxide charge, which is usually of the order of 10^{11} cm^{-2} for unirradiated devices, can increase by at least an order of magnitude. As the number of traps is limited, a saturation is observed to a value of $\sim 3 \times 10^{12}$ cm^{-2} for high-quality thermally-grown oxide [91]. The positive trapped charges induce a compensating electron accumulation layer that may compromise the insulation between n^+-electrodes. Moreover, it might increase the parasitic capacitance between adjacent regions and increase the device noise. In fact, in the case of a small inter-electrode (strip or pixel) distance a stable accumulation layer builds up, which is responsible for a growing coupling capacitance [89]. Modifications in the electric field at the surface might also be induced, affecting the voltage handling capability of the sensor with a possible large reduction of the breakdown voltage [92].

At the same time, the irradiation can increase the surface recombination velocity, which is typically less than 10 cm/s, by several orders of magnitude. In silicon sensors this effect translates into an increase of the surface component of the leakage current.

The magnitude of the surface damage is strongly dependent on the biasing conditions. Since the damage mechanism is related to the ionization process, the electric field established by applying a bias voltage reduces the electron-hole pair recombination probability leading to a steeper change in the device properties as a function of the irradiation.

In electronics, the main use of silicon dioxide is as gate insulator in MOS transistors, however since a few years high scaled technologies started using different materials with higher dielectric constants. Readout circuits suffer in particular from the effects of positive charge build-up, decreased carrier surface mobility and high density of interface states with energy levels in the band gap. Due to the creation of new interface traps, transistors suffer from the increase of the absolute value of their threshold voltage. The increased density of interface states has also an impact on the flicker noise of NMOS transistors, whose level is significantly higher compared to PMOS devices and further deteriorates after irradiation.

Since the surface damage is proportional to the absorbed energy by ionization, the dose can be specified in Gray (or rad, 1 Gray = 100 rad) and it is independent of the particle type.

3.3 Hybrid pixel detector

The main application of silicon devices in high energy physics experiments is as tracking detectors, thanks to their very high granularity.

Tracking silicon sensors can be divided into two main categories: strip and pixel. The former is characterized by a segmentation along one direction and therefore only one coordinate can be measured. To solve this inconvenience, sensors with different strip orientations are coupled or in some cases two perpendicular patterns are implemented on the two surfaces of the sensor. This technology is particularly effective for building quite large tracking detectors with an excellent resolution while containing the costs. The drawback is the reduced capability of discriminating multiple tracks, since the measurement of only one coordinate per plane can originate fake hits. To discriminate real hits from ghost ones several layers of strip detectors with different electrode orientations need to be piled up, and therefore strip detectors are not very effective in high occupancy conditions, like those of a vertex detector.

A solution to this problem, without increasing the number of detector layers, is to use pixel detectors. Because of the small area of each electrode, pixel detectors present lots of benefits in comparison to other architectures. Besides providing a more precise spatial information, the fine segmentation allows to have a lower leakage current, a better signal over noise ratio, and a reduced hit rate. The drawback is a more complex readout electronics, which increases the cost and limits their use for large areas.

In high energy experiments, characterized by very high event rates, each pixel is connected to a readout channel. The two most common solutions (Fig. 3.13) are: hybrid pixel detectors, where the signal collected in a sensitive volume is elaborated by a separate readout chip, and monolithic detectors in which sensor and electronics are integrated.

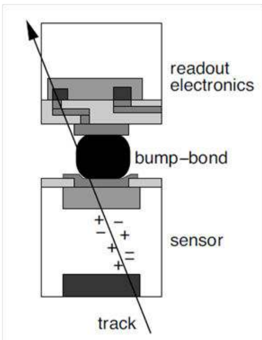

(a) Hybrid pixel

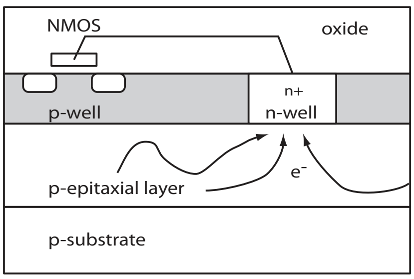

(b) Monolithic pixel

Figure 3.13: The two principal families of pixel detectors.

This last category of detectors has still limited application in experiments with high luminosity, like CMS and ATLAS at the LHC, due to the limited charge collection time, but thanks to their much lower cost with respect to the hybrid technology, lots R&D studies are ongoing to improve these detectors [93].

The vertex detectors of the LHC experiments use hybrid pixels. Ionizing particles create charges in the sensor that are collected and sent to the readout chip, which amplifies, filters

Readout electrode	Substrate	
	p-type	n-type
p^+	Double-sided process (expensive). No advantage over p^+-in-n	Typical single-sided sensor for most of the applications
n^+	Single-sided process. Considered as replacement of n^+-in-n for the future	Double-sided process. "Standard-device" if radiation hardness is required

Table 3.1: All possible combinations of substrate and electrode types.

and temporarily stores the signal until it is transferred to the periphery data buffer, where it waits for the trigger. The technique to link sensor and readout chip is called bump-bonding.

3.3.1 Planar pixel sensor

The simplest planar pixel geometry (Fig. 3.14) uses a p^+ pixel implant on a n-type substrate, which usually has a thickness between 200 and 300 μm. Electrodes are implemented on the frontside of the silicon bulk. The backside houses the ohmic contact, which is obtained with an overall n^+ implant and a metallization with aluminum. This configuration, called single-sided, is simple to realize because it is not necessary a photolithographic[4] step on the backside, which also allows to contain the cost.

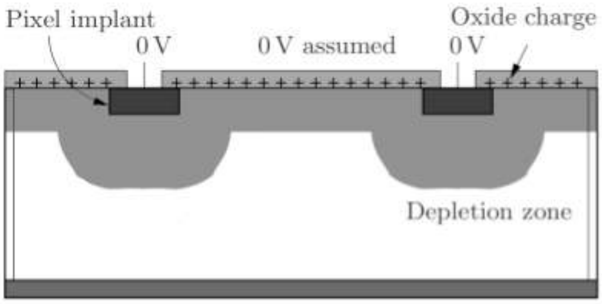

Figure 3.14: Schematic cross section of a simple silicon pad sensor [88].

Applying a positive bias on the backside, the depletion zone starts to grow from the junction into the bulk, until the bulk is completely depleted. In this type of sensors, the charge deposited by a crossing particle drifts perpendicularly to the silicon surfaces: holes to the frontside, where they are collected by the pixel electrodes, and electrons to the backside.

In principle there are two choices for the substrate doping and two choices for the doped electrodes. Four combinations are thus possible and they are listed in table 3.1.

The simplest technology to build a silicon sensor is to implement p^+ electrodes on a n-type bulk (p−in−n), as described above. However, these sensors are not used in a high radiation environment since they undergo type inversion and the junction is near the backplane contact, which means that to operate the sensor it has to be almost fully depleted.

[4]The photolithographic technique uses a photoresistive film (called photoresist or simply resist) which can be selectively removed exposing the material to light and leaving in shadow zones that must be protected.

Better performances after irradiation are showed by n−in−n sensors. In this case, after the type inversion, the depletion region extends from the readout electrodes and sensors can be used also not fully depleted, a very important feature after high irradiation when the required power could be demanding. The drawback is that the large p^+ implantation on the backside must not extend to the cutting edges of the sensor. The mechanical damage caused to the crystals by sawing the wafer makes the edges conductive and this can short the junction. For this reason, guard rings must be implemented on the backside to contain the depletion region and a double-sided process is needed. Moreover, the pixels need to be insulated one from the other by suppressing the electron accumulation layer on the surface produced by the positive charge in the oxide layer. This can be obtained by means of a p-stop deposition, a high dose implant deposited with a photolitographic step, or a p-spray deposition, a low dose implant uniformly distributed on the all surface without the need of a mask.

For applications at High Luminosity LHC (HL-LHC), the LHC upgrade foreseen for 2024 that will increase the instantaneous luminosity up to 5×10^{34} cm^{-2}s^{-1}, mainly n−in−p sensors are considered. Thanks to the p-bulk they do not undergo type inversion and, by using the n^+ electrodes, the collected charge carriers are electrons, which are less subject to trapping after irradiation. Moreover, the process is single-sided and this is of interest for producing large area pixel tracker detectors. One of the problems of this technology is that the sensor edge is not at ground, as for the n−in−n, and a high electric field region is built between the readout chip and the sensor. This can potentially cause sparks that would destroy the chip if an appropriate dielectric layer is not added in the design.

Although a p−in−p sensor is a possible design, it is usually not considered since it combines the disadvantages of the n−in−n double-sided technology with the p−in−n one, which collects holes.

The thickness of the sensor determines the mean charge deposited by a crossing particle: the thicker the sensor the higher the signal amplitude, and at the same time more material provides more mechanical strength. However, in a thicker bulk the probability of charge trapping after irradiation increases. Moreover, the material budget increases with the sensor thickness, which could affect the detector performance. For experiments at HL-LHC, sensor thicknesses between 50 and 150 μm are considered.

The size of the electrodes collecting the signal determines the resolution of the device. However, a very small pixel size entails a sharing of the deposited charge between more pixels and hence a smaller signal amplitude. Also the limitation of the number of components of the readout chip contained in each pixel should be taken into account.

3.3.2 Readout electronics

One of the biggest challenges in producing a pixel detector is to design a readout chip suited for arranging thousands of channels. This ReadOut Chip (ROC) has to contain a regular pattern of pixel unit cells, each one serving one pixel on the sensor by means of a bump-bonding connection. The high density of channels can only be addressed with highly integrated custom-designed electronic circuits realized in CMOS technology. The transistor density that can be achieved depends on the technology used, which is defined by the minimum length of the MOSFET transistors. The actual pixel ROC of CMS [94] is realized in a CMOS 250nm technology as well as the ROC for the outer layers of the ATLAS pixel detector [95], while the innermost layer has ROCs produced in CMOS 130nm [96]. The pixel detectors for experiments at HL-LHC will be realized in CMOS 65nm [97] in order to have a smaller pixel size and higher radiation hardness.

A ROC is usually divided into an analog and a digital part. The analog part has to amplify the signal coming from the pixel sensor and discriminate it from noise. This part has to cope with an increasing leakage current and a smaller signal while the radiation damage increases.

The rising time of the amplified signal must be fast enough to associate the hit to the correct bunch crossing (in the LHC case the rising time must be faster than 25 ns). At the same time the power consumption per pixel must be kept low in order to implement a cooling system with low material budget. The digital part as to cope with the high data rate. Once the comparator registers an hit, this must be associated with a time stamp and stored in a buffer waiting for the trigger decision. During this time, called trigger latency, hits from subsequent events are also registered and therefore the buffer must be able to contain the information for all these bunch crossings (128 in the case of CMS) in order not to loose information.

Usually the chip architecture can be divided into three main areas: the pixel unit cell (PUC), the column periphery and the chip periphery. A sketch of this structure is shown in Fig. 3.15.

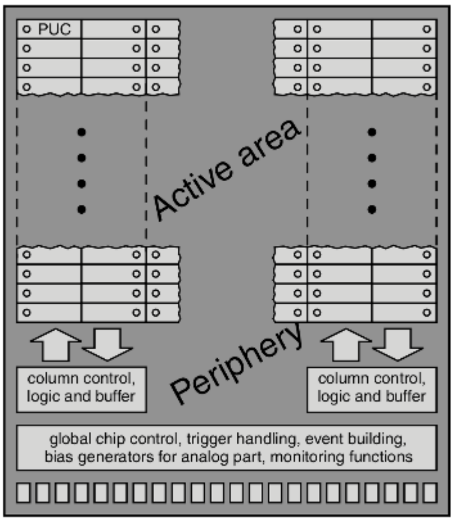

Figure 3.15: Sketch of a tipical readout chip structure [88].

The most important constrain for a readout chip is the density of transistors per unit area. This is fixed by the technology used, defined by the minimum gate-length achievable. As a consequence, the PUC dimensions are determined by the number of devices which need to be integrated.

In the PUC there are the amplification circuits, usually made of a one- or two-stage amplifier, a comparator for the threshold, and a storage where the data are saved waiting to be read out by the column periphery. For the calibration procedure, a circuit is usually present that allows to inject the charge directly into the amplifier chain instead of through the sensor.

A fundamental parameter of a silicon detector is the noise, which imposes the readout threshold and therefore the minimum recordable signal. Noise is usually expressed in terms of Equivalent Noise Charge (ENC), which allows its measurement in electrons providing an easier comparison with the expected signal.

The ENC depends on the sensor (plus parasitic) capacitance C_{DET}, on the sensor leakage current I_{DET}, on the input FET gate capacitance C_G and series noise (including both thermal and $1/f$), and on the preamplifier reset current I_{RST}. The ENC can be expressed as

$$ENC^2 = A_1 \frac{1}{\tau_P} \frac{4kT}{g_m} (C_G + C_{\mathrm{DET}})^2 + A_3 \frac{K_F}{C_G} \times (C_G + C_{\mathrm{DET}})^2 + A_2 \tau_P 2q(I_{\mathrm{DET}} + I_{\mathrm{RST}}) \quad (3.3.1)$$

where A_1, A_2 and A_3 are coefficients related to the filter, τ_P is the output pulse peaking time, g_m is the input FET transconductance, and K_F is the $1/f$ noise coefficient.

For applications in high energy physics experiments, the peaking time must be short ($<$ 100 ns) and so the main contribution to the noise comes from the sensor capacitance. The noise contribution given by the leakage current becomes important only after irradiation.

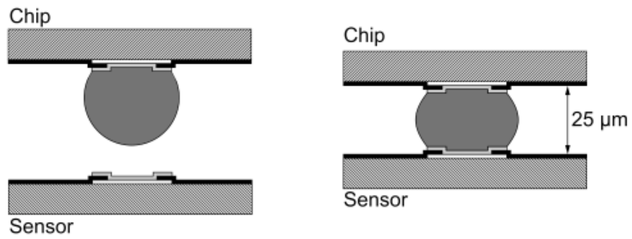

Figure 3.16: Flip-chip process for the solder bump-bonding [88].

The pixel array is normally arranged in columns or column pairs. In this way signals only pass through the column periphery at the bottom of the chip, and no electronics on the sides or above the chip is required. In the column periphery, signals wait for a valid trigger and then pass to the chip periphery, from which they are sent to the Data AcQuisition (DAQ) chain. For high rate conditions, new solutions have been studied to group pixels in regions and perform there the trigger decision [96]. This reduces the data transferred to the chip periphery, allowing to cope with a higher pixel occupancy.

The chip periphery contains the Digital to Analog Converters (DACs) used for setting the global parameters of the chip. This is the interface between the chip and the external readout chain to which the chip is connected via wire-bonding.

To reduce the insensitive area and the number of readout channels for the data acquisition, pixel detectors are often arranged in modules. In this way the information is first merged serially before being sent to the data acquisition for further processing and storage.

3.3.3 Bump-bonding

The bump-bonding process is a technique extensively used in the electronics industry for the connection of integrated circuit dies to printed circuit boards or other substrates. The bump-bonding techniques, which have been proven to work at the contact density required for particle physics, use either electroplated solder bumps or indium bumps deposited by evaporation.

The bump deposit is usually made on the wafer before cutting the single dies, except for the gold-stud bumps, for which the process can be made on single chip.

Solder bump-bonding

On the metal contacts of the chip the under-bump-metallization (UBM), made of layers of different metals, is deposited to favour the adherence with the bumps. Then a photolitographic step allows to selectively deposit the metal of the bumps. The metal used in this case is a eutectic solder[5], usually SnPb or SnAg.

Because of the low Sn vapour pressure, the eutectic solder can be hardly evaporated and the deposit is made through electroplating. This type of process produces cylinders that are turned in spheres of $\sim 20\ \mu$m diameter by the reflow process. During this process, made approximately at the temperature of 350 ℃, the bump undergoes a collapse into a truncated-sphere shape.

After applying the bumps on the chip, the UBM is also deposited on the sensor pads, and then the flip-chip is made. The chip bumps are tacked on the UBMs of the sensor by a solder flux, as shown in Fig. 3.16. After the reflow process chip and sensor self-align thanks to the superficial tension of the bumps. This type of process produces a connection between chip and sensor with $\sim 1\,\Omega$ impedance.

[5] An eutectic material is a mixture of two chemical elements, which solidifies at a lower temperature than any other composition made up of the same elements.

Indium bump-bonding

The indium bump-bonding process has been developed for applications which require good mechanical and electrical properties also at low temperature, approximately the one of liquid nitrogen. Typically the indium deposit is grown with the evaporation technique. The result is a bump with a maximum height of 10 μm [88].

The same process must be applied on both the chip and the sensor, as shown in Fig. 3.17. In this case the flip-chip can be performed at room temperature, but the best result is obtained at a temperature of approximately 100 °C. This process produces a connection with $\sim 10\,\Omega$ impedance and a distance between chip and sensor of approximately 10 μm. Actually, due to its properties, indium easily oxidises and this effect must be taken into account during the production.

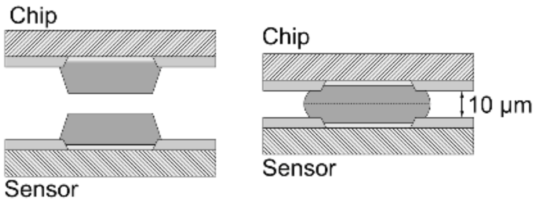

Figure 3.17: Flip-chip of an indium deposited sensor [88].

To produce an indium deposit there is also a technique similar to the solder bump-bonding described previously. This technique requires a two-masks process, one for the sputtering of the base and the other one for the indium deposit. The reflow process arranges the indium in a sphere. In this case it is also required a thin deposit of indium on the sensor contacts.

Gold-stud bump-bonding

Among the materials that can be used for bump-bonding, gold offers two important characteristics: it does not oxidise and it deforms easily, allowing a good electrical contact. Gold can be applied by electroplating or placed through stud bonding, which is more interesting for pixel application. This technique is a variation of the traditional ultrasonic wire-bonding.

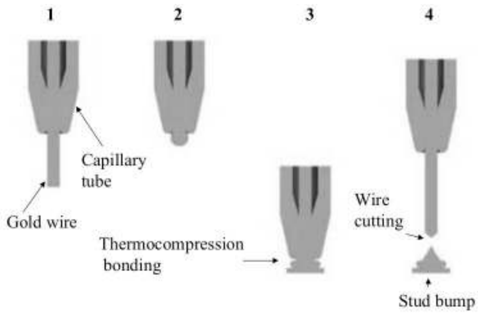

Figure 3.18: Au-stud bump formation process: a gold wire passes through a capillary tube (1), is heated (2), and pressed against the bonding pad (3). The wire is then pulled away and cut close to the stud bump (4) [88].

The wire is intentionally broken after the thermocompression bonding to the die pad and a coining process is used to make the bump more planar, as shown in Fig. 3.18. The bumps are applied one after the other. This type of process is used when the devices are already available in single pieces and not on wafer.

Chapter 4

Pixel detector studies for CT-PPS

To face the expected high radiation fluence, it was decided to build the tracking system of CT-PPS with 3D pixel sensors. In this chapter, the preparatory studies of 3D sensors produced by different vendors are presented. Initial sections are dedicated to the description of the 3D sensors and associated front-end electronics. The results of the measurements of various devices, done in laboratory and at test beams before and after irradiation, are then presented, together with the description of the used setups.

4.1 3D pixel sensors

The structure of 3D pixel sensors was proposed in 1997 [98]. The main feature of 3D sensors is that, instead of implementing the electrodes on the surfaces, as in the planar technology, they are etched in a column shape perpendicular to the surface, decoupling the sensor thickness from the distance between electrodes. 3D sensors can thus be depleted with a bias of few volts, depending on the electrode structure. Moreover, the produced charges travel for a shorter drift distance, providing a faster response with respect to planar sensors but keeping at the same time a comparable signal since the amount of generated charge only depends on the substrate thickness, which is normally the same for planar and 3D sensors. For the same reason, the radiation hardness is improved since the trapping probability is reduced. On the other hand, the reduction of the inter-electrode distance increases the pixel capacitance, which translates into a higher noise as explained in Sec. 3.3.2.

Different 3D structures have been proposed, which can be classified based on the following features:

- type of electrode: it can be a junction (p-n) or an ohmic contact (n^+-n or p^+-p);
- side of the silicon bulk from where the columns are etched;
- structure implemented on the backside in case columns do not pass completely through the substrate;
- depth of columns.
- number of readout columns per pixel (1E, 2E, ...), which determines the distance between electrodes.

The cross sections of different 3D sensors are presented in Fig. 4.1.

The fabrication processes of 3D sensors vary depending on the different structures. Generally speaking, the fabrication of 3D sensors requires a much more complex procedure with respect to that for planar sensors, increasing the production costs and lowering the yield. This is the major limitation to the use of 3D sensors for large area pixel detectors. However, their intrinsic

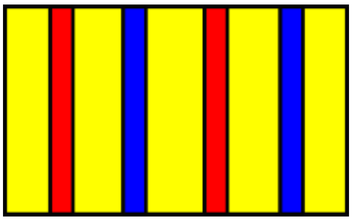

(a) junction & ohmic / junction & ohmic

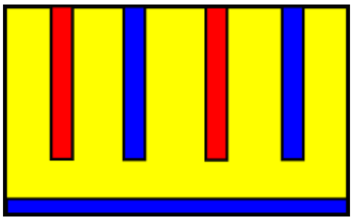

(b) junction & ohmic / ohmic surface

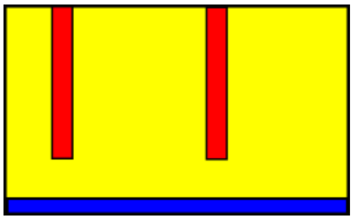

(c) junction / ohmic surface

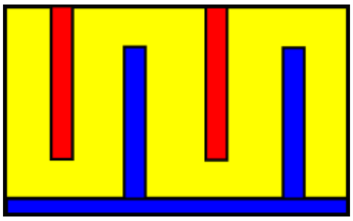

(d) junction / ohmic column and surface

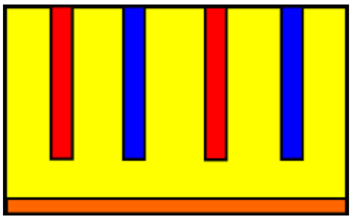

(e) junction & ohmic / SiO_2 surface

Figure 4.1: Possible layouts of 3D pixel sensors. They can be classified according to the two surface structures. Colours indicate the type of doping: yellow p^{--}, blue p^+, red n^+, orange SiO_2.

radiation hardness suggests their application in those areas where the expected radiation damage is high.

As an example, the fabrication process of the first 3Ds, produced in 1999 [99] at the Stanford Nanofabrication Facility, consisted of 25 steps, of which the principal ones are shown in Fig. 4.2:

(a) A support wafer is used to prevent possible breaking of the device during the next steps, where the temperature can reach 1250 °C [99]. Moreover, the support wafer is required to implement active edges (see in the following). After all fabrication steps are finished, the support wafer can be removed[1].

(b) Windows for subsequent steps are etched in the silicon dioxide (SiO_2). The etching of silicon dioxide uses a photoresist film deposited on the surface, which is selectively illuminated making use of a mask. The part of the resist hit by light is removed, while the remaining part protects the SiO_2 from the etching agent.

(c) 3D sensors need deep holes with small diameter. To obtain this, an anisotropic etching is necessary, which is typically the Deep Reactive Ion Etching (DRIE). The anisotropy (A) is defined in terms of speed of vertical (V_r) and lateral (V_l) etching (eq. 4.1.1):

$$A = 1 - \frac{V_l}{V_r} \tag{4.1.1}$$

This value is an essential parameter and to produce 3Ds it must be close to one. The technique, the so-called Bosch process, consists of two alternating steps [100]: reduce the spontaneous etching on the sidewalls and passivate them for controlling the etching direction. By repeating cycles of etching and passivation, deep holes can be produced.

(d) After etching, columns are empty and hence no charge can be deposited by a crossing particle. For reducing this drawback, columns can be filled with polysilicon. This process can

[1]This can seriously damage the sensor wafer and for the first fabricated sensors, treated in this section, was not applied.

be realised either after doping the electrodes or in two steps: partially before and partially after the doping. The polysilicon filling is not applied in all types of production. Another technique to increase the column efficiency is to stop the etching of the electrodes few tens on μm before reaching the opposite surface. The subsequent step is the passivation of the columns.

(e) and (f) The procedure of etching, filling and doping is repeated for the other type of electrode. In the double-sided technology, this step is performed on the opposite surface of the wafer.

(g) At the end of the fabrication procedure, a metal deposition is applied for creating pads for bump-bonding and the bias grid.

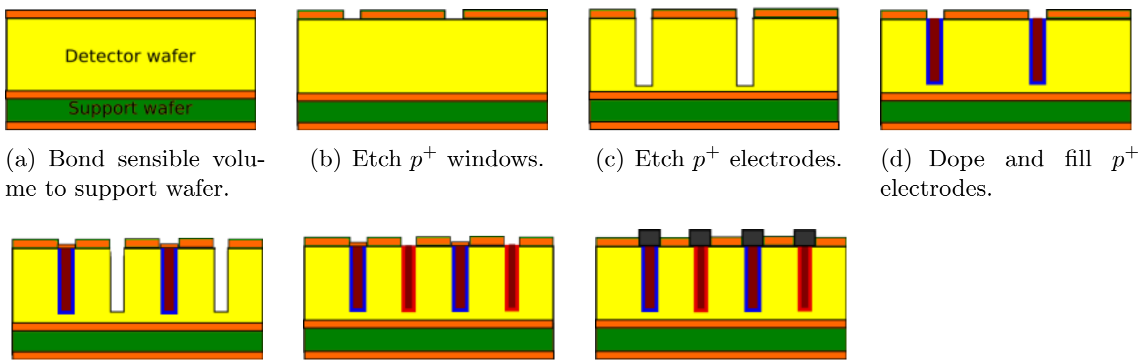

(a) Bond sensible volume to support wafer. (b) Etch p^+ windows. (c) Etch p^+ electrodes. (d) Dope and fill p^+ electrodes.

(e) Etch n^+ windows and electrodes. (f) Dope and fill n^+ electrodes. (g) Deposit aluminum contacts.

Figure 4.2: Main production steps of the first 3D pixel sensor. Colors represent: yellow p^{--}, orange SiO_2, red n^+, blue p^+, green support wafer, grey aluminum, brown polysilicon.

Another advantage of 3D sensors with respect to planar ones is that the electric filed is perpendicular to the sensor lateral edge. This feature allows to effectively implement active edges [101], which extend the sensitive area up to the sensor edge. In high energy physics experiments, active edges allow reducing the overlapping between sensors, otherwise needed because of the insensitive area under the guard rings, and thus the material budget.

The implementation of active edges is obtained by etching trenches around the margins of the device and then by doping them. In this way, the edge is itself the very last electrode and contains the electric field. In order to keep the sensor in position after the trench etching, the sensor wafer must be attached to a support wafer, as shown in Fig. 4.3. It follows that a double-sided production does not allow the implementation of active edges on all the four sides of the sensor.

An alternative solution is the implementation of the so-called slim edges [102]. In this case, a smooth reduction of the electric field is provided by a multiple fence of ohmic columns extending from the active area towards the scribe line. The result is an inactive region which can be reduced to ~ 50 μm by increasing the bias voltage.

The electrode configuration inside the pixel cell must be optimized in order to provide the required radiation hardness, which improves with shorter inter-electrode distances, i.e. a higher number of electrodes. At the same time the pixel capacitance must be kept below the front-end electronics requirements, limiting the number of electrodes. Moreover, the higher is the number of electrodes the more fragile are the devices, with the consequence of a lower production yield. Another aspect to be considered is the bump-bonding pad, which needs to be well separated from the electrodes for provide a good planarity for the bump deposition.

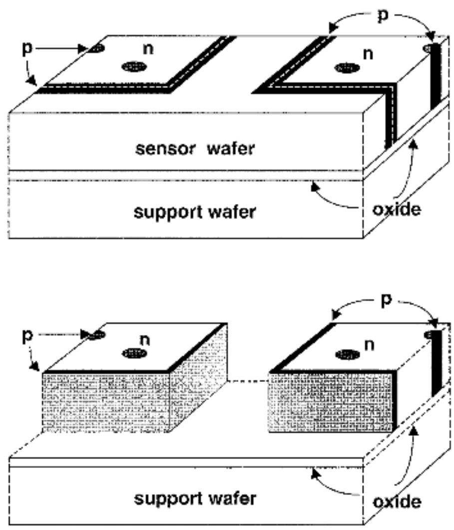

Figure 4.3: Schematic view of two adjacent active edge 3D sensors bounded to their support wafer [101]. Top sketch: after holes and trenches are etched, doped and filled. Bottom sketch: after the larger dicing trench has been etched to separate the devices.

4.1.1 3D detectors for the ATLAS IBL

The ATLAS vertex detector was upgraded in the 2014 Spring with a fourth layer of pixel detectors, the Insertable B-Layer (IBL)[103], to improve primary and secondary vertex reconstruction. Thanks to the reduction of the beam pipe diameter, the IBL detector is installed at a radius of 3.3 cm.

After several years of R&D studies, the ATLAS 3D Collaboration was able to qualify 3D silicon pixel detectors for being installed in the forward part of the IBL. This has been the first time that 3D detectors have been used in a high energy experiment.

The IBL consists of 75% of planar detectors and 25% of 3D detectors, of which half fabricated at CNM (Centro Nacional de Microelectrónica, Barcelona, Spain) and half at FBK (Fondazione Bruno Kessler, Trento, Italy). Both technologies fulfill the IBL requirement of a hit efficiency in the active area greater then 97% after irradiation to fluences of $5 \cdot 10^{15}$ n_{eq}/cm^2.

A section of the IBL is partially shown in Fig. 4.4. The layer is formed by 14 tilted and overlapped staves to guarantee the complete solid angle coverage, since sensors have slim edges.

Sensors for IBL are bump-bonded to the front-end readout chip FE-I4 [96]. This ROC, realized with the 130 nm technology, is made of 50×250 μm^2 pixel cells arranged in a 80×336 matrix. To choose the proper electrode configuration, several studies [104, 105, 106] have been done on sensors realized for the FE-I3 [95], the previous version of the ALTAS pixel ROC, with different number of readout electrodes, as shown in Fig. 4.5.

For the IBL project it was finally chosen the so-called "2E$-$250" configuration, adapted for the FE-I4 chip [103]. This configuration corresponds to the 3E one for the FE-I3 readout chip. It has an inter-electrode distance of ~ 70 μm and, considering the IBL radiation dose level, it is a good compromise between signal efficiency (charge collection) and noise.

The depletion voltage of the IBL 3D sensors is $\sim 5 - 10$ V and the breakdown voltage is required to be greater than 25 V. Measurements on sensors produced by FBK show a breakdown above 50 V while the CNM ones are above 100 V. The noise level is ~ 150 e^-. 3Ds from FBK and CNM have been irradiated to fluences close to the IBL target of $5 \cdot 10^{15}$ n_{eq}/cm^2. For these devices, the optimal voltage setting of 160 V ensures high charge collection efficiency while maintaining the noise low.

For studying hit efficiency and spatial resolution, beam tests have been performed on unir-

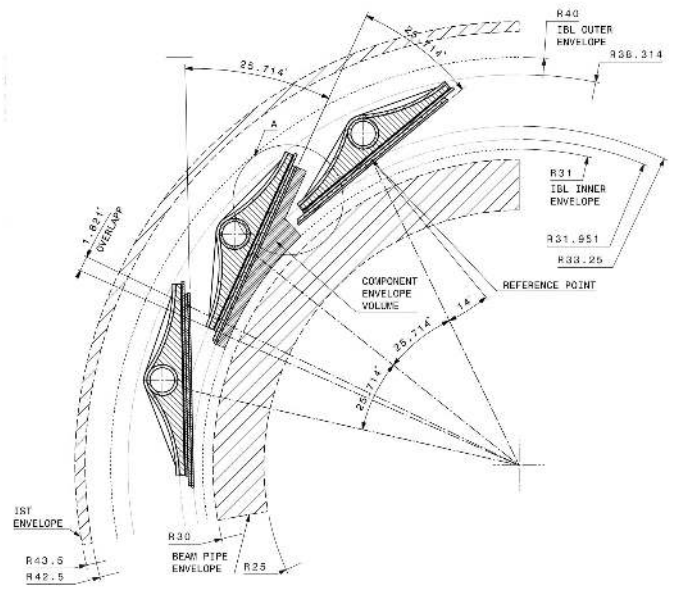

Figure 4.4: Section for the IBL layout [103].

radiated and irradiated 3D sensors, obtaining maps of the efficiency as those in Fig. 4.6. The plot at the top shows an irradiated CNM sensor placed perpendicularly to the beam, the plot in the middle an irradiated CNM sensor tilted by 15° with respect to the beam, and the one at the bottom an unirradiated FBK sensor perpendicular to the beam. In the first one the readout electrodes are not visible because the not-passing through electrodes and the high bias voltage applied allow to efficiently collect the charge even in the electrode region. When tilting the sensor by 15° with respect to the beam, the column inefficiency vanishes. For the FBK at the bottom, both readout and ohmic columns are visible, since they are fully passing through. Irradiated 3D sensors, tilted by 15°, have a total efficiency higher than 97%, which is the requirement for IBL.

4.1.2 3D detectors for HL-LHC experiments

The upgrades of the CMS and ATLAS experiments for HL-LHC aim at the complete replacement of their tracking detectors to cope with the predicted higher event pile-up (140 events/BX) and integrated luminosity of 3000 fb^{-1}. The innermost tracking layers will have to withstand very large radiation fluences up to 2×10^{16} $n_{eq}cm^{-2}$. Thanks to their intrinsic radiation tolerance, 3D sensors are very promising candidates for this application.

Due to the demanding requirements for the readout chip, a joint effort is ongoing on for designing a hybrid pixel ROC adeguate for the rate and radiation expected [108]. The new front-end chip, that will be realized in the more radiation hard 65 nm CMOS technology, will have a pixel size of 2500 μm^2 to maintain a reasonable hit occupancy in the high track density environment of the inner layers, and sufficiently fast data transmission and low power consumption. Both CMS and ATLAS are considering, at least for the innermost layers, pixel sizes of 50×50 μm^2 or 25×100 μm^2 [109, 110]. The major producers of 3D sensors started the development of devices compatible with these pixel sizes.

CNM fabricated a first R&D production with small pixels [111] but other characteristics similar to the IBL batches (for detail see Sec. 4.6.1). The silicon substrate is *p*-type with a thickness of 230 μm and a double-sided process has used to obtain 200 μm deep columns with a diameter of 8 μm. Sensors have the new pixel dimensions but are designed to be tested with

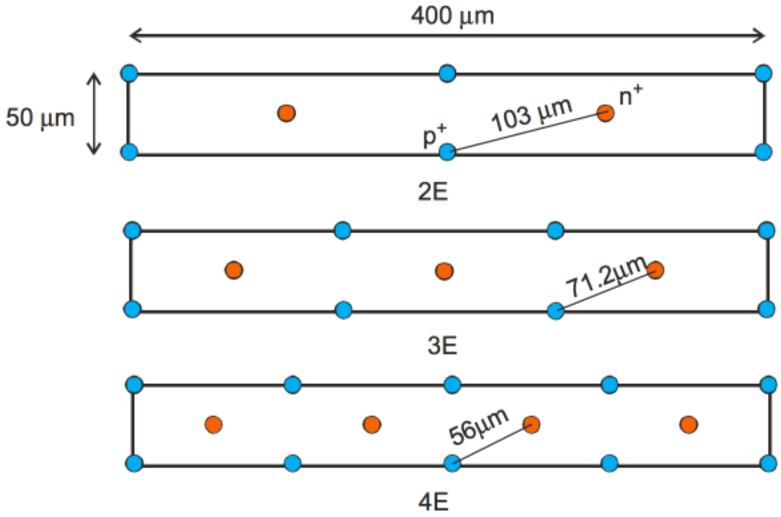

Figure 4.5: Layout of ATLAS 3D sensors with different column configurations designed for the front-end chip FE-I3. [107].

the FE-I4 chip. Due to the different pixel size between ROC and sensor, only $\sim 20\%$ of the pixels can be connected, while the other ones are grounded. Figure. 4.7 shows the layout of the CNM 50×50 μm^2 and 25×100 μm^2 pixels. Square pixels have one readout column in the center of the cell, while the rectangular ones have two readout electrodes for improving the radiation hardness and more easily depleting the pixel area near the short pitch side.

From this production, sensors bump-bonded to the FE-I4 ROC were tested on beam before and after irradiation [112]. Before irradiation, removing from the analysis the region of charge sharing with the unconnected cells, $\sim 96-97\%$ efficiency is reached already at $1-2$ V with 1.5 ke threshold. Sensors were then irradiated uniformly to 5×10^{15} n_{eq}/cm^2 at the Karlsruher Institut für Technologie and non-uniformly to a maximum fluence of 1.4×10^{16} n_{eq}/cm^2 at the CERN IRRAD Proton Facility. The results obtained after irradiation are very promising in terms of efficiency as a function of the bias voltage (Fig. 4.8). In particular, an efficiency higher than 97% is reached with 40 V and 120 V after a fluence of 5×10^{15} n_{eq}/cm^2 and 9×10^{15} n_{eq}/cm^2, respectively. The big improvement in efficiency thanks to the new pixel size can be appreciated if comparing the 50×50 1E layout to the 50×250 2E cell of the ATLAS IBL.

In the case of SINTEF (Trondheim, Norway) [113], the baseline concept is to produce 3D sensors for the HL-LHC experiments with a single-sided process [114], with a technology acquired from Stanford. Layouts with one (1E) and two (2E) readout columns have been proposed for both the two pixel sizes, as shown in Fig. 4.9.

For both types of pixels, the 1E configuration is safer to be implemented. In the 2E layouts, which will probably be required in the case of rectangular cells in order to achieve higher radiation hardness, the bump-bonding pad is indeed extremely close either to the n-electrode or to the metal bias grid, making the production very critical.

Also FBK is following the single-sided approach for the HL-LHC sensors [115]. The process starts with a substrate consisting of a Float Zone high-resistivity layer of the desired thickness ($\sim 100-150$ μm depending on the experiment specifications), directly bonded (i.e., without an oxide layer in between) to a 400μm-thick low-resistivity handle wafer, which ensures sufficient mechanical robustness.

The schematic cross-section of the proposed sensors is shown in Fig. 4.10. The direct bonding of the high-resistivity wafer to the low-resistivity handle wafer dictates the choice of different

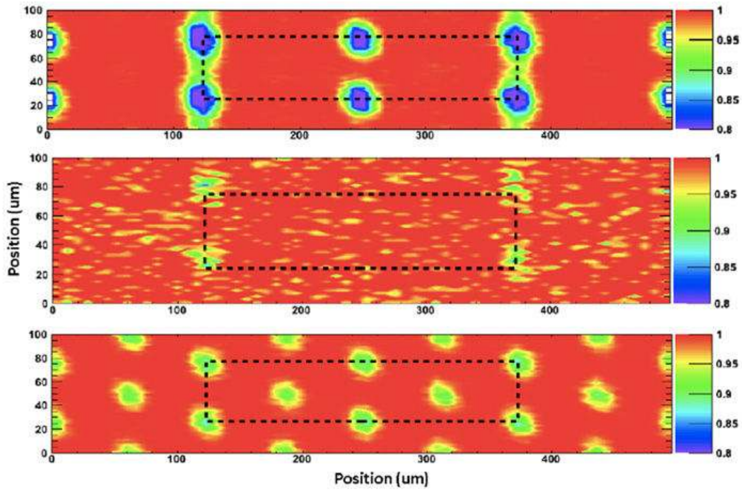

Figure 4.6: Pixel efficiency map for three 3D devices. The plot at the top shows the hit efficiency for perpendicular tracks for an irradiated CNM device operated at 160 V. The overall CNM efficiency is 96.5%. The middle plot shows the efficiency for an irradiated CNM device operated at 160 V. The track incidence is at 15° and the overall efficiency is 98.7%. The bottom plot shows the efficiency for an unirradiated FBK device operated at 20 V. For normal incidence tracks the efficiency is 98.8%. The passing through electrodes are clearly visible.

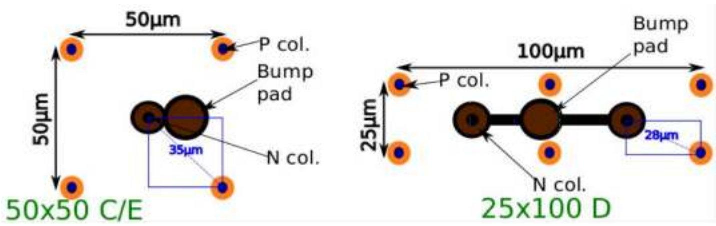

Figure 4.7: 3D cell layout for square and rectangular pixels produced by CNM for the HL-LHC pixel detectors [111].

column depths for the junction and the ohmic electrodes. The p-columns are etched first by DRIE through the whole high-resistivity silicon layer thickness and penetrate by a few μm into the low-resistivity wafer. By doing so, a good ohmic contact is made on the handle wafer, that can eventually be thinned down in the post-processing and coated with a metal layer to allow biasing the sensor from the backside. On the contrary, the n-columns do not penetrate through the entire active layer, but rather stop at a short distance (~ 25 μm) away from the low-resistivity silicon layer, in order to avoid early breakdown.

FBK sensors have a 1E layout for square pixels, as CNM, while rectangular ones can be either 1E or 2E. While the 50×50 μm^2 or the 25×100 μm^2 1E pixel cells have quite a large area to host the bumb-bonding pad, in the 25×100 μm^2 2E cell, showed in Fig. 4.11, the bump-bonding pad is very close to both the n- and the p-columns, so that misalignment problems could cause the pad to overlap the columns, thus leading to high electric fields with the risk of microdischarges.

As in the CNM production, pixel cells have been rearranged in order to be bump-bonded with the presently available FE-I4 and PSI46dig ROCs, while waiting for the new ROCs under development for HL-LHC. Recently, beam tests have been done on these devices by ATLAS [116] and CMS [117]. Due to the different sizes of ROC and sensor pixel cells, only a small portion of the sensor (1/6 for CMS and 1/5 for ATLAS layout) has been connected to the ROC and a cut on the pixel fiducial window has been applied for taking into account the charge lost

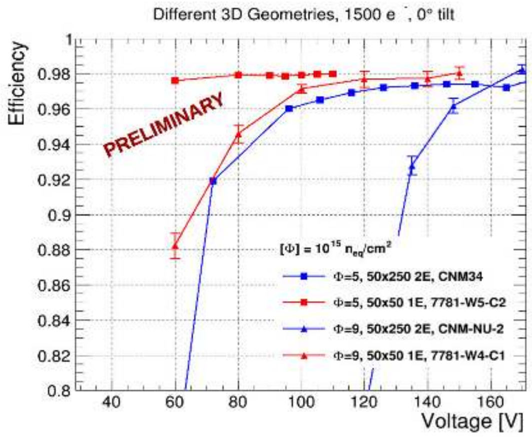

Figure 4.8: Efficiency after different fluences for CNM 3D sensors designed for the HL-LHC upgrade [112].

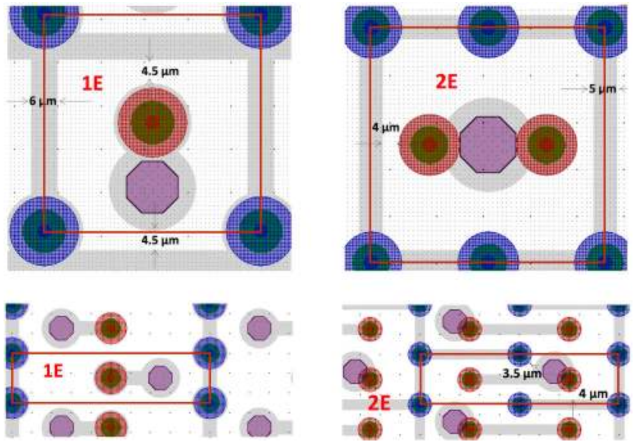

Figure 4.9: 3D cell layouts proposed by SINTEF for the HL-LHC pixel detectors [114]. Top: layouts of the square pixel with one (left) and two (right) readout columns. Bottom: layouts of the rectangular pixel with one (left) and two (right) readout columns. Layouts are not in scale.

due to sharing with the unconnected cells. The efficiency reaches the plateau at voltages lower that 2 V with a threshold of 1500 e^- (see Fig. 4.12), thanks to the very small inter-electrode distance.

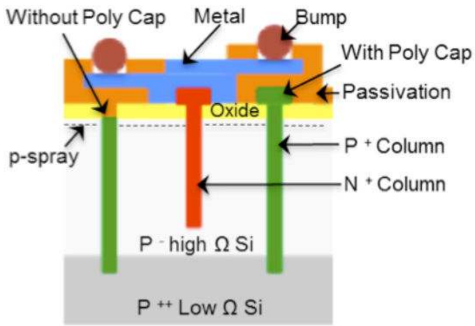

Figure 4.10: Schematic cross-section of the FBK single-sided 3D sensors [115].

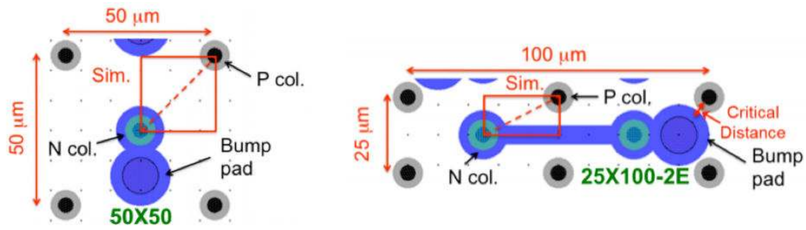

Figure 4.11: 3D cell layout for square and rectangular pixels produced by FBK for the HL-LHC pixel detectors [115].

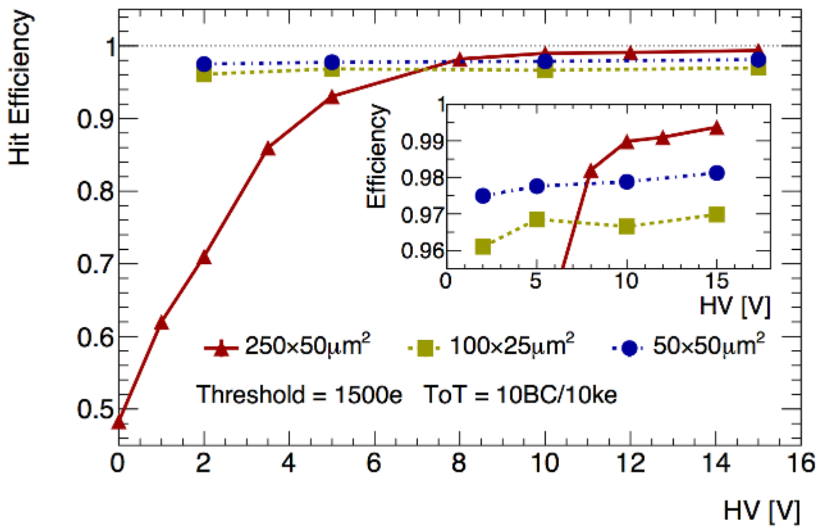

Figure 4.12: Efficiency for FBK 3D sensors with 1E layout and different pixel sizes, designed for the HL-LHC tracker upgrade [116].

4.2 PSI46dig readout chip

The 3D sensors studied in this work have been bump-bonded to the PSI46dig readout chip of CMS [118]. This chip is an evolution of the analog PSI46v2 ROC [37] and has been designed at the Paul Scherrer Institute (PSI) for the Phase I pixel detector upgrade of CMS [119]. It uses the same 250 nm CMOS technology of the PSI46v2 and the well understood core of its architecture. The layout of the full ROC is shown in Fig. 4.13.

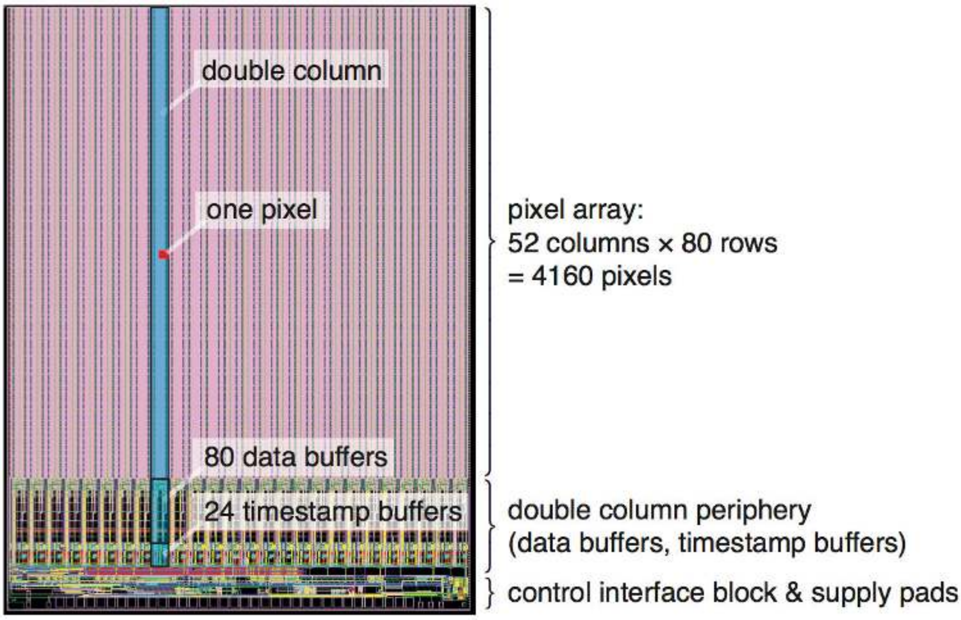

Figure 4.13: Full layout of the PSI46dig pixel chip [120]. Highlighted are the areas of a single pixel, a double column, the data buffers and the time-stamp buffers. The periphery and the supply pads handle trigger information, buffer data and the communication with the outside world.

The PSI46dig ROC consists of 52 × 80 Pixel Unit Cells (PUCs), each with a dimension of 150 μm^2, which amplify and discriminate the sensor signal. They are organized in 26 Double Columns (DCs) of 2 × 80 pixels. Each double column is controlled by a periphery that has buffers for time stamps and data. A chip periphery, common for all DCs, digitizes the signal and handles the communication with the outer electronics. An outline of these three blocks is shown in Fig. 4.14.

In the PUC, the signal from the sensor is passed through the bump-bond as input of a two-stage charge sensitive system made of preamplifier and shaper. The shaper output is sent to the comparator and, if it is above a preset threshold, is stored in a sample-and-hold circuit after a settable delay that allows to select the peak of the signal. At the same time, a fast signal is sent to the column periphery via the column OR bus to warn of the presence of hit information. The pixel becomes insensitive and waits to be read out.

The comparator threshold can be set by means of a global DAC (VthrComp), which then can be trimmed by a local DAC (TrimBit), whose full scale is set by another global DAC (Vtrim). This allows to reduce the threshold spread pixel by pixel due to offset variation in the comparator.

In the PUC a calibration circuit is also present. It is used for the laboratory tests and for the calibration in the experiment. The signal amplitude is set by the Vcal 8-bit DAC register and it works in two ranges set by the CtrlReg: in the low range, which is used for fine measurement at low signal (noise and threshold measurements), 1 Vcal corresponds to $\sim 50\ e^-$, while in the

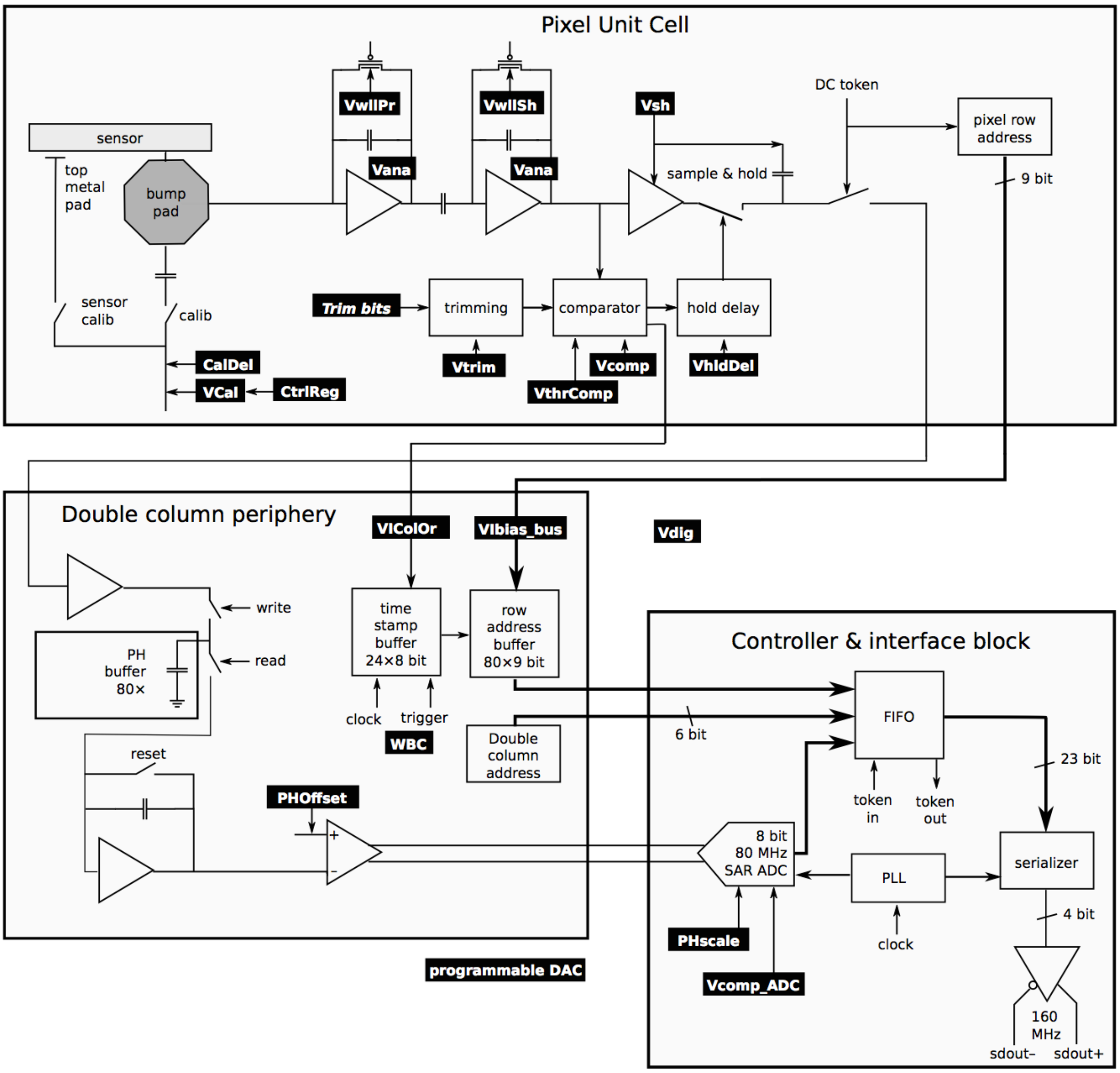

Figure 4.14: PSI46dig schematic with DACs.

high range, which is used to span all the signal range (gain calibration), 1 Vcal is $\sim 350\ e^-$. The injection can be delayed with respect to clock by using the CadDel 8-bit register, with a minimum step of $\sim$ 0.45 ns. The calibration pulse can be injected directly into the amplifier or in the sensor, thanks to the air capacitance that induces a charge which will pass though the bump-bond.

The current flowing in the comparator and in the amplifier is controlled by the Vana DAC. Its nominal value is 24 mA, which corresponds to $\sim$ 6 μA per pixel. In case it is needed, especially after irradiation, it is possible to increase this current in order to have a faster signal rising and also a lower noise, but with the drawback of increasing the power consumption.

When the asynchronous column OR signal arrives to the DC periphery, the corresponding value of the 8-bit bunch crossing counter (BC) is saved, within one clock cycle (25 ns), in the 24 time-stamp buffers. This allows to match the hit to a certain LHC bunch crossing, which runs at the same 40 MHz clock as the ROC. At the same time, the analog pulse height signal and the address of the hit pixel are sent to the periphery, where they are associated to the bunch crossing and stored in one of the 80 data buffers. This procedure is commonly called column drain. Hits in subsequent clock cycles can be correctly assigned to a certain time stamp as long as not more than two column drain operations are pending. The data stored in the buffers now wait for the trigger signal. If no trigger signal reaches the chip, old data get overwritten in the periphery.

If a trigger is received, a second 8-bit counter in the periphery that runs with a programmable offset (WBC) with respect to the primary one is saved. This value is compared with the time stamp saved in the DC peripheries and those with matching hits are put in halt in order to avoid overwriting. The WBC must be set properly in order to correctly reproduce the delay between the hit time stamp and the instant of the trigger reception. The triggered data get transferred to the central readout buffer. The charge is transferred to the 8-bit ADC (one per ROC) for being digitized. In order to match the full range of signals, the PHOffset and PHScale DACs are used to set the offset and the gain of the calibration curve, respectively.

For every hit transferred to the central readout buffer, the column number (6 bits), the row number (9 bits), and the pulse-height (8 bits) are stored, for a total of 23 bits. The readout buffer is designed as a FIFO with simultaneous read and write capability, and has a storage capacity of 64 such 23 bit-words. Every DC gets re-enabled for normal operation as soon as the data are transferred.

A pixel module usually consists of several ROCs, which send their data to a chip called Token Bit Manager (TBM) [121]. It is therefore necessary to synchronize the ROCs in order to avoid the stream lost. This is done by a token signal sent to the first ROC in the chain. Once received, the ROC sends its data to the output line and once done sends the token to the next ROC, which will immediately start its data transfer. The last ROC in the chain sends the token to the TBM and the readout ends.

All this digital part of the ROC is fed with a current controlled by the Vdig DAC. Since this current also provides the power to the ADC, a change of its value involves a recalibration of the ADC.

The ROC receives as input four Low Voltage Differential Signals (LVDSs): a 40 MHz clock, a combined calibration, trigger and reset signal, a I^2C line to program the chip registers and the token input. The ROC has two differential outputs: the token out is an LVDS signal, while the data output is a 160 MHz Low Current Differential Signal (LCDS).

Fig. 4.15 shows the output data format. Every time the ROC receives the token signal, it sends a header with a 8-bit fixed pattern followed by a 3-bit "id field". The first bit of the id field distinguishes between ROC (0) or TBM (1) header. The other two bits are used for the readback utility, which allows to measure some parameters internal to the ROC. This is done by means of the second bit of the id field that is set when the readback transmission starts, and then for the following 16 data streams the third bit of the id filed will be used to compose a 16-bit word containing the chip address and the desired DAC value.

Several versions of the PSI46dig ROC have been produced. In this work the following ROCs have been used: PSI46dig v2.0, PSI46dig v2.0b, PSI46dig v2.1 and PSI46dig v2.1respin. The v2.0 and v2.0b versions have similar characteristics and both are affected by the problem of the double column freezing, a mechanism in which, due to the architecture of the column OR, the double column goes out-of-sync when many pixels are hit in the same DC. This problem was solved in version v2.1, which however presents an unexpected influence of Vdig on the pulse height, even if this does not compromise the usage for testing purpose. The final version, used for both the Phase I pixel tracker upgrade and CT-PPS, is the so-called v2.1respin, in which the Vdig issue is solved.

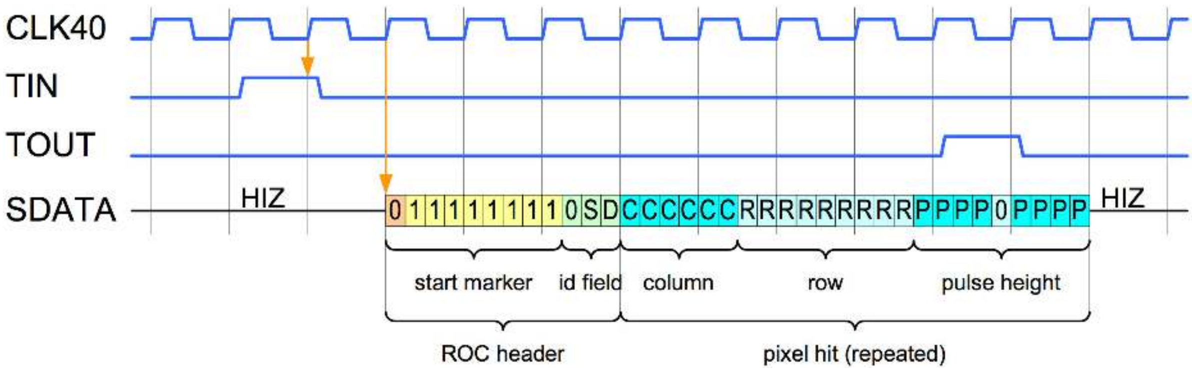

Figure 4.15: PSI46dig output data format [122].

4.3 Laboratory tests

All sensors studied in this work have been tested in the Torino laboratories before being measured on beam. This section describes the standard testing procedure.

4.3.1 ROC test

The test of the ROC is a fundamental step of the detector qualification. It allows to verify the correct functionality of the chip and to optimize its parameters in order to obtain the best performance on beam.

The ROC test is done using the so-called Digital TestBoard (DTB), developed for the CMS Phase I ROC at the PSI (Fig. 4.16). The testboard is equipped with an Altera Cyclone III FPGA to control the board and the communications with the module ROC(s). A custom digital level translator chip (LCDS–LVDS) handles all the needed levels for a proper communication with ROC and TBM. Data from the detector are stored in a 128 MB RAM. The testboard is connected to a computer via USB and is controlled by custom programs: psi46expert (a code adapted from the PSI46v2 testing program) and pXar (the code developed for this ROC).

Figure 4.16: Picture of the DTB.

A 68-pin SCSI ribbon cable (Fig. 4.17(a)), with impedance 115 Ω, connects the DTB to the ROC adapter (Fig. 4.17(b)). A single-chip detector is glued and wire-bonded to a board (Fig. 4.18(a)) that fits in the ROC adapter connector and allows the communication between the testboard and the ROC. The same board distributes the bias voltage, which is provided by an external device, a Keithley 2400 or 2410 for the sensors presented here, plugged via a lemo directly on the DTB. To protect the detector and the wire-bonds, a plastic box is screwed on the ROC board (Fig. 4.18(b)). These boxes were initially bought and modified to fit the required dimensions and later on were directly produced in Torino with a 3D printer.

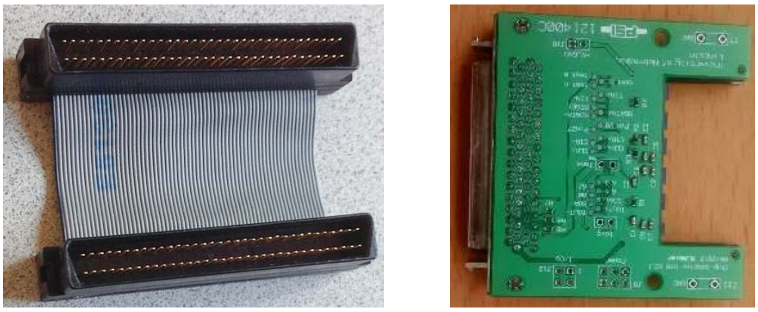

(a) SCSI cable. (b) ROC adapter.

Figure 4.17: SCSi cable (a) used to connect the DTB to the ROC adapter (b).

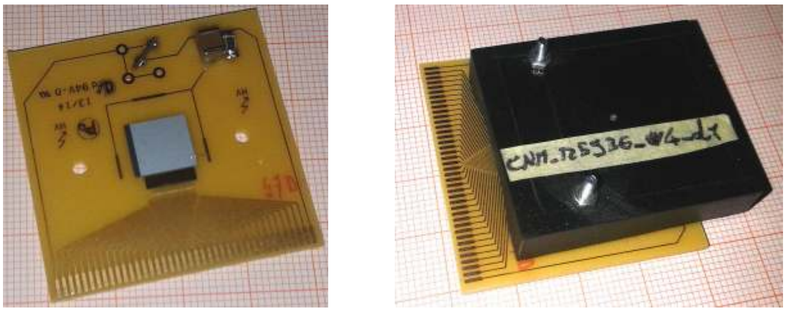

(a) ROC board. (b) Box to protect detector and wire-bonds.

Figure 4.18: ROC boards without (a) and with protection box (b).

The detectors studied in this work have passed the standard testing procedure used for the qualification of the Phase I pixel detectors. In these preparatory studies, only single-chip detectors have been tested, but in case of modules the tests are simply iterated on all ROCs of the module. In the following the tests are described. Plots shown are examples from one of the 3D detectors tested.

The first step of a ROC test is trying to see if it is possible to set the ROC registers. This is done by setting different values of the analog current and checking that it changes consistently. The analog current is then set to the nominal value of 24 mA.

The calibration circuit must then be optimized for further tests. A double efficiency scan is performed on the CadDel and VthrComp registers, obtaining the so-called "tornado plot" (Fig. 4.19). It is important to know that the input signal to the comparator is negative with respect to the baseline, while the threshold is set by a DAC whose voltage output if directly proportional to the register value. It follows that a higher VthrComp value corresponds to a lower comparator threshold. The top limit of the tornado shape corresponds to the minimum threshold before the noise starts being dominant, filling the buffer and therefore inducing an inefficiency. The horizontal width of the shape corresponds to the time window (25 ns in this case) in which the signal crosses the threshold in the triggered bunch crossing. Finally, the slope of the shape is due to the time walk for which a higher threshold is crossed by the signal after a lower one and therefore less calibration delay is necessary for being read in the correct bunch crossing window. The tornado plot is measured for one pixel and the working point is set in the center of the shape for VthrComp corresponding to 50 DAC.

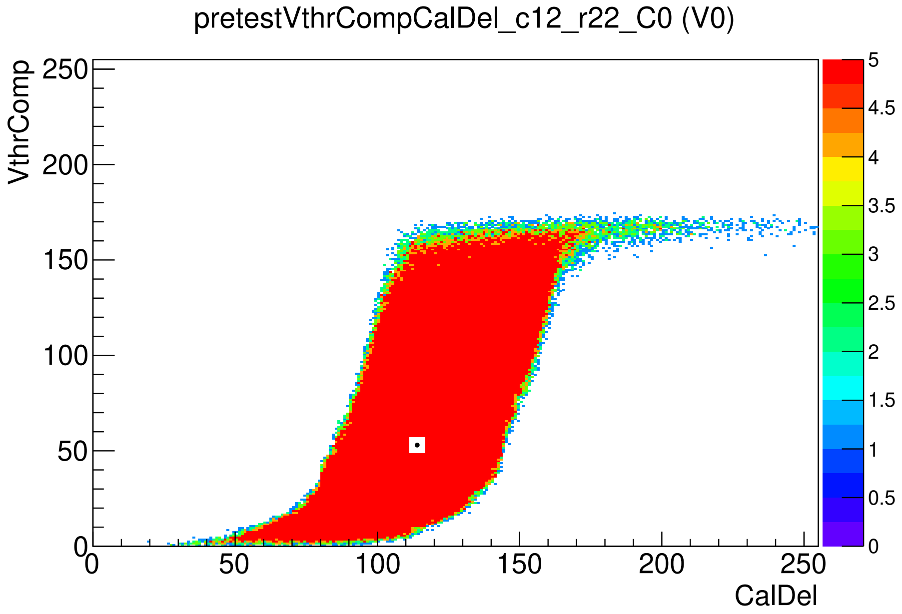

Figure 4.19: Tornado plot (efficiency in the VthrComp vs. CalDel plane).

It follows the pixel basic functionality test, which is made of three steps: the Pixel Alive, which checks that a consistent data stream reply is obtained from a hit pixel when injecting a calibration charge as input to the amplifier for all the 4160 pixels; the Address Decoding, which compares the address of the hit pixel replied by the ROC with the one in which the calibration charge is injected; and the Mask Test, in which the comparator of each pixel is disabled and it is checked that the calibration injection is correctly masked. All this steps are done on one pixel at a time while masking the others, in order to avoid cross-talk effects. The results are the three pixel maps shown in Fig. 4.20. The Pixel Alive measures the efficiency by injecting a calibration charge ten times for each pixel. The example considered shows a ROC with not excellent characteristics, with a quite large number of dead or very low efficiency pixels. The Address Decoding sets a value of 0 for the pixels already known to be bad from the Pixel Alive test. Pixels for which the address read out corresponds to the one of the injected pixel are marked with 1, otherwise with -1. The Mask Test does a similar procedure.

The next step, called Trimming, is one of the most important calibration steps to improve the detector performance. This procedure equalizes the threshold between different pixels. The method relies on the VthrComp, Vtrim and TrimBit DACs. First of all the target threshold, usually expressed in low-range Vcal units, must be decided. The default value is 35 ($\sim$ 1800 e^-) but in case of 3D sensors a higher value (40, i.e. $\sim$ 2000 e^-) might be necessary due to the higher capacitance. Once all TrimBit are set to 15 (no modification of the threshold), a charge corresponding to the target is injected in all pixels and the efficiency as a function of the VthrComp value is measured. The shape of the curve is commonly called S-curve due to its error-function-like shape[2]. The entry with the lowest VthrComp which turn on the pixels is chosen and VthrComp is set to this value. At this VthrComp value, all pixels should turn on at Vcal values higher than the target value. To find the minimal effective value of Vtrim, the test first identifies the pixel with the highest Vcal turn-on by measuring the efficiency for all

[2]For an ideal pixel without any noise, this would be a simple step function: zero effciency below the signal threshold and full efficiency above. The effect of the noise is to smear this step function. If the noise is assumed to be gaussian, the S-curve has the shape of an error function, with the width representing the noise and its 50% point corresponding to the threshold.

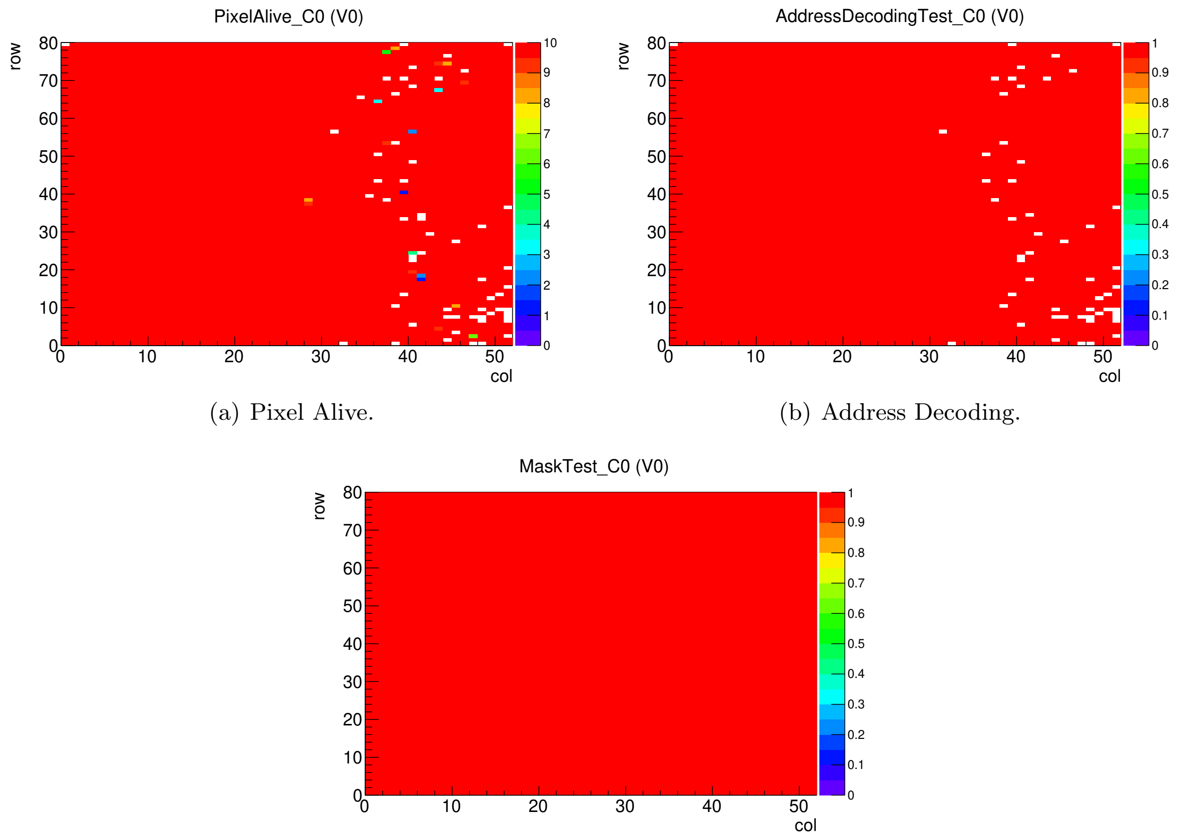

(a) Pixel Alive.

(b) Address Decoding.

(c) Mask Test.

Figure 4.20: Test results for checking pixel basic functionality.

pixels as a function of Vcal. The TrimBit for this pixel is set to 0 (maximum reduction of the threshold) and an efficiency scan as a function of Vtrim and Vcal is done in order to find the Vtrim that sets the pixel threshold to the target. For all the other pixels the TrimBits are determined by an iterative procedure. As shown in Fig. 4.21, the trimming procedure reduces the threshold RMS from ~ 350 to ~ 130 e^-.

The SCurve Test measures threshold and noise for all pixels by making an S-curve as a function of Vcal. This allows to verify the trimming procedure and also to spot noisy pixels. In the noise distribution of Fig. 4.22(a) it is visible a tail at high noise values. As it can be seen in the map of Fig. 4.22(b), this is due to the border pixels, which have larger dimensions, and hence a larger capacitance, in order to fit multiple ROCs in a module.

The Bump-Bonding Test is done to verify that all pixels are properly bonded to the sensor. In this case the calibration signal is injected directly into the sensor and an S-curve is done to measure the threshold at which the signal is observed. In case the pixel is not properly connected, the threshold is expected to be higher with respect to the distribution of the other pixels.

The Pulse Height (PH) Optimization is used to properly set the PHOffset and PHScale registers. In general, it is important that the full range of signals can be correctly digitized by the ADC. However, it is even more important to have a better resolution at low charges at the price of saturating the ADC to its maximum value (255 DAC units) when a large charge is deposited. This is required by the fact that the ability of measuring the charge of the multiple hit pixels of a cluster, which is usually low since it is shared between pixels, allows a good measurement of the charge asymmetry and hence a good space resolution. This is very important after irradiation, when the collected charge is low due to the irradiation damage.

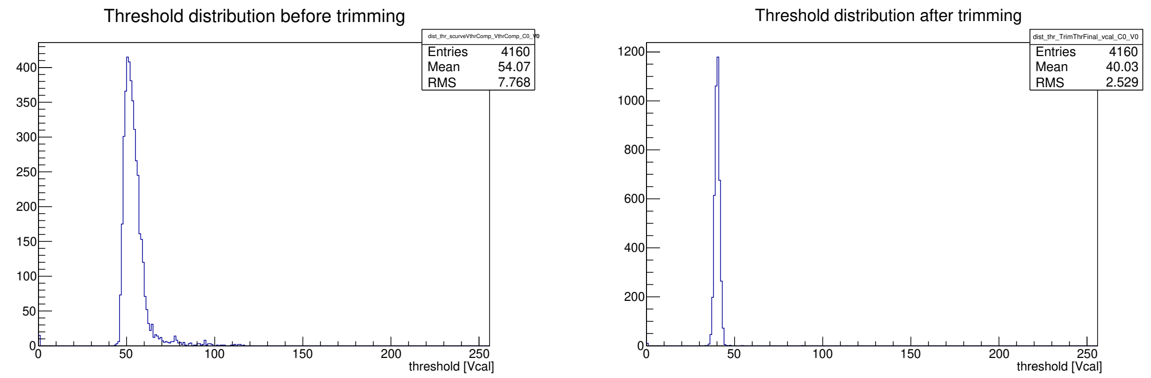

(a) Threshold distribution before the trimming procedure.

(b) Threshold distribution after the trimming procedure.

Figure 4.21: Effect of the trimming procedure on the threshold distribution.

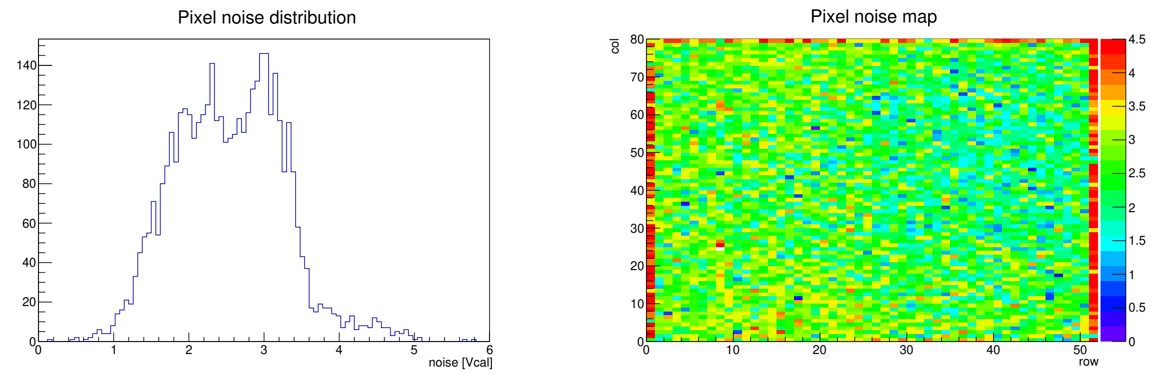

(a) Noise distribution.

(b) Noise map.

Figure 4.22: Noise distribution (a) and map (b) measured with the SCurve Test.

The final step of the ROC test is the Gain Pedestal Measurement, by which the calibration curve between the charge injected and the ADC output is derived. This step needs to be repeated in case of a different setup (laboratory or test beam), since the curve depends on the ROC external powers. It might also be needed to repeat the PH Optimization.

The points obtained with the Gain Pedestal Measurement can be fitted with the formula

$$ADC = p_4 + p_3 \cdot \tanh(p_1 \cdot Vcal + p_2) \qquad (4.3.1)$$

however the equation can be well approximated by a linear function in the low-charge region.

4.3.2 Current-voltage characteristic

Current as a function of the applied bias voltage (usually referred to as IV-curve) is one of the fundamental measurements to qualify a sensor.

In the Torino laboratory this measurement is done using a Keithley 2400 or 2410 source meter. The device is controlled by a LabVIEW program, which I developed during the PhD, through the GPIB bus present on the device. It allows to make scans with a settable step. Multiple measurements are done for each point (after waiting a fixed time ($\sim$ 2 s) in order to stabilize the circuit) to increase the accuracy.

For the unirradiated sensors the measurement is done without cooling. In this condition it would be better to do the measurement with the ROC powered off to avoid the temperature increase due to the power dissipated by the electronics. However, in this condition a high sensor current might break some ROC channels. On the experience made, a sensor current above 1 μA is already potentially dangerous for this readout chip. It should also be considered that a high current could be injected in a few channels even if the sensor global current is still below this limit.

4.3.3 Tests at controlled temperature

Tests of irradiated devices need to be done at low temperature in order to reduce the sensor leakage current and avoid the reverse annealing of the defects. In Torino these tests are done in the clean room at the Laboratorio Tecnologico of the INFN (Istituto Nazionale di Fisica Nucleare).

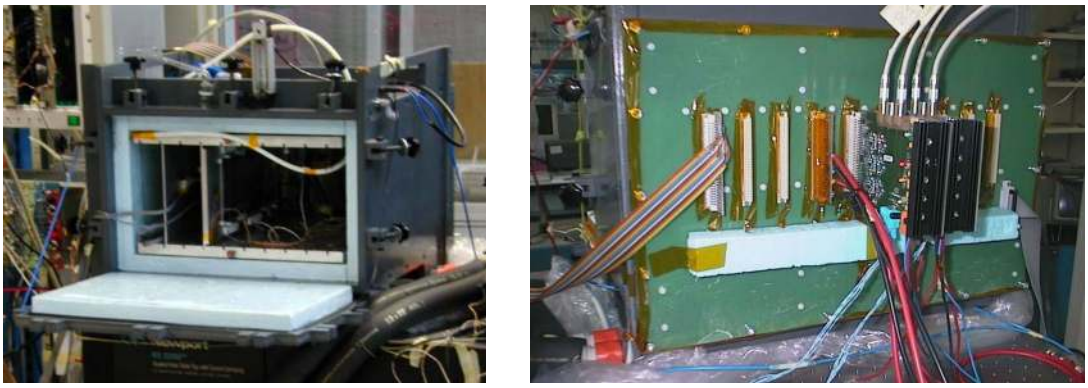

(a) Front view. (b) Back panel.

Figure 4.23: The Wien cold box in the Torino clean room.

The cold box used is the so-called "Wien cold box" developed for the CMS strip thermal tests by HEPHY - Institute of High Energy Physics of Wien. This instrument, shown in Fig. 4.23, is an air-shielded box with two Peltier cells, one on the floor and one on the ceiling. The Peltiers have a maximum voltage of 25 V and current of 13 A that allows to reach a temperature difference ΔT= 50°C between warm and cold surfaces. The power is provided by a custom power supply that in the original setup could be remotely controlled and it was interlocked in case the temperature or humidity reached alerting values. Since the use of the setup was for a limited number of days, it was decided to remove the interlocks.

The cold surfaces of the Petliers are kept at a stable temperature by a water recirculation system using a small chiller of 1.5 kW cooling power. Despite the antifreeze liquid present in the water it was decided to run the chiller at 15°C in order not to stress the system which was unused for more than ten years.

Each Peltier cell is thermally connected to an aluminum plane on which rails are machined. These rails allow to insert up to ten vertical aluminum plates that were hosting the strip modules. One of this plane was modified to host the ROC board and to screw it in order to provide a good thermal contact.

A constant flux of dry air must be provided to the box to avoid condensation on the device, which might produce discharges. The Wien cold box is equipped with a dry air inlet, which measures its humidity, and on the outlet a glass bubbler is installed, which ensures the over-pressure for contrasting the entrance of humid air. The dry air is provided by a compressor, whose output is fed into a desiccator made of several filters in cascade able to provide air at 25°C with $\sim$ 0.5% relative humidity. Alternatively, a 50 liter 200 bar dry air cylinder with similar characteristics could be used. Enough air needs to be fluxed before decreasing the temperature to guarantee a dew point temperature below the target temperature.

For this test the DTB has been placed inside the box, adding further power to be dissipated. The irradiated devices have been tested at $-10°C$. The detectors have been kept in a freezer at $-18°C$ to avoid the reverse annealing. For preventing the ice formation, the detectors have been placed in hermetic custom aluminum boxes with a dry air flux provided by two pneumatic connectors. Pictures of the detector boxes are shown in Fig. 4.24.

(a) Detector boxes in the freezer.

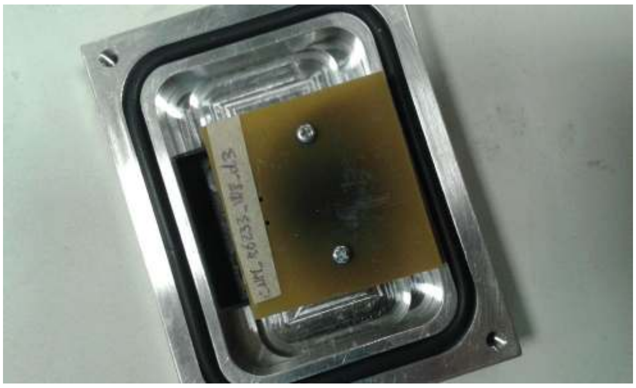

(b) Inner view of the detector box.

Figure 4.24: Detector boxes custom made in Torino to host the irradiated devices and provide an easy access for testing.

For long term storage, devices are packaged in a anti-static ESD safe cardboard box inserted in a protective aluminum shell, all in a vacuum bag to prevent condensation. The same packaging is used for shipping the irradiated detectors. In this case, to maintain the temperature low, the detector vacuum bag is placed in a cardboard box with thick polystyrene walls together with ice packs. This system maintains the detectors below 10°C for more than 24 hours, the typical shipping time, limiting the annealing.

4.4 Beam tests of 3D sensors at Fermilab

Beam tests before and after irradiation for the devices studied in this thesis were done at the Fermi National Accelerator Laboratory (FNAL, Batavia, Illinois) with 120 GeV protons.

4.4.1 Beam test setup

The track measurement is provided by a telescope made of 8 planes of CMS pixel modules read out by the PSI46v2 ROC, four upstream and four downstream with respect to the Device Under Test (DUT) position [123]. A sketch of the telescope geometry is shown in Fig. 4.25. The

8 planes are tilted by 25° with respect to the beam, along the long pitch direction, reaching a resolution of $\sigma_{\text{telescope}} = 8\ \mu$m on both x and y directions. The telescope is mounted on a double-axis motorized system that allows to center the planes on the beam, which has a dimension of 5×5 mm^2 at one standard deviation, to be compared to the 1 mm^2 of the DUT. The telescope planes are arranged to overlap in a region of 16×16 cm^2, well covering the DUT area.

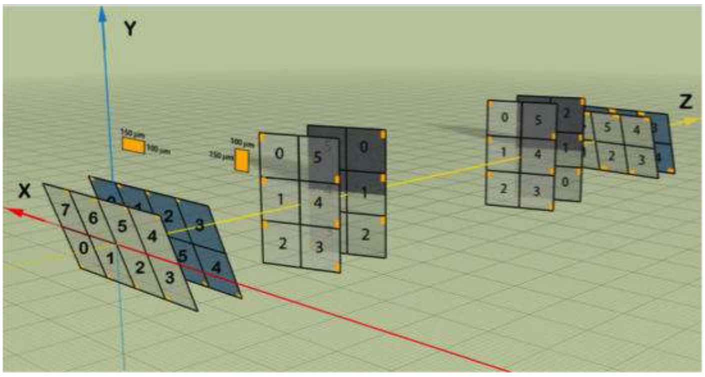

Figure 4.25: Sketch of the telescope geometry used at FNAL [123].

Telescope and DUTs are configured and read out by the CAPTAN (Compact And Programmable daTa Acquisition Nod), a DAQ system developed at FNAL [124]. The setup uses three CAPTAN boards, one for the uptream planes, one for the downstream ones, and one dedicated to the readout of up to four DUTs. The trigger is provided by the coincidence of three scintillators, two upstream and one downstream with respect to the telescope.

The DAQ boards are connected via Gigabit Ethernet to the acquisition computer, running a Visual C++ software. The software, besides controlling the three boards, sets the global registers and the TrimBits of the ROCs, and also performs calibrations using the internal charge injection of the chip. This is necessary to measure the exact noise and threshold used during the acquisition and the calibration curve needed to convert the ROC ADC output into the charge in electrons.

The bias voltage is provided to the DUTs by Keithley source meters remotely controlled. DUTs can be tilted up to 25° by a remotely controlled motor. Since the beam angle dispersion at the telescope is measured to be less than 0.01° in both x and y directions, the angle of incidence of the particles is determined by this rotation angle. Because of the positioning of the detectors done without high precision tools, an offset, estimated to be below 3°, may be present.

For irradiated devices, a carbon fiber box is mounted on the rotating system and provides the temperature and humidity control. The temperature is controlled with a Peltier and a temperature probe. A software sets the current flowing in the Peltier by using as a feedback the measurement of the probe, which is connected to the cold plate. In order to limit the material budget of the telescope and reduce the multiple scattering, the cold plate has a hole on the back of the sensor. To ensure a good thermal conductivity, a PGS (Pyrolytic Graphite Sheet) foil is attached to the back of the detector board with thermal grease. The board is then screwed with the thermal foil in contact with the cold plate. The warm side of the Peltier is connected to a chiller recirculating a water-glycol mixture. The humidity in the box is reduced by a constant nitrogen flow and monitored with a probe.

The beam test procedure starts with the setting of the DUTs on the beam line. Thanks to the laboratory test with the DTB, already optimized registers can be loaded since the beginning. Particularly important are the TrimBits, which reduce the threshold spread and hence allow to better optimize the threshold. The first acquisition step is the threshold scan, which determines the lowest threshold before the detector becomes too noisy. Only the global register VthrComp is modified so that the threshold remains trimmed. A bias scan is then started to measure the sensor behaviour as a function of the bias voltage. Finally, at fixed voltage the angle scan is performed by rotating the DUTs with respect to the beam. Before removing the DUTs from the beam line, the calibrations are done.

4.4.2 Data analysis

For the data analysis, two software programs have been developed at Milano Bicocca: 'Monicelli' for the track reconstruction and the telescope and DUT alignment, and 'Chewie' for the data analysis. Both are written in C++ and use ROOT and the QT library.

In the first step of the track reconstruction process, Monicelli reads the merged binary data file together with an xml geometry file describing the overall configuration and the geometrical details of the telescope detectors. This geometry description is the starting point for the alignment and contains space coordinates and rotation angles of the detector planes. The subsequent step loads the calibration curves to convert the ADC value into the electron charge. At this point the clusters can be determined and the detector hits are converted into points in a three-dimensional space.

It follows the track finding: for each pair of points in the first and last plane a straight line is traced. All points of the other planes which are in a selectable window (usually in the order of 1 cm at the beginning of the alignment procedure, 500 μm at the end) around the line are associated to the track. Cuts on the minimum number of points per track (6) and the maximum number of points per plane (5) are applied to reject low quality tracks. This step needs to be repeated every time any other procedure modifies the geometry.

The distances of the points from the track (residuals) are used for aligning the detectors. The residuals for each plane are plotted for the x and y coordinates, and the histogram mean is used for the translations. After the track search, the procedure can be repeated if necessary.

Once the residuals are correctly centered, the next step is the fine alignment of the telescope planes. This is done by means of an iterative algorithm that exploits a least-squares minimization to compute the first order roto-translation corrections. In order to improve the performance, the algorithm is only applied to events with single tracks and with cluster size lower or equal 2. Due to the small beam angular dispersion, the fit does not have resolution on the z-position of the detector that must be fixed. The least-square minimization is repeated a number of times. Usually 5 iterations are enough for converging to stable values.

The final step is the DUT alignment. The devices are aligned one at a time. To improve the performances, the procedure must be repeated a few times by fixing and releasing different coordinate transformations. If the modifications to the geometry are large, a new track search might be needed.

At this point the geometry is ready to be used for the data processing. The geometry can be saved in the same xml format used for the starting geometry or in a root file where the calibration functions are also stored. The entire procedure must be repeated every time the setup changes: DUT rotation, telescope movement or access to work on the setup.

Since Monicelli performs the track reconstruction, it is necessary to run it on all the collected data. This is done automatically by the MonicelliExpress macro. Data are then ready to be analyzed with the Chewie program.

Three different qualities of alignment are required. A "fast" alignment is done during the data taking to have a preliminary geometry for validating almost online the data and eventually apply modifications to the setup; this requires $\sim$ 20k events. A "good" geometry ($\sim$ 50k events) is needed for the preliminary data analysis. The "final" geometry is then obtained by repeating the telescope alignment and the DUT alignment with all the available data of the run chosen for the alignment procedure.

The full procedure needs to be run for each needed geometry. To speed up the process, I developed a script, called MonicelliUltra, to perform all the steps previously described. It needs as input an xml file in which reconstruction and alignment parameters are set. The script can be used for the fast alignment during data taking as well as for the final alignment for the data analysis. Moreover, when several alignments have to be run, one can profit from GNU Parallel [125], a shell tool for executing jobs in parallel and automatically loading a new process when the previous one is finished. In this way the user only has to create the xml files for all the alignments and the scrips will run them. Since log files are saved, in case for any reason the program fails, the user can proceed by hand starting from the point where the automatic procedure failed.

When all the geometries have been produced, MonicelliExpress can be run on the complete data set, obtaining the files ready for the analysis. It has been found that small oscillations of the DUT position occur run by run, probably due to the way the DUTs are attached to the telescope. These variations are quite small (usually of the order of $10-15$ μm) but could affect the final results. MonicelliExpress can repeat the DUT alignment leaving free the corrections for x, y and γ (the rotation around the z-axis) and fixing the other parameters. In this way, all runs are corrected for these oscillations.

Actually, to speed up the analysis, one has the possibility at this point to already discriminate between good from bad runs, which sometimes occur when one detector gets stuck during data taking. To this end, instead of running the MonicelliExpress script, it is used the so-called MegaScript that also runs an express version of the analysis code, ChewieExpress, which can also mask bad pixels. GNU Parallel is used to launch several jobs in parallel. The script automatically sends an email at the end of each job, reporting the efficiency, resolution and mean collected charge, which can be used to determine the quality of the run.

To have a better access to this information and also a more convenient bookkeeping of the log files, I wrote a python script to search for all these emails and mine the information. It then updates a Google Drive spreadsheet which contains all the relevant information of each run. Good runs are selected for the analysis.

Chewie is a multi-threaded software for the analysis of the beam test data. It is divided into modules and the ones used are the so-called Window, Efficiency, Charge and Resolution. The Window module plots the hit maps for all the detectors (telescope and DUT). This step is essential to determine empty pixels that need to be removed from further analysis. However, this step does not allow to select low efficient pixels because of the not-uniformity of the beam on the sample.

To detect the double column freezing which affects the v2.0 version of the PSI46dig, I added in this step plots which show the column efficiency as a function of the event number. As can be seen in the example of Fig. 4.26, the double column freezing manifests with a stop of the hit detection for all the pixels of the double column. In the following analysis pixels are excluded after their freezing instant, not to underestimate the real performance of the detector.

The first detector characteristic that is evaluated is the efficiency, by checking that the pixel pointed by the track has registered a signal. In order to reduce the impact of the track reconstruction error, nearby pixels are checked also. For this reason, pixels at the edges or near a bad pixel are excluded for this measurement. I have defined as bad pixels those with an efficiency 7 standard deviations away from the detector average. Also pixels near a frozen double column are excluded. In the Efficiency module I added the measurement of the edge efficiency, which is important for CT-PPS and will be presented later.

The next measurement obtained from the beam test data is the collected charge. This is of particular interest after irradiation for evaluating how the damage influences the properties of the sensor. It also allows to determine the asymmetry plot. This is obtained by plotting the

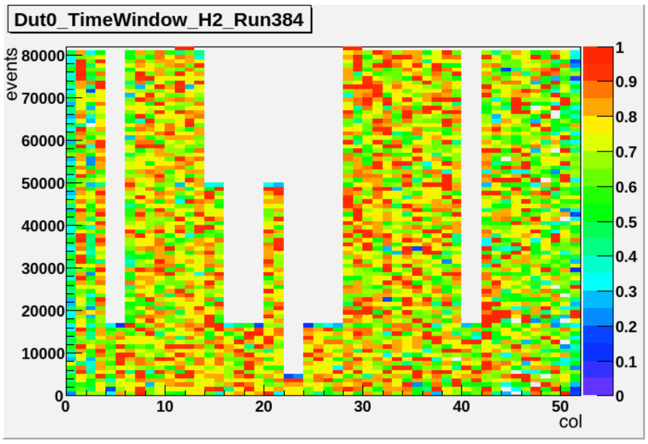

Figure 4.26: Column efficiency as a function of the event number for a detector suffering double column freezing.

charge asymmetry between two adjacent pixels forming a cluster (size 2 cluster), defined as

$$\text{Asymmetry} = \frac{Q_{\text{left}} - Q_{\text{right}}}{Q_{\text{left}} + Q_{\text{right}}} \tag{4.4.1}$$

where Q_{left} is the charge collected by the left pixel and Q_{right} the one collected by the right one. An example plot of the charge asymmetry as a function of one of the pixel coordinates is shown in Fig. 4.27. Fitting with a straight line the linear region between the two pixels in the middle of the plot, the asymmetry function is obtained, which allows to convert the charge asymmetry of a size 2 cluster into a track position, with higher precision with respect to the one obtained by the simpler charge centre-of- gravity.

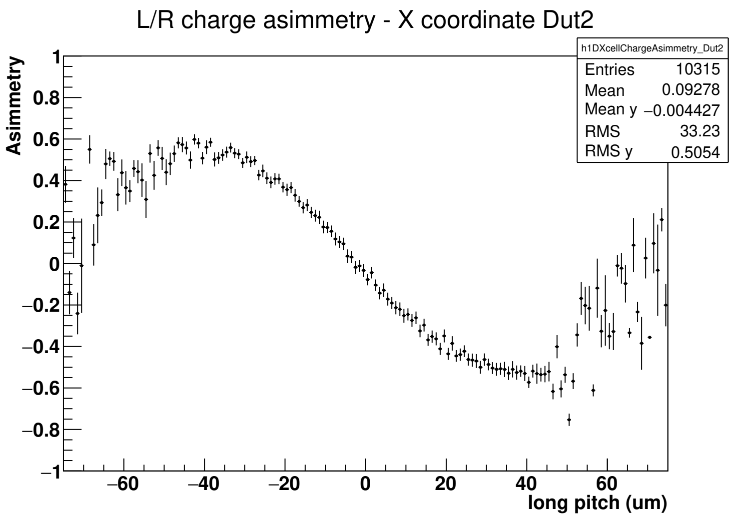

Figure 4.27: Charge asymmetry as a function of the long pitch coordinate for a 3D sensor tilted by 20° with respect to the beam direction. The horizontal axis is set such to have the edge between the two hit pixels in the center of the plot.

The last step of the analysis is the residual evaluation, from which the resolution is extracted. This part can take advantage of the asymmetry calculation done in the charge analysis for improving the resolution of size 2 clusters. Examples of the residuals for size 1 and size 2 clusters are shown in Fig. 4.28. Residuals of size 1 clusters (Fig. 4.28(a)) are fitted with a square function convoluted with a gaussian: the width of the square function represents the transverse section of the pixel area seen by the beam while the sigma of the gaussian (σ^2_{cls1}) takes into account the resolution of the telescope and the fact that the pixel regions in which size 1 and size 2 clusters occur overlap. Residuals of size 2 clusters (Fig. 4.28(b)) are calculated using the charge asymmetry between the two pixels and are fitted with a gaussian.

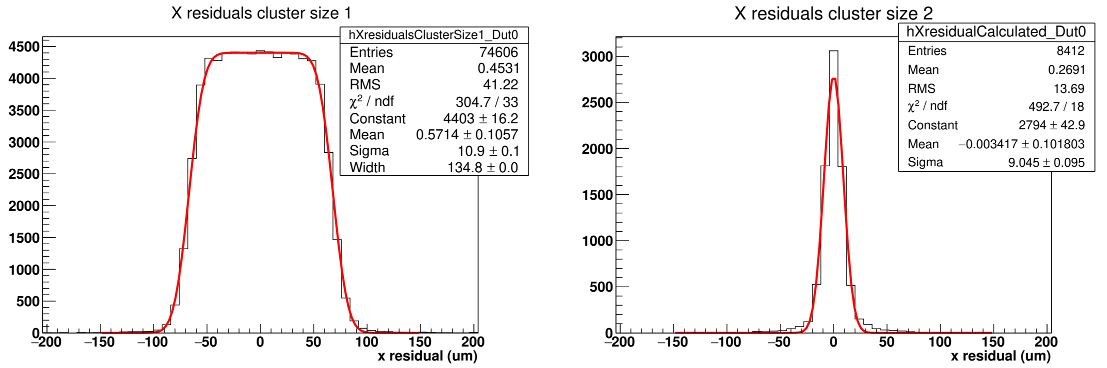

(a) Size 1 cluster residuals before irradiation.

(b) Size 2 cluster residuals before irradiation.

Figure 4.28: Examples of residuals for size 1 and size 2 clusters before irradiation.

The values obtained from the fit of the residual distributions can be used to determine the resolution of the detector for clusters of size 1 and 2:

$$\text{resolution}_{\text{cls1}} = \sqrt{\left(\frac{\text{width}}{\sqrt{12}}\right)^2 + \sigma^2_{\text{cls1}} - \sigma^2_{\text{telescope}}} \tag{4.4.2}$$

$$\text{resolution}_{\text{cls2}} = \sqrt{\sigma^2_{\text{cls2}} - \sigma^2_{\text{telescope}}} \tag{4.4.3}$$

After running the Megascript on all the runs taken during the beam test, the user checks all the runs by looking at the Google spreadsheet and eventually bad runs are discarded. At this points, Chewie is executed on runs taken in the same conditions of threshold, bias and angle.

In some cases, especially after irradiation, ROCs may have pixels misbehaving and showing a lower efficiency. For this reason, the bad pixel maps produced during the efficiency step are used to generate a xml mask file which is used as an input for ChewieExpress for a re-run in order to obtain the final analyzed files.

4.5 FBK 3D sensors

The first beam test campaign on 3D detectors for CT-PPS has been done with sensors designed at the University of Trento and processed by the Fondazione Bruno Kessler (FBK, Trento, Italy). Ten sensors were bump-bonded to PSI46dig v2.0 and v2.0b ROCs. With respect to the PSI46v2 analog ROC used in our previous measurements [126], the new chip allows to run with a lower threshold and after higher levels of irradiation dose. Sensors and ROCs were bump-bonded at Fraunhofer Institute for Reliability and Microintegration (IZM, Berlin, Germany) with SnAg bumps. Assemblies were then glued and wire-bonded in Torino before being tested. In the following sections the characteristics of these sensors and the results of the test campaign are presented.

4.5.1 FBK 3D sensor characteristics

The 3D sensors of this study come from the FBK production for the ATLAS IBL [127], in particular from batches 11 and 12. The layout of the wafer, shown in Fig. 4.29, contains 3 1E

(1 readout column per pixel) sensors with the CMS design. The wafer substrate is a Float Zone p-type high resistance silicon with a nominal thickness of 230 μm.

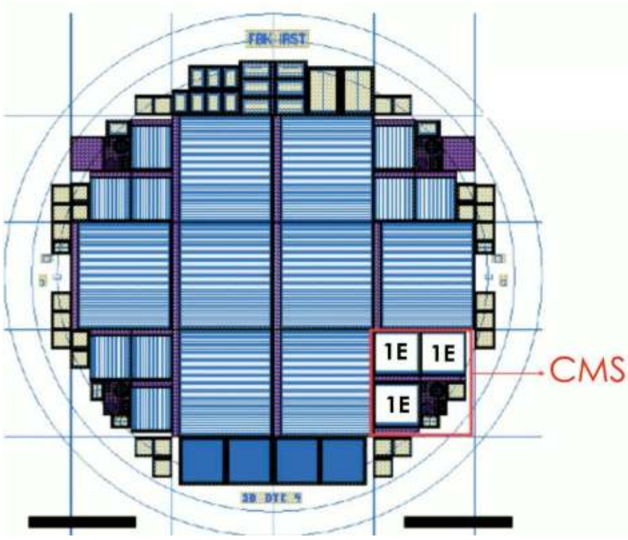

Figure 4.29: Wafer layout of the FBK ATLAS IBL production.

The sensors are produced with the 3D Double-side, Double-Type-Column (3D-DDTC) technology: the n^+ (readout) electrodes are etched from the frontside of the wafer, while the p^+ (ohmic contacts) are etched from the backside. Both types of electrodes are hollow and completely passing through the bulk. The insulation, both on front and back surfaces, is provided by a p-spray implantation. A schematic cross section of a FBK 3D-DDTC sensor is shown in Fig. 4.30(a). The FBK 1E pixel configuration is shown in Fig. 4.30(b).

The pixel area is 150×100 μm^2 except for those pixels in the first and last columns (double length along the horizontal coordinate, 300×100 μm^2) and for the ones in the last row (double vertical dimension, 150×200 μm^2). Pixels at the top corners have therefore double dimensions in both vertical and horizontal coordinates (300×200 μm^2) (Fig. 4.30(c)).

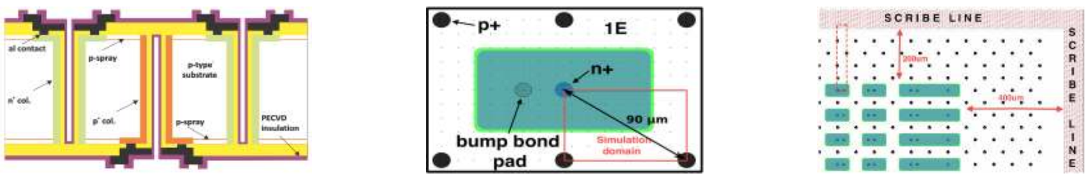

(a) FBK 3D-DDTC cross section.

(b) FBK 3D 1E pixel layout.

(c) FBK 3D sensor edge layout for the bottom-right corner in the convention used in this thesis.

Figure 4.30: Cross section, pixel electrode configuration and edge layout of the FBK 3D sensors under study.

The sensor edges have a dimension of 400 μm in the long pixel-pitch direction (left and right edges in the convention used in this thesis) and 200 μm in the short pixel-pitch direction (top and bottom edges). Multiple p-type column fences are implemented around the sensitive area of the sensor in order to contains the depletion region extension.

4.5.2 Irradiation at the Karlsruher Institut für Technologie

Detectors were irradiated at Karlsruher Institut für Technologie (KIT, Karlsruhe, Germany) within the AIDA Collaboration. Irradiation was performed uniformly with 23 MeV protons to fluences of $1 - 3 - 6 - 10 \times 10^{15}$ n_{eq}/cm^2. The corresponding ionizing dose is $150 - 450 - 900 - 1500$ Mrad. It was decided to push the irradiation to high levels of fluence to observe the behavior of the leakage current, even if it was known that the ROC would not have survived to fluences higher than 3×10^{15} n_{eq}/cm^2. During irradiation, samples were cooled down by a flow of cold nitrogen gas ($\sim -30°C$). The detectors were placed in a thermally and electrically insulated box. Since the beam spot has a diameter of only 4-8 mm, samples were scanned by mounting the box on a controlled XY-stage.

4.5.3 IV curves

Current-voltage characteristics, shown in the plots of Fig 4.31, were measured with the sensors already bump-bonded to the ROCs, before and after irradiation. One of the limitations of this production is a breakdown voltage of $\sim 30 - 35$ V. This is due to high electric field regions between the n^+ electrodes and p-spray which generate an avalanche multiplication already at quite low voltages. Actually, this does not constitute a limitation for their use before irradiation, since already at very low voltages ($5 - 10$ V) the sensor is fully depleted.

The sensors tested from batch 11 were selected on the basis of their IV current measured directly on the wafer. This technique uses a temporary metal deposition, later removed before the sensor bump-bonding, which shorts all the n-electrodes [128]. The sensor labeled FBK_11_43_02 shows a resistive behaviour of the current, indicating that the sensor was damaged during the bump-bonding or the subsequent handling. All the other sensors show a current below 500 nA and a breakdown higher than 30 V, both compatible with the expected characteristics of this production.

Sensors from batch 12 were not measured with temporary metallization and were chosen on the basis of the quality of the ATLAS sensors in the same wafer. However these CMS sensors did not show the same quality and their breakdown is below 10 V. Therefore, these sensors have not been tested on beam and have been sacrificed to be irradiated to 10^{16} n_{eq}/cm^2.

For most of the applications, the low breakdown voltages are not a limitation after irradiation because it is expected for these sensors that the breakdown voltage increases as a function of the irradiation dose. In fact, the breakdown in these 3D sensors is due to high electric field regions between n^+ electrodes and p-spray. Positive charges created by the irradiation in the SiO_2 - Si interface locally reduce the electric field, allowing to bias the sensor to higher voltages.

In the case of CT-PPS, where sensors are subjected to a very non-uniform irradiation, a low break down could be a limitation. The breakdown would increase only in the irradiated region, while the rest of the sensor induces the same breakdown of the non irradiated devices.

A possible solution to this issue is to implement n-electrodes not fully passing through. This solution was studied by FBK and both simulation and the first results on sensors indicated a breakdown exceeding 100 V already before irradiation [129, 130]. However, due to an excessive wafer bowing, sensors could not be bump-bonded and the performances after coupling them to the ROC are not available.

The irradiation of the tested sensors showed a behavior of the leakage current compatible with the expectations. Currents have been measured at $-12°C$ because of a problem with the chiller used at the test beam, which limited the minimum temperature of the detector to this value. Sensors irradiated at 1 and 3×10^{15} n_{eq}/cm^2 show a quite flat plateau, before reaching the breakdown at 60 and 160 V, respectively.

Since no annealing was done in order to reproduce the conditions of CT-PPS (sensors need to be kept at low temperature also when off and in parking position due to the heating generated

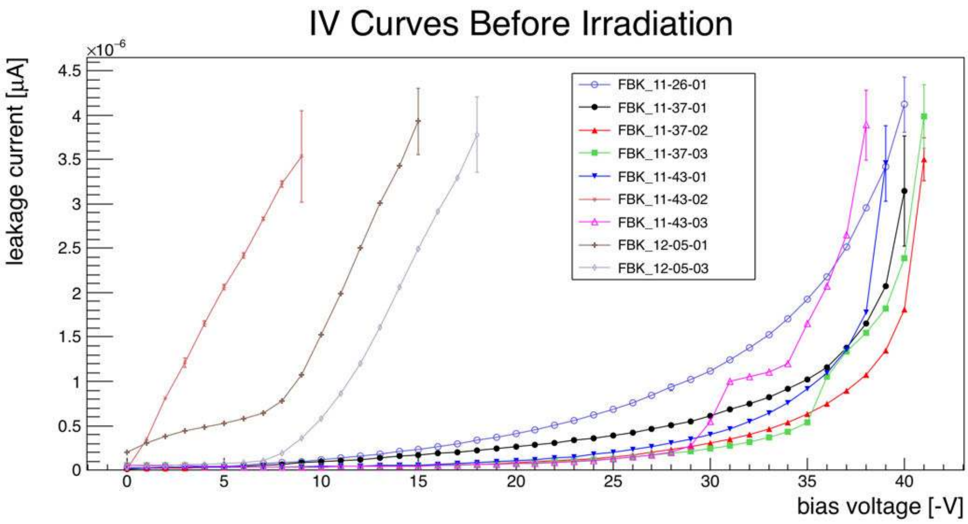

(a) IV curves before irradiation.

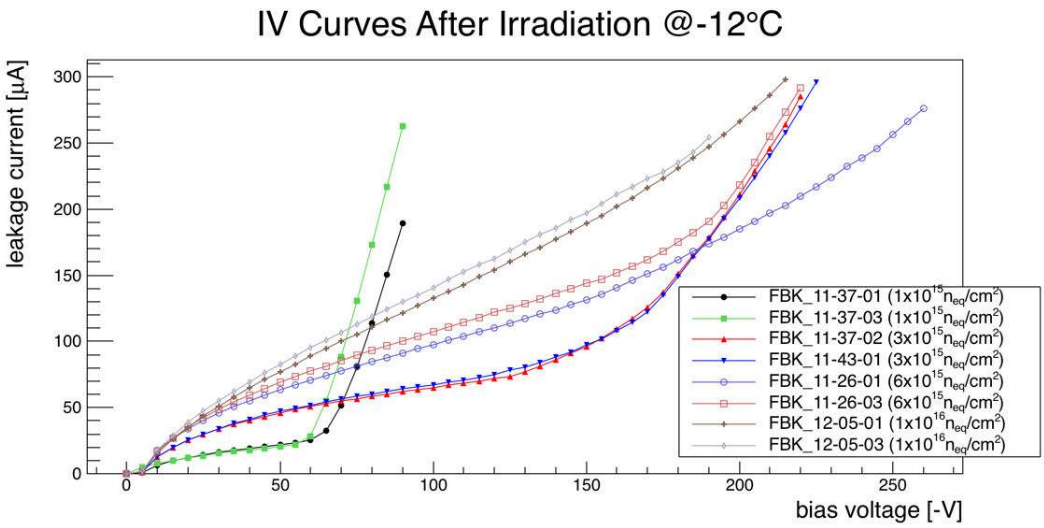

(b) IV curves after irradiation.

Figure 4.31: IV curves before (a) and after (b) irradiation.

by the beam), a direct comparison of the leakage current could not be done. However, the current increase is evident.

4.5.4 Laboratory tests

Detectors went through the standard calibration with the DTB in Torino. Before irradiation sensors have been tested at room temperature, after irradiation at $-10°$. No particular issue has been found on these detectors before irradiation.

After irradiation, because of the low energy of the protons used at KIT, the large deposited dose seriously damaged the ROCs, which are qualified up to 120 MRad only [131]. A manual optimization of the ROC registers was done, in particular to obtain the linearity between the amount of charge injected and the ADC output. An increase of the ROC digital supply voltage from 2.5 V to 2.8 V was required for the devices irradiated to 3×10^{15} n_{eq}/cm^2.

In order to to optimize the ADC linearity, scans of the ADC as a function of several internal ROC registers have been performed for a low charge ($\sim$ 7 ke) and a high charge ($\sim$ 70 ke) injected, choosing the values which better separate the two outputs. Since these DACs are not uncorrelated, the procedure has been iterated a few times.

The final calibration curves of the 4 detectors irradiated to 1×10^{15} n_{eq}/cm^2 and 3×10^{15} n_{eq}/cm^2 are shown in Fig. 4.32. All ROCs show a linearity region which saturates at ~ 100 Vcal in the high range, corresponding to ~ 35 ke. For the ROC bump-bonded to the FBK_11_37_03 sensor only few points of the calibration curve could be collect, but the trend is still well visible. The ROC of the FBK_11_37_02 shows a step at ~ 170 Vcal, indicating a problem in the ADC conversion for high collected charges. Since this effect occurs only for signal higher then ~ 60 ke, no real problems are expected at the test beam due to this issue.

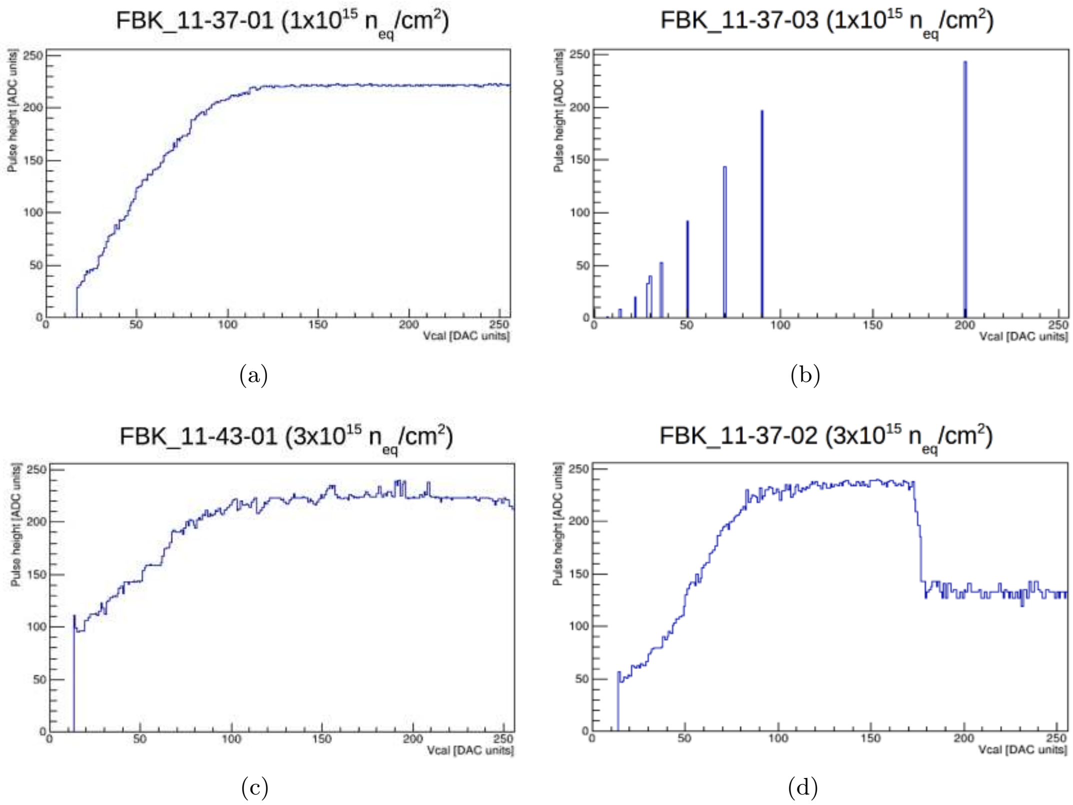

Figure 4.32: ADC output as a function of the injected charge expressed in high range Vcal units (1 Vcal $\simeq$ 350 e).

4.5.5 Noise and threshold

The method used to optimize the ROC threshold at the test beam is based on the efficiency, which is calculated almost online while taking data. The starting value of the threshold for each pixel is the one obtained with the trimming procedure in laboratory. The scan is performed by varying only the global threshold register; the last point in the efficiency plateau before the drop due to the noise filling the buffers is the one chosen for the rest of the data taking.

After finding the working point, the measurement of the S-curve is repeated to determine the noise. Before irradiation the threshold values vary from 1.8 to 3.0 ke^-, depending on the detector noise (from 180 to 200 e^-), while after irradiation, with noise from 250 to 350 e^-, the threshold is ~ 2.5 ke^- for FBK_11_37_01 and FBK_11_37_02 and ~ 3.6 ke^- FBK_11_43_01. This last detector showed several noisy pixels which triggered the double column freezing, requiring a higher threshold with respect to the other detectors. The increase of noise showed after irradiation is mainly attributed to the damage of the ROCs due to the extremely high ionizing dose deposited.

4.5.6 Test beam results

The beam tests on the sensors have been done in April and August 2014 for unirradiated and irradiated devices, respectively. The irradiated FBK_11_37_03 detector was accidentally broken, probably during handling of the detector while installing it in the tracking telescope and no data are available.

As already said these ROCs were subjected to the double column freezing and therefore the thresholds were not dictated by the efficiency of the ROCs only but also from the fact that higher thresholds for the irradiated devices with respect to the laboratory were required to have a large enough area of working pixels.

During the bias scan, the voltage to be applied for the angle scan is determined. Values are shown for all detectors in Tab. 4.1. For unirradiated sensors, the bias voltage was set 5 V lower than the breakdown voltage. For irradiated devices, as suggested by the sensor designer, the bias voltage was pushed into the breakdown region in order to improve the efficiency. However, probably due to a thermal run away, the current of sensor FBK_11_37_02 increased too much and the power supply went into compliance, reducing the effective applied voltage. This was not continuously monitored during data acquisition and it was understood only at the end of the data taking. Fortunately, the issue occurred only for the last points of the angle scan, while the other data could be collected.

Sensor	Fluence (n_{eq}/cm^2)	Bias (-V)
FBK_11_26_01	0	30
FBK_11_26_03	0	30
FBK_11_37_01	0	30
FBK_11_37_02	0	30
FBK_11_37_03	0	30
FBK_11_43_01	0	30
FBK_11_43_03	0	25
FBK_11_37_01	1×10^{15}	85
FBK_11_37_02	3×10^{15}	150
FBK_11_43_01	3×10^{15}	145

Table 4.1: Table of bias voltages chosen for each sensor after the bias scan.

Collected charge

In Fig. 4.33 typical maps of the charge collected within a pixel before irradiation are shown for different values of the bias voltage; for these measurements the sensor was placed perpendicular to the beam (angle 0°). The plotted charge is the mean value, not the Landau Most Probable Value (MPV), for which a much higher statistics than that available would be needed. For this reason, values are slightly higher than those expected for 230 μm thick sensors ($\sim$ 18.4 ke$^-$). It is possible to observe that already at 15 V (Fig. 4.33(c)) the collected charge saturates.

The corresponding collected-charge maps after irradiation fluences of 1×10^{15} n_{eq}/cm^2 and 3×10^{15} n_{eq}/cm^2 are shown in Figs. 4.34 and 4.35, respectively. Thanks to the increased breakdown voltage, higher bias values than before irradiation can be applied.

Both before and after irradiation it is clearly visible the lower charge collected in the area nearby the readout electrode in the center of the pixel. This is due to the fact that tracks are not completely perpendicular and so part of the track passes through the hollow column. The normalization of these plots is done on the hits seen by the detector and no effect due to inefficiencies is present.

These charge plots show the charge collected by the hit pixel and do not consider the charge

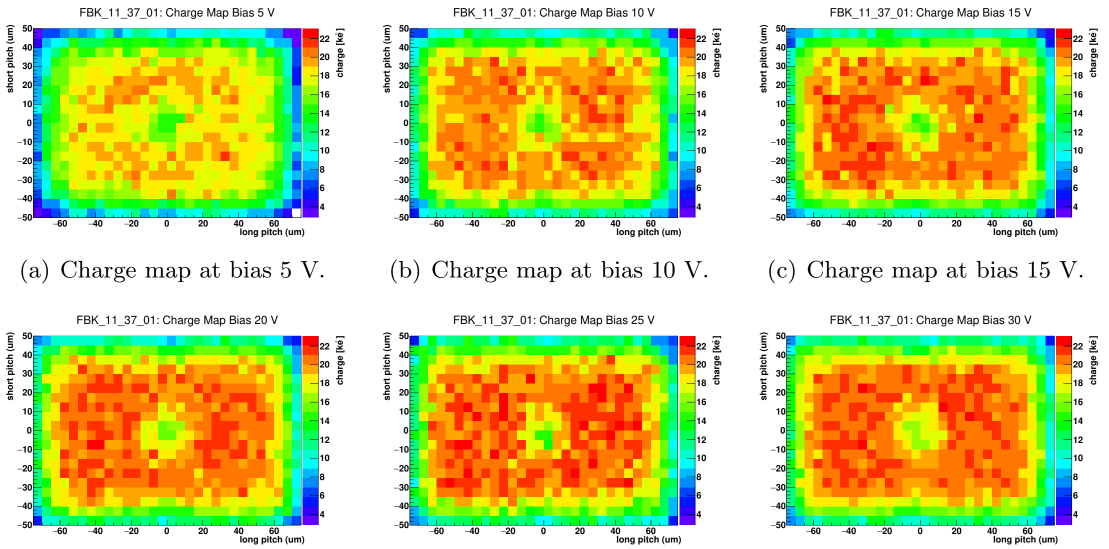

(a) Charge map at bias 5 V. (b) Charge map at bias 10 V. (c) Charge map at bias 15 V.

(d) Charge map at bias 20 V. (e) Charge map at bias 25 V. (f) Charge Map at bias 30 V.

Figure 4.33: Collected-charge maps vs bias at angle 0° for a FBK sensor before irradiation.

possibly collected by the neighboring pixels in case of cluster sizes higher than one. For this reason, in the area near the edges of the pixel the amount of charge is lower.

For perpendicular tracks, since in the case of 3D sensors the electric field points toward the center of the pixel, clusters of size 2, induced by the diffusion of the electron clouds into the adjacent pixel, are limited to the region close to the pixel edge. This is clear from Fig.4.36(a), where the pixel map of the probability of clusters of size 2 is shown. In the case of perpendicular tracks, an increase of the bias voltage implies a stronger electric field, which suppresses the diffusion in the direction parallel to the sensor surface and hence reduces the probability of clusters of size 2. This effect, also known as self-screening effect, is visible in the plot of Fig. 4.36(b).

Figure 4.37 shows the collected charge at different angles after an irradiation fluence of 1×10^{15} $\mathrm{n_{eq}/cm^2}$. The left-right asymmetry, which appears when rotating the sensor with respect to the beam direction, can be probably related to a top-bottom asymmetry in the pixel cell. This asymmetry is probably caused by the n^+ implant located on the top surface (the blue rectangle in the layout of Fig. 4.30(b)), which modifies the ideal electric field parallel to the surfaces of a 3D sensor. Before irradiation no effect should be observed, but after irradiation, when trapping has a strong effect on the collected charge, an asymmetric charge collection in the pixel area could show up for tilted tracks.

Efficiency

Figure 4.38 shows the efficiency as a function of the bias voltage for detectors placed perpendicularly to the beam direction, before and after irradiation. Before irradiation (Fig. 4.38(a)) the maximum efficiency can be reached already at 5 V, as expected from the collected charge shown in Fig. 4.33(a), which is well above the ~ 2.5 $\mathrm{ke^-}$ threshold in the entire pixel area. Sensor FBK_11_26_01 shows a higher efficiency because it was erroneously placed at an angle of $\sim 3°$ with respect to the beam.

Figure 4.38(b) indicates that after irradiation the efficiency never saturates, even at the maximum bias voltage. This is due to the fact that the electric field near the short edge of the pixel remains too low to always collect enough charge to pass the threshold, as it can also be seen in the pixel efficiency maps in Fig. 4.39. For this reason, sensors with more than one

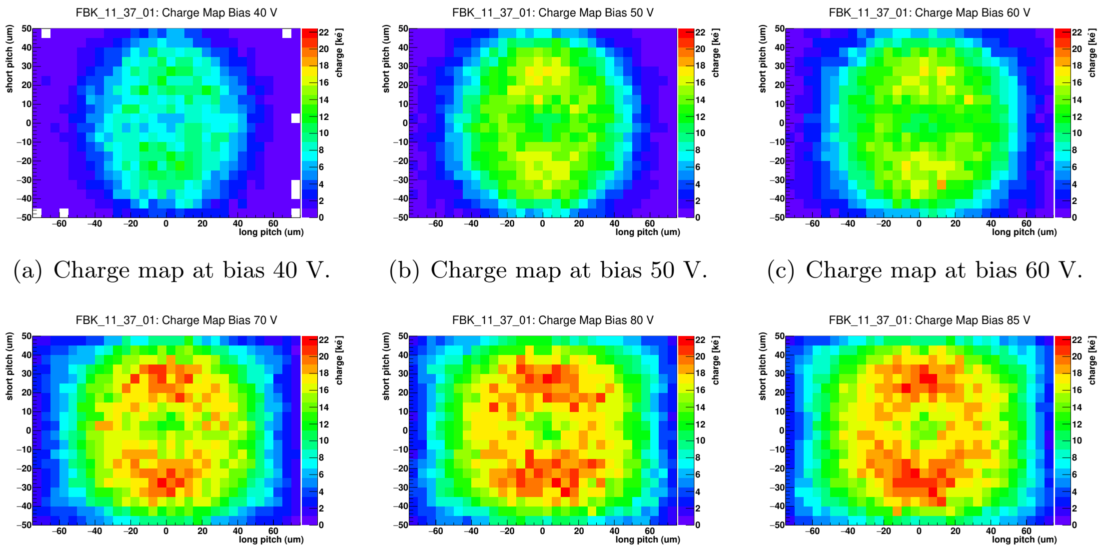

(a) Charge map at bias 40 V. (b) Charge map at bias 50 V. (c) Charge map at bias 60 V.

(d) Charge map at bias 70 V. (e) Charge map at bias 80 V. (f) Charge Map at bias 85 V.

Figure 4.34: Collected-charge maps vs bias at angle 0° after an irradiation of 1×10^{15} $\mathrm{n_{eq}/cm^{-2}}$.

readout column per pixel should be more efficient after irradiation. Finally, as expected by considering the higher threshold used for detector FBK_11_43_01, its efficiency is lower with respect to the other detector irradiated to the same fluence (FBK_11_37_02).

The efficiency as a function of the rotation angle before irradiation is shown in Fig. 4.40. The efficiency for all the tested detectors already saturates at 5° with a global efficiency greater than 99.5% (Fig. 4.40(a)), thanks to the fact that already after a small rotation angle the geometrical inefficiency of the columnar electrodes is completely restored, as visible in Fig. 4.40(b)

Figure 4.41 indicates that the detector inefficiency due to irradiation can be partially recovered by rotating the devices. The different behavior of sensor FBK_11_37_02 is related to the thermal run away previously cited. Unfortunately the problem was understood too late to repeat the scan. Values for this sensor at 0° and 5° are anyway reliable and show the absolute value of the efficiency after an irradiation fluence of 3×10^{15} $\mathrm{n_{eq}/cm^2}$.

Edge efficiency

A key feature required by the silicon detectors for the CT-PPS tracking system is the reduction of the inefficient area at the edge of the sensor toward the beam. A typical plot for studying the edge efficiency is shown in Fig. 4.42. The efficiency is measured as a function of the position along a detector row; the vertical line indicates the geometrical edge of the last pixel, which in this case is at 400 μm from the edge of the sensor. The histogram is fitted with a S-curve and the distance between the geometrical edge of the last pixel and the inflection point is taken as efficient edge (EE).

The expected increase of the efficient edge as a function of the bias voltage, thanks to the extension of the depletion region towards the edge, is demonstrated in Fig. 4.43(a). By rotating the sensor, the efficient edge expands also for geometrical reasons (Fig. 4.43(b)). Considering a tilting angle of 20° with a bias voltage of 30 V, about 70 μm of efficient edge can be gained. This effect is not visible after irradiation because at a fluence of 10^{15} $\mathrm{n_{eq}/cm^2}$ the efficiency is below 50% already at the edge of the last pixel.

Although the tested sensors have an edge of 400 μm, FBK demonstrated the feasibility of implementing edges of only 100 μm or smaller [102]. This would allow to reach an inefficient edge of only 30μm before irradiation.

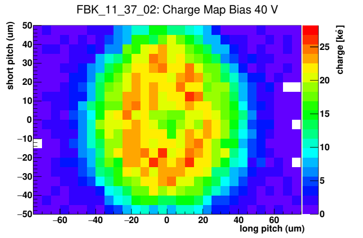

(a) Charge map at bias 40 V.

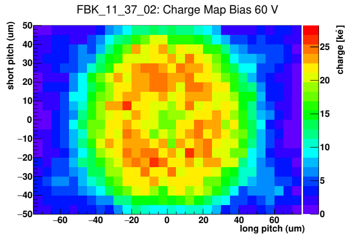

(b) Charge map at bias 60 V.

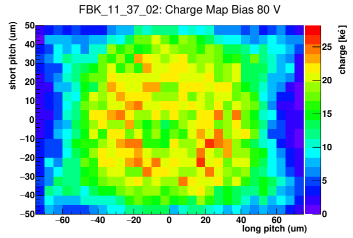

(c) Charge map at bias 80 V.

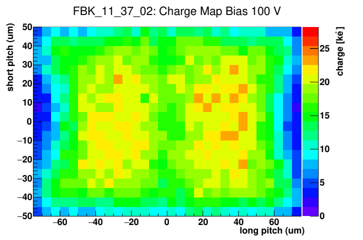

(d) Charge map at bias 100 V.

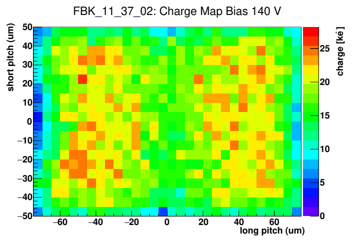

(e) Charge map at bias 140 V.

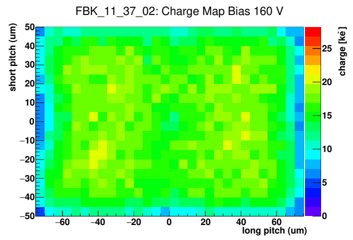

(f) Charge Map at bias 160 V.

Figure 4.35: Collected-charge maps vs bias at angle 0° after an irradiation of 3×10^{15} n_{eq}/cm^2.

Resolution

Figure 4.44 shows the probability of having clusters of two hit pixels (cluster size 2) along the short size of the pixel as a function of the rotation angle, before and after irradiation. It has been chosen to plot the cluster size probability only along columns to highlight the effect of tilting the sensor with respect to an axis parallel to the pixel column direction.

As expected, in both plots the cluster size 2 probability increases as a function of the angle; however, after irradiation the hits with cluster size 2 are less then 10% at an angle of 20°. The lower values for sensor FBK_11_43_03 are due to the higher threshold. Once again, this is a clear indication that the short edges of the pixel are critical areas after irradiation and pixel configurations with more than one readout column per pixel should be preferred after radiation damage.

Resolutions along the long pitch coordinate before irradiation as a function of the rotation angle are presented in Fig. 4.45, separately for clusters of size 1 and 2. Resolutions along the other coordinate are not plotted since no rotation has been applied that direction; due to the low cluster size 2 probability for a non-tilted 3D sensor, the resolution can be well approximated by the pitch divided by the square root of twelve (~ 29 μm). The cluster size 1 resolution improves by rotating the detectors, reaching a value of ~ 30 μm at 20°. This is due to the fact that the effective area of the pixel seen by the beam reduces. The cluster size 2 resolution slightly worsens as a function of the angle and it is ~ 8 μm at 20°. This is a consequence of the electric field in 3D sensors, which limits the formation of clusters of size 2 only nearby the pixel edge.

For the same reason, at angles close to zero it is reasonable to make the assumption that if a particle produces a cluster of size 2 then it has crossed the sensor in correspondence of the edge of the two hit pixels. To demonstrate that, Fig. 4.46 shows the sigma of the gaussian curve obtained by fitting the distribution of the residuals with the previous assumption (called "digital") or with the standard charge asymmetry calculation (called "calculated"). One can notice that the digital approximation well reproduces the values of the charge-asymmetry-calculated residuals up to an angle of 5°. In CT-PPS it could be interesting to consider this approximation for the y-coordinate because no rotation is foreseen in that direction.

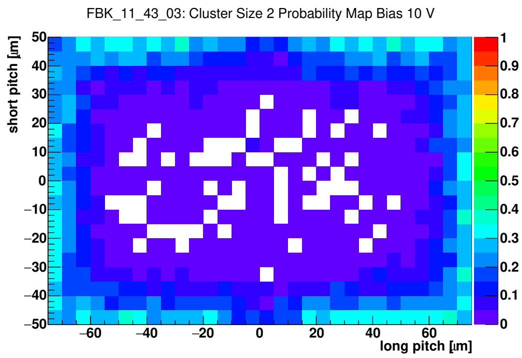

(a) Pixel map of cluster size 2 probability.

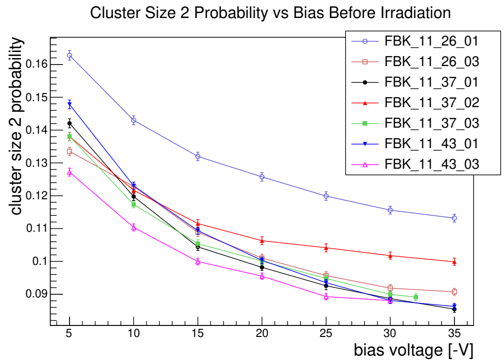

(b) Cluster size 2 probability as a function of the bias voltage.

Figure 4.36: Due to the electric field configuration in the 3D sensor, cluster sizes higher than one are strongly suppressed for perpendicular tracks and limited to the pixel edges (a). Moreover, the higher the bias voltage (i.e. the electric field) the lower the cluster size 2 probability (b).

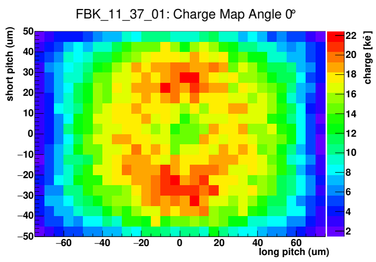

(a) Charge map at angle 0°.

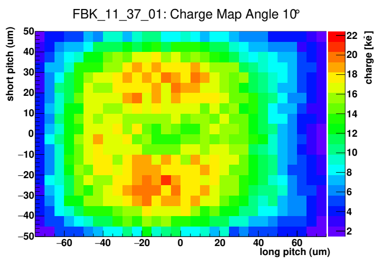

(b) Charge map at angle 10°.

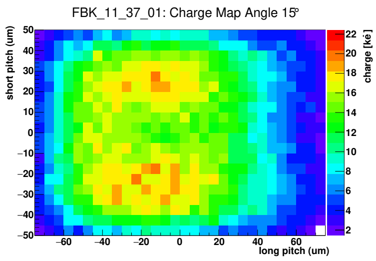

(c) Charge map at angle 15°.

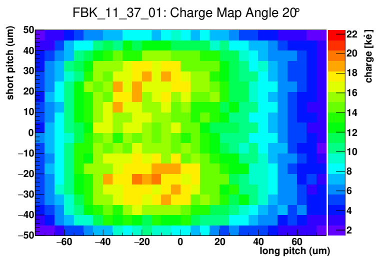

(d) Charge map at angle 20°.

Figure 4.37: Collected-charge maps at different angles after irradiation of 1×10^{15} n_{eq}/cm^2.

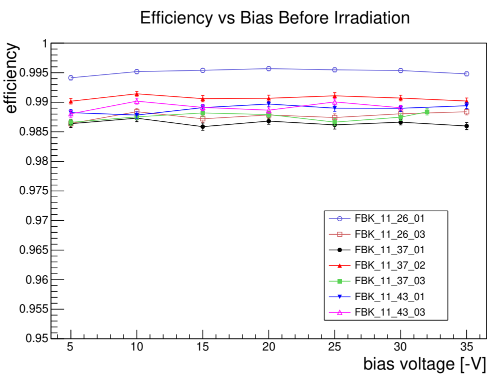

(a) Efficiency before irradiation.

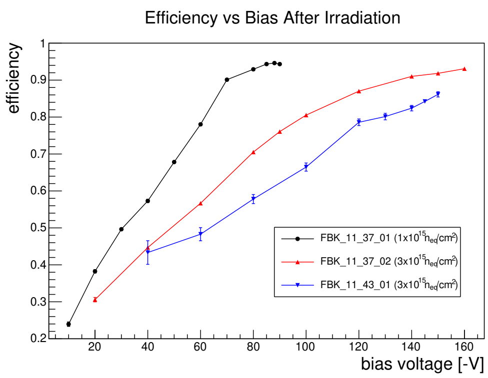

(b) Efficiency after irradiation.

Figure 4.38: Efficiency before and after irradiation vs bias at angle 0°.

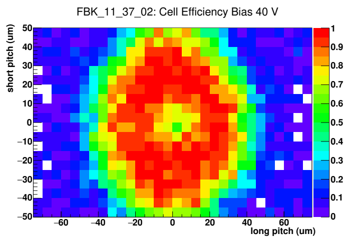

(a) Efficiency map at bias 40 V.

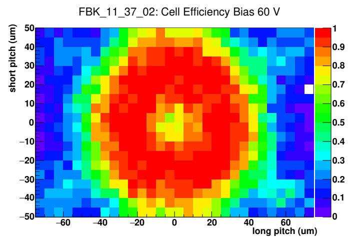

(b) Efficiency map at bias 60 V.

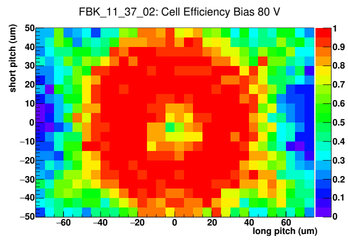

(c) Efficiency map at bias 80 V.

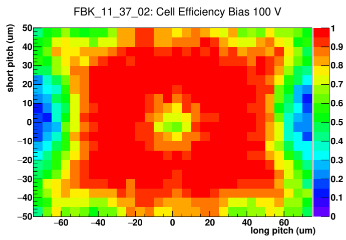

(d) Efficiency map at bias 100 V.

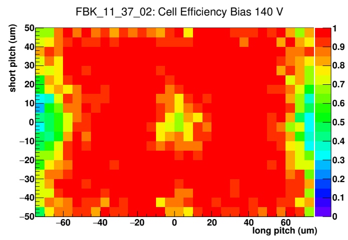

(e) Efficiency map at bias 140 V.

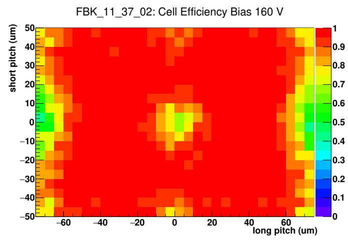

(f) Efficiency Map at bias 160 V.

Figure 4.39: Efficiency maps vs bias at angle 0° after irradiation of 3×10^{15} n_{eq}/cm^2.

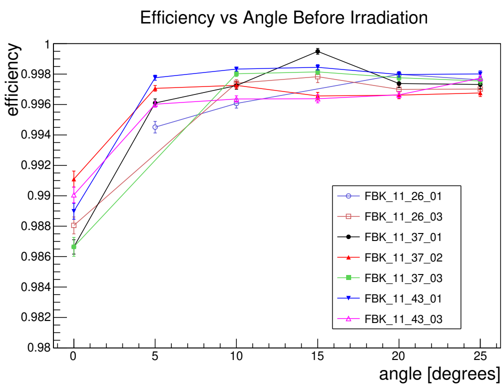

(a) Detector efficiency vs rotation angle.

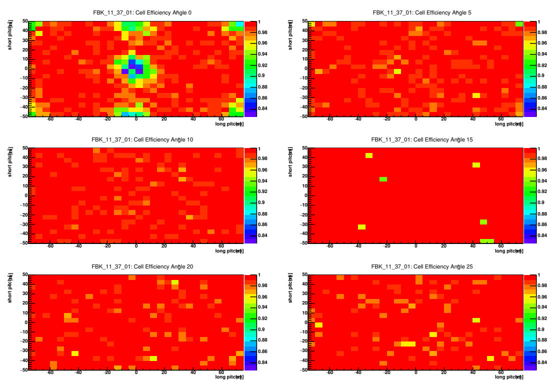

(b) FBK_11_37_01 pixel efficiency maps at different angles.

Figure 4.40: Detector efficiency and pixel efficiency maps before irradiation as a function of the rotation angle.

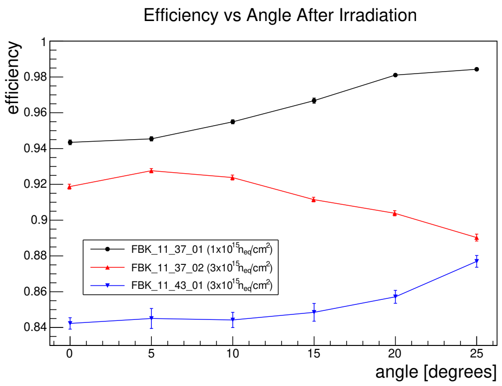

(a) Detector efficiency vs rotation angle.

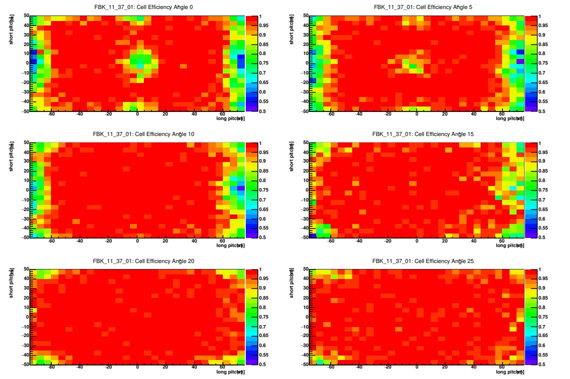

(b) FBK_11_37_01 pixel efficiency maps at different angles.

Figure 4.41: Detector efficiency and pixel efficiency maps after irradiation as a function of the rotation angle.

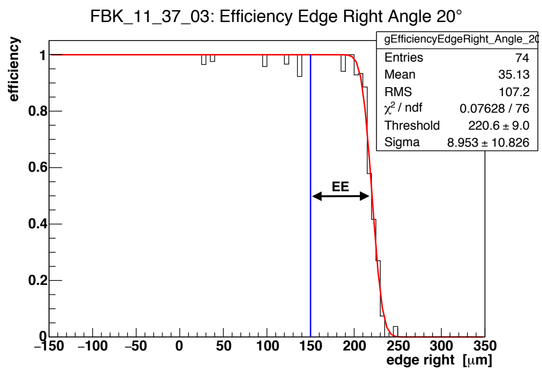

Figure 4.42: Edge efficiency. The vertical blue line indicates the geometrical border of the last pixel. EE indicates the size of the efficient edge.

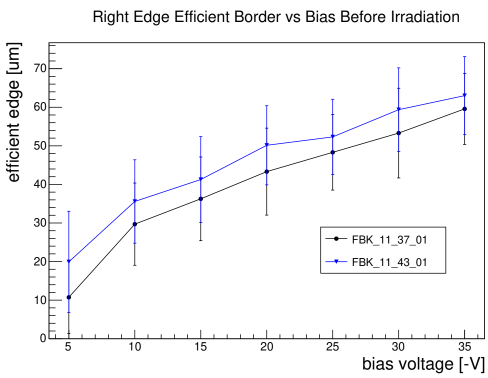

(a) Efficient edge (EE) vs bias before irradiation.

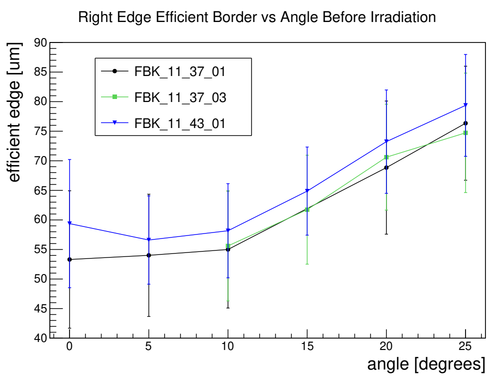

(b) Efficient edge (EE) vs angle before irradiation.

Figure 4.43: Efficient edge beyond the last-pixel geometrical border, shown as a function of the bias voltage and the rotation angle before irradiation.

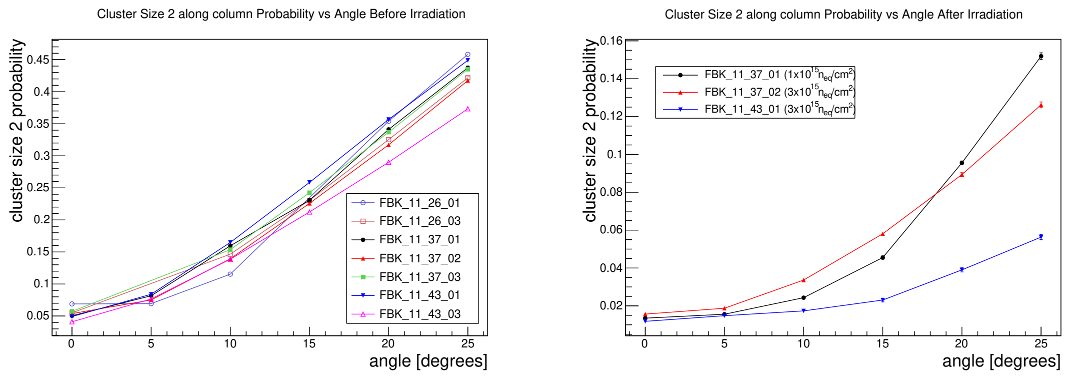

(a) Cluster size 2 probability before irradiation. (b) Cluster size 2 probability after irradiation.

Figure 4.44: Cluster size 2 probability before and after irradiation as a function of the rotation angle.

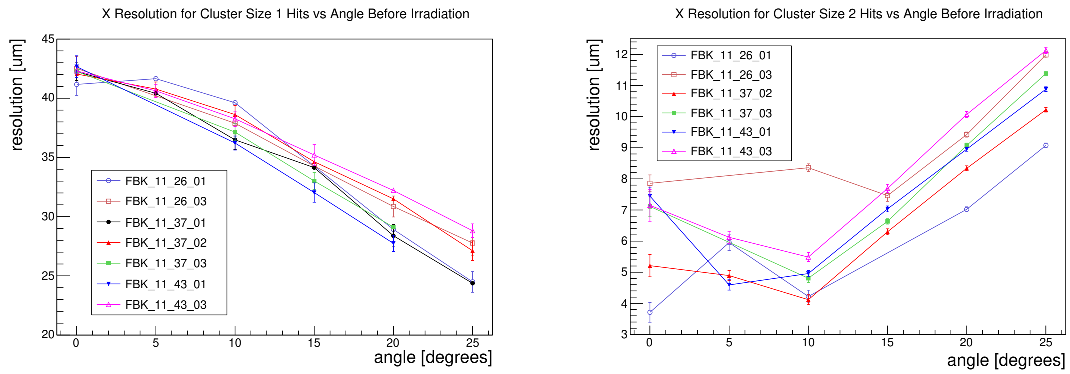

(a) Cluster size 1 resolution before irradiation. (b) Cluster size 2 resolution before irradiation.

Figure 4.45: Resolution for clusters of size 1 and 2 before irradiation.

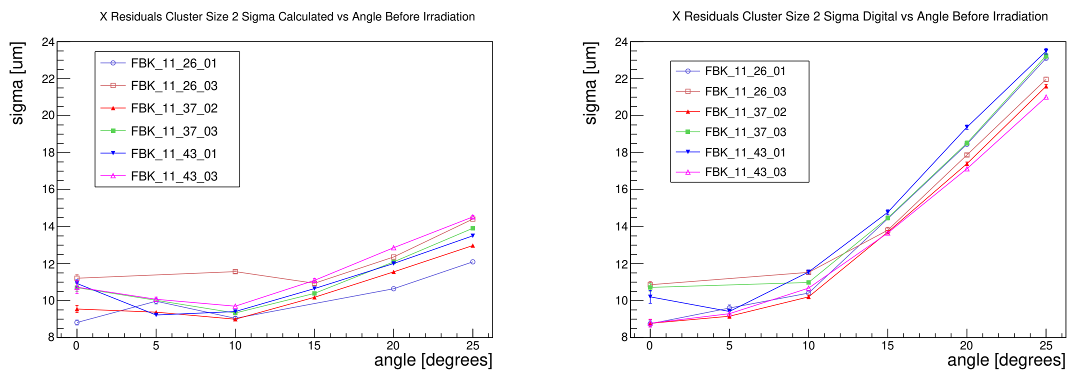

(a) Charge-asymmetry-calculated residuals. (b) Digital residuals.

Figure 4.46: Sigma of the gaussian obtained by fitting the cluster size 2 residuals evaluated with the charge asymmetry method (a) and the digital approximation (b).

4.6 CNM and SINTEF 3D sensors

The second beam test campaign on 3D sensors has been done on sensors designed by the Centro Nacional de Microelectrónica (CNM, Barcelona, Spain). In the same campaign also sensors from SINTEF (Trondheim, Norway) have been tested. Actually, SINTEF was not considered for producing the sensors for CT-PPS due to the unavailability of the production line. However, at the moment of the beam tests their sensors were the only ones available with two readout columns per pixel and it was decided to include them in the campaign.

Eight CNM and two SINTEF sensors were bump-bonded to the PSI46dig v2.1 version of the CMS digital ROC. Although this ROC was not yet suitable for the final detector, no problems were expected for the beam tests and, more important, the double column issue was solved. The bump-bonding deposition on the ROCs was done at RTI (Research Triangle Park, NC, U.S.A.) and they were flip-chipped to the sensors at X-ray Imatek (Barcelona, Spain).

Sensors for the flip-chip were selected based on the IV measurements by CNM that were acquired by placing the sensors with the UBM on a metal chuck and applying the bias voltage to the backside. This procedure does not guarantee that all the pixels are connected but it still gives an estimation of the breakdown voltage. Indeed, strong differences have been found between the IV curves measured by CNM and the ones measured in Torino after bump-bonding, and only 5 flip-chipped devices over 8 were selected for further tests.

Also the two SINTEF sensors have been chosen by looking at the IV curves measured with the temporary metallization. After wire-bonding, one of the sensors was unfortunately shorted. This has been attributed to the fact that it was wrongly chosen to use a conductive glue to attach the assembly to the board. Since SINTEF sensors are single-sided, the bias grid is on the surface close to the ROC. Moreover, the ROCs have been extracted from a wafer thinned down to 150 μm. Probably, some conductive glue overhang from the ROC and went in contact with the sensor, shorting it.

In the following sections, the results for these CNM and SINTEF detectors of laboratory and beam tests, before and after irradiation, are presented.

4.6.1 CNM and SINTEF 3D sensor characteristics

Both SINTEF and CNM sensors have been extracted from the wafers realized for the ATLAS IBL [127]. In both high resistivity p-type wafers, 3 single ROC sensors compatible with the PSI46 ROC layout are present in the bottom left corner of the wafer, as for the FBK ones. The layout is shown in Fig. 4.47. While the CNM and FBK sensors were finally selected for being installed in the ALTAS innermost pixel layer, production at SINTEF did not take place because of the low yield of the pre-production batches [114].

CNM sensors are produced with double-sided technology [132], with n-columns etched from the frontside (bump-bonding side) and p-columns from the backside. The schematic cross section of a CNM 3D sensor is shown in Fig. 4.48(a). Columns do not pass all through the silicon substrate but stop at a short distance from the opposiste surface. In particular, sensors are 230 μm thick (same thickness of the FBK ones) and the columns are 200 ± 10 μm deep. The insulation between n-type columns is provided by a p-stop implant.

Tested sensors have one readout column per pixel (1E layout) as shown in Fig. 4.48(b) and the ohmic electrodes have a configuration similar to the FBK one: one column at the pixel corners and an additional column in the middle of the long pitch to increase locally the electric field and improve the performances after irradiation.

Although CNM implemented for this ATLAS production a 3D guard ring that is grounded throughout the front-end chip [127], for the CMS sensors a column fence similar to the one in the FBK sensors has been adopted. The resulting slim edge has a dimension of 400 μm on the left and right sides and of 200 μm on top and bottom sides. The layout of the bottom left

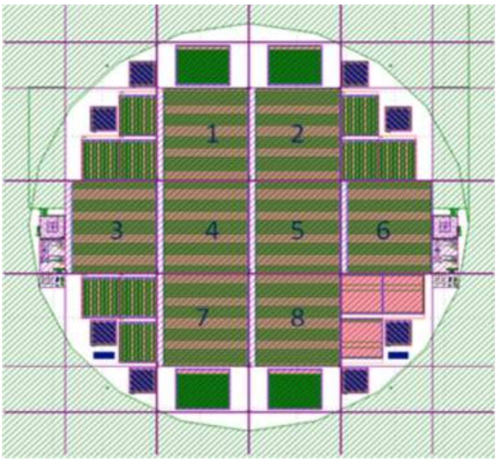

(a) CNM wafer layout [127].

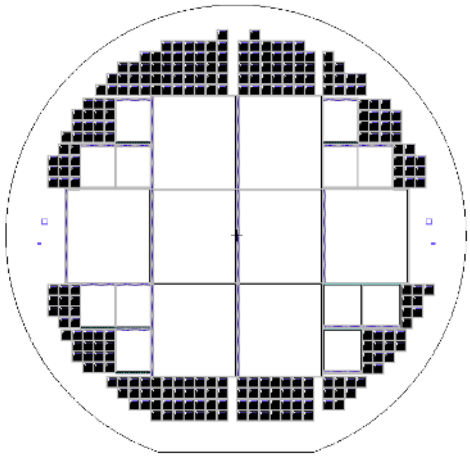

(b) SINTEF wafer layout.

Figure 4.47: Layout of the wafers from which the tested sensors have been extracted.

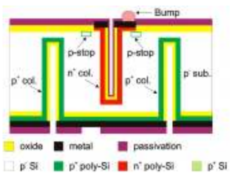

(a) CNM schematic cross section.

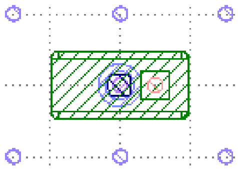

(b) CNM 3D 1E pixel layout.

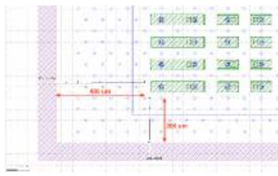

(c) CNM 3D sensor edge layout for the bottom-right corner in the convention used in this thesis.

Figure 4.48: Cross section, pixel electrode configuration and edge layout of the CNM 3D sensors under study.

corner of the sensor is shown in Fig. 4.48(c). Also in this case the edge pixels have a double dimension.

SINTEF sensors are produced is single-sided technology, meaning that both electrode types are etched from the front surface, which is the one facing the ROC. Sensors are 200 μm thick. The schematic cross section of the 3Ds produced at SINTEF is shown in Fig. 4.49(a). Columns are fully passing through the wafer and are completely filled with polysilicon to mitigate the geometrical inefficiency for perpendicular tracks, even if the polysilicon has a poor charge collection efficiency. The inter-pixel insulation is provided by a p-spray layer implanted on the two surfaces.

Tested SINTEF sensors have two readout columns per pixel (2E layout) as shown in Fig. 4.49(b). As a result, the pixel is composed by two elementary cells with an inter-electrode distance of 62.5 μm. This configuration is of particular interest after irradiation because the effect of trapping is expected to be less with respect to the 1E layout and at the same time the noise is not so high as for the 4E layout [126]. For this reason, also SINTEF sensors have been tested in the CT-PPS preparatory studies.

Thanks to the single-sided technology, SINTEF sensors implement active edges by means of etched trenches completely filled with p^+ doped polysilicon. Such technology requires a handler wafer oxide-bonded to the device wafer. In this particular case it was decided not to remove the handle wafer, in order to avoid this dangerous process. The active edge is implemented at 87 μm from the last n-type electrode (Fig. 4.49(c)) on three sensor sides: top, bottom and left. Since the single-sided technology implements the biasing grid on the surface facing the ROC,

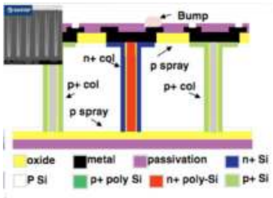

(a) CNM schematic cross section.

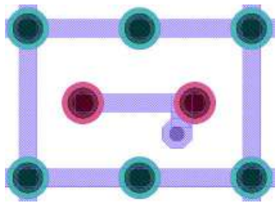

(b) SINTEF 3D 2E pixel layout.

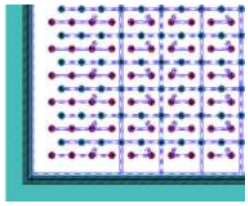

(c) SINTEF 3D sensors edge layout for the bottom-right corner in the convention used in this thesis.

Figure 4.49: Cross section, pixel electrode configuration and edge layout of the SINTEF 3D sensors under study.

Detector	Requested Fluence (p/cm^2)	Time In	Time out	Measured Fluence (n_{eq}/cm^2)
CNM_w8_d1 CNM_w8_d3 CNM_w7_d3	1.6×10^{15}	06/09/2015 13:58	08/09/2015 21:08	$0.77 \times 10^{15} \pm 7.0\%$
CNM_w4_d2 SINTEF_C2_CMS1	4.8×10^{15}	03/09/2015 19:40	13/09/2015 10:30	$2.3 \times 10^{15} \pm 7.0\%$

Table 4.2: Irradiation doses at the CERN IRRAD Proton Facility.

the right edge has instead an extension tab of ~ 1.5 mm to host the HV wire-bonding pad [133]. As for the CNM, edge pixels have double dimensions.

4.6.2 Irradiation at the CERN PS IRRAD Proton Facility

Detectors have been irradiated to fluences of 1×10^{15} n_{eq}/cm^2 and 3×10^{15} n_{eq}/cm^2 at the CERN IRRAD Proton Facility with 23 GeV/c protons. The corresponding dose is about 52 and 156 Mrad, respectively. To be irradiated the sample is placed on a shuttle table which allows the sensor positioning without accessing to the beam area. During the irradiation no cooling is applied and the samples are at room temperature.

The standard beam size is a gaussian with a full width half maximum (FWHM) of 12×12 mm^2. Differently from KIT, no beam scan is performed during the irradiation and this causes a non-uniform damage on samples of $\sim 1 \times 1$ cm^2 like the ones presented here. To evaluate the total fluence, a thin 1×1 cm^2 aluminum foil is mounted in front of the samples and after the irradiation it is measured how much it gets activated. Moreover, the beam profile is constantly measured by a 9×7 array of Beam Position Monitors (BPM), separated from each other by 4.5 mm. The full history of the irradiation is saved and it is accessible by the OP Webtool of CERN[3].

Three CNM detectors have been irradiated to 1×10^{15} n_{eq}/cm^2, and one CNM and one SINTEF to 3×10^{15} n_{eq}/cm^2. Table 4.2 shows the requested fluence in p/cm^2 (the hardness factor is 0.63), the starting and ending time of the irradiation, and the fluence measured with the aluminum foil.

In order to obtain the full history of the irradiation, a python script have been used to retrieve the full history of the irradiation from the BPM website. By merging the information from all the spills, the irradiation profiles for the two groups of samples can be obtained (Fig. 4.50). Since the BPMs do not provide a a reliable measurement of the absolute fluence, the plots have

[3] https://op-webtools.web.cern.ch/irrad/bpm.php

been normalized to the fluence measured from the aluminum foil activation. For doing that it has been made the reasonable assumption that the foil was centered on the reference axis of the BPMs.

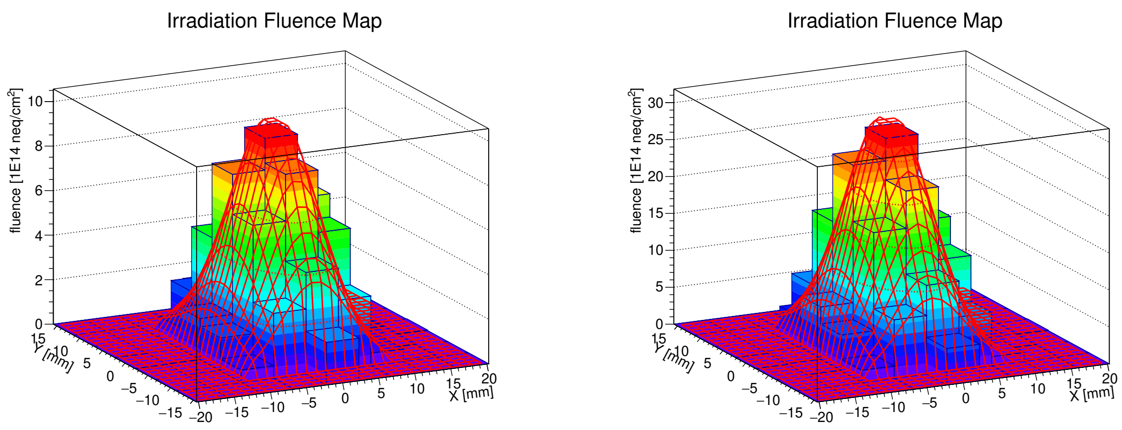

(a) Irradiation profile of the 1×10^{15} n_{eq}/cm^2 sample. (b) Irradiation profile of the 3×10^{15} n_{eq}/cm^2 sample.

Figure 4.50: Irradiation profiles for the two samples, extracted from the BPMs and normalized by the aluminum foil activation measurement.

The shape from the BPMs has been fitted using a double gaussian to model the beam profile. As one can observe from the fluence distribution plots, the target value is reached only in the center of the sample for both the irradiation classes, while at the edge of the device ($\pm$5 mm from the beam center) the dose reduces by $\sim$ 40%.

4.6.3 IV curves

Figure 4.51(a) shows the current-voltage curves before irradiation for the 5 CNM and 1 SINTEF sensors tested on beam. As expected, CNM sensors generally present a high breakdown of the order of 100 V or more already before irradiation, apart from sensor CNM_w8_d3 that has the breakdown at $\sim$ 30 V. For these sensors the current plateau is between 1 and 3 μA. The SINTEF sensor has the breakdown at $\sim$ 45 V and a leakage current ranging in the hundreds of nA.

After irradiation, IV curves in Fig. 4.51(b) are in linear scale to better highlight the dependence of the current increase on fluence. Curves were measured at -10°C in the Torino laboratory but since the beam tests were done at -20°C, the leakage current has been scaled to this temperature using the formula [134]

$$I(T_R) = I(T)\left(\frac{T_R}{T}\right)^2 \exp\left(-\frac{E_g}{2k_B}\left[\frac{1}{T_R}-\frac{1}{T}\right]\right) \tag{4.6.1}$$

where T_R is the reference temperature to which the current is scaled and T is the temperature at which it has been measured.

Thanks to the irradiation the breakdown voltage increased up to 90 V for the SINTEF and above 180 V for all the CNM sensors, including those that showed a low breakdown before irradiation.

4.6.4 Laboratory tests

All the detectors were measured in Torino before going to test beam. No particular issue has been found during the calibration procedure on unirradiated detectors. However, during the

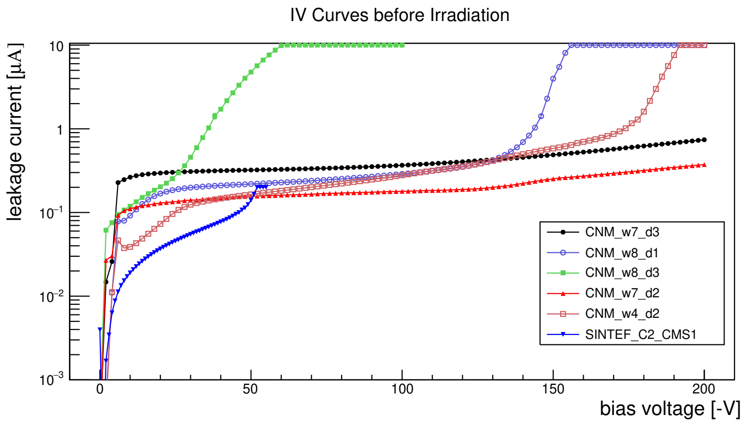

(a) IV curves before irradiation.

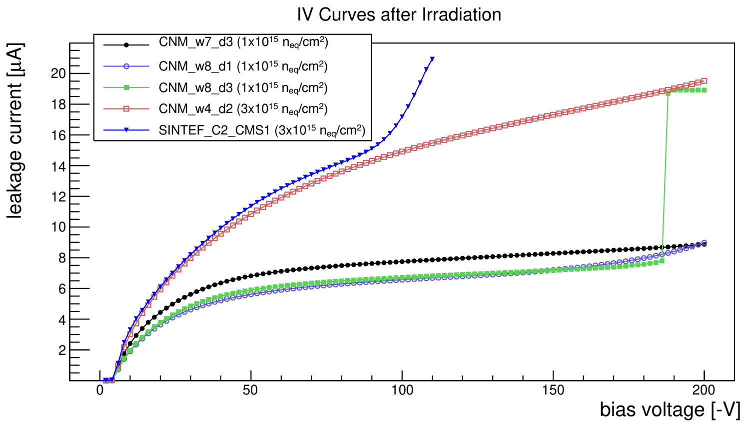

(b) IV curves after irradiation.

Figure 4.51: IV curves for CNM and SINTEF sensors before (a) and after (b) irradiation.

beam test a serious bump-bonding problem was spotted on the CNM_w7_d2 detector. The result of the bump-bonding test in laboratory and the hit map measured at the test beam are shown in Fig. 4.52. The bump-bonding test, done by injecting the calibration charge through the sensor and by measuring the threshold at which the signal is registered, should find a higher threshold for the not connected pixels with respect to the good ones, but in this case the bad bumps are not so evident. This issue occurred also for other sensors and it might be that the bump-bonding test algorithm, effective for the planar sensors, does not provide a reliable feedback for 3D sensors. For this reason, it was decided to qualify all the CT-PPS modules with X-rays to properly identify missing bump connections (see Sec. 5.4.2).

After irradiation several problems were found due to the non-uniformity of the delivered dose. Figure 4.53 shows two tornado plots for the same ROC, one of a little irradiated pixel and the other of a pixel near the peak of the deposited dose. According to the study on the beam-spot distribution, the difference in dose between the two pixels should be around 40%. The more irradiated pixel has a reduced range in which the threshold can work. Moreover, the left and right edges of the shape are less steep with respect to the edges of the less irradiated pixel, indicating that the amplifier stage is slower.

These two symptoms indicate that the analog current powering the more irradiated pixel is lower with respect to the target value. Unfortunately, no adjustment of the setting solved this problem. This is probably related to the fact that registers which can speed up the amplifier, mainly the analog currents or the amplifier stage feedbacks, are global values and hence a modification of this setting increases the speed also of the less irradiated pixels. It has been

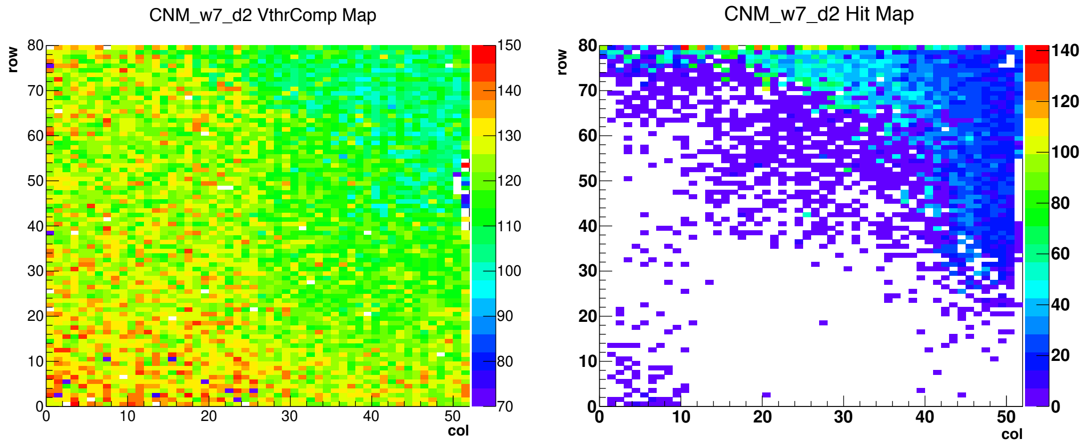

(a) Bump-bonding map.

(b) Hit map.

Figure 4.52: Bump-bonding map (a) and hit map (b) for CNM_w7_d2.

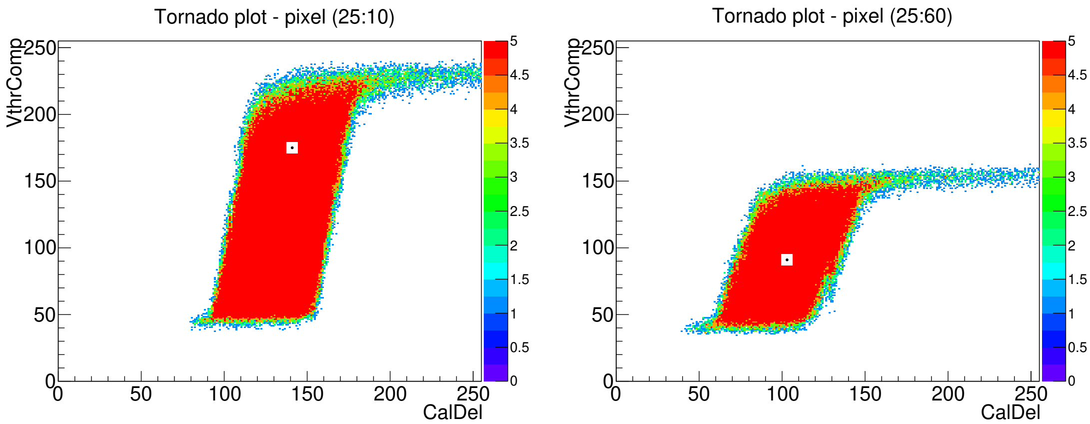

(a) Low irradiated pixel.

(b) High irradiated pixel.

Figure 4.53: Tornado plots for pixels of the same ROC with different irradiation dose.

excluded the hypothesis that the effect is related to 3D sensors since the same effect has been observed by Fermilab colleagues on planar devices. Since it is related to the readout chip only, it means that it depends on the deposited ionizing dose. This effect is particularly disturbing for the CT-PPS detectors since a highly non-uniform distribution of the irradiation is expected. Therefore, a deep investigation has been performed which will be presented in Sec. 5.5.

The resulting behaviour on the detector is that pixels that receive different irradiation doses acknowledge the hit at different times. The sketch of Fig. 4.54 shows that when a hit exceeds the threshold it is assigned to a certain time window. When the trigger signal arrives, the ROC looks into the buffer for hits acknowledged the exact number of WBC clock cycles before. Since the trigger signals need three clock cycles to be decoded, there is no way to retrieve hits belonging to adjacent bunch crossings.

In case of non-uniform irradiation, pixels may reply in different bunch crossings depending on the received dose. The result, shown in Fig. 4.54, is that selecting different WBC values one can trigger hits belonging to different areas of the ROC, but if the difference in irradiation is too high it is not possible to read all the pixels at the same time.

This has also consequences on the calibration of the ROC since it is not possible to include all the pixels in a single calibration step. In particular, trimming becomes problematic because

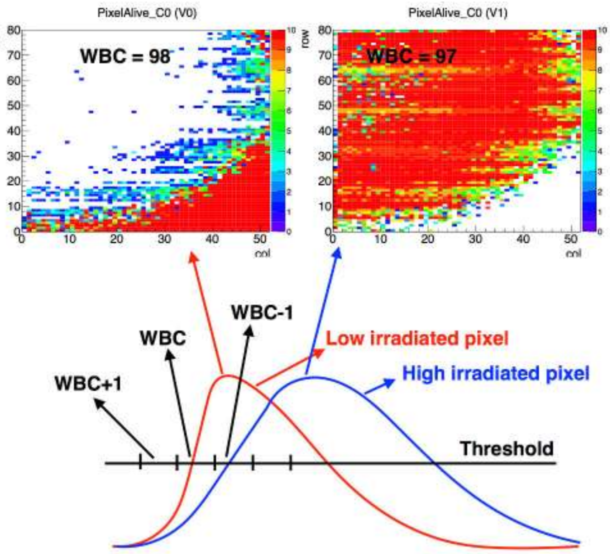

Figure 4.54: Effect of a non-uniform irradiation on the pixel amplifier and consequence on the pixel map.

the information of all the pixels is needed. It was finally decided to modify the trimming code in order to trim separately the two irradiated regions and merge offline the trim bits. For favouring the most irradiated part, the trim bits of the other region were increased by one DAC unit so to increase their threshold and avoid that the ROC became noisy in the less irradiated region, which is also less interesting for this study.

The ROC connected to the CNM_w8_d3 was probably damaged during the irradiation and it was not possible to set its global threshold and test it on beam.

4.6.5 Noise and threshold

As for the FBK sensors, the thresholds trimmed in laboratory were optimized at the test beam in order to lower them as much as possible, compatible with the noise. Although before irradiation the expected noise should be between 150 and 200 e^-, the CNM_w8_d1 and SINTEF_C2_CMS1 sensors showed a noise of 390 and 600 e^-, respectively. This required setting their threshold to a higher value ($\sim$ 4200 and $\sim$ 5400 e^-, respectively). Since no particular issue was found during the calibration in laboratory, which was repeated after the beam tests, this behavior is attributed to an incorrect setting of the ROC registers at the test beam.

After irradiation, the noise of the two devices has been measured to be between 170 and 240 e^-, with thresholds from 1600 and 2200 e^-, respectively.

4.6.6 Test beam results

In the following sections the results of the beam tests before and after irradiation are presented. Concerning the non-uniform irradiation issue, it is mitigated at the test beam by the fact that the clock of the FNAL telescope is longer with respect to the LHC clock. The telescope runs at 26 MHz, which is half of the Fermilab main injector frequency [135], and thus the time window in which a hit can be registered within the same bunch crossing is 38 ns instead of the 25 ns at the LHC. For the following results, only the region of the highly irradiated pixels is considered and pixels close to the transition regions are also excluded from the analysis.

Collected charge

Maps of the collected charge for a CNM sensor placed perpendicular to the beam are shown in Fig. 4.55. Saturation is reached at ~ 15 V. In the case of the SINTEF sensor, thanks to the shorter inter-electrode distance, saturation of the collected charge is reached earlier at ~ 10 V (Fig. 4.56).

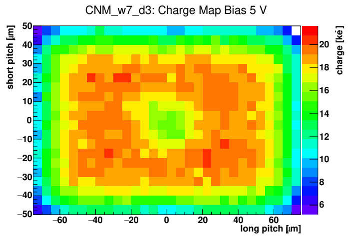

(a) Charge map at bias 5 V.

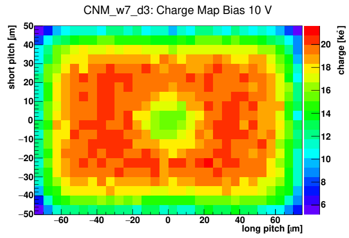

(b) Charge map at bias 10 V.

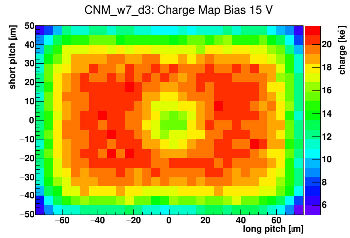

(c) Charge map at bias 15 V.

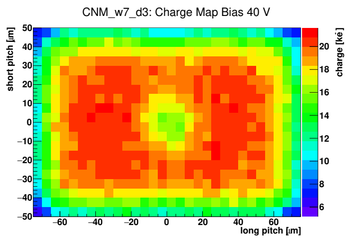

(d) Charge map at bias 40 V.

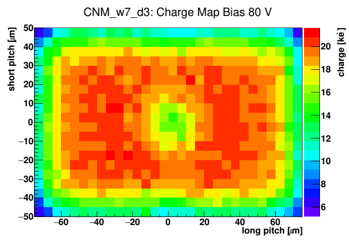

(e) Charge map at bias 80 V.

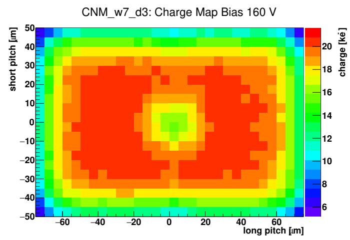

(f) Charge Map at bias 160 V.

Figure 4.55: Collected-charge maps vs bias at angle 0° for the CNM_w7_d3 sensor before irradiation.

While before irradiation the 2E pixel layout does not provide significant improvements, after irradiation a substantial difference is observed between the 1E and 2E configurations. In particular, the comparison between the 1E CNM device (Fig 4.57) and the 2E SINTEF one (Fig 4.58) shows that the 2E sensor starts to have a good charge collection in the entire pixel area at ~ 70 V while for the 1E sensor ~ 160 V are needed. However, thanks to the already high breakdown voltage before irradiation, CNM sensors can sustain these high values of bias voltage and can properly work after an irradiation of 3×10^{15} n_{eq}/cm^2.

It is also interesting to notice how the charge collection efficiency is higher in regions between electrodes of opposite doping type thanks to the higher electric field, with the consequence that in the center of the 2E layout a lower charge is collected. Nevertheless, this region is less critical than the edges of the pixel since it is not subject to charge sharing.

By measuring the collected charge, the position of the beam relative to the DUT can be estimated. The collected-charge map of the entire detector is fitted using a constant minus a rotated gaussian profile in order to reproduce the variation of the charge collection efficiency for different irradiation doses.

By using the center of the irradiation obtained by the fit and the irradiation profiles measured by the BPMs, it is possible to estimate the irradiation map of the detector.

A qualitative check of reconstructed position of the irradiation peak can be done by looking at the blackened shape on the backside of the detector board produced by the irradiation. The Pixel Alive using the DTB, the collected-charge map, the estimated dose profile from the fit, and the backside of the board are shown for the four irradiated detectors tested on beam in Figs. 4.59, 4.60, 4.61, and 4.62, respectively. On the last plot, the red square corresponds to the position of the active area of the detector and the orange ellipse to that of the fitted irradiation profile. Note that left and right are inverted with respect to the other plots.

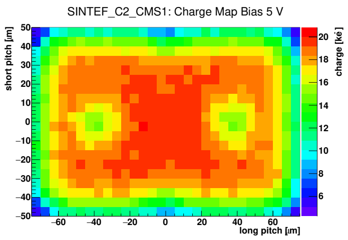

(a) Charge map at bias 5 V.

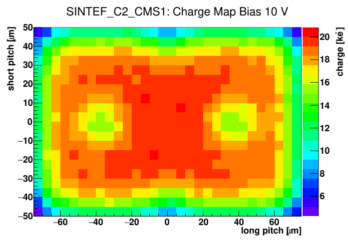

(b) Charge map at bias 10 V.

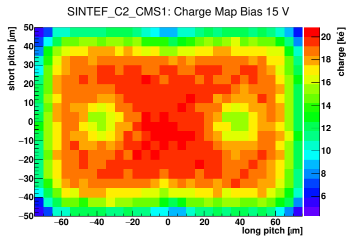

(c) Charge map at bias 15 V.

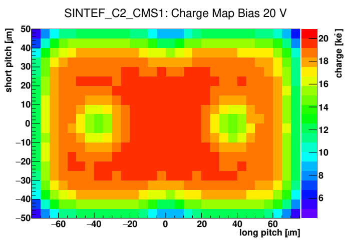

(d) Charge map at bias 20 V.

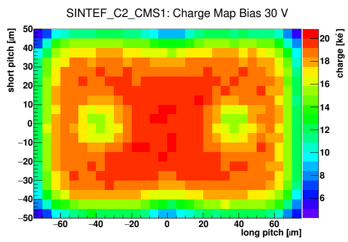

(e) Charge map at bias 30 V.

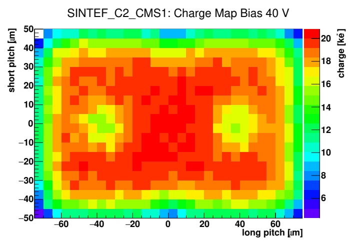

(f) Charge Map at bias 40 V.

Figure 4.56: Collected-charge maps vs bias at angle 0° for the SINTEF_C2_CMS1 sensor before irradiation.

From these studies on the irradiation profile it is possible to roughly determine the dose range in which all pixels can register the hit in the same bunch crossing. The results indicate that pixels with an irradiation down to 50% of the maximum can be read out in the same 25 ns time window of the most irradiated one.

With the reasonable assumption that the proton beam of the CERN IRRAD Facility is monochromatic, the ratio in fluence also represents the ratio in ionizing dose, which is actually causing the modification of the ROC behaviour. Since the detector active region in the same time window is inside the $\sim$ 50% profile of the irradiation peak for both fluences, it can be expected that the time shift is linear with the dose.

Although this method gives an estimate of the non-uniform irradiation effect, it is subject to the uncertainties of the charge map and the profile fits and a more controlled study has been later performed to address this critical issue for the functioning of the ROC in the CT-PPS conditions (see Sec. 5.5).

Efficiency

Figure 4.63 shows the efficiency of the CNM and SINTEF detectors, before and after irradiation, as a function of the bias voltage. Before irradiation, the efficiency saturates at $\sim$ 15 V and its maximum strongly depends on the threshold. For this reason, the CNM_w8_d1 and SINTEF_C2_CMS1 efficiency of $\sim$ 96% is slightly lower than for other detectors, which are above 98%.

After irradiation, both devices irradiated to 10^{15} n_{eq}/cm^2 reach the plateau at $\sim$ 70 V. Instead, for the detectors irradiated to 3×10^{15} n_{eq}/cm^2 a big difference is found in their behaviour depending on the number of readout electrodes per pixel. Despite the fact that the bias voltage for the SINTEF sensor could not exceed 80 V, a steeper increase of the efficiency as a function of the bias can be clearly seen when comparing to the 1E CNM sensor irradiated to the same fluence (CNM_w4_d2).

Pixel efficiency maps after irradiation as a function of the bias voltage are shown in Fig. 4.64 and 4.65 for the CNM_w4_d2 and SINTEF_C2_CMS1, respectively. The behaviour of the 1E detector is similar to the one found for the FBK sensors, with the growing of the efficient

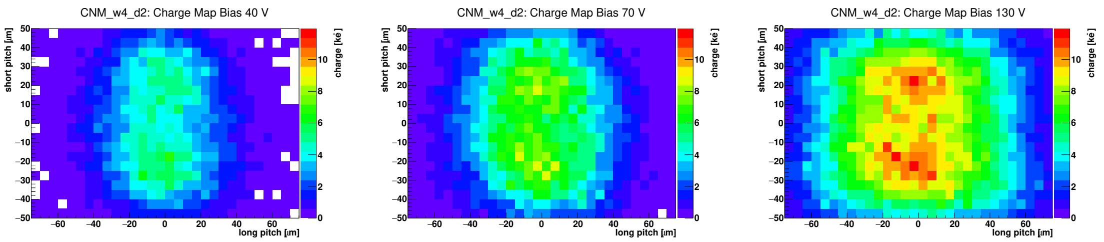

(a) Charge map at bias 40 V. (b) Charge map at bias 70 V. (c) Charge map at bias 130 V.

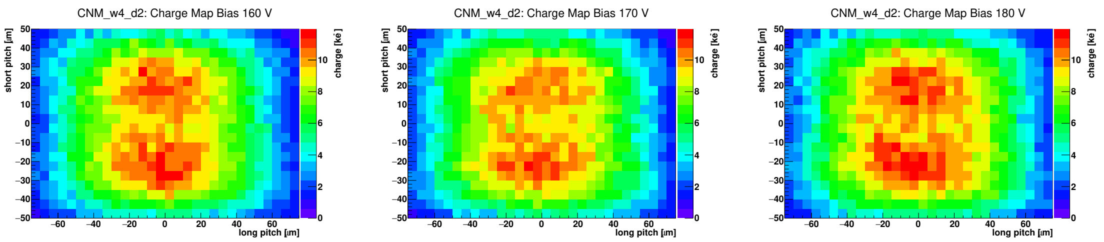

(d) Charge map at bias 160 V. (e) Charge map at bias 170 V. (f) Charge Map at bias 180 V.

Figure 4.57: Collected-charge maps vs bias at angle 0° for the CNM_w7_d3 sensor after a fluence of 3×10^{15} n_{eq}/cm^2.

area around the readout electrode. The 2E SINTEF shows already at low voltages a higher efficiency in correspondence to the ohmic contacts, which means that the electric field is high enough for collecting holes and inducing a signal above the threshold.

Figures 4.66 and 4.67 show the detector efficiency as a function of the rotation angle before and after irradiation, respectively. Before irradiation, the three detectors with lower threshold recover from the electrode geometrical inefficiency already at 5°, while the other two, because of the higher threshold, need to be tilted to $10 - 15°$. After irradiation, a bigger rotation is needed to recover the inefficiency of the corner electrodes.

Edge efficiency

As explained in Sec. 4.5.6, it is possible to evaluate the efficient edge by measuring the efficiency beyond the geometrical border of the edge pixels. The plots in Fig. 4.68 show this value for the four sensor edges.

For the CNM detectors, the efficiency can extend on the left and right edges, which are the interesting ones, up to 100 μm before saturating. The value strongly depends on the threshold applied at the edge pixels, which having double dimension are more difficult to trim to the target threshold.

It is interesting to compare these results with the those obtained by the ATLAS Forward Physics (AFP) group on CNM sensors bump-bonded to the FE-I4 ROC [136]. The ATLAS CNM sensors have a 3D guard ring surrounding the sensitive area and connected to ground. Due to this structure, the depletion region is contained and the measured extension of the efficient edge is a few μm only. This indicates that the column fence layout should be strongly preferred for the CT-PPS detectors.

The SINTEF sensor has active edges on top, bottom and right sides. Considering that the active edge is implemented at 87 μm from the last n-electrode, the measured values correspond to the expected ones. It is also worth noticing that the complete active edge depletion is already reached at 10 V. The left edge has an extension tab for the bias pad and the efficient edge can reach in this case 90 μm.

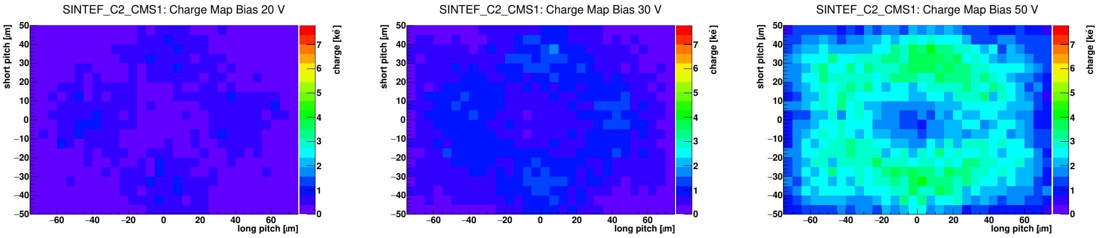

(a) Charge map at bias 20 V. (b) Charge map at bias 30 V. (c) Charge map at bias 50 V.

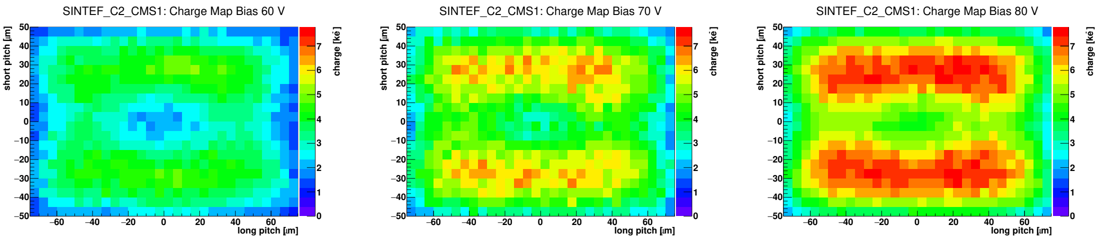

(d) Charge map at bias 60 V. (e) Charge map at bias 70 V. (f) Charge Map at bias 80 V.

Figure 4.58: Collected-charge maps vs bias at angle 0° for the SINTEF_C2_CMS1 sensor after a fluence of 3×10^{15} n_{eq}/cm^2.

Resolution

Figure 4.69 shows the cluster size 2 probability as a function of the rotation angle before and after irradiation, which in both cases increases due to geometrical reasons. Before irradiation, a large dependence on the threshold is measured and therefore it is not possible to evaluate a difference between 1E and 2E configuration. After irradiation, considering the two sensors at 3×10^{15} n_{eq}/cm^2, a large improvement of the cluster size 2 probability can instead be seen for the 2E (SINTEF_C2_CMS1) with respect to the 1E (CNM_w4_d2) configuration.

In Fig. 4.70 the resolutions for clusters of size 1 and 2 along the long pitch direction are shown for the unirradiated devices. In the case of clusters of size 1, the dependence on the threshold is strong. For clusters of size 2 the results are not so clear. Considering only the sensors with a threshold close to the target one of this readout chip, it is possible to estimate the resolution at 20°, which is approximately the tilting angle of CT-PPS. In this condition, the resolution is ~ 27 μm and ~ 10 μm for clusters of size 1 and 2, respectively.

After irradiation the electric field at the edges of the pixel is not strong enough to guarantee a large region of charge sharing, even when tilting the detector, as can be also observed from the cluster size 2 probability plot. As a result, the resolution for clusters of size 1 is not strongly dependent on the tilting angle (Fig. 4.71(a)). For the same reason and for the fact that only a fraction of the pixels has been considered in the analysis because of the non-uniform irradiation issue, the fit of the charge asymmetry can be done over a limited amount of data, which leads to a worse resolution for clusters of size 2 with respect to that evaluated before irradiation (Fig. 4.71(b)).

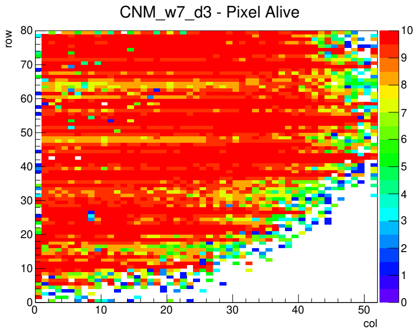

(a) Pixel Alive map in laboratory.

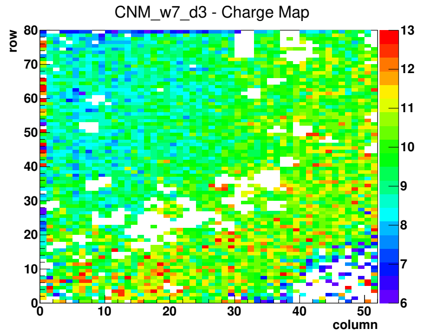

(b) Collected-charge map (ke$^-$) measured at the test beam.

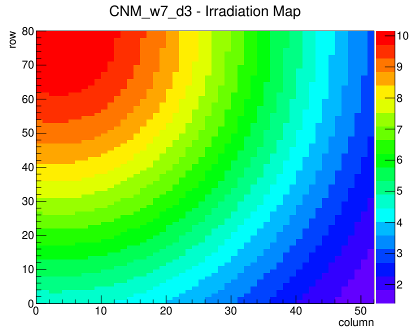

(c) Irradiation map in 10^{14} n_{eq}/cm^2.

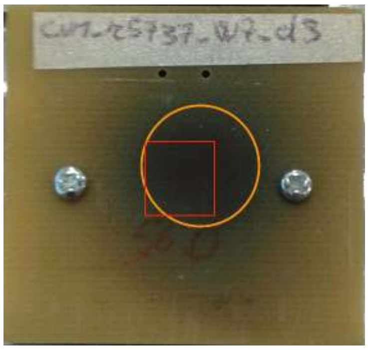

(d) Blackening of the carrier board.

Figure 4.59: Study of the irradiation profile for the detector CNM_w7_d3.

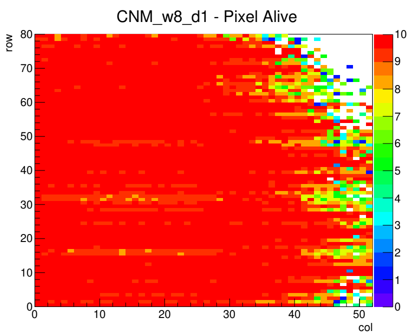

(a) Pixel Alive map in laboratory.

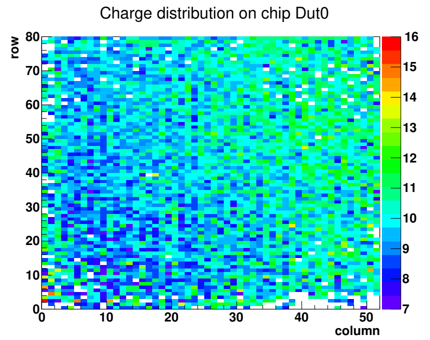

(b) Collected-charge map (ke$^-$) measured at the test beam.

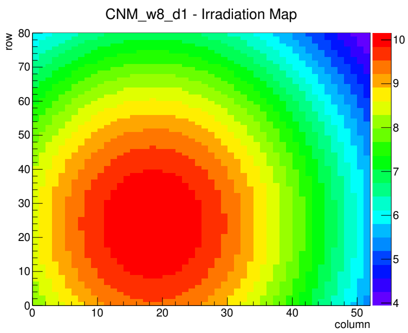

(c) Irradiation map in 10^{14} n_{eq}/cm^2.

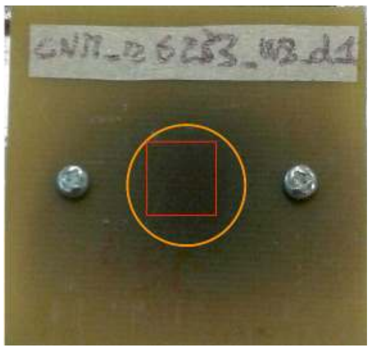

(d) Blackening of the carrier board.

Figure 4.60: Study of the irradiation profile for the detector CNM_w8_d1.

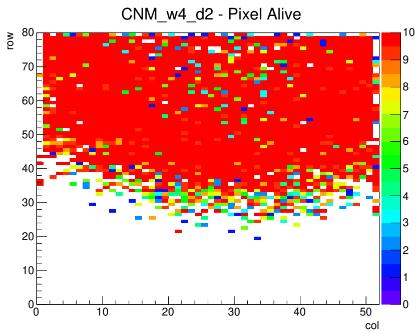

(a) Pixel Alive map in laboratory.

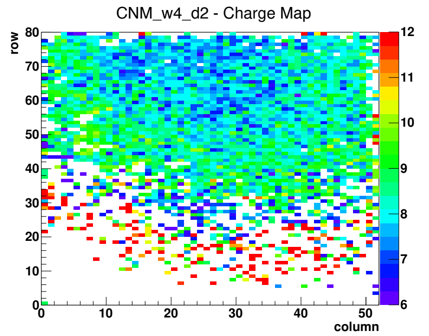

(b) Collected-charge map (ke^-) measured at the test beam.

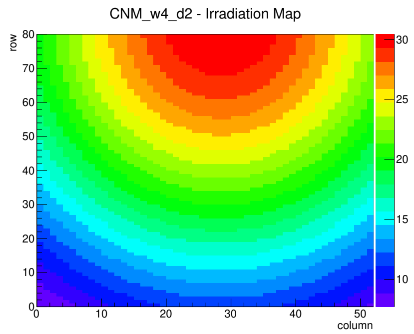

(c) Irradiation map in 10^{14} n_{eq}/cm^2.

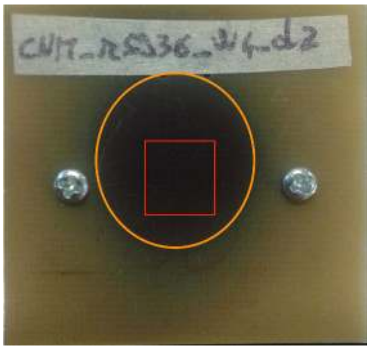

(d) Blackening of the carrier board.

Figure 4.61: Study of the irradiation profile for the detector CNM_w4_d2.

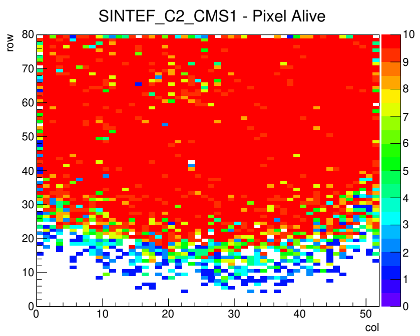

(a) Pixel Alive map in laboratory.

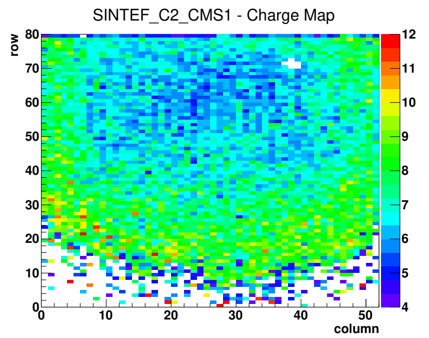

(b) Collected-charge map (ke^-) measured at the test beam.

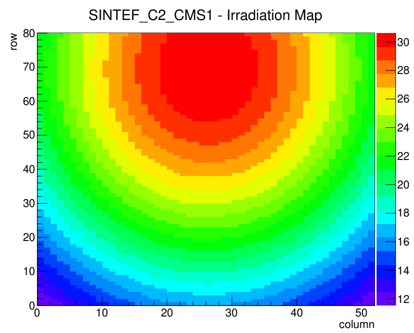

(c) Irradiation map in 10^{14} n_{eq}/cm^2.

(d) Blackening of the carrier board.

Figure 4.62: Study of the irradiation profile for the detector SINTEF_C2_CMS1.

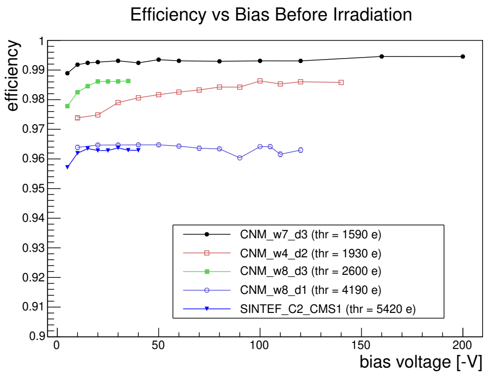

(a) Efficiency before irradiation.

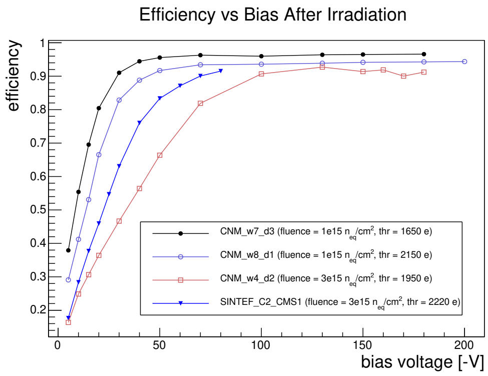

(b) Efficiency after irradiation.

Figure 4.63: Efficiency of the CNM and SINTEF sensors.

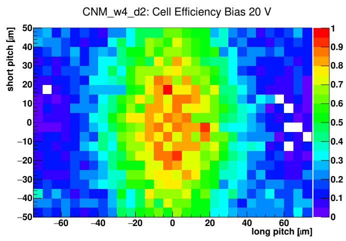

(a) Efficiency map at bias 20 V.

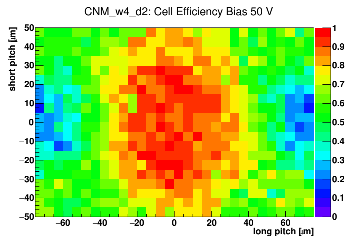

(b) Efficiency map at bias 60 V.

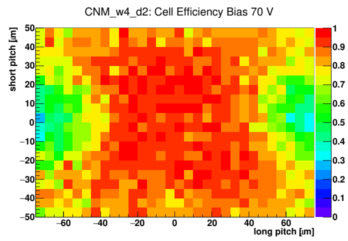

(c) Efficiency map at bias 80 V.

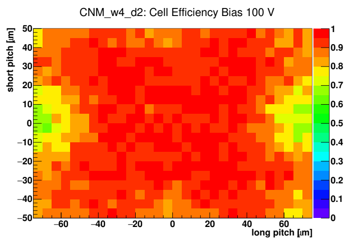

(d) Efficiency map at bias 100 V.

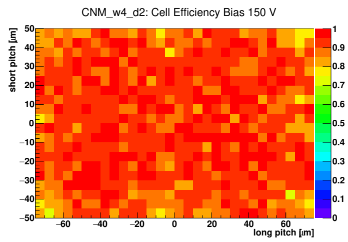

(e) Efficiency map at bias 150 V.

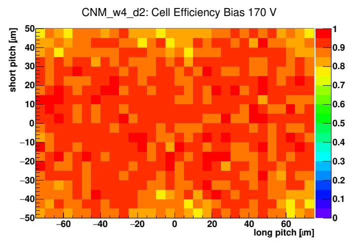

(f) Efficiency Map at bias 170 V.

Figure 4.64: 1E CNM efficiency maps vs bias at angle 0° after irradiation to 3×10^{15} n_{eq}/cm^2.

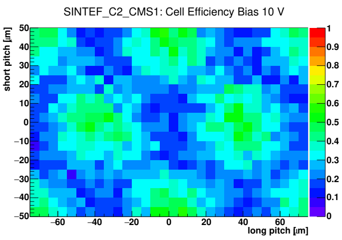

(a) Efficiency map at bias 10 V.

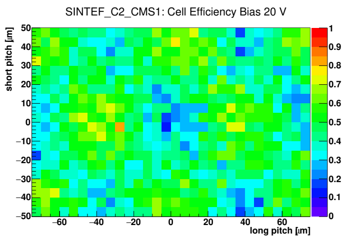

(b) Efficiency map at bias 20 V.

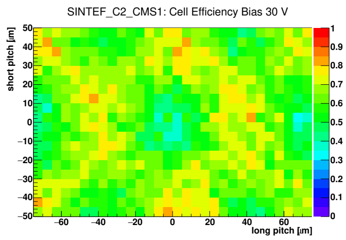

(c) Efficiency map at bias 30 V.

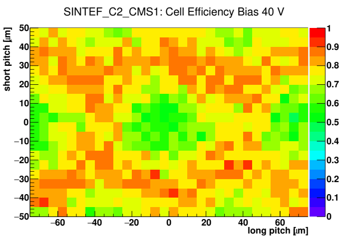

(d) Efficiency map at bias 40 V.

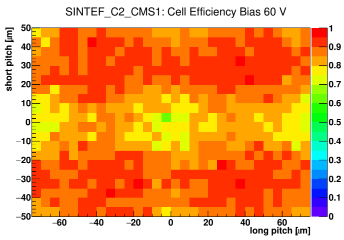

(e) Efficiency map at bias 60 V.

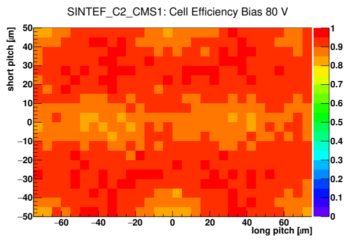

(f) Efficiency Map at bias 80 V.

Figure 4.65: 2E SINTEF efficiency maps vs bias at angle 0° after irradiation to 3×10^{15} n_{eq}/cm^2.

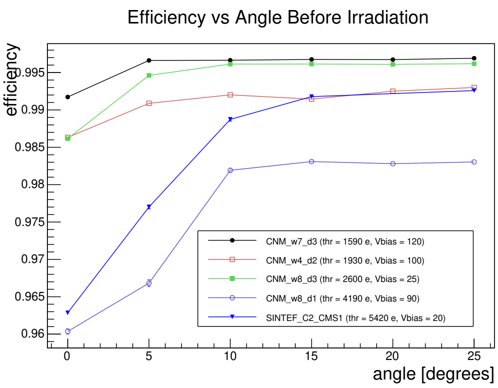

(a) Detector efficiency vs rotation angle.

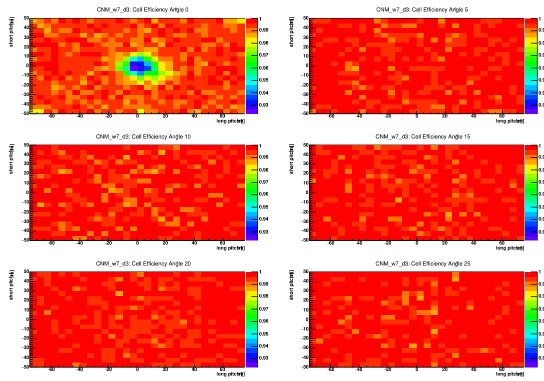

(b) CNM_w7_d3 pixel map efficiency at different angles.

Figure 4.66: Detector and pixel map efficiency before irradiation as a function of the rotation angle.

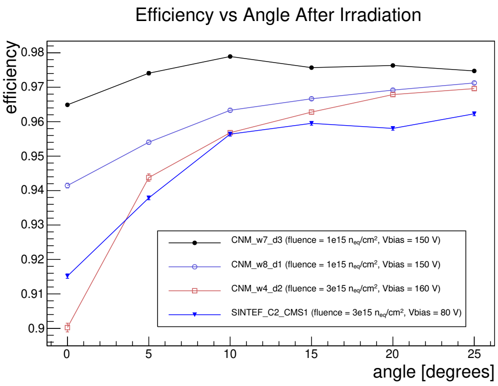

(a) Detector efficiency vs rotation angle.

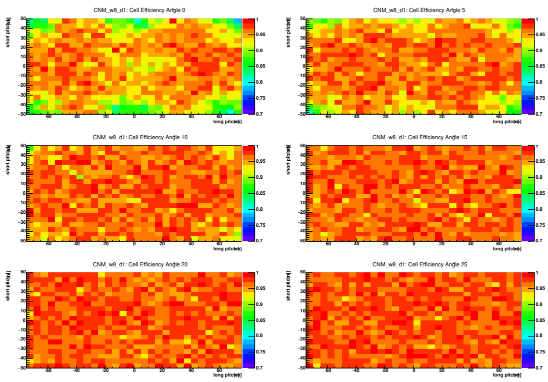

(b) CNM_w8_d1 pixel map efficiency at different angles.

Figure 4.67: Detector and pixel map efficiency after irradiation as a function of the rotation angle.

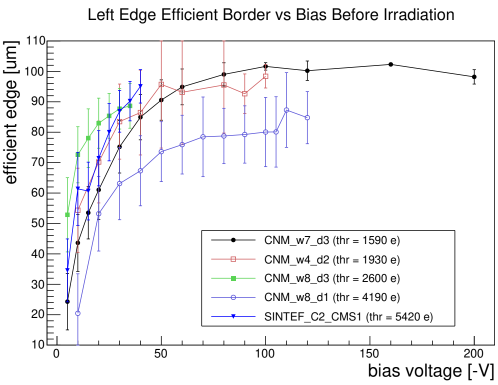

(a) Efficient left edge.

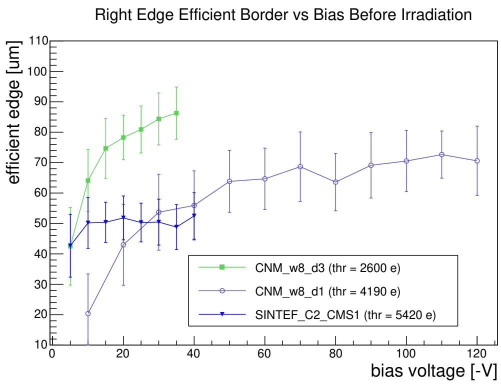

(b) Efficient right edge.

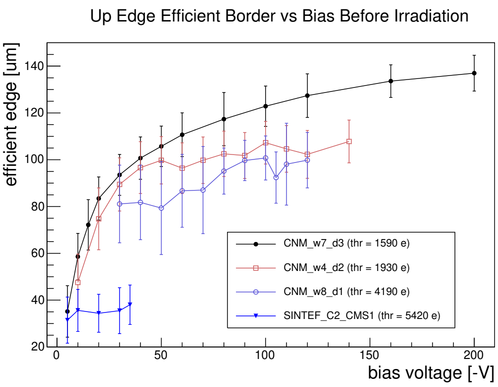

(c) Efficient top edge.

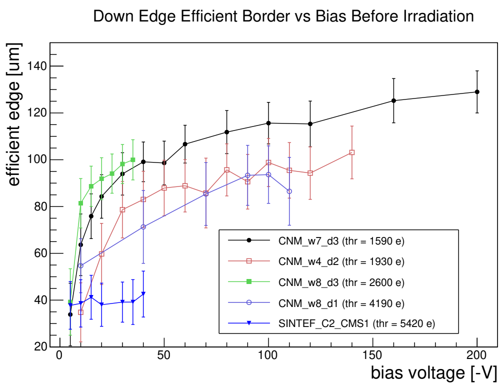

(d) Efficient bottom edge.

Figure 4.68: Efficient edges beyond the last-pixel geometrical border as a function of the bias voltage before irradiation.

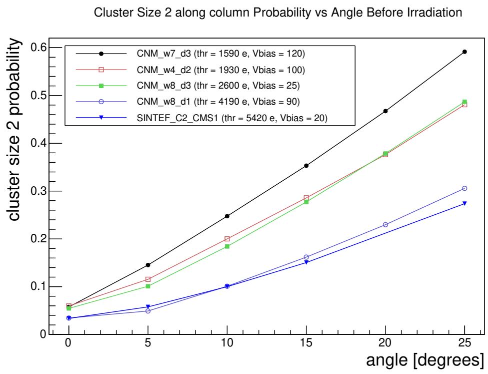

(a) Cluster size 2 probability before irradiation.

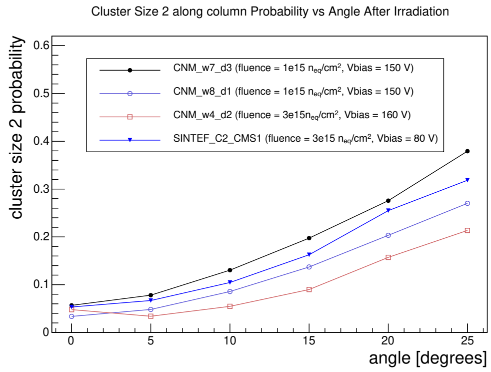

(b) Cluster size 2 probability after irradiation.

Figure 4.69: Cluster size 2 probability before and after irradiation as a function of the rotation angle.

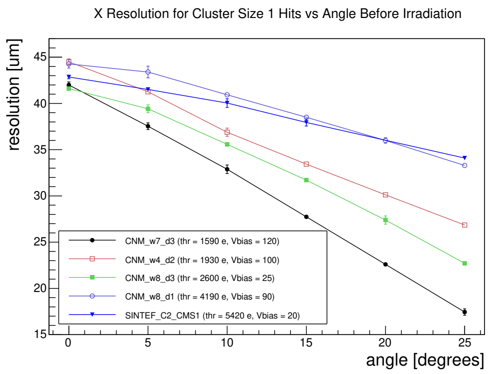

(a) Cluster size 1 resolution before irradiation.

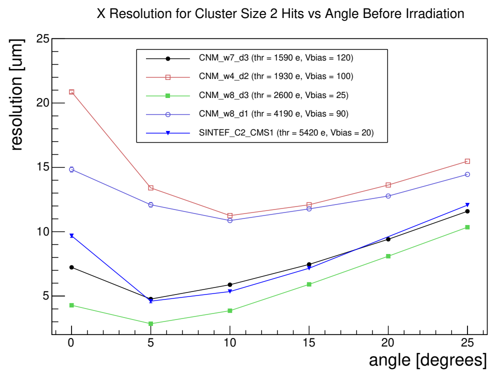

(b) Cluster size 2 resolution before irradiation.

Figure 4.70: Resolution for clusters of size 1 and 2 before irradiation.

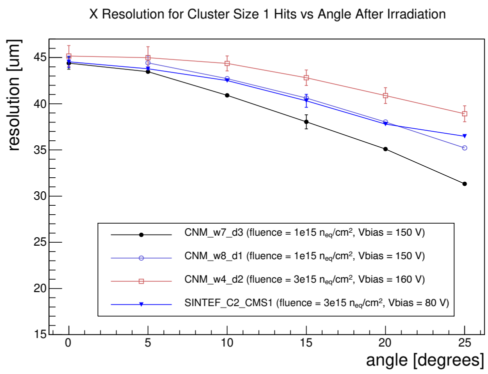

(a) Cluster size 1 resolution after irradiation.

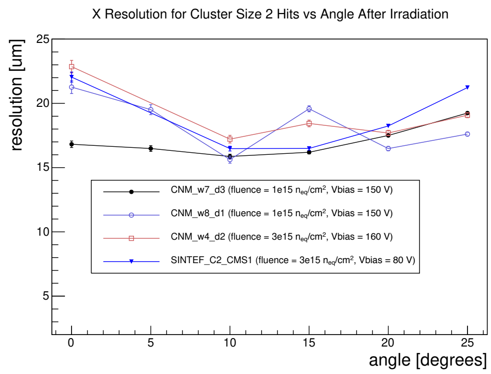

(b) Cluster size 2 resolution after irradiation.

Figure 4.71: Resolution for clusters of size 1 and 2 after irradiation.

4.7 Comparison between FBK and CNM sensor results

The test beam and irradiation campaigns presented in this chapter allowed the qualification of 3D sensors as baseline choice for the CT-PPS pixel tracking detector.

The results presented for CNM and FBK sensors before irradiation do not indicate a preference of one of the two technologies in terms of performance. In particular, both of them reach the full efficiency at very low bias voltages ($10-15$ V) and the geometrical inefficiency of the hollow columns can be restored by tilting the sensor less then 10°, which is compatible with the detector positioning in the CT-PPS pots. Also the resolution (~ 25 μm for clusters of size 1 and ~ 10 μm for clusters of size 2) and cluster size 2 probability ($\sim 35\%$) are comparable for the two types of sensors and meet the requirements. The only difference is represented by the extension of the efficient region towards the sensor edge, which in the CNM sensors is more pronounced. However, this is not due to a different edge structure, which is identical, but to the much higher breakdown of these CNM sensors, which instead is limited for this particular FBK production.

While before irradiation the low breakdown only reduces the extension of the efficient edge, after irradiation it is a critical limitation for the CT-PPS data taking. In fact, because of the non-uniform irradiation, part of the sensor will require at a certain point a higher bias voltage to be properly operated and this will cause the rest of the sensor to go into breakdown, if too low. The low breakdown of this production has been addressed by FBK and this limitation could be solved in a later production [137].

Also the results for the irradiated sensors do not show a clear preference between the two technologies. In the case of the FBK detectors, the irradiation at KIT provided a larger dose on the ROCs, making more difficult their optimization. In particular, their threshold is higher with respect to the CNM one, and this explains why a few more tens of Volts are required to obtain comparable efficiency maps.

An effective improvement after irradiation has been only observed with the 2E configuration of the SINTEF sensor, indicating that this layout should be preferred in the CT-PPS conditions. However, as already pointed out, SINTEF was not able to guarantee the production.

The upgrade of the FBK production line from 4" to 6" wafers, which interfered with the CT-PPS schedule, eventually drove the choice and CNM was selected for producing the CT-PPS modules.

Chapter 5

Pixel modules for CT-PPS

This chapter describes the production of the 3D pixel modules for the CT-PPS project.

In the first part, the characteristics of the sensors optimized for this application are presented. Two batches of twelve wafers each were fabricated by CNM and the results of the sensor qualification are reported.

To certify the production, a test beam campaign was carried out on single-chip modules from the final wafers and the results are discussed.

The last section of the chapter presents the non-uniform irradiation studies done with X-rays to further investigate the issue showed by the PSI46dig ROCs after the irradiation at the CERN IRRAD Proton Facility (Sec. 4.6.2).

5.1 3D sensor production at CNM

The production by CNM of the CT-PPS 3D pixel sensors started in spring 2015 and was divided in two batches of 12 wafers each. The sensor design was also done at CNM.

5.1.1 Sensor characteristics

The 3D sensors fabricated by CNM for CT-PPS are double-sided, with non-passing-through columns, as the ones tested during the preparatory studies presented in the previous chapter. The used wafers are 4" p-type Float Zone, high-resistivity, $< 100 >$ silicon crystal wafers. The silicon substrate is 230 μm thick and the columns are 200 μm deep with a diameter of 10 μm.

The layout of the wafer is shown in Fig. 5.1(a). Two pixel configurations have been chosen for the CT-PPS production, with one (1E, Fig. 5.1(b)) and two (2E, Fig. 5.1(c)) readout columns. Due to the shorter inter-electrode distance, 2E sensors ensure better performance after irradiation but their expected yield is lower because of the higher column density. For this reason, 1E sensors were included in the wafer layout as backup solution, choosing the configuration with ohmic columns located only in the pixel corners and no electrode implemented in the middle of the long pitch side.

The module sizes implemented in the wafer are listed in Tab. 5.1. The module dimension is expressed in terms of number of bump-bonded ROCs. The baseline detector foresees the use of 2×3 sensors, read out by 6 ROCs, but the electronics is also compatible with 2×2 modules. Each wafer also contains 2×1 modules, single-chip modules, and diodes for testing purposes.

Sensors have a 200 μm slim edge made with a p-doped column fence, as shown for the two different configurations in Fig. 5.2. It should be noticed that edge pixels are not of double dimensions as for the previously tested sensors. This is due to the fact that in CT-PPS most of the tracks will be close to the sensor edge facing the beam and smaller pixels allow to reduce the occupancy and improve the resolution. According to the PSI46dig designers, the

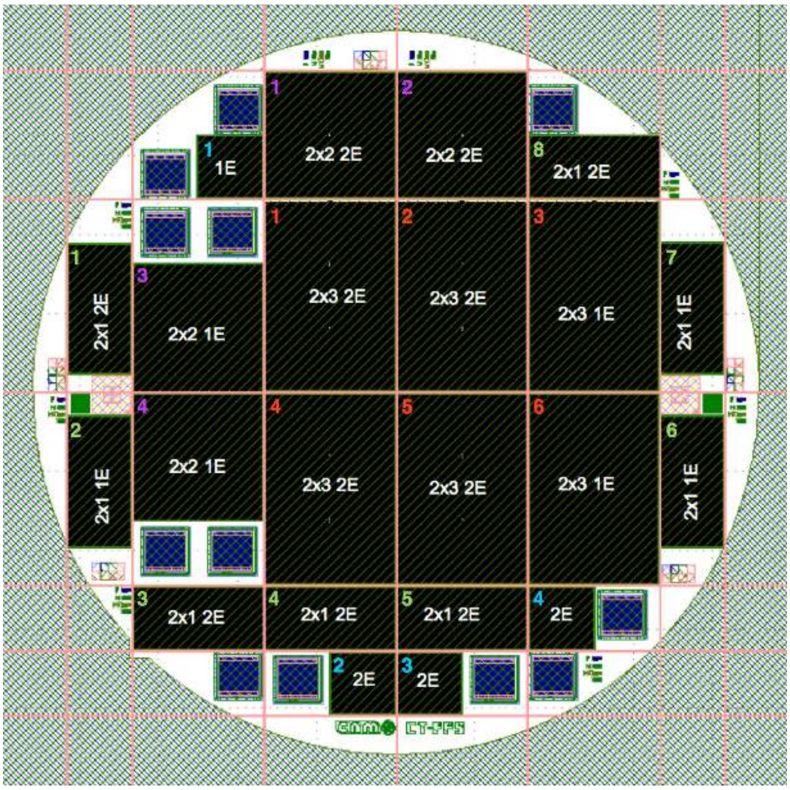

(a) Wafer layout for the CT-PPS 3D sensors produced at CNM.

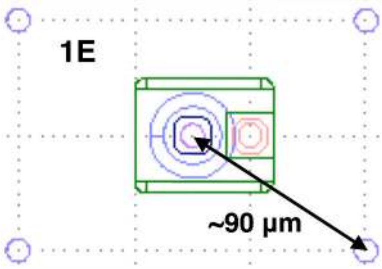

(b) 1E pixel layout.

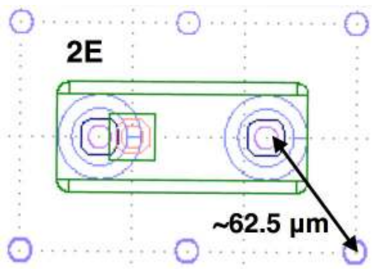

(c) 2E pixel layout.

Figure 5.1: CNM 3D sensors produced for CT-PPS.

ROC functionality should not be affected by this change of the sensor pixel size and therefore capacitance.

Dimensions of the pixels located inside the sensor module at the border of two different ROCs could not be changed, in order to preserve enough space for bump-bonding the ROCs. Fig. 5.3 shows the sensor layout in correspondence of the corner between four ROCs. While in the case of the 1E configuration the pixels at the edges are simply 2 or 4 pixel cells together, in the 2E configuration the egde pixels have only 3 or 4 readout columns (instead of 4 or 8) to contain the capacitance increase.

5.1.2 Module classification

After the completion of the production process, modules were classified and selected based on their IV and CV-characteristics, measured by means of a temporary metal deposition which shorts all the bump-bonding pads.

Based on the experience gained in the preparatory studies and defining V_{depl} the bias voltage at which the sensor is fully depleted, sensors were accepted if:

Quantity	Size	2E	1E
6	2×3	4	2
4	2×2	2	2
8	2×1	5	3
4	1×1	3	1
Diodes		6	6

Table 5.1: Type and size of sensors contained in each wafer. Size is expressed in terms of number of bump-bonded ROCs.

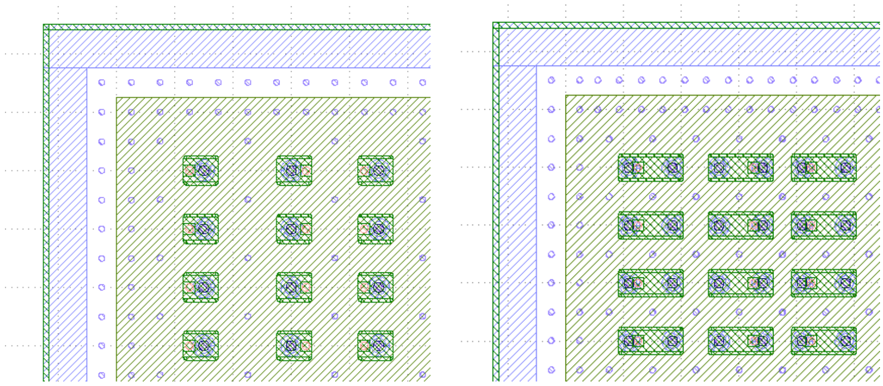

(a) 1E edge layout. (b) 2E edge layout.

Figure 5.2: Slim edge structure of the CT-PPS sensors.

- Wafer bow $< 200\ \mu$m
- $V_{depl} < 20$ V
- Breakdown voltage > 35 V
- $[I(25\text{V})/I(20\text{V})] < 2$

Sensors which fulfill the requirements were then classified in three categories depending on the current measured at the operation voltage $V_{op} = V_{depl} + 10$ V and at room temperature. Since in the wafer there are sensors of different sizes, I is defined as the amount of current per ROC.

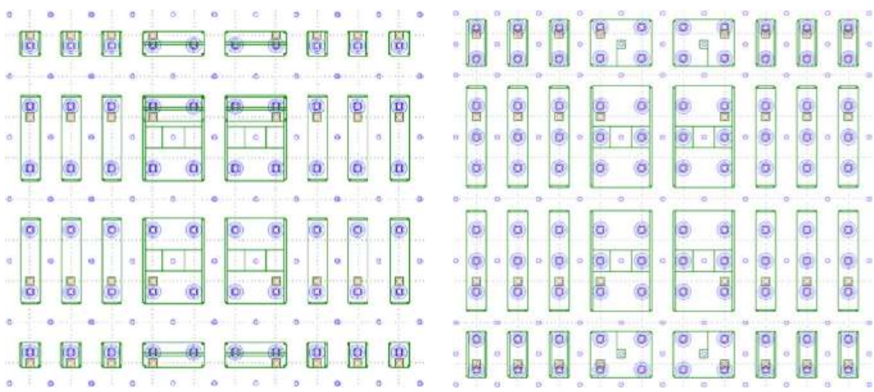

(a) 1E edge layout. (b) 2E edge layout.

Figure 5.3: CT-PPS sensor layout in correspondance of the corner between 4 ROCs.

- Class A: $I(V_{op}) < 2\ \mu$A
- Class B: 2 μA$< I(V_{op}) < 10\ \mu$A
- Class C: $I(V_{op}) > 10\ \mu$A

Based on our experience, only class A and B sensors can be properly read out using the PSI46dig chip, so also class C sensors were discarded.

5.1.3 Production results

Two batches have been produced and tested with the temporary metal deposition. Due to the large differences the test results are discussed separately.

First batch

The first batch was completed in December 2015. Five out of the twelve wafers broke during the production process. The electrode characteristics have been measured on a test wafer and the result of one measurement is shown in Fig. 5.4. The column diameter is compatible with the 10 μm requirement and the mean column length is 202 ± 5 μm, with an expected dispersion over the different wafers of ± 10 μm. All wafers fulfill the requirement with respect to the bow, with values from 55 and 155 μm.

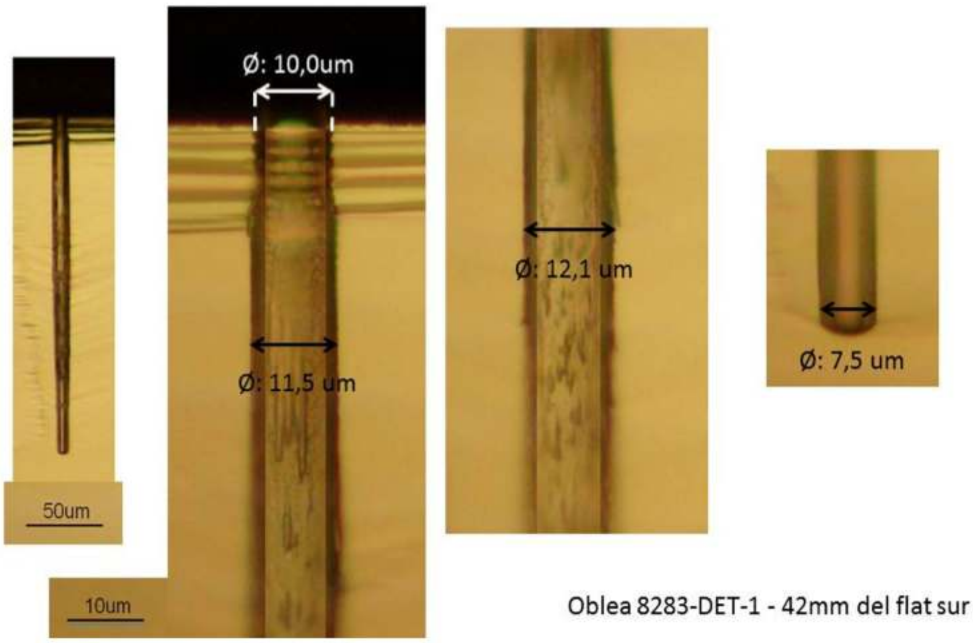

Figure 5.4: Electrode measurement on the test wafer.

The depletion voltage of the sensors has been derived by the CV curves measured on diodes belonging to the same wafer and the results show that the sensors are fully depleted between 5 and 10 V, as required.

From the IV curve point of view, the quality of the sensors is not as high as expected. Tab. 5.2 shows the classification of the 2×2 and 2×3 modules.

The total yield of class A + class B sensors is quite low, especially for the 2E pixel configuration. Due to these results, the baseline geometry (2E 2×3 modules for all the 24 pixel planes) could not be implemented. Since 2×2 modules still guarantee a sufficient acceptance, which is concentrated in the region close to the beam, it was decided to install both 2×3 and 2×2

Pixel configuration	total number	Rejected	Class A	Class B	Class C	A + B
2 × 3 2E	28	6	3	10	9	13
2 × 3 1E	14	3	7	2	2	9
2 × 2 2E	14	0	4	9	1	13
2 × 2 1E	14	2	6	5	1	11
Total	70	20	26	13	1	46

Table 5.2: Classification of modules from the first batch based on their IV characteristics.

modules. Based on the test beam measurements (Sec. 5.4), also 1E sensors were considered for the installation, getting a total of 46 modules, enough for the construction of the 24 + spare planes needed for building the whole 2017 CT-PPS detector.

Second batch

The second batch was completed in May 2016. Almost all sensors showed a too low breakdown voltage, between 5 and 15 V. Applying the selection criteria mentioned in the previous paragraph, only two 2 × 3 and one 2 × 2 could be selected. The reason of this failure has been attributed by CNM to a problem with the implantation of the p-stop around the n-electrodes, a procedure carried out by an external company due to a technical issue with one of the CNM production lines. The low breakdown is possibly related to a higher implanted dose with respect to the design.

To recover the production a low-fluence neutron irradiation is under study (5-10$\times10^{13}$ n_{eq}/cm^2) followed by annealing to reduce the leakage current (180 min at 200°C). This procedure already showed a large improvement of the breakdown for other CNM devices [138]. Due to the limited fluence, the trapping probability due to this pre-irradiation is expected to be low.

To validate the procedure, one of the wafers of this second batch was sacrificed, cut before removing the temporary metal deposition, and sent to the Reactor Center irradiation facility at the Jozef Stefan Institute in Ljubljana, where it was irradiated with neutrons to a fluence of (5×10^{13} n_{eq}/cm^2). Figure 5.5 shows the IV curves of six modules before and after irradiation plus annealing. A moderate increase of the breakdown is obtained after the neutron irradiation. Considering that the sacrificed wafer was selected among those showing the worse IV characteristics, a better improvement might be expected when starting with sensors with initial higher breakdown.

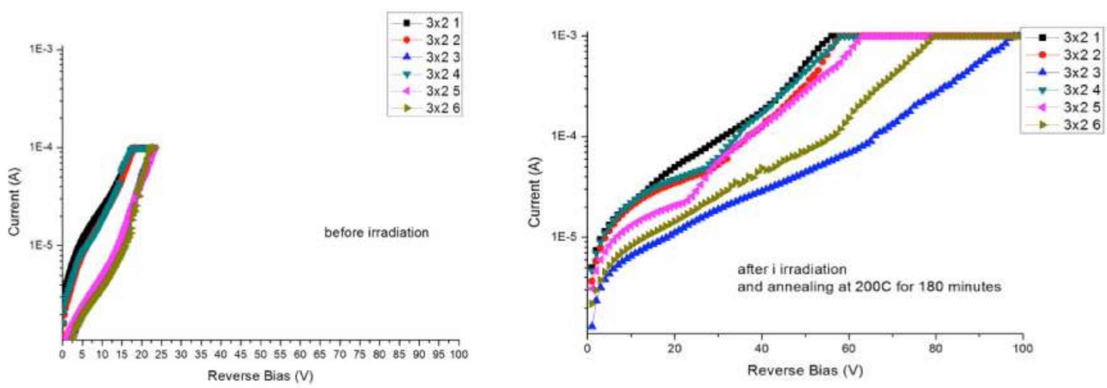

(a) Before irradiation.

(b) After irradiation and annealing.

Figure 5.5: IV curves for six modules of the second CNM batch before (a) and after (b) irradiation with neutrons to 5×10^{13} n_{eq}/cm^2 followed by annealing at 200°C for 180 min.

One of the limitations of the irradiation at the Ljubljana facility is that only samples with a maximum elliptic cross section with axis of 7 and 5 cm can be irradiated. Therefore, it would be necessary to remove the temporary metal, deposit the under-bump metallization and cut the wafer before the irradiation. In this situation, sensors would need to be bump-bonded to the ROCs to validate the result of the irradiation. Since this procedure would be expensive and low efficient, alternative irradiation facilities are being considered for irradiating the whole wafer and so being able to evaluate the results before the flip-chip.

Because of the low yield of the first batch and the issue showed by the second one, the production of a third batch was launched at CNM; wafers are expected by end of spring 2017.

5.2 PSI46dig ROC wafers for CT-PPS

The two ROC wafers used for CT-PPS come from the CMS production for the Phase I pixel tracker upgrade. The only difference is the thinning of the wafer that, having less stringent requirements in material budged, is to 200 μm instead of the 175 μm of the Phase I wafers.

ROCs went through the standard qualification procedure of the CMS pixel detector: wafers are qualified at PSI by means of a probe station, sent to IZM for the bump-bonding deposition and the ROC dicing, and then ROCs are tested again at INFN-Padova. Chips are divided in 5 classes depending of the number of defective pixels, threshold distribution, ADC characteristics, digital and analog current behaviour and major issues like shortcut, programming error or other basic functionality problems. For the Phase I production, only class 1 ROCs (expected behavior of ADC and threshold, and no defective pixels) were chosen.

Figures 5.6 and 5.7 show the qualification results of the CT-PPS wafers before (left) and after (right) the wafer thinning, bump-bonding deposition and dicing. It is possible to observe that for both wafers the number of class 1 ROCs (green) drastically reduces. Specifically, most of the ROCs turned into class 2, whose difference with respect to class 1 is related to the presence of up to 4 defective pixels.

It was noticed that ROCs passing from class 1 to class 2 have the extra bad pixels only in the last row. By measuring the tornado plot of the defective pixels, one can see (Fig. 5.8) that the working point (black rectangle) in CalDel and VThrComp obtained from a pixel in the center of the ROC (left) does not work for the defective pixels (right).

This problem has been investigated by inspecting the ROCs with the microscope, discovering that the left and right cutting edges of the ROCs showed irregularities, possibly related to the different thickness of these wafers with respect to those used for the Phase I tracker. No other reason was found to explain the degradation of the ROC quality which only affected these two particular wafers.

Nevertheless, an important consideration is that this issue does not compromise the usage of these ROCs for the detector. In fact, it must be considered that the real working point during data taking will have a lower and trimmed threshold. This corresponds to the top region of the tornado plot, which overlaps for the two pixels shown in Fig. 5.8. Hence all the pixels are expected to behave correctly. To account for this issue, during the module qualification procedure the threshold trimming needs to be done first in order not to affect the subsequent steps. For the final bump-bonding, ROCs of class 1 and 2 have been used.

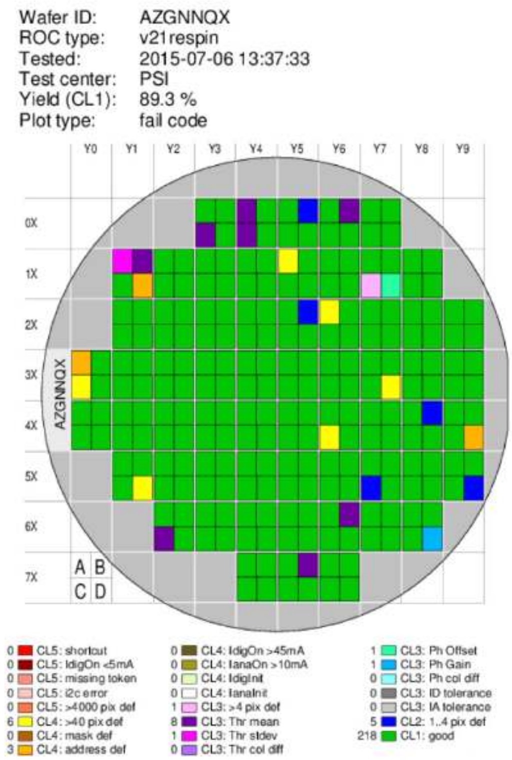

(a) Before dicing.

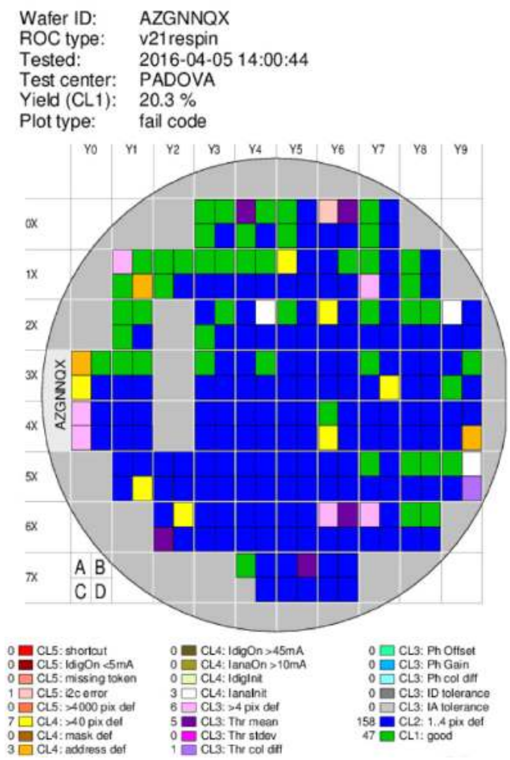

(b) After dicing.

Figure 5.6: Qualification results of wafer ARGNNQX. The 12 missing ROCs have been removed before the testing procedure and bump-bonded to single-chip sensors for the beam tests described in Sec. 5.4.

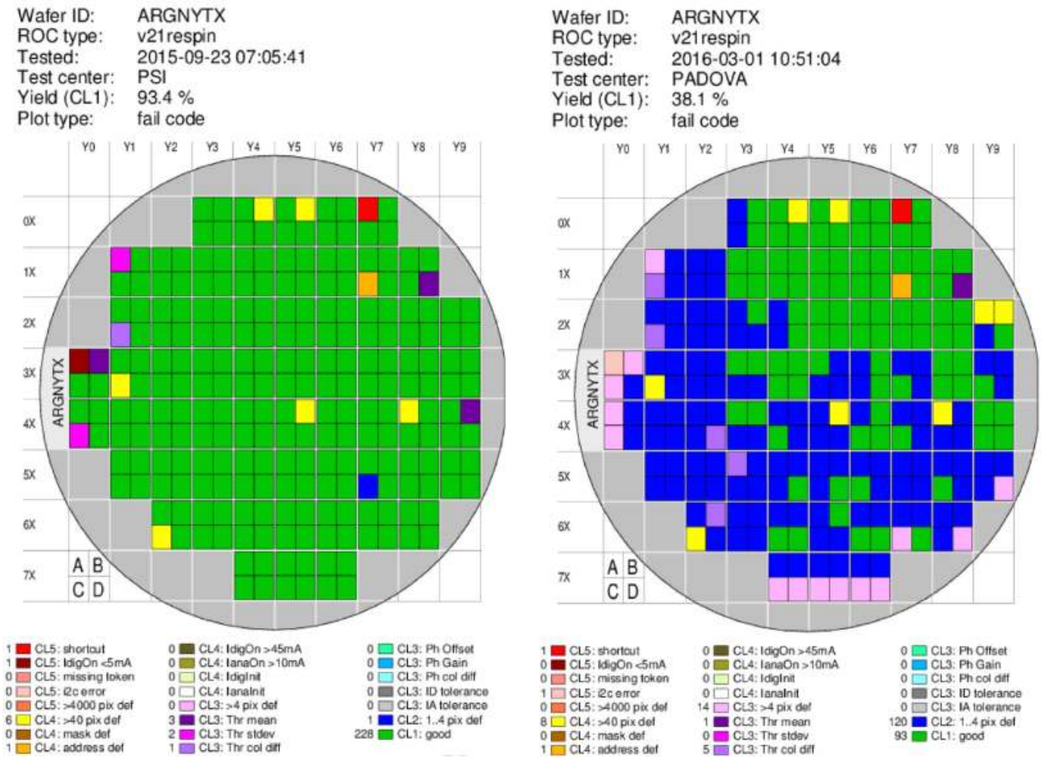

(a) Before dicing. (b) After dicing.

Figure 5.7: Qualification results of wafer ARGNYTX.

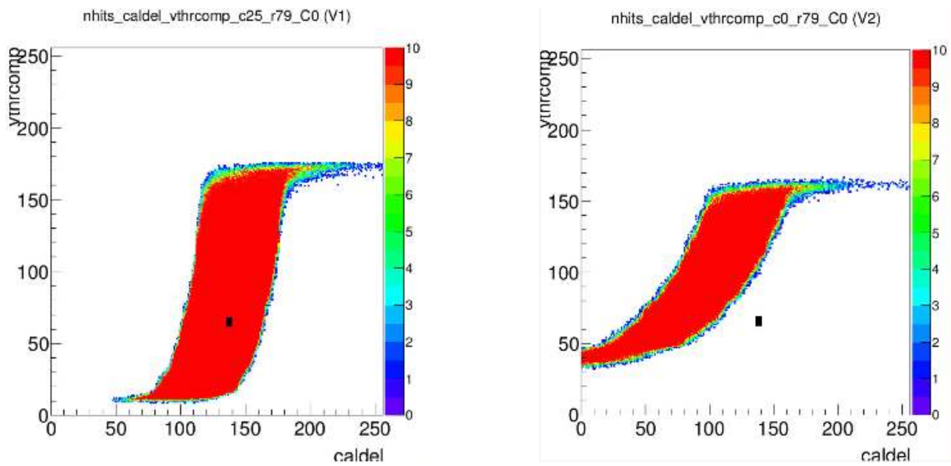

(a) Good central pixel. (b) Defective pixel.

Figure 5.8: Tornado plots for a good and a defective pixel. The black rectangle indicates the ROC working point as evaluated from a central good pixel.

5.3 Bump-bonding at IZM

The bump-bonding of the ROCs to the sensor modules was carried out at IZM.

Both sensor and ROC wafers are subjected to the Under Bump Metallization (UBM) electroplating, after which sensor modules are diced. On the ROC wafer the SnAg bumps are deposited and the wafer then passes the reflow step to shape the bumps in a spherical profile. The ROC wafer is now thinned down to 200 μm and finally diced. ROCs selected as described in the previous section are flip-chipped to the sensor modules chosen on the basis of their IV characteristics.

In February 2016 10 single-chip sensors from the first CT-PPS batch were bump-bonded to ROCs from the AZGNNQX wafer. These assemblies, two 1E and eight 2E of both class A and B, have been used to verify the sensor production and the bump-bonding procedure. The latter has been further validated with the assembly of 10 modules (two 2×3 and eight 2×2) completed in May 2016. After this test, the remaining 36 modules of Tab. 5.2 (20 2×3 and 16 2×2) were bump-bonded and received in September 2016.

5.4 Test beam on single chip modules

In this section the results of the characterization in laboratory and on beam of single-ROC sensors from the CT-PPS production are presented. More 2E sensors have been selected since CNM 1E detectors have already been tested during the preparatory studies described in the previous chapter. Because of the limited number of class A sensors, also class B sensors have been chosen for these tests in order to check their characteristics and validate their usage in the final detector installation. The list of the tested sensors is reported in Tab. 5.3, with the wafer number and the detector number according to the notation of Fig. 5.1(a)

Due to the installation time constraints, an irradiation campaign could not be carried on these sensors, but the expected performances are very similar to those obtained in the preparatory studies.

5.4.1 IV curves

The current-voltage characteristics of the single-ROC modules bump-bonded to be tested on beam are shown in Fig. 5.9.

Both 1E sensors present a higher breakdown voltage with respect to the 2E ones. Moreover, a clear separation between class A and B sensors is visible. In particular, class B devices do not show a plateau and hence it is difficult to estimate the maximum voltage that can be applied. Measurements have been performed with the ROC switched on, in order to avoid its damage,

Detector name	wafer	dice	layout	class
CNM_CT-PPS_10_1	10	1	1E	A
CNM_CT-PPS_11_1	11	1	1E	A
CNM_CT-PPS_2_2	2	2	2E	B
CNM_CT-PPS_5_2	5	2	2E	B
CNM_CT-PPS_5_4	5	4	2E	B
CNM_CT-PPS_10_2	10	2	2E	B
CNM_CT-PPS_10_4	10	4	2E	A
CNM_CT-PPS_11_4	11	4	2E	A
CNM_CT-PPS_12_3	12	3	2E	A
CNM_CT-PPS_12_4	12	4	2E	A

Table 5.3: Single-ROC sensors from the CT-PPS production tested on beam.

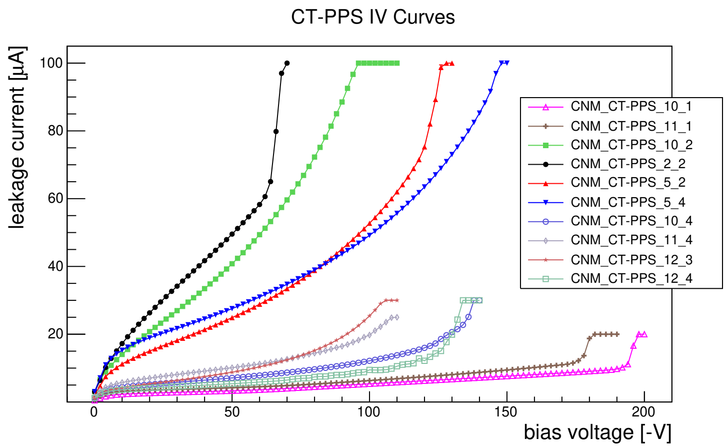

Figure 5.9: IV curves of the tested single-ROC sensors from the CT-PPS production.

and without controlling the temperature. Since the ROC induces a temperature increase of several degrees, the absolute value of the current could not be used to classify the sensors. As previously explained, the measurements on wafer before bump-bonding were used to this purpose.

5.4.2 Laboratory tests with X-ray

The bump-bonding quality has been studied with X-rays. When a bump is missing, it is expected that no hits are registered in that pixel, apart from some noise which can be minimized if the threshold is correctly set.

The X-ray tube is an ERESCO 42 MF4 Portable X-ray Unit, with a 200 kV Directional Radiating Tube Head, air cooled, available at the University of Torino where it is mainly used for cultural heritage physics. The aperture of the emitted beam is 60° and 40° in the horizontal and vertical plane, respectively; hence, no accurate detector positioning is required. The device was placed at $\sim$ 50 cm from the tube window. At this distance, the applied voltage of 50 kV and the required current of 4 mA are sufficient to provide a large statistics for all pixels with an acquisition time of 100 s. Figure 5.10 shows the setup. The 3D modules connected to the DTB were positioned in front of the X-ray tube, while the PC used for the data acquisition and the power supply were located close to the system but beyond a concrete wall to be protected.

Low hit regions have been observed for a few detectors. An example is provided in Fig. 5.11(a). Although the reason of this effect could not be clarified, no evidence of similar patterns has been observed in the efficiency maps measured on beam, as shown in Fig. 5.11(b) for the same detector of Fig. 5.11(a). Therefore, modules showing this issue were not discarded.

5.4.3 Noise and threshold

Standard laboratory tests were performed on the detectors in order to optimize the ROC parameters before going to the test beam. Thresholds were trimmed using the DTB at 35 Vcal, corresponding to $\sim$ 1800 e^-. At the test beam this value was further optimized for each single detector. Thanks to the lower noise, the threshold for the 1E detectors is lower ($\sim$ 1650 e^-) than that for 2E detectors (between $\sim$ 1800 e^- and $\sim$ 2300 e^-).

The depletion voltage was estimated by measuring the detector noise as a function of the bias voltage. Specifically, the sensor can be considered fully depleted when the noise-bias voltage curve reaches the minimum. Because of the dependence of the noise on the capacitance, this curve is equivalent to the capacitance-voltage one obtained on the diodes by CNM. The noise as a function of the bias voltage for the tested detectors is shown in Fig. 5.12.

Figure 5.10: X-ray test setup.

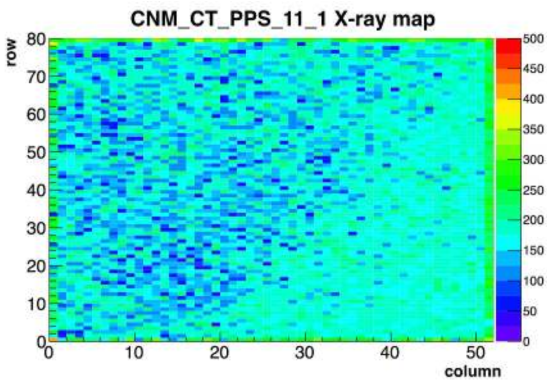

(a) X-ray map.

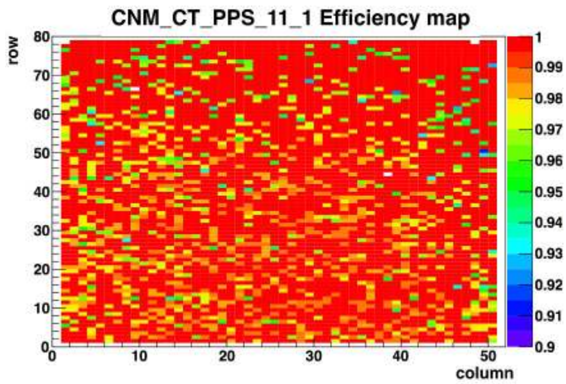

(b) Efficiency map.

Figure 5.11: X-ray and efficiency maps for the same detector. The pattern observed with the X-ray test is not seen on the efficiency map.

A clear difference between 1E and 2E detectors can be observed. As expected considering larger number of electrodes in the pixel cell, the noise of 1Es is lower ($\sim$ 180 e$^-$) than that of 2Es ($\sim$ 210 e$^-$ $-$ 240 e$^-$). For the same reason the plateau is reached more quickly by 2E detectors. A depletion voltage of 5 and 3 V for 1E and 2E sensors, respectively, was estimated from these curves.

5.4.4 Test beam results

Single-chip detectors have been measured on beam at FNAL with the same data taking and analysis procedure used in the preparatory studies. In the following, the results of the beam tests are presented.

Efficiency

The hit efficiency of the detectors as a function of the bias voltage is shown in Fig. 5.13(a). The zoom allows to appreciate the very low depletion voltages, 3 (5) V for 2E (1E) devices. These values are compatible with those derived from the noise measurements. A very important

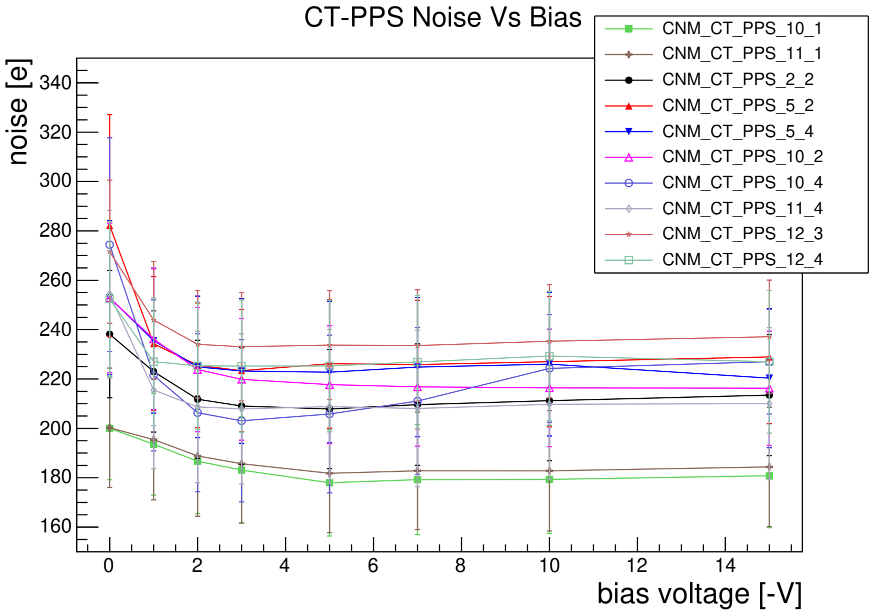

Figure 5.12: Noise-voltage characteristics for the tested sensors. The error bars represent the RMS of the gaussian used to fit the noise distribution.

conclusion from these efficiency measurements is also that there is no difference between class A and B sensors from the efficiency point of view.

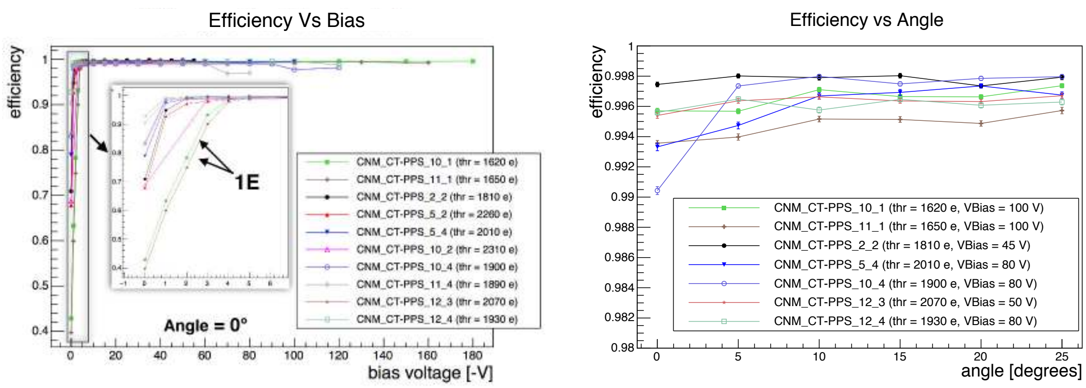

(a) Efficiency vs bias voltage.

(b) Efficiency vs rotation angle.

Figure 5.13: Efficiency as a function of bias voltage (a) and rotation angle (b) for single-ROC sensors from the first CT-PPS batch.

A drop of efficiency is observed for some detectors when the bias voltage is set close to the breakdown value. This is caused by noisy pixels and the full efficiency can be easily recovered by slightly increasing the threshold. It can also be noticed that a sizable efficiency can be reached even without applying the bias voltage. This indicates that the build-in voltage of the junction provides a sufficiently large depletion region. Also in this case a substantial difference between 1E and 2E detectors can be found, due to the inter-electrode distance.

The efficiency does not increase as a function of the rotation angle between the sensor and the beam direction (Fig. 5.13(b)). In fact, the not-fully-passing-through columns guarantee an already high efficiency at 0°. At 20°, a tilting angle close to the one in CT-PPS, an efficiency higher than 99.4% is achieved.

Edge efficiency

As explained previously, the reduction of the insensitive edge of the sensor is a key requirement for CT-PPS. Figure 5.14 shows how the efficient edge extends as a function of the bias voltage. Specifically, at 40 V about 150 μm and 90 μm of the 200 μm slim edge can be recovered for 2E and 1E sensors, respectively, indicating a clear advantage in using 2E devices. Values obtained for 1E sensors are compatible with those obtained for the CNM sensors tested during the preparatory studies.

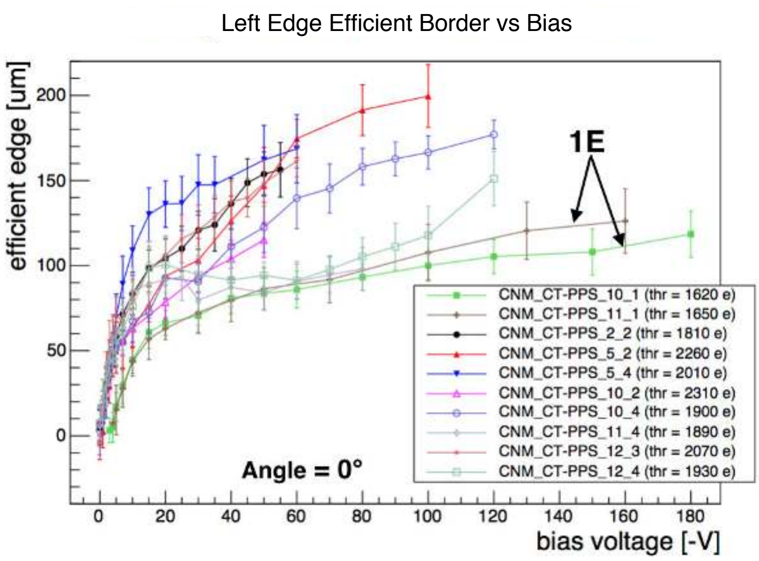

Figure 5.14: Efficiency extension as a function of the bias voltage for the CT-PPS single-ROC tested sensors.

Resolution

The resolution is estimated for clusters of size 1 and 2 separately, as explained in chapter 4. To provide a global value, resolutions of the two cluster types are weighted by their cluster size probability. To this purpose, the probability of size 2 clusters is calculated, assuming zero the probability of higher size clusters. The resolutions in both x and y coordinates are presented in order to verify the CT-PPS requirements.

In the x-coordinate it is possible to profit from the detector rotation with respect to the beam direction, which increases the cluster size 2 probability, as shown in Fig. 5.15(a). This is the relevant coordinate since in the CT-PPS Roman pots the detectors will be rotated in the same way. The global resolution in x is shown in Fig. 5.15(b) as a function of the rotation angle. As expected, the resolution improves with the angle and reaches $\sim$ 22 (25) μm for 2E (1E) detectors at 20°. Considering that six planes will be installed in each station, the required 10 μm resolution can be achieved.

In the case of the y-coordinate, no rotation is present and hence most of the tracks produce clusters of size 1, with only a small contribution of clusters of size 2. The measured global resolution is $\sim$ 27 μm without any difference between 1E and 2E sensors. Considering the six planes, a resolution of 11 μm can be achieved in CT-PPS. Moreover, since the planes will be slightly staggered in the y-coordinate, an improvement of the resolution is expected. The same effect should not be present in the x-coordinate since the detectors will be glued very precisely in order to minimize the distance from the Roman pot thin window.

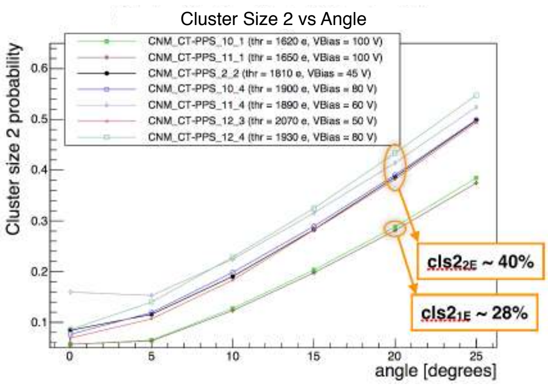

(a) Cluster size 2 probability vs rotation angle.

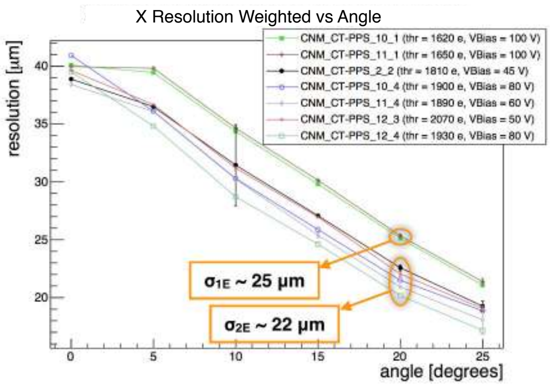

(b) Weighted resolution in the x coordinate vs rotation angle.

Figure 5.15: Cluster size 2 probability as a function of the rotation angle (a). This is used for weighting cluster size 1 and 2 resolutions in the x direction and estimate the global value (b).

5.5 ROC non uniform irradiation studies

The timing issue highlighted by the tests performed on the single-chip detectors not uniformly irradiated at the CERN IRRAD Proton Facility (Secs. 4.6.2 and 4.6.4) has been further investigated with a specific study on the PSI46dig readout chip.

Six ROCs coming from the CT-PPS AZGNNQX wafer were glued and wire-bonded in Torino to the ROC boards. The irradiation was performed at an X-ray facility available at CERN[1]. The dose delivered by the machine was calibrated and its uncertainty is estimated to be ±20% or better.

In order to reproduce the non-uniform irradiation, a metal filter was inserted between the X-ray window and the ROC. Two different filters were used: a copper one to have a binary irradiation, and an aluminum one, milled on purpose to reproduce the expected irradiation shape.

The thickness of the two filters was evaluated based on the results of a GEANT4 [15] simulation. The physics interactions of the photons were simulated with the Penelope model [139], which is commonly used as low-energy electromagnetic model for $e^{\pm}$ and photons. In particular, Rayleigh scattering, Compton scattering, and photoelectric effect are included to reproduce the interactions with matter of the X-rays. Electrons produced by the primary interaction are simulated considering ionization, multiple scattering, and Bremsstrahlung.

The photon energy distribution is sampled according to the measured spectrum for the tungsten target (Fig. 5.16), produced with the tube powered to 50 kV. Photons are generated perpendicularly to the ROC face and uniformly distributed on it.

To simulate the irradiation to the ROC, the chip was defined as a silicon dioxide volume with constant thickness and the dose was calculated as a function of the filter thickness by designing a triangular filter placed in front of the chip. The simulated doses on the silicon dioxide as a function of the thickness of a filter made of copper or aluminum material are shown in Fig. 5.17.

Since the copper filter strongly suppresses the dose already in a few hundred microns, it was not possible to produce with this material a shape able to modulate the dose. However, a 2 mm-thick copper filter with a 2 mm-wide slit was manufactured to perform a binary irradiation on a small selected region. The small thickness of this filter allowed to place the ROC very close to the X-ray tube, thus profiting from the maximum irradiation rate (∼ 8 Mrad/h @ 1 cm).

[1] http://proj-xraymic.web.cern.ch/proj-xraymic/

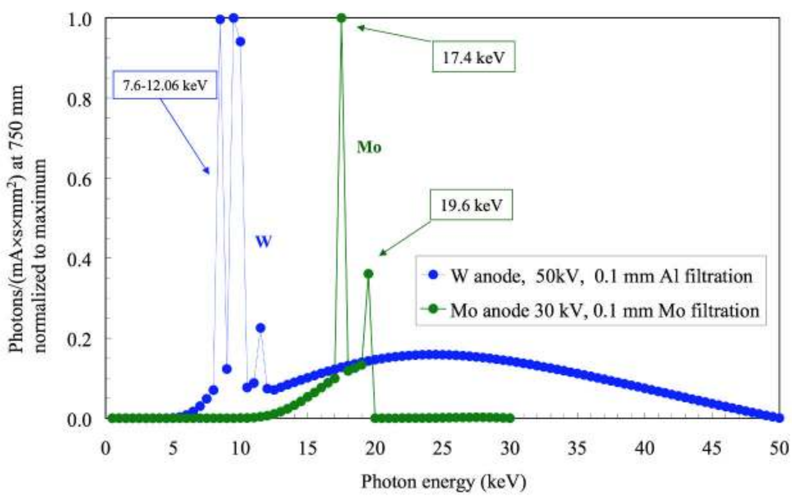

Figure 5.16: Photon spectra of the CERN X-ray machine. The tungsten target was used for this study.

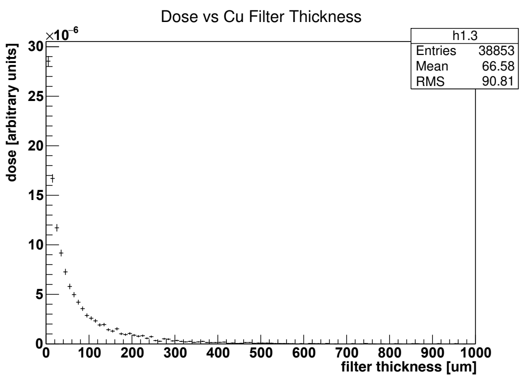

(a) Copper filter.

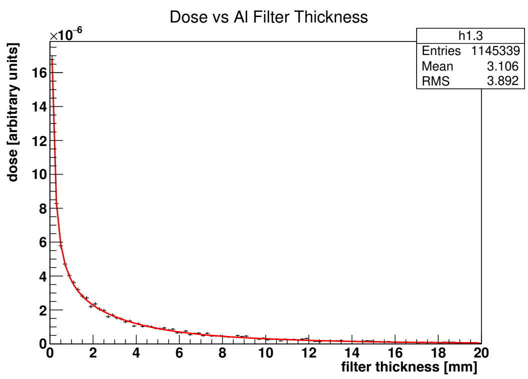

(b) Aluminum filter.

Figure 5.17: Dose deposited in the silicon dioxide as a function of the filter thickness.

In the case of aluminum, several mm are needed to stop the X-rays and this allows to modulate the radiation. The dose as a function of the filter thickness was fitted with a Landau multiplied by a polynomial function of degree eight, which best reproduced the simulation results. The dose distribution foreseen for the ROC was derived from a minimum-bias hit map measured with the CT-PPS strips in a run taken in 2016 (Fig. 5.18(a)), assuming that the dose deposited in the ROC is directly proportional to the proton hits. Using this map and the fitted curve, a histogram was obtained which gave the various filter thicknesses as a function of the position (Fig. 5.18(b)). The minimum thickness was fixed to 0 mm since the dose delivered by the machine is a known value. The maximum thickness was 15.5 mm.

The mapped thicknesses were converted by means of a ROOT macro first into a CAD and then into a CAM file to be passed to a milling machine (Fig. 5.18(c)). Finally, since GEANT4 allows to simulate objects described in CAD format, the shaped filter was verified to well reproduce the expected hit map (Fig. 5.18(d)). With the aluminum filter the X-ray tube was positioned at 5 cm, corresponding to a dose rate of ~ 3.6 Mrad/h.

Both copper and aluminum filters were realized by the mechanical laboratory of INFN-Torino. Figure. 5.19 shows the two filters mounted on top of the ROC, which is surrounded by a 3D-printed plastic spacer. Since the aluminum filter was produced with a 3 mm spherical bur, this did not allow to perfectly reproduce the simulated shape, resulting in a small shift of

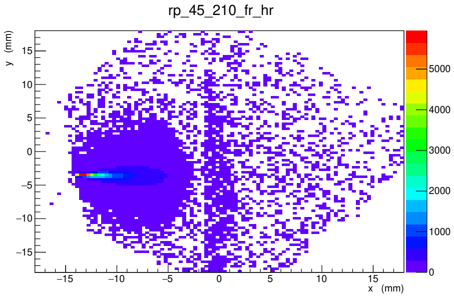

(a) Strip hit map.

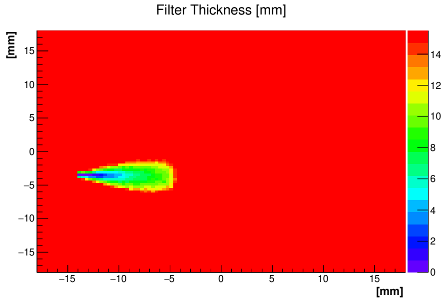

(b) Filter thickness map.

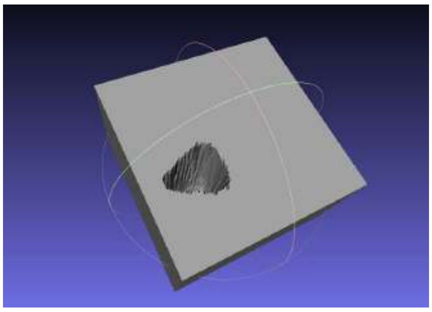

(c) Filter in CAD format.

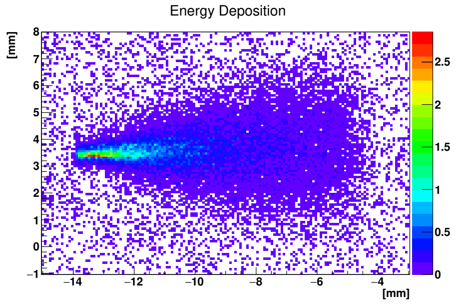

(d) Simulation with the filter.

Figure 5.18: Spets for the aluminum filter design.

the minimum thickness point towards the center of the ROC. Both filters were positioned in such a way that the shape was well contained within the ROC.

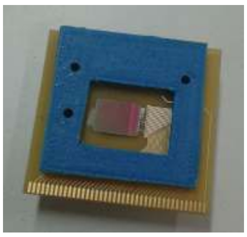

(a) ROC surrounded by the plastic spacer.

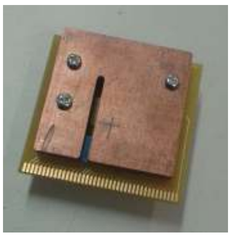

(b) Copper filter.

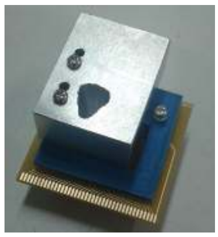

(c) Aluminium filter.

Figure 5.19: Pictures of the filters mounted on the ROC for the X-ray irradiation.

The expected dose for the 2017 data taking was estimated combining information from the CT-PPS TDR and the CERN IRRAD Proton Facility. Here, with protons of 23 GeV, a fluence of 1.61×10^{15} p/cm^2 corresponds to 52 Mrad and it can be assumed that the released dose remains the same for protons of 6.5 TeV. Simulations reported in the TDR indicate that the foreseen peak irradiation corresponds to 5×10^{15} p/cm^2 for 100 fb^{-1}. According to these numbers, the delivered dose rate is $\sim$ 1.61 Mrad/fb^{-1}. Assuming an integrated luminosity of 40 fb^{-1} for 2017, the maximum expected dose is 64.5 Mrad, which is the dose the ROCs have been irradiated to in this study.

The irradiation was carried out at the beginning of November 2016, with the X-ray tube set to 40 kV and 50 mA. Two ROCs could be irradiated since the machine was available for 48 hours only. To reduce the setup timing, the machine chuck temperature was set to 20°C, thus avoiding cooling and dry air pumping.

The first irradiation was done using the copper filter, repeating the measurements in steps of 8.05 Mrad. After 64.5 Mrad, the filter was removed, the ROC was placed at 8 cm from the tube, and a dose of 10 Mrad was delivered uniformly to the chip at a rate of ~ 2 Mrad/h.

To evaluate the effect of the irradiation, tornado plots have been produced for all the ROC pixels, from which the shift in time of the irradiated pixels has been measured. Plots in Fig. 5.20 show the overlap of the tornado plots for an irradiated and a non-irradiated pixels. While increasing the dose, the overlap reduces. In particular, for the irradiated pixel the tornado plot moves to lower Vcal values, a higher time walk is visible and the threshold working range reduces, which are all symptoms compatible with a lower bias current in the ROC amplifier. At the same time, the threshold range of the non-irradiated pixels increases, which can be attributed to the fact that bias current is subdivided among all the amplifiers while keeping constant the total value (24 mA). As a consequence, non-irradiated pixels receive a higher current. As expected, the horizontal width of the tornado distribution remains constant since it must correspond to the 25 ns bunch crossing spacing. From this, it is possible to evaluate that the bunch crossing time window corresponds to ~ 60 CalDel units.

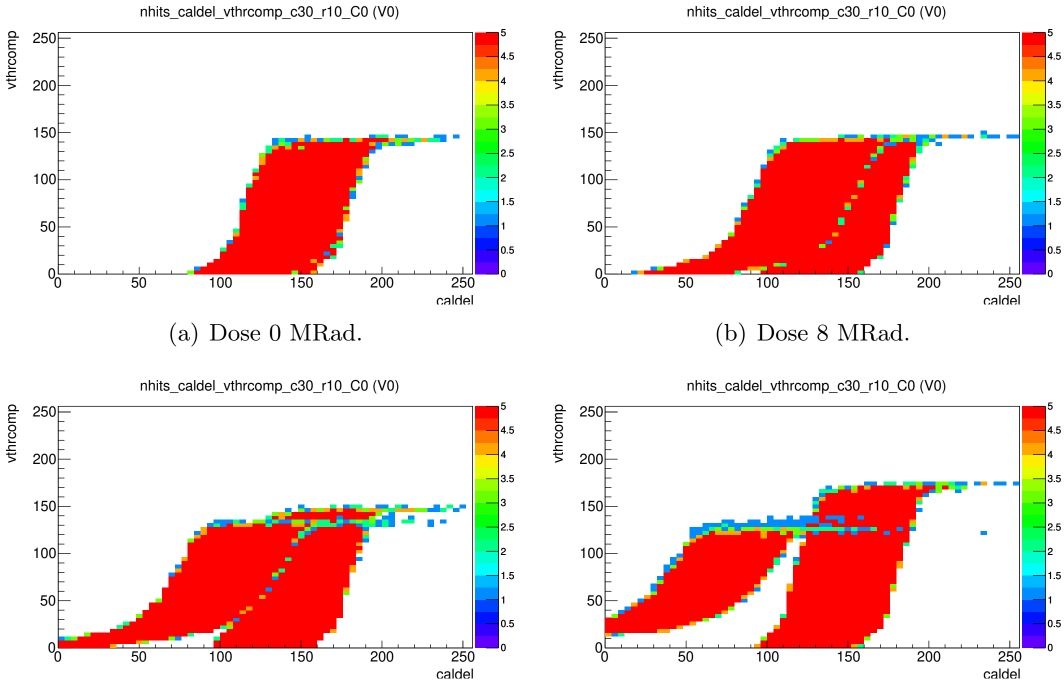

(a) Dose 0 MRad.

(b) Dose 8 MRad.

(c) Dose 16 MRad.

(d) Dose 32 MRad.

Figure 5.20: Overlaps of tornado plots for an irradiated and a non-irradiated pixels.

The central CalDel value of the tornado distribution has been measured by fixing the VThrComp value to that obtained by trimming the threshold at 1800 e^-, reduced by 5 DAC units to improve the overlap at high irradiation. The map of the central CalDel values (Fig. 5.21) clearly shows the strong effect of the non-uniform irradiation for the region of the ROC not covered by the copper filter.

The average values of the tornado CalDel centers for highly irradiated and non-irradiated pixels have been evaluated and their difference is plotted as a function of the dose in Fig. 5.22. Measurements for the irradiation with the copper filter are represented with the blue points. A linear increase of the delay in absolute value can be observed. After an irradiation of $\sim$ 32 Mrad, the analog current was increased without any positive effect but values remained perfectly compatible. This is attributed to the fact that both irradiated and non-irradiated pixels, receiving a higher current, become faster but the time shift between them does not change.

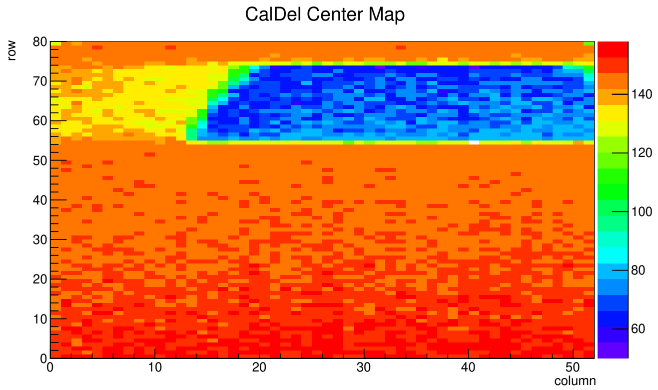

Figure 5.21: Map of the central CalDel values derived from the tornado plots of all the ROC pixels, after 32 Mrad of non-uniform irradiation between the regions covered and not covered by the copper filter.

After ~ 64 Mrad, the ROC was uniformly irradiated with another 10 Mrad and a sensible recovery can be seen. Since no saturation effect appeared during the non-uniform irradiation, the improvement cannot be attributed to an equalization of the pixel behaviour. Instead, it can be related to the irradiation of the ROC periphery, which is the area where the biasing circuits are located.

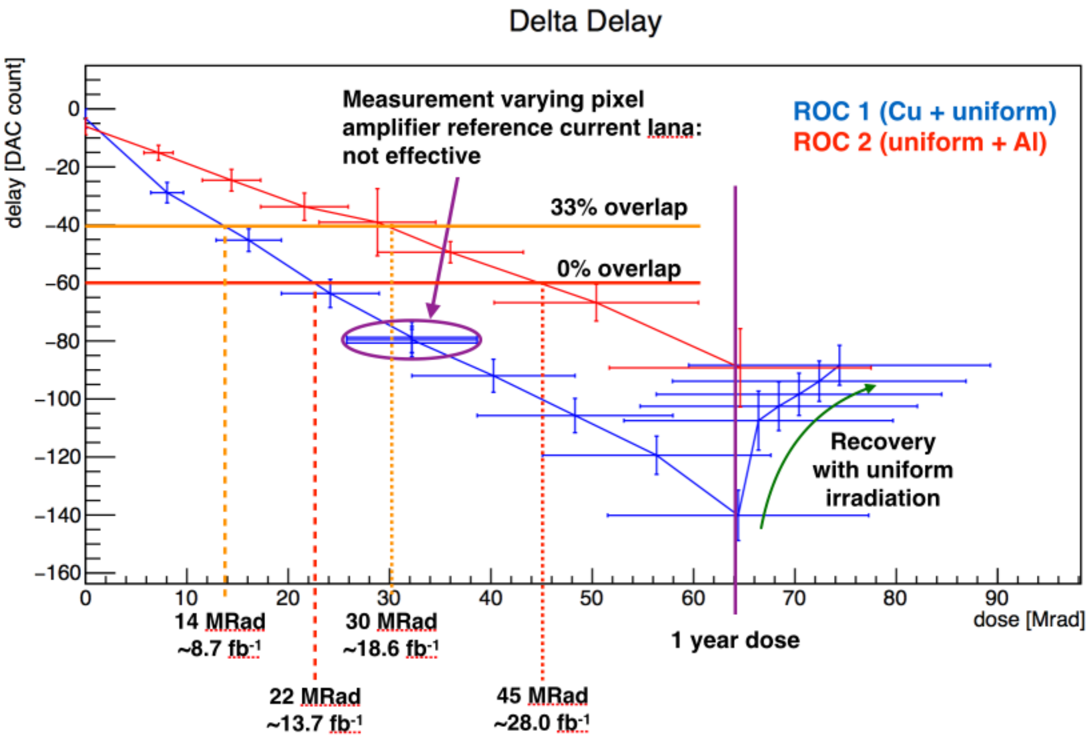

Figure 5.22: Delay between irradiated and non-irradiated pixels in CalDel units plotted as a function of the dose for the two irradiation tests. See the text for the details.

Because of the improvement observed in the previous test after the uniform post-irradiation of the ROC, the second ROC was pre-irradiated uniformly to 10 Mrad before covering it with the aluminum filter. An irradiation procedure identical to the one followed in the test with the copper filter was then applied. The measurements are represented in red in Fig. 5.22. The 10 Mrad dose of the pre-irradiation is not shown and the delays are plotted as a function of the dose accumulated with the non-uniform irradiation. Also in this case the linearity is evident but the curve is less steep. This is attributed to the uniform dose given in advance. This hypothesis is supported by the fact that the delay at $\sim$ 64 Mrad corresponds to the value obtained for the binary irradiated ROC after the 10 Mrad uniform dose.

To evaluate the effect on the readout efficiency, the dose and the corresponding luminosity for 33% and 0% overlap of the tornado plots can be estimated from the fitted curves with and without the uniform pre-irradiation. These two values have been chosen since down to 33% overlap it is reasonably possible to read all pixels in the same bunch crossing window, while with a lower overlap a different readout strategy will have to be implemented. The results indicate that a uniform pre-irradiation of 10 Mrad can shift the 33% overlap point from $\sim$ 14 Mrad ($\sim$ 8.7 fb^{-1}) to $\sim$ 30 Mrad ($\sim$ 18.6 fb^{-1}) and the 0% overlap point from $\sim$ 22 Mrad ($\sim$ 13.7 fb^{-1}) to $\sim$ 45 Mrad ($\sim$ 28.0 fb^{-1}).

Thanks to the modulated dose provided by the aluminum filter, the pixel area where there will be an efficiency loss due to this timing issue can be estimated, considering at least a 33% overlap of the tornado plots and assuming the uniform pre-irradiation of 10 Mrad. The maps of the central CalDel values derived from the tornado plots of all the pixels are shown in Fig. 5.23 as a function of the dose. Pixels with less than 33% overlap are white.

It can be concluded that there should still be a sufficient overlap for all the pixels up to $\sim$ 18 fb^{-1}, allowing a standard readout within the same bunch crossing window. For larger integrated luminosity, it can be seen that the white pixel region extends, resulting in a hole in the efficiency map.

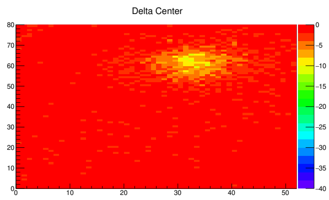

(a) Dose 7.2 MRad (4.4 fb^{-1}).

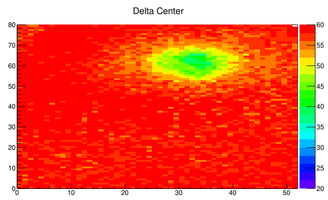

(b) Dose 14.4 MRad (8.9 fb^{-1}).

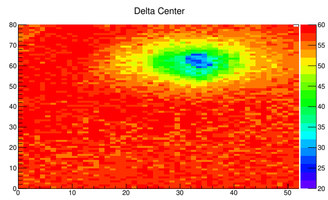

(c) Dose 21.5 MRad (13.4 fb^{-1}).

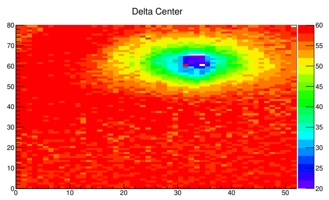

(d) Dose 28.8 MRad (17.9 fb^{-1}).

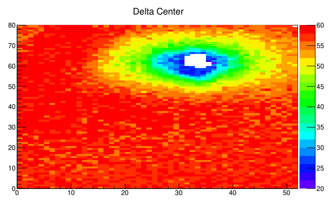

(e) Dose 30.6 MRad (22.4 fb^{-1}).

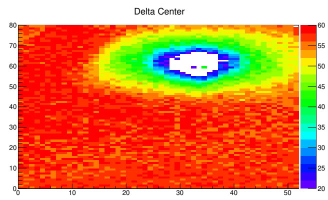

(f) Dose 50.2 MRad (31.2 fb^{-1}).

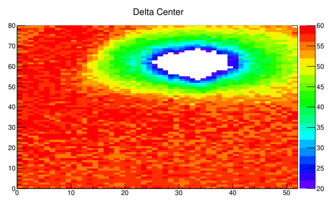

(g) Dose 64.6 MRad (40.1 fb^{-1}).

Figure 5.23: Maps of the central CalDel values derived from the tornado plots of all the pixels of the ROC irradiated with the aluminum filter, plotted as a function of the dose. Pixels with less than 33% overlap are white.

Due to the limited time and the difficulties in handling irradiated modules, a uniform pre-irradiation could not be done on the detector modules for CT-PPS. A different readout scheme is being studied to deal with this issue and one possibility could be to read out different planes of the same station with different latencies, in order to still fully reconstruct the track.

Chapter 6

The CT-PPS tracking detector production and installation

The first section of this chapter describes the qualification and selection of the modules for the CT-PPS tracker, and their assembling in the detector package to be inserted in the Roman pots for the 2017 data taking.

The data acquisition system of the CT-PPS tracker is then presented. It is based on the Phase I Pixel Online Software [140], which has been adapted to the CT-PPS configuration. The DAQ system has been tested together with the final detector packages in the same conditions of cooling and secondary vacuum expected in the Roman pots.

The last part of the chapter is dedicated to the installation of the detectors in the LHC tunnel and their commissioning. The preliminary results of the CT-PPS pixel tracker during the run for the alignment of the pots are presented.

6.1 Bump-bonded module qualification

In this section, the procedure for selecting the final modules is described. Besides rejecting the bad modules, these tests allow to choose the best module orientation, since a 180° rotation can be applied to the module in order to face the best quality ROCs toward the beam. Only sensors from the first CNM batch are used.

6.1.1 Hybrid flex and Token Bit Manager

The RPix hybrid flex is a 4-layer circuit printed in a kapton support, to which the module is wire-bonded thus providing power, clock, and trigger distribution to the ROCs and bias voltage to the sensor. The flex hybrid, shown in Fig. 6.1 with a bonded module, is connected to the RPix Portcard. The circuit has been designed in Genova for the specific CT-PPS requirements, starting from the Phase I Pixel High Density Interconnect (HDI) [141]. In particular, it has to host modules with dimension 3×2 but also 2×2, and it needs to fit in the Roman pot.

The flex hybrid hosts the so-called Token Bit Manager (TBM) [121]. The main tasks of the TBM are the distribution of the clock signal as well as the L1 trigger and the coordination of the ROC readout by generating the readout tokens. A TBM consists of two cores, Data Keepers, and a Communication and Control hub which distributes the I2C commands to the correct ROC.

After receiving a trigger signal, the external readout token is passed to the ROCs and the TBM header and trailer are added to the data stream. If another trigger arrives before the readout has finished and the token is received back, it is placed in an internal stack with 32 slots. Once 16 slots are filled and not cleared, subsequent triggers are stored in the stack but

Figure 6.1: Picture of a RPix flex hybrid with a 3×2 module wire-bonded on it. The numbers on the module indicate the I2C ROC addresses which also correspond to the numbering convention used in the DAQ. In case of 2 × 2 modules, ROCs 2 and 3 are not present. The calibrated holes needed for the precise alignment of the planes in the detector package are hooped in red, while the other holes in the TPG layer are for the screws used for fixing together the six planes.

no token is sent to the ROCs. In order to keep the DAQ synchronized, for these triggers the TBM only returns header and trailer, marked with the NoTokenPass flag.

Additional features of the TBM can be controlled via a set of register banks. These include various counters, automatic detection and reset in case of high-occupancy events, as well as programmable delays for all data streams and signals. The 160 MHz data streams from the ROCs are multiplexed to form one 320 MHz signal. Using the non-return-to-zero invert technique and 4-to-5 bit encoding, the signal is converted to 400 MHz and then sent through the RPix Portcard to the Pixel OptoHybrid (POH).

The flex also hosts a PT1000 Resistance Temperature Detector (RTD) close to the module side opposite to the beam. It monitors the plane temperature during data taking and also gives rise to an interlock signal in case anomalous values are found. This is needed because the detector operates in a secondary vacuum and a clogging of the cooling lines would cause a large increase of the temperature, irreparably damaging the modules.

In order to provide a good power dissipation, the flex and the module are glued on a TPG layer encapsulated in an aluminum foil, which is connected to the aluminum structure on the two sides of the detector package where the cooling pipes are connected. Two types of TPG geometries have been produced, which are characterized by the position of the module. In the detector package, the two types of plane alternate staggered by 800 μm, in order to avoid that the larger pixels in between two ROCs are aligned causing a reduction of the resolution.

Two prototype versions of the flex hybrid have been produced before the final one. Prototypes, glued on a vetronite layer, have been used for testing the modules in laboratory.

6.1.2 Test procedure

After the bump-bonding of the good quality sensors, all modules have been tested in Torino and Genova for selecting the high quality ones.

Modules were temporary glued to a prototype flex by means of a gel-pak film. This solution allowed to wire-bond the module to the flex hybrid without gluing it so that it could be easily removed after the tests. In order to validate this procedure, two modules were sacrificed to prove that a second wire-bond could be repeated without problems. A third wire-bond was also tried but difficulties were encountered due to the limited size of the ROC pads for the wire-bonds.

The testing procedure is the same one applied for the single-chip modules, as described in Sec. 5.4.2. After verifying, by measuring its voltage-current characteristic, that the sensor has not been damaged, the ROC calibration and optimization is performed. The final step is the X-ray test to check the bump-bonding quality. The module is then detached from the hybrid and stored in its protective box.

A summary with the significant plots of the performed tests is shown in Fig. 6.2 for a good 2x3 module. Concerning the IV curve, it can be noticed that the current limit imposed for the sensor qualification can not be applied to this measurement since no cooling is used and the ROC increases the sensor temperature by several degrees. Very few dead pixels are spotted with the Pixel Alive test and no unconnected bumps are found with the X-ray measurement. From the S-curves the threshold is determined to be uniform on the entire module and only a limited number of noisy pixels is found. Because of the larger size, pixels at the border between two ROCs show a $\sim 50\%$ higher noise. The blue ellipse on the left of the pixel maps indicates the beam position. In case bad pixels or unconnected bumps are found close to this module side, but still in a limited number, the module is mounted on the flex tilted by 180°.

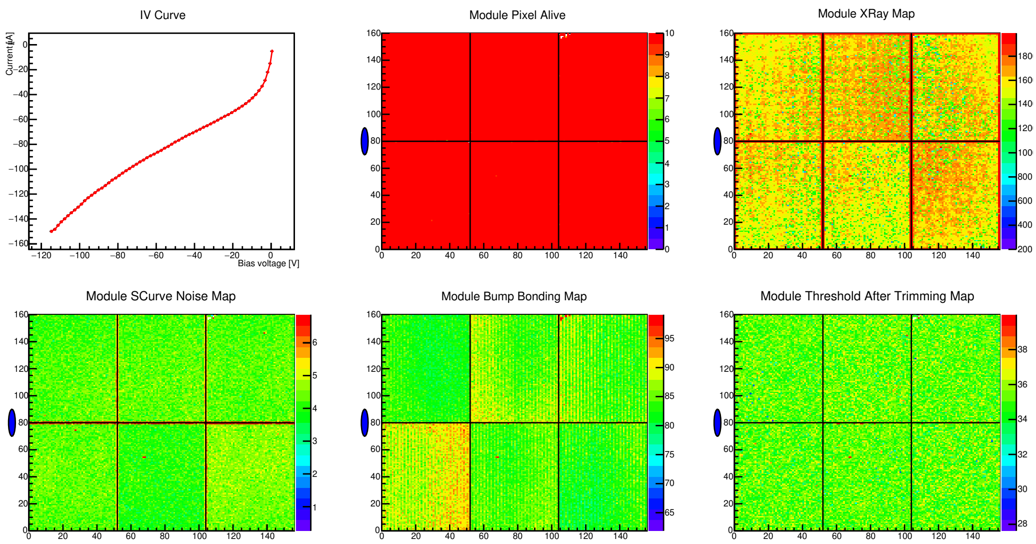

Figure 6.2: Example of summary plots for a good quality module.

For all the modules the qualification results and information are saved in an online repository. For a simplified access, the most important information (quality of the detector, final orientation, number of bad, noisy or unconnected pixels, IV characteristic, link to the location of ROC parameters) are organized in a spreadsheet.

Modules are subdivided in 5 classes, depending on the qualification results, and identified by the following flags:

- Green: high quality module to be used for the final detector.
- Light green: few defects that do not prevent the module usage.
- Light blue: timing problem in decoding the ROC data stream. The problem could be related to the wire-bonding and needs further investigation; meanwhile the module is discarded.

- Orange: serious defects, better not to use the module.

- Red: major problem that prevents using the module.

6.1.3 Results

The qualification results for all the bump-bonded modules are presented in Tab 6.3 according to the colour code explained above. It must be said that all the 'red' modules were damaged during handling or wire-bonding at the beginning of the testing campaign. Two 2×2 modules were not fully qualified since they were used for testing the RPix portcard.

Module	Layout	Class on wafer
3x2_b1w1d2	2E	B
3x2_b1w1d3	1E	B
3x2_b1w1d5	2E	B
3x2_b1w1d6	1E	B
3x2_b1w2d3	1E	A
3x2_b1w2d4	2E	B
3x2_b1w2d6	1E	A
3x2_b1w5d2	2E	B
3x2_b1w5d3	1E	A
3x2_b1w5d4	2E	B
3x2_b1w5d5	2E	B
3x2_b1w5d6	1E	A
3x2_b1w6d1	2E	B
3x2_b1w6d4	2E	B
3x2_b1w11d1	2E	B
3x2_b1w11d5	2E	B
3x2_b1w11d6	1E	A
3x2_b1w12d1	2E	A
3x2_b1w12d2	2E	A
3x2_b1w12d3	1E	A
3x2_b1w12d4	2E	A
3x2_b1w12d6	1E	A

Table 6.1: 3×2 modules

Module	Layout	Class on wafer
2x2_b1w1d1	2E	B
2x2_b1w1d2	2E	B
2x2_b1w2d1	2E	B
2x2_b1w2d2	2E	A
2x2_b1w2d4	1E	A
2x2_b1w5d1	2E	B
2x2_b1w5d2	2E	A
2x2_b1w5d3	1E	A
2x2_b1w5d4	1E	A
2x2_b1w6d1	2E	B
2x2_b1w6d2	2E	B
2x2_b1w6d3	1E	B
2x2_b1w6d4	1E	B
2x2_b1w10d1	2E	A
2x2_b1w10d3	1E	B
2x2_b1w10d4	1E	A
2x2_b1w11d1	2E	B
2x2_b1w11d2	2E	B
2x2_b1w11d3	1E	A
2x2_b1w11d4	1E	A
2x2_b1w12d1	2E	B
2x2_b1w12d2	2E	A
2x2_b1w12d3	1E	B
2x2_b1w12d4	1E	B

Table 6.2: 2×2 modules

Table 6.3: Module qualification results. Sensors are from the first CNM batch

Considering the 3×2 modules, all the 22 devices have been tested and 18 have been selected for the final assembly, of which 10 are 2E sensors. Concerning the 2×2 modules, 22 (of 24) have been tested and 16 have been selected, of which 7 are 2E.

In total 34 modules resulted available for the detector production, with a safe margin with respect to the 24 initially needed. Moreover, it was finally decided to start the 2017 data taking with only one station of pixel detectors per arm, continuing to use the well known TOTEM strip detectors for the other RPs, therefore reducing the number of needed modules to only 12.

6.2 CT-PPS DAQ software

The CT-PPS data acquisition software is based on the CMS Pixel tracker Online Software (POS). Thanks to the strong similarities between the two detectors, it has been possible to profit from the development done for the central pixel tracker, implementing the changes required by the hardware differences. The CT-PPS online software maintains all the relevant features of the POS, which allows an easy merging of the code modifications and maybe a future integration of the two systems.

The CMS pixel online software is based on the xdaq[1] toolkit and is built from a number of different components (applications). The top level application is the *PixelSupervisor*, which is responsible for the overall coordination of the DAQ by managing the supervisors that directly control the hardware. The three main supervisors are: the *PixelFECSupervisor* that provides the interface to the pixel FECs; the *PixelFEDSupervisor* that controls FEDs; and the *PixelTKFECSupervisor* that controls the tracker FEC hardware. Two other supervisors are present in the POS code: the *PixelDCSSupervisor* and the *PixelTCDSSupervisor*. The first one allows to interface the DAQ with the Detector Control System (DCS) for monitoring the detector conditions, but for the moment it is not yet implemented. The second one is the Timing and Control Distribution System (TCDS) interface and is presently the same for CT-PPS and the central pixel detector.

The online software is based on plain text configuration files divided in 20 categories (*detconfig, nametraslation, dac, trim, mask, tbm, portcard, calib,* etc.). These files contain the settings for all the objects that are controlled by the software: ROCs, TBMs, devices on the portcard (POH, DOH, etc.), μTCA boards, calibration instructions. Each of the configuration categories is organized in a folder containing sub-folders for each of the configuration versions, which in turn contain the files for all the devices for which that configuration is needed (for example, the configuration files for all the detector TBMs). These 20 types of setting files need to be loaded at each run and the versions associated to the run are collected in a file. The ensemble of the 20 category versions is associated to an unique key number. The full list of all the 20 category files together with the corresponding key are saved in a file. In this way it is always possible to recover the conditions whereby a run was acquired.

An important difference between the central pixel and the CT-PPS trackers is the naming scheme, which is related to the detector layout. The software is structured in such a way that each ROC has a unique name that is then converted into a 32-bit number. From the ROC name, indicated in the *detconfig* file, the online software retrieves the names of the files containing all the information needed for its hardware configuration: registers (*dac* configuration), trim parameters (*trim* configuration), and pixel to be masked (*mask* configuration). In the same way, the TBM associated to the ROC (*tbm* configuration) is found. Moreover, thanks to the *nametraslation* configuration, the associated FED and FECs reading and controlling the module with that ROC are identified.

An example of a ROC name explaining the coding scheme is:

CTPPS_SEC45_RP023_PLN0_ROC1

where

- SEC indicates the sector (45 or 56).
- RP is the Roman pot number as indicated in Fig. 6.3. For the 2017 data taking the pixel stations are installed in the Roman pots with numbers 023 and 123.
- PLN in the plane number, which can go from 0 to 16 (for future applications), with number 0 referring to the first plane traversed by the protons.

[1]https://svnweb.cern.ch/trac/cmsos

- ROC is the ROC number, which can go from 0 to 16, following the same numbering scheme of the token chain reported in Fig. 6.1.

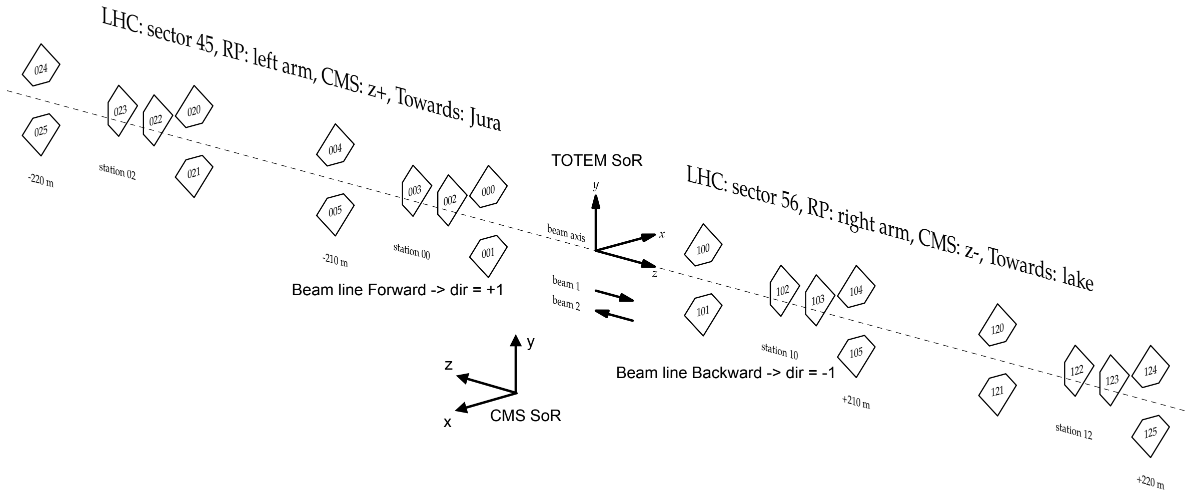

Figure 6.3: The RP naming scheme. The different CMS and TOTEM coordinate systems are also indicated.

Unlike the central pixel detector, it is possible by means of the RPix portcard to selectively switch ON or OFF the analog and digital power of the ROCs of a plane. This feature allows to exclude a detector with major problems without affecting the others. This mechanism takes advantage of the channel that controls the DCDC converter of the central pixel detector. Since in the CT-PPS case the material budget of the powering cable is not an issue, the DCDC converter was not included in the RPix portcard design and this channel has been connected to switches. This feature has been included in the CT-PPS online software by using the flag "noInit". A ROC marked with this flag is not programmed but remains powered. If instead all the ROCs of a module are set with this flag, the module is completely switched off by removing the power.

The online software functionality has been tested with a detector package installed in a Roman pot, with secondary vacuum and temperature at $\sim -25°$C in order to reproduce the CT-PPS conditions. The online software should be able to perform all the testing and calibration procedures previously done with the DTB and that are needed for the detector commissioning. Thanks to the module testing procedure done with the DTB, ROC and TBM registers were already optimized. The values obtained by this procedure have been loaded in the configuration files as a starting point. Results of the main tests of the online software functionality are presented below.

The efficiency map, expressed in percentage, of a 3×2 module is showed in Fig. 6.4.

As with the DTB, noise and threshold of each pixel can be determined by an S-curve measurement. Figure 6.5 presents the noise distribution for all the pixels of the detector package (six planes). To guarantee the full depletion of the sensors, a bias voltage of -10 V is applied. It is worth remembering that a Vcal unit corresponds to 50 e^-.

The trimming procedure is based on an offline algorithm which uses as input the thresholds measured at different values of VThrComp, VTrim and TrimBits, and produces as output the new threshold parameters. It is an iterative procedure that requires good values to start with. The threshold distributions before and after the trimming procedure with the online software are presented in Fig. 6.6. A reduction of the threshold RMS of $\sim 30\%$ can be observed after trimming. The increase of the mean threshold from ~ 1600 to 2060 e^- reflects the different

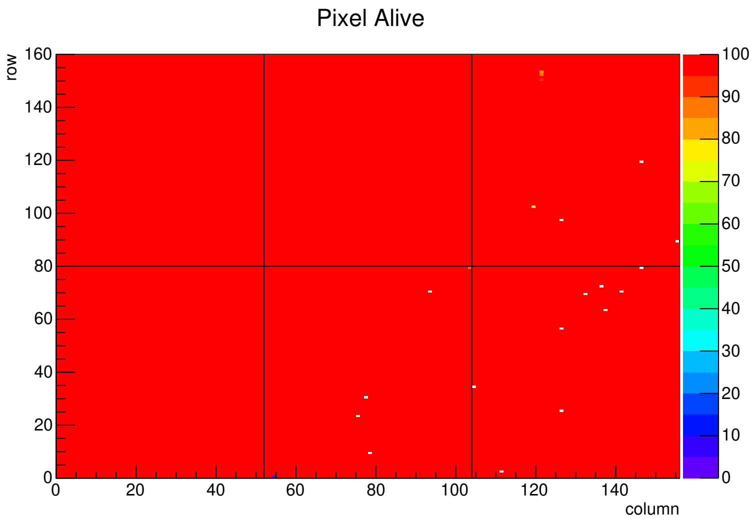

Figure 6.4: Pixel alive map for a 3×2 module.

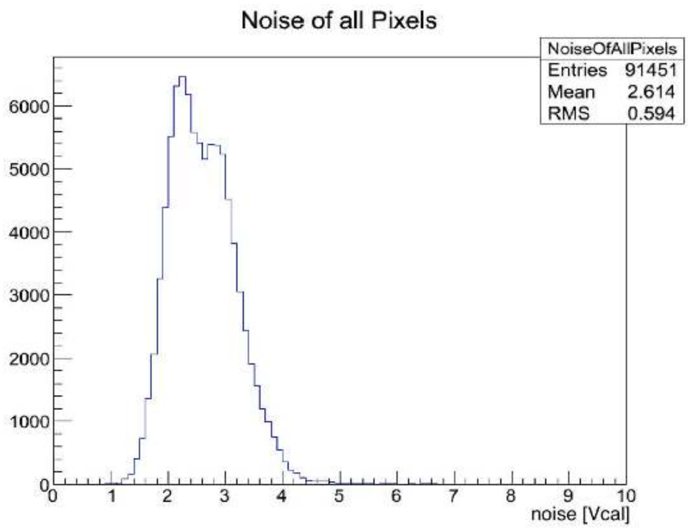

Figure 6.5: Noise distribution for all pixels of a detector package.

target threshold of the DAQ with respect to the DTB. Nevertheless, the final threshold is still very low if compared to the ~ 18000 e$^-$ expected for a MIP.

Finally, the gain calibration and the pulse height optimization are discussed. The gain calibration procedure allows to calibrate the ROC 8-bit ADC for converting the pulse height expressed in ADC counts into the charge in electrons. In first approximation, the gain calibration curve can be fitted with a straight line in the linear region before the ADC saturation. The slope and intercept of this curve provide an estimate of the region in which the ADC is linear. The distribution of the two values for all the pixels of the detector package is shown in Fig. 6.7. Considering the average values and that the ADC saturates at 255 counts, it can be derived that in this condition the ADC is linear up to 22.4 ke$^-$ with ~ 180 available counts.

To improve the ADC performances, the DAQ software provides a calibration which optimizes slope and intercept for all the pixels by scanning the pulse height registers PHOffset and PHScale of the ROC. Figure 6.8 shows the slope and intercept distributions obtained doing the gain calibration after the optimization of the ADC working point. Using the same approach as before, the linear range is extended up to 40 ke$^-$ with ~ 230 available counts.

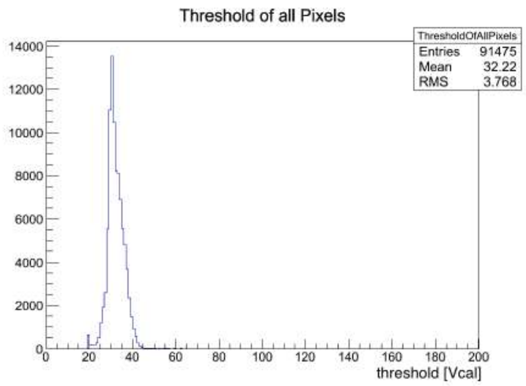

(a) Before trimming.

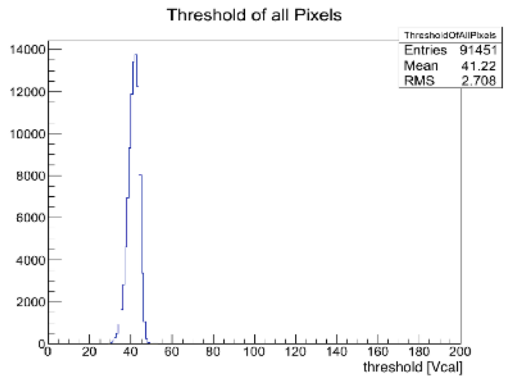

(b) After trimming.

Figure 6.6: Threshold distribution for all the pixels of a detector package before and after trimming with the online software.

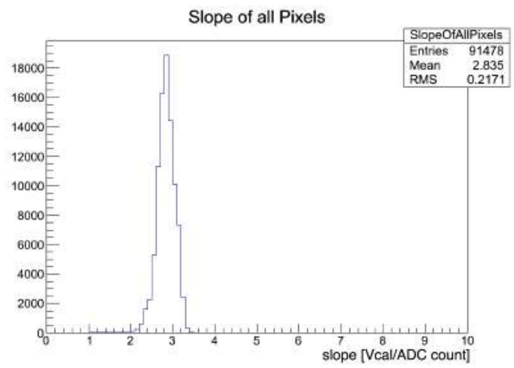

(a) Slope.

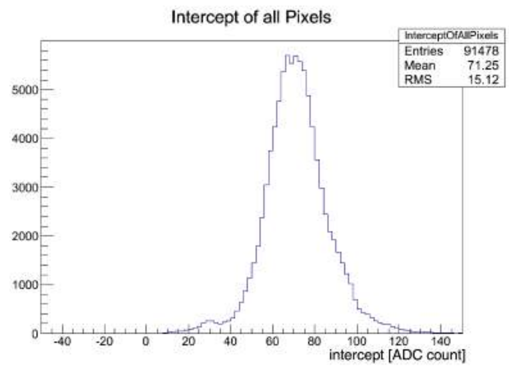

(b) Intercept.

Figure 6.7: Slope and intercept distributions for the straight line fitting the gain calibration curves obtained before the pulse height optimization.

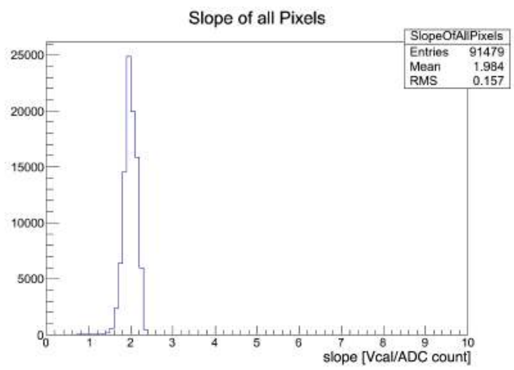

(a) Slope.

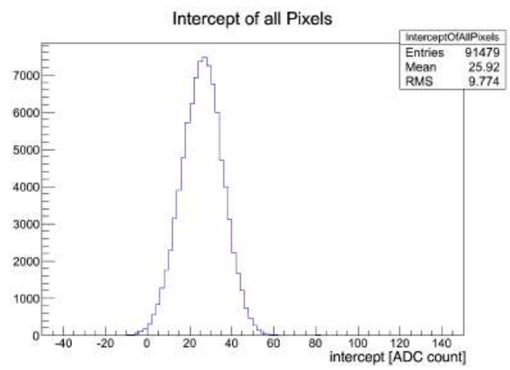

(b) Intercept.

Figure 6.8: Slope and intercept distributions for the straight line fitting the gain calibration curves obtained after the pulse height optimization.

6.3 Station assembly

A fundamental requirement for the CT-PPS tracking system is the precise alignment of the modules in the detector package in order to minimize the distance between the modules and the Roman pot thin window. This requires the precise gluing of the module on the flex hybrid with the TPG layer attached. The picture of Fig. 6.9 shows the custom tool produced in Genova for the gluing. The flex hybrid is positioned on the tool by using 2 mm-diameter dowels inserted in the alignment holes shown in Fig. 6.1. The module is glued with a silicone-based glue and pressed in position by a weight of 200 g for 24 hours.

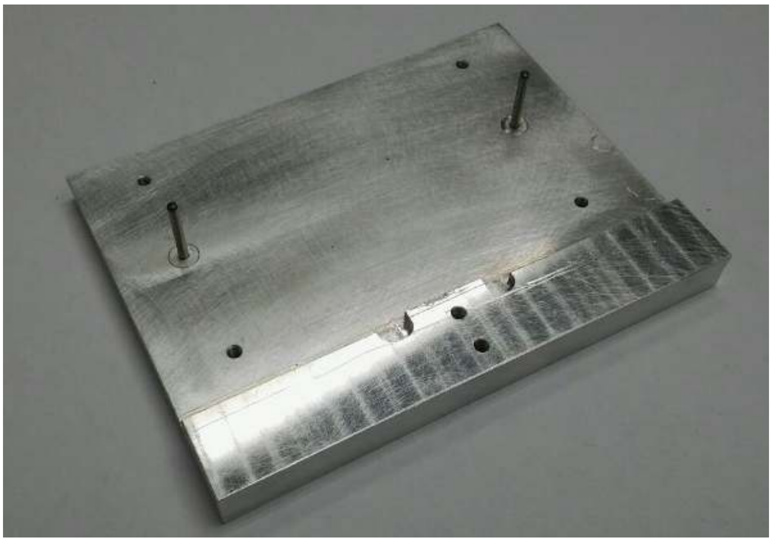

Figure 6.9: Custom tool for precision gluing of the module to the flex. The two dowels keep in position the TPG layer while the module is glued in contact with the machined wall.

The two stations to be installed in the LHC tunnel have been assembled at CERN. A picture of the mounted detector package is shown in Fig. 6.10.

Planes are screwed to aluminum supports connected to the cooling pipes. To improve the thermal contact Dow Corning TC-5022 thermal grease is used. 2 mm dowels allow to align the TPG layer carrying the module with respect to the aluminum supports. On each aluminum support two planes are screwed, one for each type of TPG layer geometry, forming a sub-element of the detector package. Three sub-elements are then assembled together and precisely aligned with 4 mm dowels to build the detector package. The package is completed with front and back structures that, besides protecting the modules, allow the correct positioning of the package within the Roman pot. When inserting the detectors into the pot, copper springs on the back structure push the package in contact to the opposite pot wall where machined alignment contacts are implemented.

Positioning the modules close to the pot bottom thin side facing the beam needs a more accurate procedure. The module edge positions are measured with a 1 μm resolution laser. Since the planes are tilted, aluminum shims are leaned to the module edges to have a flat surface for the measurement. In this way, the most prominent plane position is measured, while the relative positions of the other planes will be obtained by aligning with protons.

After determining the plane position, screws with precision washers are installed on the detector package in order to go in contact with the Roman pot bottom thick wall and locate the detector planes at 200 μm from the thin window. Considering the pot wall planarity and the manufacturing precision of screws and washers, the uncertainty on this distance is quoted to be 50 μm.

For connecting the detector package to the cooling system, the lateral sides are machined

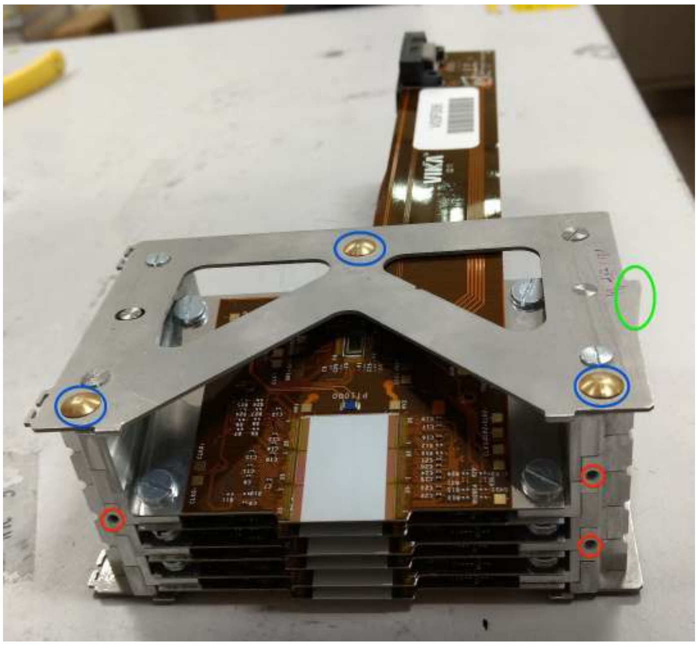

Figure 6.10: Picture of the mounted detector package. The holes for the screws used for detecting the distance from the thin window are hooped in red. The green circle indicate the spacer from the lateral RP wall, while the blue ones point out the contacts for the front wall. On the opposite side, not visible in the photo, the springs to ensure the contact are present.

in order to host the pipes. To provide a good thermal contact, a plane with the same grooves is screwed on the lateral sides of the package to fix the pipes. In addition to the PT1000 temperature sensors located on each plane, four of which can be read out by means of the station temperature connector, other four PT1000 sensors are installed on the cooling lines, one on the inlet and one on the outlet of both cooling lines. Both sensors use a 2-wire readout and a calibration is needed to take into account the voltage drop along the wires from the Roman pot to the counting room where the Embedded Local Monitor Board (ELMB) for temperature measurement is located.

When the detector package is ready, the six flex hybrids are connected to the RPix portcard and the full station is assembled (Fig. 6.11). A first check of the complete station, connected to a replica of the services present in the LHC tunnel, is done in laboratory with the DAQ software and the Detector Control System (DCS) readout for temperature, pressure, and radiation monitors.

The final detector packages consist of 5 planes of 3×2 modules plus a 2×2 module. Planes have been arranged to have an almost uniform distribution of 1E and 2E configurations. For the module lists see Tabs. 6.4 and 6.5.

Figure 6.11: Picture of a CT-PPS tracking station. The detector package visible at the bottom is connected by the flex hybrids to the RPix portcard located at the top.

6.4 Station test at H8 CERN beam line

Before installation, assembled stations have been tested in the CERN H8 hall in the same conditions of cooling and vacuum of the LHC tunnel.

The mechanical verification of the space constraints was done with a perfect replica of the Roman pot structure present in the tunnel, also by using mockups of the detector package. Moreover, the insertion procedure could be checked.

Once a detector package was inserted and screwed to the Roman pot structure, vacuum tests were performed by lowering the pressure below the resolution of the pressure gauge ($\sim$ 1 mbar). After stopping the pump, the leak rate was measured to be $\sim$ 0.5 mbar/h in both cases, showing a reasonable vacuum tightness.

The subsequent step was to check the cooling lines by pressurizing them with freon and seeking for leaks with a sniffer close to the joints. Detectors were then cooled down to -25°C before switching the power on. After the complete configuration of the modules, an increase of $\sim$ 2°C was measured on the detector planes, as shown in Fig. 6.12.

To verify that the modules and the electronics were not damaged during the installation and also that no problems developed by running at low temperature, Pixel Alive and SCurve tests were performed, after applying -10 V to bias the sensors. These were also important tests for the final electronics chain since for the first time the DOH mezzanine (DOHM) for the Slow Control of the RPix portcard was used, together with the final cables and optical fibers to be installed in the tunnel.

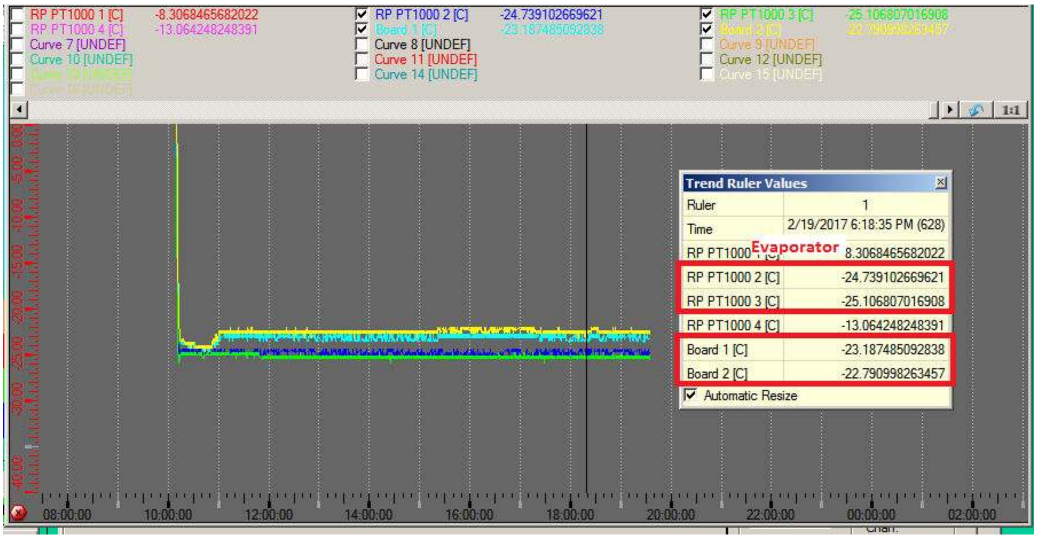

Figure 6.12: Temperature measured at the H8 Roman pot setup on two detector planes (yellow and light blue) and cooling lines (green and blue) as a function of time. An increase of $\sim 2°C$ can be observed on the planes when switching the power on (11:00).

plane	sensor	size	layout	max HV (-V)	current (μA)
0	CNM_CT_PPS_3x2_b1w12d6	3x2	1E	100	0.7
1	CNM_CT_PPS_2x2_b1w1d2	2x2	2E	100	2.8
2	CNM_CT_PPS_3x2_b1w11d1	3x2	2E	90	3.5
3	CNM_CT_PPS_3x2_b1w11d6	3x2	1E	45	4.0
4	CNM_CT_PPS_3x2_b1w5d4	3x2	2E	90	2.6
5	CNM_CT_PPS_3x2_b1w5d2	3x2	2E	130	2.8

Table 6.4: Modules installed in sector 45. The current refers to the value measured at the maximum bias voltage. The current resolution is 0.1 μA and the bias voltage refers to the set voltage, while the effective one may differ by $\pm 0.3\% \pm 0.2$ V [143].

The final safety check was to verify that bias voltages close to the breakdown values did not cause discharges at the foreseen low pressure conditions, since it is known that low pressures could induce discharges at relative low voltages [142]. A conservative current compliance of 5 μA was set on the CAEN HV power supply and the bias voltage was raised keeping the current below this limit. No malfunctioning of the modules was observed, thus verifying that discharges do not occur in the CT-PPS working vacuum conditions at least up to 140 V.

Tables 6.4 and 6.5 list the modules installed in the two detector packages, together with the maximum bias voltage and the relative measured leakage current. Only two sensors, one per pot, have a low breakdown voltage, but still high enough with respect to the depletion voltage to guarantee high efficiency, at least for the first part of the data taking before experiencing high irradiation.

plane	sensor	size	layout	max HV (-V)	current (μA)
0	CNM_CT_PPS_3x2_b1w12d2	3x2	2E	110	1.2
1	CNM_CT_PPS_2x2_b1w6d2	2x2	2E	90	3.0
2	CNM_CT_PPS_3x2_b1w5d6	3x2	1E	130	0.9
3	CNM_CT_PPS_3x2_b1w12d1	3x2	2E	30	4.9
4	CNM_CT_PPS_3x2_b1w5d3	3x2	1E	140	0.9
5	CNM_CT_PPS_3x2_b1w1d3	3x2	1E	80	3.8

Table 6.5: Modules installed in sector 56. The current refers to the value measured at the maximum bias voltage. The current resolution is 0.1 μA and the bias voltage refers to the set voltage, while the effective one may differ by $\pm 0.3\% \pm 0.2$ V [143].

6.5 Detector installation

The two CT-PPS pixel tracker stations have been installed in March 2017 in sector 45 and 56 of the LHC tunnel. Thanks to the experience of the Roman pot team of TOTEM, the operation went very smoothly. A picture of the technician inserting a station is shown in Fig. 6.13. As a further precaution against HV discharges, a 25 μm-thick kapton foil has been inserted between the thin window and the detector package.

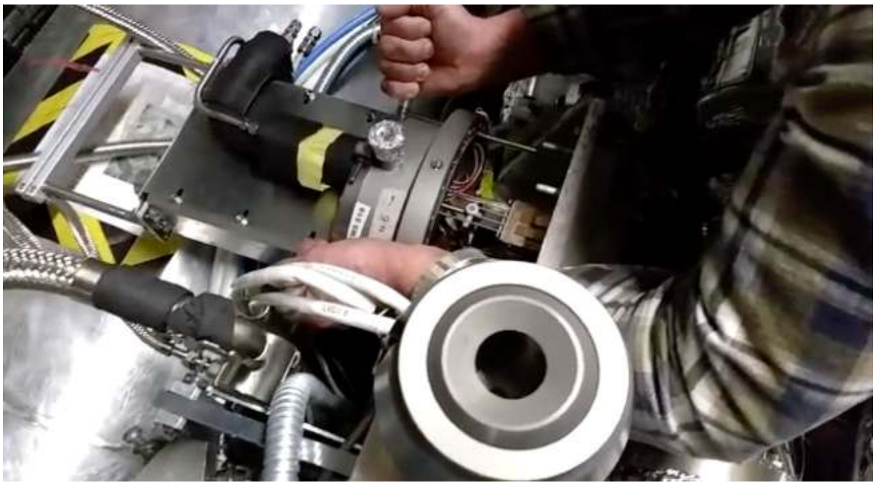

Figure 6.13: Insertion of the detector station in the Roman pot of sector 45.

After sealing the pots and starting the pumps, the leak rates have been measured to be ~ 3 and ~ 2 mbar/day for sector 45 and 56, respectively. The vacuum pumps start when the pressure reaches 20 mbar and stop when it goes lower than 10 mbar. The higher value has been chosen to have a maximum dew point of ~ -35°C. The cooling system has been set at ~ -25°C.

Digital and analog low voltages of the RPix portcard have been set to 2.8 and 1.8 V, respectively. For the high voltage, two CAEN A1512 boards, one per sector, have been installed in the Underground Service Cavern (USC). Each plane is powered by a dedicated channel to have the flexibility required by the different breakdown voltages of the installed sensors. A hardware voltage limit of 200 V is set on the CAEN boards since the non-uniform irradiation should not strongly increase the breakdown voltage. Anyway, being the HV power supplies located in USC, this value can be easily changed. The current compliance has been set for the moment to 10 μA.

Pressure and temperature sensors have been connected to the CMS Detector Control System (DCS) and Detector Safety System (DSS). DCS values have been calibrated compensating for the cable resistance. Since this is not possible with the DSS, which controls the status of the system and triggers the emergency actions, a difference of ~ 10 degrees is present between the DSS and DCS readings and the DSS emergency threshold has been set accordingly.

The μTCA crate housing the DAQ boards is located in the USC cavern. The connection between the DOHM and RPix portcards in the tunnel and the μTCA boards in the USC is provided by optical fibers, whose signal attenuation has been measured to guarantee the proper transmittance. The fiber length is the same for the two sectors to simplify the timing optimization. Two bundles per sector of twelve fibers each, one bundle for the DOHM and the other one for the RPix portcard, are used. Fibers from the portcard consist of data fibers (from 1 to 6), which are connected to the FED, and fast command fibers (from 9 to 12), connected to the pixel FEC.

A tracker FEC provides four channels, with each channel hosting four connections for the DOHM fibers. From the DOHM bundle, fibers 1, 2, 11 and 12 are connected to the tracker FEC while the other fibers are not used. The four available channels are sufficient for the two installed stations plus the other two that are expected to substitute the strip stations. The tracker FEC is identical from the hardware point of view to the pixel FEC, but the firmware is different.

The FED has a custom hardware which allows to directly connect a twelve-fiber bundle. Since each fiber comes directly from a POH, a FED reads up to 12 modules. Although one FED is presently enough, two FEDs have been installed in the crate to take into account the other two pixel stations that are expected to be installed. Each FED is directly connected to the Front-end Readout Link (FRL) through an optical 10 Gb/s transceiver to transfer the data to the CMS central DAQ.

Finally, the μTCA crate hosts a AMC13 board that provides clock, timing, and control signals to the FECs and FEDs. This board can also generate trigger and clock, which have been used during the tests in laboratory. During data taking, these signals must be provided by the central DAQ in order to maintain the synchronization. For this reason, the AMC13 is connected to the Timing and Control Distribution System (TCDS).

6.6 Detector commissioning

The commissioning phase foresees a long list of checks to be accomplished by CT-PPS before being stably included in the CMS central data acquisition. All the tests previously performed on the detectors at H8 were repeated. The CT-PPS pixel DAQ was subjected to stress runs with the central DAQ by using random triggers, in order to prove its reliability in running within the CMS data acquisition chain. The first LHC fills with few proton bunches were then used for finding the correct latency and qualifying the detector for the data taking. The last step of the commissioning phase that could be included in this thesis is the first alignment run, taken on May 22nd with the new LHC optics for 2017. The most relevant steps of the pixel detector commissioning are described in the following.

Verification of the DCS and DSS readings and proof of the action matrix in case of failures that might impact the safety conditions for the detector and the LHC are preliminary unavoidable steps. The CT-PPS DCS panel, with the main parameters for the pixel stations highlighted, is shown in Fig. 6.14. The safety actions are triggered by the DSS system, which is in charge of switching off the detector in case cooling or vacuum conditions are outside the safety margins.

Some attention must also be paid to the HV, which has to be applied only after the portcard is switched on and configured, giving power to the ROCs. In fact, based on the acquired experience, applying the HV to a non-powered ROC might damage some pixels. This effect is assumed to be due to the sensor leakage current entering in a pixel unit cell. For the same reason, in case the LV goes off also the HV is switched off by the DCS.

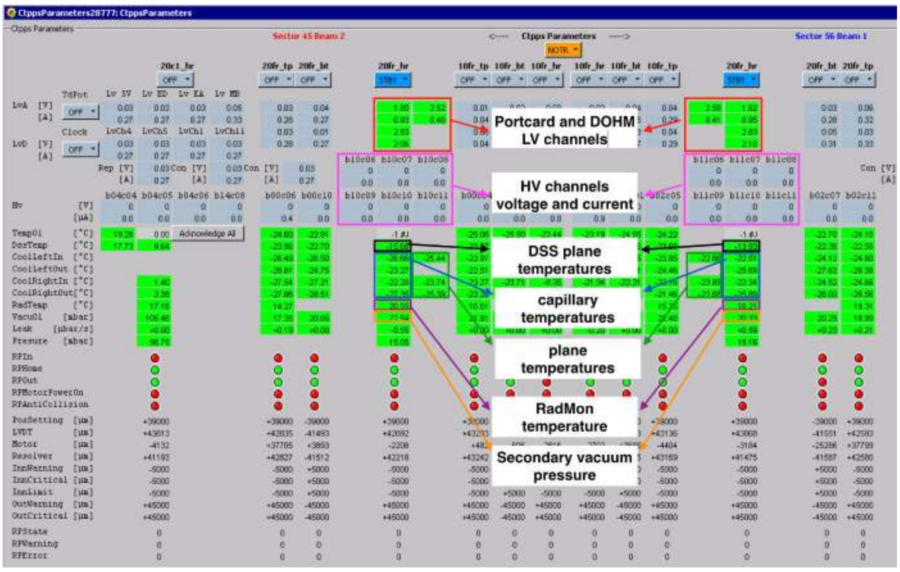

Figure 6.14: Screen shot of the CT-PPS panel with the pixel station parameters highlighted.

The integrity and functionality of the detector after installation has been verified by configuring the modules and performing their calibration. An evidence of being able to communicate with the portcard for powering and setting the ROCs is the increase of the plane temperature by 2°C shown in Fig. 6.15, which is consistent with what was observed during the H8 tests.

Preliminary Pixel Alive tests have been performed for each plane at the maximum bias voltage (see Tabs. 6.4 and 6.5) and the module maps, presented in Fig. 6.16 and 6.17 for sectors 45 and 56 respectively, do not show any serious problem.

For the rest of the commissioning, the HV has been set to -30 V for all the planes. This value provides a large margin above the depletion voltage (-3 - -5 V) and also ensures the extension of the efficient region beyond the geometrical edge of the pixel of ~ 70 and ~ 130 μm for 1E and 2E sensors, respectively. It is a reasonable value for the start of the data taking but it will need to be increased as the module irradiation increases. Bias scans will be frequently performed measuring the efficiency of the detectors.

The results of the S-curve measurement are shown in Fig. 6.18 for all the pixels of the installed modules. The thresholds have been equalized to the target value of 50 Vcal (1 Vcal $\simeq$ 50 e^-) and the measured average value is ~ 2030 e^- with a dispersion of ~ 134 e^-. The noise is measured to be ~ 127 e^- with a tail at higher values due to the large pixels at the border between ROCs. The noise distribution indicates that the set threshold is probably conservative and could be lowered. This possibility needs to be verified with particles to see if the beam induces external noise.

Once the threshold is set, the percentage of inefficient channels has been evaluated by means of the Pixel Alive test. Considering as bad pixels those having an efficiency lower than 90%, the number of bad pixels is 129, less then 0.05% of the channels. Hot pixels have been measured by sending 10000 triggers to the ROCs and considering noisy a pixel that registers at least one hit. 118 ($<$ 0.05%) hot pixels have been identified, with a rate of noisy hits per pot of less than one per event.

The last step of the detector calibration has been the optimization of the gain parameters. Figure 6.19 shows the distributions of intercept and slope of the straight line fitting the ADC counts as a function of the injected charge. From the distributions it can be evaluated that the ADC linear range goes up to ~ 38 ke^- with ~ 230 available counts.

The calibrations performed in the commissioning phase ensure the correct detector operation

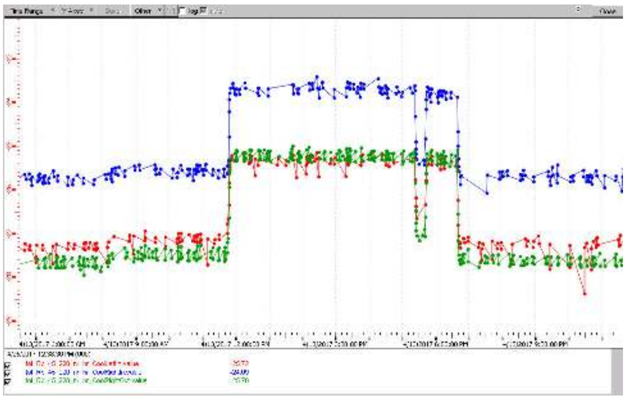

(a) Temperatures on TPG for sector 45.

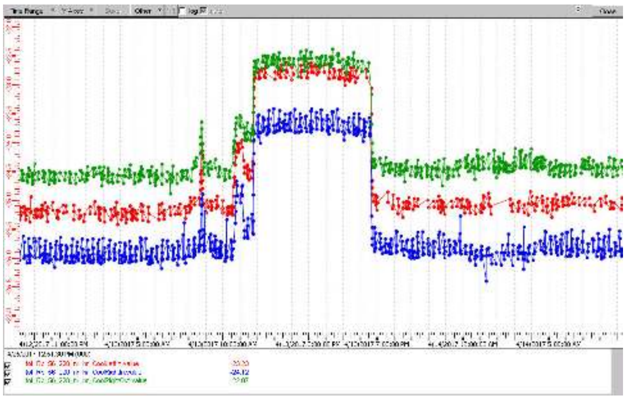

(b) Temperatures on TPG for sector 56.

Figure 6.15: The DCS plot shows the temperature, in °C, as a function of time, measured with the PT1000 sensors placed on the TPG for three planes on each side. The temperature variation due to the power ON and OFF on the modules is compatible with the results obtained during the test at H8.

at the beginning of the data taking. Due to the radiation damage, a constant monitoring of ROCs and sensors will be required and the calibration procedure is foreseen to be repeated weekly.

The CT-PPS pixel DAQ has been first tested using the so-called miniDAQ, a light version of the CMS DAQ. The detector has been successfully tested running with a random trigger rate of 100 kHz, the maximum rate expected for the 2017 data taking. In order to better reproduce the data taking conditions, the HV has been switched off and the threshold has been lowered to $\sim$ 1400 e^- in order to obtain $\sim$ 24 noisy hits per trigger per station. This value has been chosen by assuming an average of 4 hits per plane, which is an overestimation of the 1.9 average number of fired channels measured by the strip planes during the 2016 data taking. In these conditions the detector has been able to run for several hours without interruptions.

An important requirement of any CMS sub-detector DAQ system is the ability of re-synchronizing the acquisition without stopping the data taking. Moreover, the event counter should restart from 0. This has been successfully checked for CT-PPS by sending a resync command every $\sim$ 5 s while taking runs with a 20 Hz random trigger. Figure 6.20 shows the event counter resetting every $\sim$ 100 triggers, in accordance with the trigger frequency and the rate of re-synchronization.

As a further test, the threshold has been reduced to 1250 e^- and a run at 120 kHz has been taken. In these conditions, the hit rate per trigger per pot was 69 ± 43, which crashed the run because the FED went out-of-sync. Manually issuing a resync recovered the run, confirming

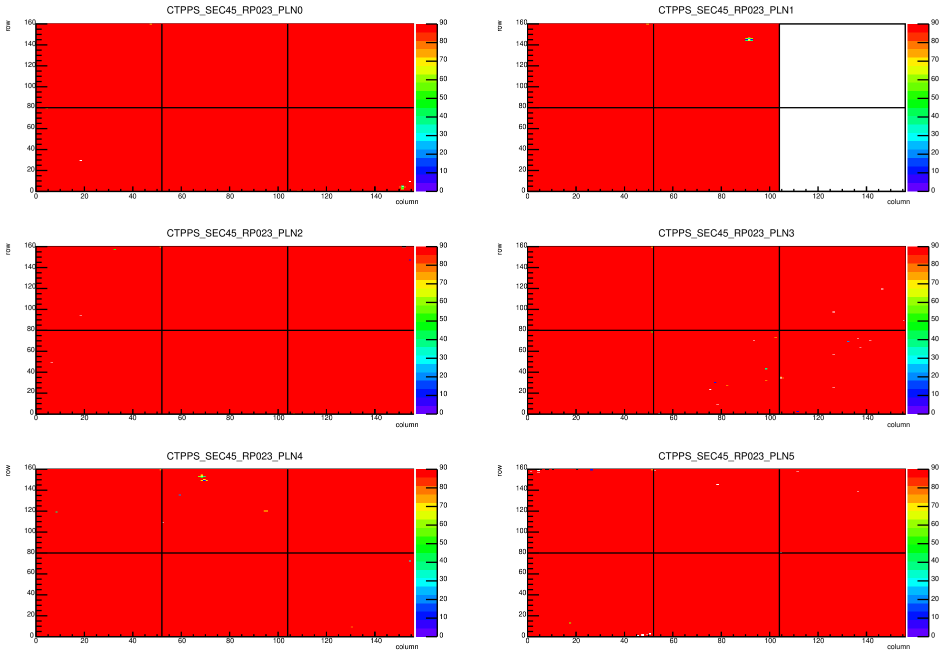

Figure 6.16: Module maps of the Pixel Alive test at the maximum HV for sector 45.

the effectiveness of the command.

Qualification of the CT-PPS pixel DAQ system for participating in the CMS data taking has been obtained running with the central DAQ system similar tests as those performed with the miniDAQ. In particular, a 0.5 Hz re-synchronization test has been done while running with 100 kHz random trigger without crashing the run. This test also proved that the dead time caused by the CT-PPS subsystem is smaller then 0.01%. In general, the system demonstrated to well react to all the standard stress tests and to be able to run with the CMS central DAQ system.

A very important step in the commissioning procedure is the measurement of the correct latency of the detector.

A global run taken with a random trigger during an LHC fill with a single proton bunch was used for this purpose. The LHC filling scheme consists of 3564 bunches (from 0 to 3563) which can be filled with protons. In that particular run, the colliding bunch was the number 1. When a trigger is issued to the detector, the FED provides the corresponding bunch, hence a random trigger can scan over all bunches. If the detector latency is not correctly set, the trigger on the colliding bunch cannot see any hits apart some noise, while the random trigger can register an activity at another bunch. Measuring the offset between the colliding bunch at which the collisions occur and the bunch where some activity is observed by the random trigger, the latency shift can be determined.

Figure 6.21 shows for both pixel stations the activity in the RP as a function of the bunch number. In order to discriminate between particles and noise, at least 5 planes over 6 were required to register hits. Unfortunately, the frequency of random triggers written on disk was only 10 Hz and the detectors were in the "garage" position (the farthest distance from the beam). So, only two events, one per pot, were measured. However, since both events were registered at the same bunch number, the latency could be determined. The bunch number found by the random trigger was 3486. Since this is a cyclic counter, 79 is the difference with respect to the real injected bunch. Therefore, the WBC of the ROCs has been changed from 100 to 179.

In order to check the latency, a subsequent run was taken during a fill with two colliding

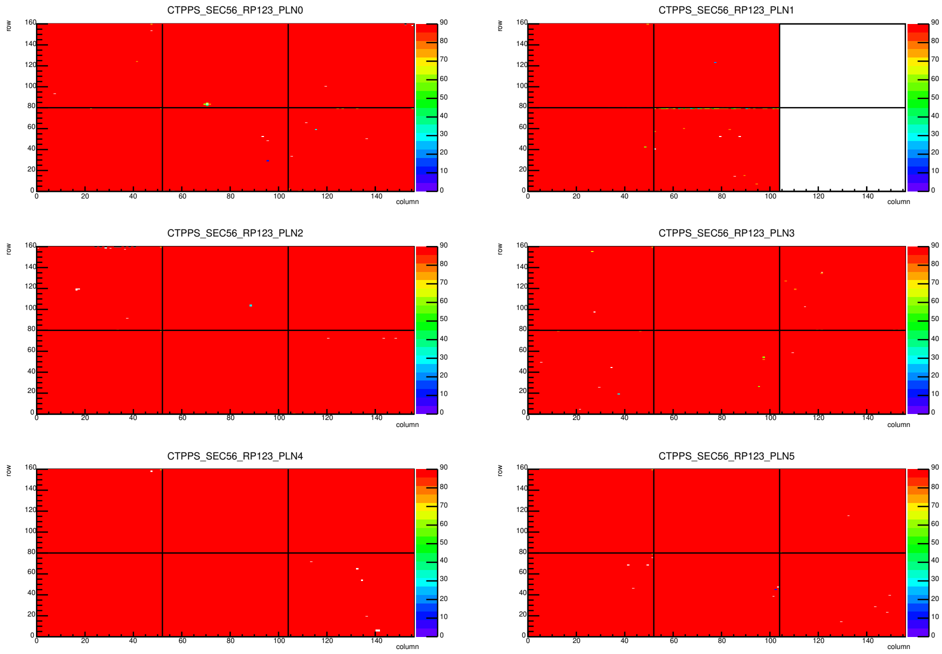

Figure 6.17: Module maps of the Pixel Alive test at the maximum HV for sector 56.

bunches, corresponding to numbers 1 and 1786. Figure 6.22 shows for both pots the bunch crossing numbers for which at least 5 planes registered hits. The bunch crossing numbers correspond to the expected ones, thus proving that the latency of the detector has been set in the correct way.

Having the correct latency, a long run was acquired with the trigger synchronized with the two colliding bunches. A subset of $\sim$ 1 million triggers has been used to produce Fig 6.23, which shows for both detector stations the hit maps of all the planes. Being the stations in the "garage" position, the maps show a quite uniform distribution of the hits generated by protons widely out of the beam envelop or by showers due to particle interactions with the LHC elements. Although these hits have no physical interest, they prove that the CT-PPS pixel tracking detector is correctly read out by the CMS DAQ system and that it is ready for data taking.

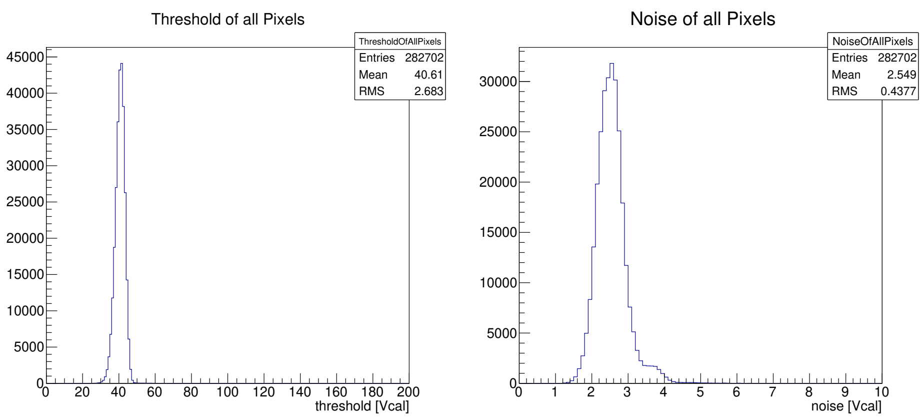

(a) Threshold distribution for all pixels. (b) Noise distribution for all pixels.

Figure 6.18: Pixel threshold and noise distributions for all the installed modules.

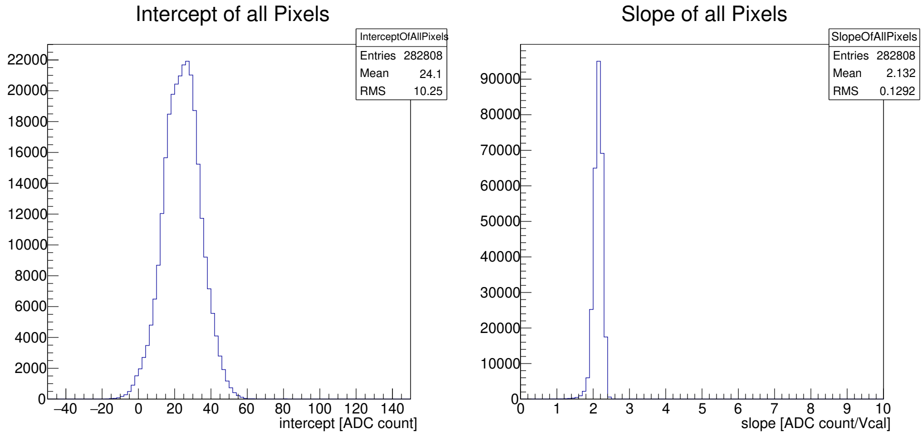

(a) Intercept distribution for all pixels. (b) Slope distribution for all pixels.

Figure 6.19: Distributions of intercept and slope of the straight line fitting the ADC characteristics for all the installed modules.

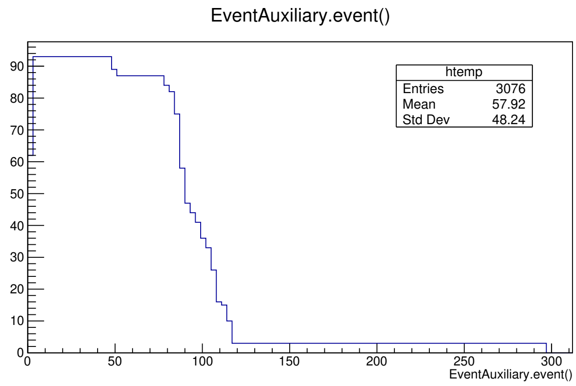

Figure 6.20: Event count to test the effectiveness of the resync command. As expected with a 20 Hz random trigger and a re-synchronization every ~ 5 s, the event counter resets every ~ 100 triggers.

The last step of the commissioning procedure that is presented in this thesis is the alignment run taken on May 22nd with the final LHC optics for 2017, of which only a very preliminary result can be included since the analysis of the data is presently ongoing.

For this special run, completely dedicated to CT-PPS, the pots were carefully inserted, approaching the beam at 8.5σ. During the initial phase of the procedure, while the pots were slowly moving and their distance with respect to the beam determined, several runs were taken with different clock delays in order to measure the fine timing of the stations. This information will crucial for determining the sampling point and associate all the hits within the same time window[2]. These data are being analyzed offline to obtain the precise timing settings.

The rest of the alignment run was taken using the timing settings obtained in previous runs, which already ensured a very high efficiency. Figure 6.24 shows the hit maps of all the pixel modules installed in the two stations. It is clearly visible the expected profile of the protons exiting from the beam envelope. The analysis of the collected data just started. Data will allow to measure the position of the modules with respect the beam and to align the planes with respect to each other. Both information will be crucial for the reconstruction of the data which

[2]Hits with lower collected charge pass the threshold later with respect to hits with higher signals and it is important that all hits are associated to the correct bunch crossing.

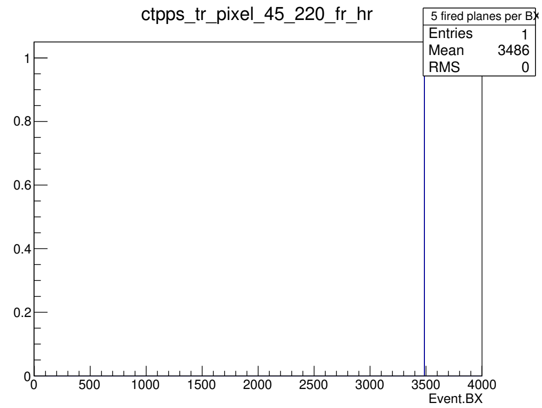

(a) Pixel detector in sector 45.

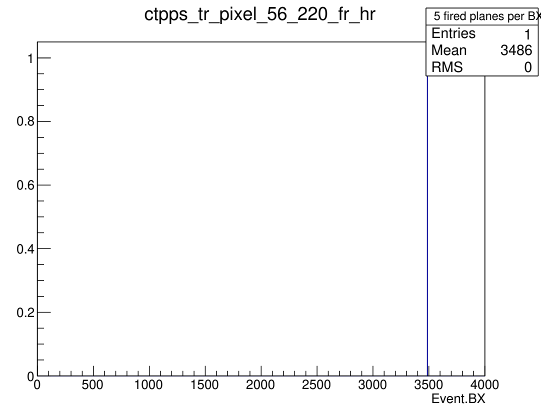

(b) Pixel detector in sector 56.

Figure 6.21: Events with at least 5 hit planes per pot as a function of the bunch number, taken with a random trigger that allows to scan over all bunches.

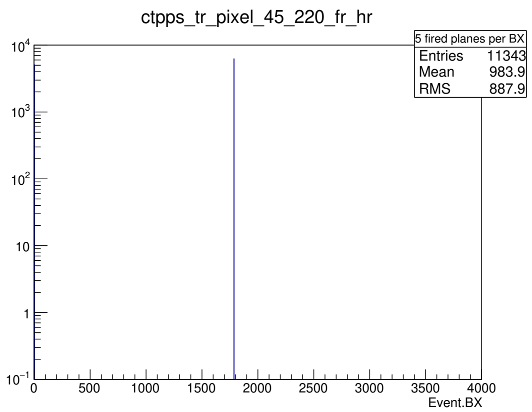

(a) Pixel detector in sector 45.

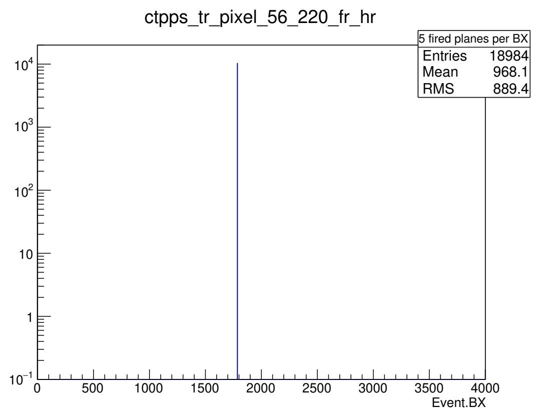

(b) Pixel detector in sector 56.

Figure 6.22: Events with at least 5 hit planes per pot as a function of the bunch number. Data have been taken triggering on the colliding bunches, corresponding to the numbers 1 and 1786. Due to the horizontal scale, the events at bunch number 1 are barely visible.

will be collected in 2017.

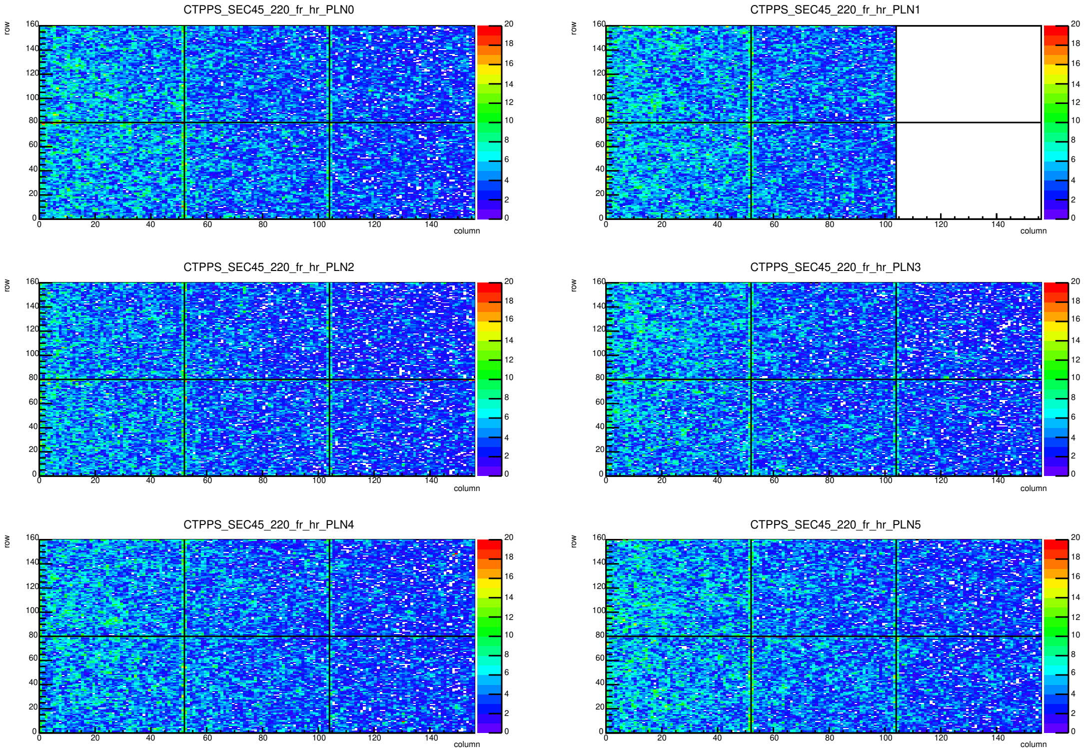

(a) Pixel detector hit maps in sector 45.

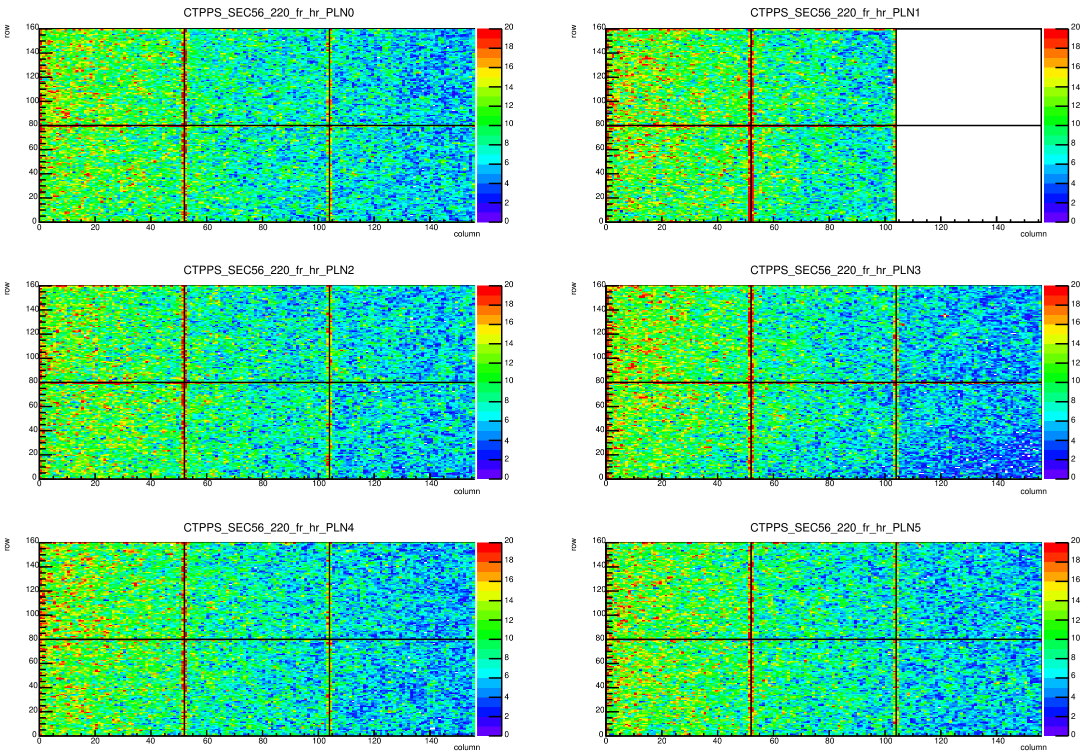

(b) Pixel detector hit maps in sector 56.

Figure 6.23: Hit maps of all the modules, obtained in the "garage" position during a fill with two colliding bunches. The larger occupancy observed in sector 56 is due to the different optics of the two beams, as also observed by the other CT-PPS detectors.

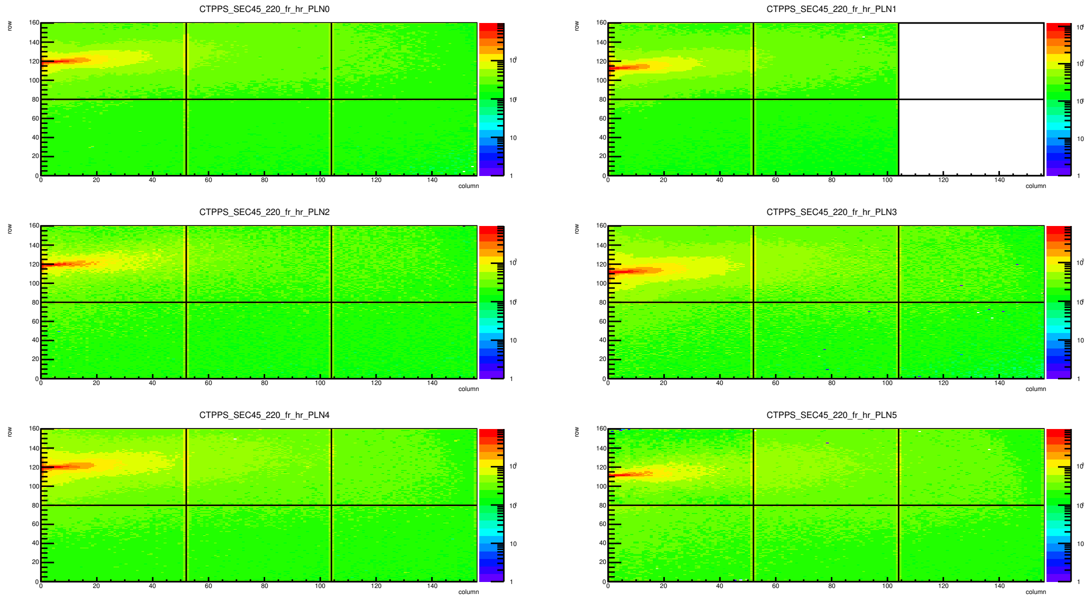

(a) Pixel detector hit maps in sector 45.

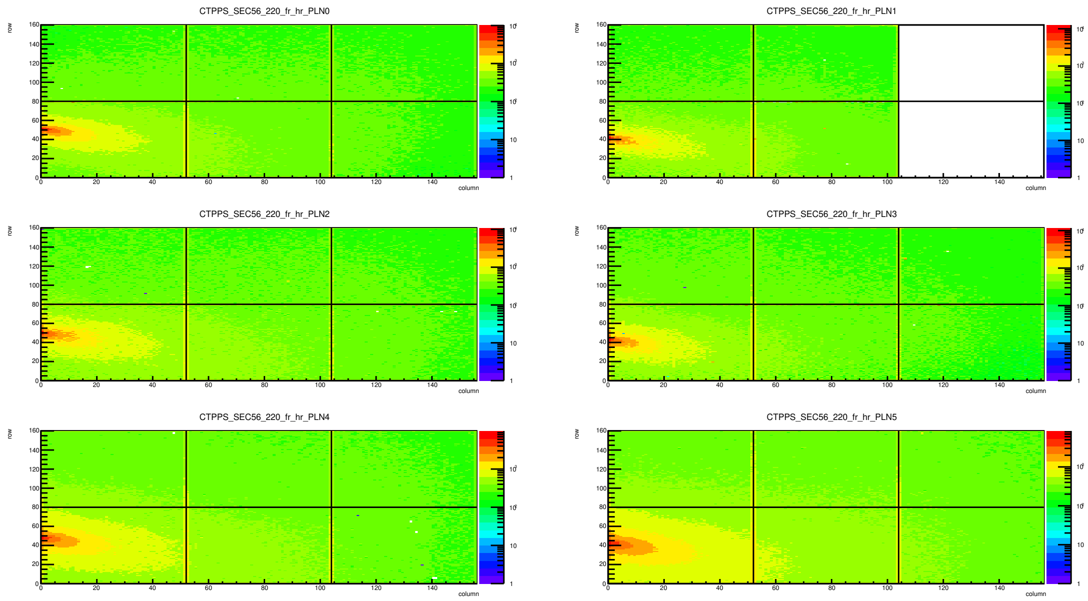

(b) Pixel detector hit maps in sector 56.

Figure 6.24: Hit maps of the CT-PPS pixel modules acquired during the alignment run. The shift of the beams with respect to the center of the modules is in accordance with the ~ 4 mm expected on the basis of the 2017 LHC optics.

Chapter 7

Summary and conclusions

This thesis presents the work done for the design, construction, installation, and commissioning of the CT-PPS 3D pixel tracking detector, recently added to the CMS experiment at the Large Hadron Collider. The aim of the project is the measurement of the leading protons emerging intact from the interaction and that escape at very small angles inside the LHC beam pipe, having lost only a small fraction of their momentum.

The detector is installed in movable structures, called Roman pots, in order to approach the beam at a few millimeters. Due to the small distance from the beam, a large radiation damage is expected. Moreover, events with multiple tracks are expected during the nominal running conditions of the LHC. Considering these conditions, 3D silicon pixel detectors have been chosen as baseline design for the CT-PPS tracking stations. 3D sensors consist of an array of columnar electrodes of both doping types that penetrate through the silicon bulk perpendicularly to the surface. This structure decouples the inter-electrode distance from the sensor thickness, allowing to reduce the drift path of the charge carriers without decreasing the total generated charge. Thanks to the reduced inter-electrode distance, the charge collection efficiency after irradiation is improved.

Several tests have been carried out on prototypes from the different 3D sensor producers (CNM, FBK, and SINTEF). Pixel layouts with a single readout electrode (1E) or two readout electrodes (2E) per pixel have been considered. The sensors, bump-bonded to the PSI46dig ROC that has been developed for the Phase I upgrade of the CMS pixel tracker, have been characterized in laboratory at the University of Torino. By using the Digital TestBoard with the software pXar, developed at PSI, the ROC parameters have been optimized, in particular the threshold has been trimmed at ~ 2000 e^-, about 10 times the noise of these devices.

3D prototypes have been measured at the Fermilab Test Beam Facility with 120 GeV protons by using a telescope with resolution of ~ 8 μm. Beam tests have been performed before and after irradiation at the expected fluences of $1 \div 3 \times 10^{15}$ n_{eq}/cm^2). FBK sensors have been irradiated within the AIDA Collaboration at the Karlsruher Institut für Technologie (KIT, Karlsruhe, Germany), where the facility provides a uniform irradiation on the samples with 23 MeV protons. CNM and SINTEF sensors have been irradiated not uniformly at the CERN IRRAD Proton Facility with 23 GeV protons.

The analysis of the beam test data indicates that the full depletion of the sensors is reached at very low bias voltages (< 10 V with a dependence on the threshold) and that the inefficiency due to the hollow electrodes can be completely recovered by rotating the detector with respect to the beam direction by less than 10°. Irrespective of the specific sensor, a mean efficiency higher than 99.5% before irradiation has been obtained, which remains higher than 95% after irradiation. Resolutions of ~ 25 μm and ~ 10 μm for clusters of size 1 and 2, respectively, with a cluster size 2 probability of $\sim 35\%$, have been reaches for angles of 10°. Considering that the detector packages consist of 6 planes, these results fulfill the CT-PPS requirements.

Another crucial request for the CT-PPS tracker is an insensitive region of the detector as small as possible on the side facing the beam. Both FBK and CNM sensors implement a 200 μm slim edge with a p-type column fences containing the electric field. Thanks to this layout, the efficient region can be extended of more than 100 μm beyond the geometrical edge of the pixel by increasing the applied bias voltage. The tested SINTEF sensor has instead an active edge, with the efficient region extending up to few microns from the sensor edge.

After irradiation, the expected increase of the breakdown voltage has been measured, which is very important for being able to apply an electric field high enough to still efficiently collect the charge. Indeed, an effective improvement after irradiation has been only observed with the 2E configuration of the SINTEF sensor, indicating that this layout should be preferred in the CT-PPS conditions.

Sensors for the final detector have been fabricated by CNM, a choice also driven by the availability of the production line. Sensors are implemented on 4" p-type high-resistivity Float Zone wafers with a thickness of 230 μm. Columnar electrodes are 200 μm deep with a diameter of 10 μm. The wafer layout contains 2×3 (6 ROCs) devices as baseline sensors, 2×2 (4 ROCs) sensors as backup solution, plus smaller test structures. 2E sensors ensure better performance after irradiation but their expected yield is lower because of the higher column density. For this reason, 1E sensors have been included in the wafer layout. Two batched of 12 wafers each have been produced by CNM. The first batch had a low yield of class A sensors. The second production had a serious issue during the implantation of the p-stop insulation around the readout electrodes and the breakdown of all sensors was well below the requirements. A third batch is currently in production. For assembling the two needed detector packages, 1E and 2×2 modules have also been used.

Sensors, bump-bonded at IZM to PSI46dig ROCs from the CMS Pixel Phase I production, have been qualified in laboratory and also with X-rays for checking the quality of the bump-bonding. Ten single-ROC detectors have been tested at Fermilab, showing for the 2E layout better performances with respect to the prototypes in terms of depletion voltage ($\sim 3 - 5$ V), extension of the efficient region at the sensor edge (~ 150 μm), and resolution (~ 22 μm). At the same time, measurements indicate that 1E modules anyway accomplish the CT-PPS requirements and can be used for the detector.

By using a temporary wire-bonding to the RPix flex hybrid, all modules have been qualified in Torino and Genova laboratories, selecting 34 modules for the final assembling over the initial 46. Two complete detector stations have been mounted at CERN and tested with the final backend electronics before installation in the LHC tunnel, in the same conditions of cooling and secondary vacuum. To this purpose, the DAQ software has been developed, based on the Pixel Online Software of the central tracker.

The two tracking stations have been installed along the LHC beam line in March 2017. The detectors have been connected to DCS and DSS for the service control and safety actions. The detector performances have been verified and no damage occured during the installation. Both dead and noisy pixels are less than 0.05% using a threshold at ~ 2000 e$^-$. Thanks to the trimming procedure the threshold RMS has been reduced to ~ 135 e$^-$. The ADC scale has been optimized in order to have a linearity range up to charges of 38 ke$^-$.

The CT-PPS pixel detector is now included in the CMS global DAQ chain after having passed all the standard stress tests. The tuning of the latency has been successfully performed. The detector recently participated in the Roman pot alignment run, a special run for CT-PPS with the pots at 8.5σ from the beam. The collected data will allow to measure the position of the modules with respect the beam and to align the planes with respect to each other. Both information will be crucial for the reconstruction of the data that will be collected in 2017.

Based on the LHC foreseen plan, the new CT-PPS pixel tracking detector will collect $\sim$ 40 fb^{-1} of data during the 2017 running operations, opening with the measurements of central exclusive production new possibilities of physics searches.

Bibliography

[1] The CMS and TOTEM diffractive and forward physics working group, “Prospects for Diffractive and Forward Physics at the LHC,” Tech. Rep. LHCC-G-124. CERN-LHCC-2006-039-G-124. CMS-Note-2007-002. TOTEM-Note-2006-005. CERN-TOTEM-Note-2006-005, CERN, Dec 2006.

[2] M. G. Albrow, T. D. Coughlin, and J. R. Forshaw, “Central Exclusive Particle Production at High Energy Hadron Colliders,” *Prog. Part. Nucl. Phys.*, vol. 65, pp. 149–184, 2010.

[3] V. A. Khoze, A. D. Martin, and M. G. Ryskin, “Double diffractive processes in high resolution missing mass experiments at the Tevatron,” *Eur. Phys. J.*, vol. C19, pp. 477–483, 2001. [Erratum: Eur. Phys. J.C20,599(2001)].

[4] J. A. M. Vermaseren, “Two Photon Processes at Very High-Energies,” *Nucl. Phys.*, vol. B229, pp. 347–371, 1983.

[5] S. P. Baranov, O. Duenger, H. Shooshtari, and J. A. M. Vermaseren, “LPAIR: A generator for lepton pair production,” in *Workshop on Physics at HERA Hamburg, Germany, October 29-30, 1991*, pp. 1478–1482, 1991.

[6] TOTEM Collaboration, “TOTEM Upgrade Proposal,” Tech. Rep. CERN-LHCC-2013-009. LHCC-P-007, CERN, Geneva, Jun 2013.

[7] TOTEM Collaboration, “Timing Measurements in the Vertical Roman Pots of the TOTEM Experiment,” Tech. Rep. CERN-LHCC-2014-020. TOTEM-TDR-002, Sep 2014.

[8] K. Öesterberg, “Recent and planned measurements from totem.” Presentation at Forward Physics WG: diffraction and heavy ions, Trento, September 2016.

[9] V. Khoze, A. Martin, and M. Ryskin, “Double-diffractive processes in high-resolution missing-mass experiments at the Tevatron,” *Eur. Phys. J.*, vol. C 19, pp. 477–483 and erratum ibid. C 20 (2001) 599, 2001.

[10] C. Marquet, C. Royon, M. Saimpert, and D. Werder, “Probing the Pomeron structure using dijets and γ+jet events at the LHC,” *Phys. Rev.*, vol. D88, no. 7, p. 074029, 2013.

[11] M. Albrow *et al.*, “CMS-TOTEM Precision Proton Spectrometer,” Tech. Rep. CERN-LHCC-2014-021. TOTEM-TDR-003. CMS-TDR-13, Sep 2014.

[12] J. Monk and A. Pilkington, “ExHuME: A Monte Carlo event generator for exclusive diffraction,” *Comput. Phys. Commun.*, vol. 175, pp. 232–239, 2006.

[13] G. Corcella *et al.*, “HERWIG 6.5 release note,” 2002.

[14] T. Sjostrand, S. Mrenna, and P. Z. Skands, “A Brief Introduction to PYTHIA 8.1,” *Comput. Phys. Commun.*, vol. 178, pp. 852–867, 2008.

[15] J. Allison *et al.*, "Geant4 Developments and Applications ," *IEEE Transactions on Nuclear Science*, vol. 53, pp. 270–278, 2006.

[16] J. de Favereau, X. Rouby, and K. Piotrzkowski, "Hector: A Fast simulator for the transport of particles in beamlines," *JINST*, vol. 2, p. P09005, 2007.

[17] "CMSSW." Online. Avaiable: `https://twiki.cern.ch/twiki/bin/view/CMSPublic/WorkBookCMSSWFramework`.

[18] M. Trzebinski, *Study of QCD and Diffraction with the ATLAS detector at the LHC*. PhD thesis, Cracow, INP, 2013.

[19] S. Chatrchyan *et al.*, "Study of exclusive two-photon production of W^+W^- in pp collisions at $\sqrt{s} = 7$ TeV and constraints on anomalous quartic gauge couplings," *JHEP*, vol. 07, p. 116, 2013.

[20] V. Khachatryan *et al.*, "Evidence for exclusive $\gamma\gamma \to W^+W^-$ production and constraints on anomalous quartic gauge couplings in pp collisions at $\sqrt{s} = 7$ and 8 TeV," *JHEP*, vol. 08, p. 119, 2016.

[21] M. Boonekamp, A. Dechambre, V. Juranek, O. Kepka, M. Rangel, C. Royon, and R. Staszewski, "FPMC: A Generator for forward physics," 2011.

[22] T. Aaltonen *et al.*, "Observation of Exclusive Charmonium Production and $\gamma\gamma \to \mu^+\mu^-$ in $p\overline{p}$ Collisions at $\sqrt{s} = 1.96$ TeV," *Phys. Rev. Lett.*, vol. 102, p. 242001, Jun 2009.

[23] S. Chatrchyan *et al.*, "Exclusive $\gamma\gamma{\to}\mu^+\mu^-$ production in proton-proton collisions at $\sqrt{s} = 7$ TeV," *Journal of High Energy Physics*, vol. 2012, no. 1, p. 52, 2012.

[24] V. Khoze, A. Martin, and M. Ryskin, "Prospects for new physics observations in diffractive processes at the LHC and Tevatron," *The European Physical Journal C - Particles and Fields*, vol. 23, no. 2, pp. 311–327, 2002.

[25] C. Royon, "Forward physics at the LHC: from the structure of the Pomeron to the search for γ-induced resonances," vol. arXiv, p. 1606.07675, 2016.

[26] S. Fichet, G. von Gersdorff, O. Kepka, B. Lenzi, C. Royon, and M. Saimpert, "Probing new physics in diphoton production with proton tagging at the Large Hadron Collider," *Phys. Rev. D*, vol. 89, p. 114004, Jun 2014.

[27] L. Randall and R. Sundrum, "Large Mass Hierarchy from a Small Extra Dimension," *Phys. Rev. Lett.*, vol. 83, pp. 3370–3373, Oct 1999.

[28] S. Fichet, G. von Gersdorff, O. Kepka, B. Lenzi, C. Royon, and M. Saimpert, "Probing new physics in diphoton production with proton tagging at the Large Hadron Collider," *Phys. Rev. D*, vol. 89, p. 114004, Jun 2014.

[29] S. Chatrchyan *et al.*, "The CMS experiment at the CERN LHC," *JINST*, vol. 3, p. S08004, 2008.

[30] G. Aad *et al.*, "The ATLAS Experiment at the CERN Large Hadron Collider," *JINST*, vol. 3, p. S08003, 2008.

[31] A. A. Alves, Jr. *et al.*, "The LHCb Detector at the LHC," *JINST*, vol. 3, p. S08005, 2008.

[32] The ALICE Collaboration, "ALICE: Physics Performance Report, Volume I," *Journal of Physics G: Nuclear and Particle Physics*, vol. 30, no. 11, p. 1517, 2004.

[33] C. O'Luanaigh, "The Large Hadron Collider," Jan 2014.

[34] C. Lefèvre, "The CERN accelerator complex. Complexe des accélérateurs du CERN." Dec 2008.

[35] D. Kotlinski, "Status of the CMS Pixel detector," *JINST*, vol. 4, no. 03, p. P03019, 2009.

[36] J. Karancsi, "Operational Experience with the CMS Pixel Detector," Tech. Rep. CMS-CR-2014-368, CERN, Geneva, Nov 2014. Comments: Pixel2014 Conference proceeding.

[37] H. C. Kaestli *et al.*, "Design and performance of the CMS pixel detector readout chip," *Nucl. Instrum. Meth.*, vol. A565, pp. 188–194, 2006.

[38] The CMS Collaboration, "CMS Tracker Detector Performance Results." `https://twiki.cern.ch/twiki/bin/view/CMSPublic/DPGResultsTRK`.

[39] M. Lipinski, "Overview and present status of the CMS Phase 1 pixel upgrade," *Nucl. Instrum. Meth.*, vol. A824, pp. 27–29, 2016.

[40] V. Karimäki *et al.*, *The CMS tracker system project: Technical Design Report*. Technical Design Report CMS, Geneva: CERN, 1997.

[41] The CMS Collaboration, *The CMS electromagnetic calorimeter project: Technical Design Report*. Technical Design Report CMS, Geneva: CERN, 1997.

[42] The CMS Collaboration, *CMS Physics: Technical Design Report Volume 1: Detector Performance and Software*. Technical Design Report CMS, CERN, 2006.

[43] A. Bornheim, "Timing performance of the CMS electromagnetic calorimeter and prospects for the future," *PoS*, vol. TIPP2014, p. 021, 2014.

[44] G. Baiatian *et al.*, "Design, Performance, and Calibration of CMS Hadron-Barrel Calorimeter Wedges," 2007.

[45] S. Abdullin *et al.*, "Design, performance, and calibration of the CMS Hadron-outer calorimeter," *Eur. Phys. J.*, vol. C57, pp. 653–663, 2008.

[46] S. Dasu *et al.*, "CMS. The TriDAS project. Technical design report, vol. 1: The trigger systems," 2000.

[47] P. Sphicas, "CMS: The TriDAS project. Technical design report, Vol. 2: Data acquisition and high-level trigger," 2002.

[48] V. Berardi *et al.*, *Total cross-section, elastic scattering and diffraction dissociation at the Large Hadron Collider at CERN: TOTEM Technical Design Report*. Technical Design Report TOTEM, Geneva: CERN, 2004.

[49] M. Berretti, S. Lami, and A. Scribano, "Measurement of the forward charged particle pseudorapidity density in pp collisions at $\sqrt{s} = 7$ TeV with the TOTEM experiment.," Sep 2012. Presented 27 Nov 2012.

[50] G. Anelli *et al.*, "The TOTEM experiment at the CERN Large Hadron Collider," *JINST*, vol. 3, p. S08007, 2008.

[51] S. Lami, G. Latino, E. Oliveri, L. Ropelewski, and N. Turini, "A triple-GEM telescope for the TOTEM experiment," *Nucl. Phys. Proc. Suppl.*, vol. 172, pp. 231–233, 2007.

[52] U. Amaldi *et al.*, "The Energy dependence of the proton proton total cross-section for center-of-mass energies between 23 and 53 GeV," *Phys. Lett.*, vol. B44, pp. 112–118, 1973.

[53] G. Antchev and others., "Measurement of Elastic pp Scattering at $\sqrt{s} = 8$ TeV in the Coulomb-Nuclear Interference Region – Determination of the ρ Parameter and the Total Cross-Section," Tech. Rep. CERN-PH-EP-2015-325, CERN, Geneva, Dec 2015.

[54] G. Ruggiero *et al.*, "Characteristics of edgeless silicon detectors for the Roman Pots of the TOTEM experiment at the LHC," *Nucl. Instrum. Meth.*, vol. A604, pp. 242–245, 2009.

[55] G. Ruggiero *et al.*, "Characteristics of edgeless silicon detectors for the Roman Pots of the TOTEM experiment at the LHC," *Nucl. Instrum. Methods Phys. Res., A*, vol. 604, no. 1-2, pp. 242–245, 2009.

[56] C. C. Collaboration, "Search for new physics in high mass diphoton events in proton-proton collisions at 13TeV," 2015.

[57] "Search for resonances decaying to photon pairs in 3.2 fb^{-1} of pp collisions at $\sqrt{s} = 13$ TeV with the ATLAS detector," Tech. Rep. ATLAS-CONF-2015-081, CERN, Geneva, Dec 2015.

[58] S. Fichet, G. von Gersdorff, and C. Royon, "Scattering light by light at 750 GeV at the LHC," *Phys. Rev.*, vol. D93, no. 7, p. 075031, 2016.

[59] T. A. collaboration, "Search for resonant production of high mass photon pairs using $12.9\,\mathrm{fb}^{-1}$ of proton-proton collisions at $\sqrt{s} = 13$ TeV and combined interpretation of searches at 8 and 13 TeV," Tech. Rep. CMS-PAS-EXO-16-027, CERN, Geneva, 2016.

[60] T. A. collaboration, "Search for scalar diphoton resonances with 15.4 fb^{-1} of data collected at $\sqrt{s}$=13 TeV in 2015 and 2016 with the ATLAS detector," 2016.

[61] J. Kašpar, "CT-PPS data taking and physics programme." Presentation at Forward Physics WG: diffraction and heavy ions, Trento, September 2016.

[62] J. Troska, S. Detraz, S. S. E. Nasr-Storey, P. Stejskal, C. Sigaud, C. Soos, and F. Vasey, "Prototype pixel optohybrid for the CMS phase 1 upgraded pixel detector," *JINST*, vol. 7, no. 01, p. C01113, 2012.

[63] V. Vacek, G. D. Hallewell, S. Ilie, and S. Lindsay, "Perfluorocarbons and their use in Cooling Systems for Semiconductor Particle Detectors," *Fluid Phase Equilib.*, vol. 174, pp. 191–201, 2000.

[64] N. Cartiglia *et al.*, "Design optimization of ultra-fast silicon detectors," *Nucl. Instrum. Methods Phys. Res., A*, vol. 796, pp. 141 – 148, 2015. Proceedings of the 10th International Conference on Radiation Effects on Semiconductor Materials Detectors and Devices.

[65] M. Berretti, "The diamond time of flight detector of the {TOTEM} experiment," *Nucl. Instrum. Methods Phys. Res., A*, 2016.

[66] F. Anghinolfi *et al.*, "NINO: An ultra-fast and low-power front-end amplifier/discriminator ASIC designed for the multigap resistive plate chamber," *Nucl. Instrum. Meth.*, vol. A533, pp. 183–187, 2004.

[67] J. Christiansen, "HPTDC High Performance Time to Digital Converter," tech. rep., CERN, Geneva, 2004. Version 2.2 for HPTDC version 1.3.

[68] J. Frisch *et al.*, "Status of the LCLS Experiment Timing System," in *Proceedings, 1st International Beam Instrumentation Conference (IBIC2012): Tsukuba, Japan, October 1-4, 2012*, 2012.

[69] M. G. Albrow *et al.*, "Quartz Cherenkov counters for fast timing: QUARTIC," *JINST*, vol. 7, no. 10, p. P10027, 2012.

[70] "Timing Measurements in the Vertical Roman Pots of the TOTEM Experiment," Tech. Rep. CERN-LHCC-2014-020. TOTEM-TDR-002, Sep 2014.

[71] M. Berretti, "Totem diamonds detector development." Presentation at 3rd Elba Workshop on Forward Physics @ LHC Energy, May 2016.

[72] H.F-W. Sadrozinski et al., "Ultra-fast silicon detectors," *Nucl. Instrum. Meth.*, vol. A 730, pp. 226–231, 2013.

[73] G. Pellegrini *et al.*, "Technology developments and first measurements of Low Gain Avalanche Detectors (LGAD) for high energy physics applications," *Nucl. Instrum. Methods Phys. Res., A*, vol. 765, pp. 12 – 16, 2014.

[74] N. Cartiglia, "4d pixel detectors." Presentation at 8th International Workshop on Semiconductor Pixel Detectors for Particles and Imaging., September 2016.

[75] N. Cartiglia *et al.*, "Beam test results of a 15 ps timing system based on ultra-fast silicon detectors," 2016.

[76] F. Cenna *et al.*, "Weightfield2: A fast simulator for silicon and diamond solid state detector," *Nucl. Instrum. Methods Phys. Res., A*, vol. 796, pp. 149 – 153, 2015.

[77] F. Cenna, "TOFFEE: a fully custom amplifier-comparator chip for timing applications with silicon detectors." Presentation at TWEPP 2016 - Topical Workshop on Electronics for Particle Physics, September 2016.

[78] M. Deile, "Status of Roman Pot Insertion Tests." Presentation at the CT-PPS Collaboration meeting, October 2015.

[79] M. Deile, "RP insertions 2016: Physics Acceptance & Interaction with Beam Environmen." Presentation at rd Elba Workshop on Forward Physics @ LHC Energy, June 2016.

[80] M. Deile, "Beam conditions, alignment and calibration runs in 2017," May 2017.

[81] K. A. Olive *et al.*, "Review of Particle Physics," *Chin. Phys.*, vol. C38, p. 090001, 2014.

[82] M. Rogalla *et al.*, "Radiation studies for GaAs in the ATLAS inner detector," *Nucl. Instrum. Methods Phys. Res., A*, vol. 395, no. 1, pp. 45 – 48, 1997.

[83] S. M. Sze and K. K. Ng, *Physics of Semiconductor Devices.* McGraw-Hill Company, 2002.

[84] S. Sze, *Semiconductor Devices, Physics and Technology, 2nd edition.* John Wiley and Sons, 2002.

[85] V. A. J. van Lint, T. M. Flanagan, R. E. Leadon, J. A. Naber, and V. C. Rogers, *Mechanisms of Radiation Effects in Electronic Materials.* John Wiley & Sons, 1980.

[86] M. Moll, *Radiation Damage in Silicon Particle Detectors.* PhD thesis, Hamburg university, 1999.

[87] G. Lindström et al., "Radiation hardness of silicon detectors - a challenge from high-energy physics," *Nucl. Instrum. Meth.*, vol. A 426, pp. 1–15, 1999.

[88] L. Rossi et al., *Pixel Detectors - From Fundamentals to Applications.* Springer, 2006.

[89] J. Wüstenfeld, *Characterisation of Ionisation-Induced Surface Effects for the Optimisation of Silicon-Detectors for Particle Physics Applications.* PhD thesis, University of Dortmund, Germany, 2001.

[90] R. Wunstorf *et al.*, "Damage-induced surface effects in silicon detectors," *Nucl. Instrum. Meth.*, vol. A 377, no. 2, pp. 290 – 297, 1996.

[91] J. J Zhang *et al.*, "Study of X-ray radiation damage in silicon sensors," *JINST*, vol. 6, no. 11, p. C11013, 2011.

[92] R. Klanner *et al.*, "Study of high-dose X-ray radiation damage of silicon sensors," *Nucl. Instrum. Meth.*, vol. A 732, pp. 117 – 121, 2013.

[93] W. Snoeys, "CMOS monolithic active pixel sensors for high energy physics," *Nucl. Instrum. Meth.*, vol. A 765, pp. 167 – 171, 2014.

[94] H. C. Kaestli *et al.*, "Design and performance of the CMS pixel detector readout chip," *Nucl. Instrum. Meth.*, vol. A 565, pp. 188–194, 2006.

[95] Ivan Perić et al., "The FEI3 Readout Chip forthe ATLAS Pixel Detector," *Nucl. Instrum. Meth.*, vol. A 565, pp. 178–187, 2006.

[96] M. Karagounis et al., "Development of the ATLAS FE-I4 pixel readout IC for B-layer Upgrade and Super-LHC," *CERN-2008-008*, pp. 70–75, 2009.

[97] N. Demaria *et al.*, "RD53 Collaboration and CHIPIX65 Project for the development of an innovative Pixel Front End Chip for HL-LHC," *PoS*, vol. IFD2014, p. 010, 2015.

[98] S. Parker, C. Kenney, and J. Segal, "3D — A proposed new architecture for solid-state radiation detectors," *Nucl. Instrum. Meth.*, vol. A 395, pp. 328–343, 1997.

[99] C. Kenney, S. Parker, J. Segal, and C. Storment, "Silicon Detectors with 3-D Electrode Arrays: Fabrication and Initial Test Results," *IEEE Trans. Nucl. Sci.*, vol. 46, pp. 1224–1236, 1999.

[100] J. Bhardwaj and H. Ashraf, "Advanced silicon etching using high density plasmas," *SPIE*, vol. 2639, pp. 224–233, 1995.

[101] C. J. Kenney, S. Parker, and E. Walckiers, "Results From 3-D Silicon Sensors With Wall Electrodes: Near-Cell-Edge Sensitivity Measurements as a Preview of Active-Edge Sensors," *IEEE Trans. Nucl. Sci.*, vol. 48, pp. 2405–2410, 2001.

[102] M. Povoli, A. Bagolini, M. Boscardin, G.-F. Dalla Betta, G. Giacomini, E. Vianello, and N. Zorzi, "Slim edges in double-sided silicon 3D detectors," *JINST*, vol. 7, no. 01, p. C01015, 2012.

[103] M. Capeans et al., "ATLAS Insertable B-Layer Technical Design Report," tech. rep., CERN-LHCC-2010-013, 2010.

[104] P. Grenier *et al.*, "Test beam results of 3D silicon pixel sensors for the ATLAS upgrade," *Nucl. Instrum. Meth.*, vol. A 638, no. 1, pp. 33 – 40, 2011.

[105] P. Hansson *et al.*, "3D silicon pixel sensors: Recent test beam results," *Nucl. Instrum. Meth.*, vol. A 628, no. 1, pp. 216 – 220, 2011. 2010 Proceedings of the 12th International Vienna Conference on Instrumentation.

[106] M. Mathes *et al.*, "Test Beam Characterization of 3-D Silicon Pixel Detectors," *IEEE Transactions on Nuclear Science*, vol. 55, pp. 3731–3735, Dec 2008.

[107] G.-F. Dalla Betta *et al.*, "Development of 3D-DDTC pixel detectors for the ATLAS upgrade," *Nucl. Instrum. Meth.*, vol. A 636, no. 1, Supplement, pp. S15 – S23, 2011. 7th International Hiroshima Symposium on the Development and Application of Semiconductor Tracking Detectors.

[108] J. C. Chistiansen and M. L. Garcia-Sciveres, "RD Collaboration Proposal: Development of pixel readout integrated circuits for extreme rate and radiation," Tech. Rep. CERN-LHCC-2013-008. LHCC-P-006, CERN, Geneva, Jun 2013.

[109] G. Steinbrück, "Small pitch pixel sensors for the CMS phase II upgrade," in *2015 IEEE Nuclear Science Symposium and Medical Imaging Conference (NSS/MIC)*, pp. 1–6, Oct 2015.

[110] R. Bates, "ATLAS pixel upgrade for the HL-LHC," *PoS*, vol. VERTEX2015, p. 006, 2015.

[111] D. V. Furelos *et al.*, "3D sensors for the HL-LHC," in *Proceedings, 18th International Workshop on Radiation Imaging Detectors (IWORID 2016): Barcelona, Spain, July 3-7, 2016*, 2016.

[112] D. V. Furelos, "Beam test measurements of irradiated 3D pixel sensors with 50×50 μm^2 pixel size." Presentation. 12th Trento Workshop on Advanced Silicon Radiation Detectors, Trento, Italy.

[113] "Sintef, Oslo, Norway." Online. Avaiable: `http://www.sintef.no/home/`.

[114] M. Povoli, "Status of single-sided 3D detector development at SINTEF." Presentation. 10th Anniversary Trento Workshop on Advanced Silicon Radiation Detectors, Trento, Italy.

[115] D. Sultan, G.-F. D. Betta, R. Mendicino, M. Boscardin, S. Ronchin, and N. Zorzi, "First production of new thin 3D sensors for HL-LHC at FBK," vol. 12, p. C01022, 2017.

[116] H. Oide, "3D sensors measurements with FEi4 read-out chips." Presentation. 12th Trento Workshop on Advanced Silicon Radiation Detectors, Trento, Italy.

[117] A. Messineo, "Pixel Detectors Development for CMS Phase-2 Upgrade." Presentation. 12th Trento Workshop on Advanced Silicon Radiation Detectors, Trento, Italy.

[118] H. C. Kaestli, "Frontend electronics development for the CMS pixel detector upgrade," *Nucl. Instrum. Meth.*, vol. A 731, pp. 88 – 91, 2013. PIXEL 2012.

[119] A. Dominguez *et al.*, "CMS Technical Design Report for the Pixel Detector Upgrade," Tech. Rep. CERN-LHCC-2012-016. CMS-TDR-11, Sep 2012.

[120] F. Meier, *psi46dig pixel chip External Specification Manual*, 2016.

[121] E. Bartz, *Token Bit Manager 08C Chip Documentation*, 2015.

[122] B. Meier, "Roc submission." Internal presentation at the CMS Tracker week, 2012.

[123] S. Kwan *et al.*, "The pixel tracking telescope at the Fermilab Test Beam Facility," *Nucl. Instrum. Meth.*, vol. A 811, pp. 162–169, 2016.

[124] M. M. Turqueti *et al.*, "CAPTAN: A hardware architecture for integrated data acquisition, control, and analysis for detector development," 2008. FERMILAB-PUB-08-527-CD.

[125] O. Tange, "Gnu parallel - the command-line power tool," *;login: The USENIX Magazine*, vol. 36, pp. 42–47, Feb 2011.

[126] E. Alagoz et al., "Simulation and laboratory test results of 3D CMS pixel detectors for HL-LHC," *JINST*, vol. 7, no. 08, p. P08023, 2012.

[127] G. Darbo, "Experience on 3D silicon sensors for ATLAS IBL," *JINST*, vol. 10, no. 05, p. C05001, 2015.

[128] "3D silicon sensors: Design, large area production and quality assurance for the ATLAS IBL pixel detector upgrade," *Nucl. Instrum. Meth.*, vol. A 694, pp. 321–330, 2012.

[129] M. Povoli *et al.*, "Layout and process improvements to double-sided silicon 3D detectors fabricated at FBK," in *IEEE Nucl. Sci. Symp. Conf. Rec.*, p. 1334, 2012.

[130] G.-F. D. Betta *et al.*, "Investigation of leakage current and breakdown voltage in irradiated double-sided 3D silicon sensors," *JINST*, vol. 11, no. 09, p. P09006, 2016.

[131] D. Hits and A. Starodumov, "The CMS Pixel Readout Chip for the Phase 1 Upgrade," *JINST*, vol. 10, no. 05, p. C05029, 2015.

[132] G. Pellegrini *et al.*, "3D double sided detector fabrication at IMB-CNM," *Nucl. Instrum. Meth.*, vol. A 699, pp. 27–30, 2013.

[133] C. Da Viá *et al.*, "3D silicon sensors: Design, large area production and quality assurance for the ATLAS IBL pixel detector upgrade," *Nucl. Instrum. Meth.*, vol. A 694, pp. 321–330, 2012.

[134] A. Chilingarov, "Temperature dependence of the current generated in Si bulk," *JINST*, vol. 8, no. 10, p. P10003, 2013.

[135] K. Koba and *et al.*, "Slip stacking experiments at fermilab main injector," in *Proceedings of the 2003 Particle Accelerator Conference*, vol. 3, pp. 1736–1738 vol.3, 2003.

[136] J. Lange, E. Cavallaro, S. Grinstein, and I. L. Paz, "3D silicon pixel detectors for the ATLAS Forward Physics experiment," *JINST*, vol. 10, no. 03, p. C03031, 2015.

[137] N. Zorzi, "Latest developments for the improvement of double-sided 3D detectors fabrication at FBK." Presentation. 8th Trento Workshop on Advanced Silicon Radiation Detectors, Trento, Italy.

[138] S. Grinstein, "3D Sensors for the HL-LHC." Presentation, 2016. 11th Trento Workshop on Advanced Silicon Radiation Detectors, Trento, Italy.

[139] F. Salvat, "PENELOPE-2014: A Code System for Monte Carlo Simulation of Electron and Photon Transport," *OECD NEA Data Bank/NSC DOC(2011)/5 OECD Nuclear Energy Agency, Issy-les-Moulineaux*, 2011.

[140] A. Ryd et al., *CMS Pixel Online Software and Calibrations*, September 2013.

[141] C. L. Phillips, "High Density Interconnect for the CMS Phase 1 Pixel Upgrade: Electrical Test and Visual Inspection," Aug 2015.

[142] M. Klas and S. Matejcik, "dc breakdown in air, oxygen and nitrogen at micrometer separations," Jan 2010.

[143] CAEN, *Technical Information Manual, MOD. A 1512 12 CH FLOATING HV BOARD*, Mar 2014.